University of Southampton

Faculty of Social Sciences
School of Mathematical Sciences

Critical phenomena in gravitational collapse

by

Patrick Georges Jean Bourg

ORCiD: 0000-0003-0015-0861

A thesis for the degree of
Doctor of Philosophy

25 January 2022

University of Southampton

Abstract

Faculty of Social Sciences
School of Mathematical Sciences

Doctor of Philosophy

Critical phenomena in gravitational collapse

by Patrick Georges Jean Bourg

This thesis' main aim is the study of the critical collapse of an ultrarelativistic perfect fluid in axisymmetry in $2+1$ dimensions. The study of critical collapse in this dimension is easier than in higher dimensions, notably because, even in axisymmetry, all variables only depend on time and radius. The main downside, however, is that studying critical collapse in $2+1$ dimensions necessitates the presence of a negative cosmological constant Λ.

To set the stage, we review the relevant literature concerning critical collapse. We also thoroughly study the above system in $3+1$ dimensions, restricted to spherical symmetry, both numerically and semi-analytically. Finally, we give a brief overview of anti-de Sitter space in any dimensions, as well as the rotating black-hole solution in $2+1$ dimensions.

We proceed by closely analyzing all rigidly rotating perfect fluid solutions in $2+1$ dimensions, with negative Λ and with general barotropic equation of state $P = P(\rho)$. These solutions turn out to be of crucial importance to the critical collapse of the perfect fluid. With the restriction of a regular center and finite total mass M and angular momentum J (rotating stars), they form a two-parameter family of solutions. Not all pairs (M, J) can be realized as stars, but when they do, spacetime is asymptotically anti-de Sitter, without horizons or closed timelike curves.

In order to perform our study, we develop a high-resolution shock-capturing formulation of the Einstein-perfect fluid system. In axisymmetry, in $2+1$ dimensions, there are *two* conserved quantities. They correspond to the angular momentum J, and a generalization of the Kodama conserved mass M. The associated two conserved matter currents are used in the stress-energy conservation, so that M and J are conserved during the evolution. We demonstrate pointwise and ℓ^2-norm convergence of the code in the test cases of generic dispersion and collapse, and stable and unstable rotating stars.

We then carry out the study of the critical collapse of a perfect fluid, with linear equation of state $P = \kappa\rho$, first restricting to spherical symmetry. We find that the associated critical phenomena are quite different from their $3+1$ counterparts: the critical solution is type I or II, depending on the value of κ. Furthermore, the type I critical solution is shown to be static, as expected, while the type II critical solution is surprisingly *not* self-similar. Instead, it is quasistatic, meaning that the solution shrinks adiabatically to zero size, going through the sequence of static solutions.

Finally, we generalize the above study to rotating initial data. We still find the same demarcation separating type I and II phenomena. In the type I case, the critical solution is now stationary. In the type II case, the picture is more subtle: for small angular momenta, we find type II phenomena and the critical solution is quasistationary. As the black-hole threshold is approached, the spin-to-mass ratio of the critical solution *increases* as it contracts, and hence so does that of the black hole created at the end. As extremality is approached, the contraction of the critical solution smoothly ends, so that the formation of extremal black holes is avoided.

Contents

Research Thesis: Declaration of Authorship

Print name: **Patrick Georges Jean Bourg**

Title of thesis: **Critical phenomena in gravitational collapse**

I declare that this thesis and the work presented in it is my own and has been generated by me as the result of my own original research.

I confirm that:

1. This work was done wholly or mainly while in candidature for a research degree at this University;
2. Where any part of this thesis has previously been submitted for a degree or any other qualification at this University or any other institution, this has been clearly stated;
3. Where I have consulted the published work of others, this is always clearly attributed;
4. Where I have quoted from the work of others, the source is always given. With the exception of such quotations, this thesis is entirely my own work;
5. I have acknowledged all main sources of help;
6. Where the thesis is based on work done by myself jointly with others, I have made clear exactly what was done by others and what I have contributed myself;
7. Parts of this work have been published as:
    - C. Gundlach and P. Bourg. "Rigidly rotating perfect fluid stars in $2+1$ dimensions". Phys. Rev. D **102**, 084023 (2020).
    - C. Gundlach, P. Bourg, and A. Davey. "A fully constrained, high-resolution shock-capturing, formulation of the Einstein-fluid equations in $2+1$ dimensions". Phys. Rev. D **104**, 024061 (2021).
    - P. Bourg and C. Gundlach. "Critical collapse of a spherically symmetric ultrarelativistic fluid in $2+1$ dimensions". Phys. Rev. D **103**, 124055 (2021).
    - P. Bourg and C. Gundlach. "Critical collapse of an axisymmetric ultrarelativistic fluid in $2+1$ dimensions". Phys. Rev. D **104**, 104017 (2021).

Signed: Date: 25 January 2022

Acknowledgements

First, I would like to thank my supervisors Prof. Carsten Gundlach and Prof. Leor Barack for their expertise and guidance throughout my PhD. They were always available and willing to answer questions and offer advice. This thesis and my academic development would not have been what they are now without their support and patience.

I would like to thank the Southampton Relativity group as a whole for creating a friendly and exciting environment.

I would also like to express my gratitude to Dr Inês Ancieto and Dr Ian Hawke, for their invaluable feedback during my progression reviews.

I extend my thanks to all my fellow PhD colleagues for making my time in Southampton enjoyable.

Finally, I am grateful for the continual support of my family. Their encouragements were crucial at multiple times during my PhD.

Chapter 1

Introduction

1.1 Gravitational collapse and singularity formation

Nature can be reduced to the interaction of four fundamental forces: gravitation, electromagnetism, the strong and weak nuclear forces. To put it simply, one could say that the goal of physics is to understand how these four forces act and interact with each other to create the world around us. These four fundamental forces can be roughly split into two categories: on the one side, we have the Standard Model, which unifies the latter three forces into one coherent framework. On the other side, we have the theory of general relativity, describing the force of gravity. General relativity is a rather difficult theory to apprehend, notably because it introduces many unfamiliar notions. One such example is that space and time are not independent, static concepts on which events take place. Instead, they form a single entity, spacetime, which dynamically responds to the motion of matter living in it. Nonetheless, the theory, now more than a century old, has survived the test of time and proven to be one of the most well-tested theories in scientific history.

One of the most interesting objects in general relativity, first discovered by Schwarzschild, is the existence of massive compact objects, whose gravitational pull is so strong that nothing, not even light, can escape it: *black holes*. Black holes are a surprising mixture of simplicity and complexity. They are simple in the sense that, in the case of gravity minimally coupled to electromagnetism, black-hole solutions are completely characterized by three parameters: their mass M, charge Q and angular momentum J. This fact makes up the celebrated no-hair theorem [5, 6]. However, black holes are not always so simple, since for other matter fields, such as some minimally-coupled scalar fields [7] and non-Abelian fields [8, 9], the outside of the black hole is not described by only three parameters. To contrast with the no-hair theorem, these kind of black holes are called *hairy black-holes*. Additionally, black holes contain a singularity at their "center", signifying that the theory breaks down there.

Nowadays, black holes have become part of the daily lives of astronomers. On the observational front, black holes are routinely detected, thanks to gravitational-waves detectors (such as LIGO and Virgo) [10–13]. Astrophysically, stellar objects, born from remnants of other stars, persist over long periods of time, due to a delicate balance between their own gravitational

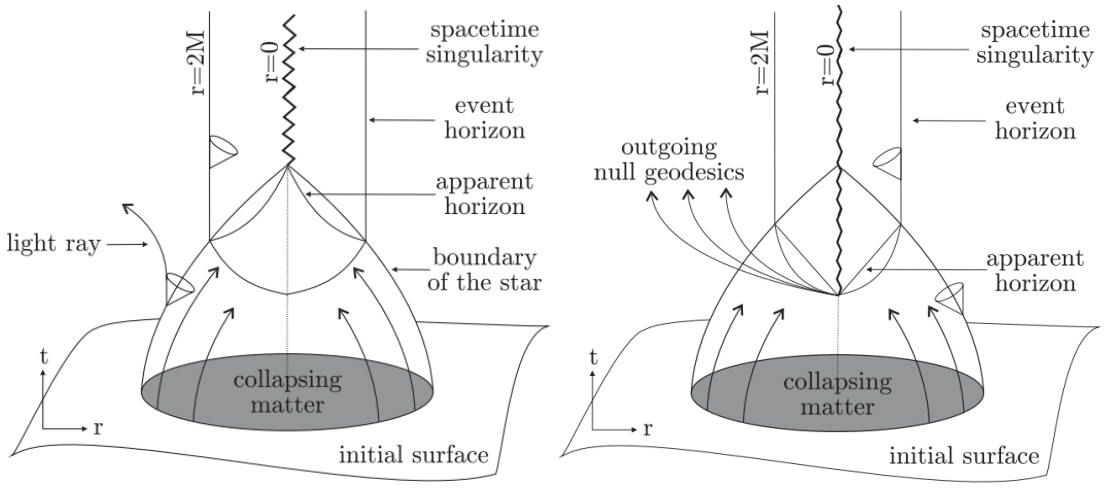

FIGURE 1.1: Typical formation of a spacetime singularity from gravitational collapse. On the left, the event horizon forms before the formation of the singularity, so that the latter is hidden, as in the homogeneous Oppenheimer-Snyder dust model. On the right, the singularity is naked for a short time, before being covered by the event horizon, as in the inhomogeneous dust model. Image credit: [15].

attraction and their internal nuclear reactions. Eventually, once the nuclear fuel has been exhausted, gravity takes over and the star begins to contract into itself. Part of the star is ejected in a violent explosion, called a supernova. The final fate of the stellar remnant primarily depends on its mass, becoming either a white dwarf, a neutron star or a black hole. In the latter scenario, known as gravitational collapse, no known physical force is able to halt this process. From the classical point of view, this collapse ends after some finite amount of proper time, at which the star has collapsed down to a single point. If taken at face value, the density of the object and the curvature of spacetime are infinite at that point: a singularity has formed.

On the theory front, much progress has also been made to understand these interesting objects. It is, however, worth taking a step back and appreciate the fact that black holes are very counter-intuitive entities. As a matter of fact, it should come as no surprise that these black-holes solutions were, at first, dismissed as no more than a mathematical curiosity. After all, if general relativity turns out to correctly describe the gravitational force, then how could there possibly be natural processes which cause matter to collapse in such a catastrophic way and produce these galactic entities? At around the same time, exact solutions of the Einstein equations were found by Friedmann, Lemaître and others, which were plausible cosmological models of our universe, such as the now well-known FLRW model. The problem, however, was that those models predicted that the universe's origin was a singular point, where densities and curvatures diverge. Similarly, but in the opposite time direction, Oppenheimer and Snyder [14] considered a spherically symmetric, homogeneous pressureless star (dust). They showed that such a configuration will undergo gravitational collapse and a black hole would eventually form; see left picture in Fig. 1.1. Both of these models strongly hinted that singularity formation in general relativity was much more realistic than first anticipated.

Note that, up until this point, we refrained from discussing exactly what these singularities are. In general relativity, it is important to distinguish between two different types of spacetime

singularities [6]. The first one is usually what one has in mind when talking about singularities. Namely, singularities are those points or regions in spacetime where curvature is infinite. Note that "curvature" is not completely unambiguous. It does not refer to any components of the Riemann tensor, because the Riemann tensor is coordinate dependent. Instead, "curvature" refers to some curvature invariants whose divergences are not tied to a poor choice of coordinate system. Two typical examples are the Ricci scalar $\mathrm{Ric} := g^{\mu\nu}R_{\mu\nu}$ (useful only when matter fields are present) and the Kretschmann scalar $R^{abcd}R_{abcd}$.

The second type of singularity refers to the geodesic incompleteness of spacetime. A geodesic is said to be complete if one can extend an affine parameter of the geodesic to $\pm\infty$. Roughly speaking, if a spacetime admits incomplete geodesics, then this means that there are "obstructions" that prevent the geodesic to be extended. Note that this definition has a priori nothing to do with a curvature invariant blowing up. For example, consider Minkowski spacetime in which a single point has been removed from the manifold. This truncated spacetime is still certainly flat, so no curvature invariant will blow up. There are no singularities of "the first type". On the other hand, this spacetime is incomplete because some geodesics will stop at the truncated point. Of course, this kind of singularity is not very interesting as it is rather artificial. In particular, one can "patch up" spacetime in order to remove this singularity. In this case, the incompleteness arises because spacetime was *extendible*. A spacetime is said to be extendible if it is isometric to some larger spacetime. It is easy to see that extendible spacetimes are geodesically incomplete.

More interesting are those spacetimes which are inextendible, but still geodesically incomplete. This is the case, for example, for the Kruskal solution (the maximal extension of the Schwarzschild solution). This spacetime is geodesic incomplete, but the nature of the incompleteness is quite different from the previous example: curvature also diverges where the geodesics stop. This divergence is then manifested in the incompleteness of spacetime.

It should be noted that, at the time where the Oppenheimer-Snyder dust model and the cosmological models were discovered, most researchers were still not convinced that black-hole formation was a generic feature of general relativity [16]. The most common rebuttal of those models was the assumption of spherical symmetry. By restricting the consideration to such a highly symmetrical situation, it is not very surprising that singularities can form. In fact, this is not a feature unique to general relativity. In newtonian mechanics for example, it is well known that spherical collapse can lead to singularity formation [17, 18]. Could it then be that black-hole formation in general relativity is also an artifact of spherical symmetry?

This debate was eventually resolved when, in 1965, Penrose showed [19, 20] that singularities (in the form of geodesic incompleteness) can form generically and their formation is not tied to a particular matter field or symmetry assumptions. The theorem states:

Penrose's singularity theorem: *A spacetime M cannot be geodesically complete if the following holds: 1) $T_{ab}V^aV^b \geq 0$ for all null vectors V^a, where T_{ab} is the stress-energy tensor (null-energy condition); 2) there is a non-compact Cauchy surface Σ in M (causality condition);*

3) there is a closed trapped surface $\mathcal{F}$ in M.

In order to appreciate the generality of this theorem, let us go over its three assumptions. First, the null-energy condition is one of several other energy conditions (other notable ones being the dominant, weak and strong conditions) that can be applied to a matter content, without specifying this content explicitly. The null-energy condition is the "weakest" of all these conditions in that many of the commonly used energy conditions (see above) imply it. An illuminating interpretation of this condition can be made by noticing that, through the Einstein equations, this condition is equivalent to $R_{ab}V^aV^b \geq 0$. It then implies that congruences of null geodesics are non-diverging. This is a consequence of the *Raychaudhuri equation*, which describes the focusing effect of gravity on lightrays. This can also be intuitively interpreted to say that the null-energy condition ensures that gravity is attractive [6]. The second condition requires the existence of a *Cauchy surface*. This requirement is natural from a deterministic point of view. By definition, the existence of a Cauchy surface Σ implies that the entire manifold M is uniquely determined from data specified on Σ [21]. In virtually all realistic situations, the Cauchy surface is non-compact. Finally, a trapped surface is a spacelike two-surface $\mathcal{F}$ (usually a two-sphere), such that the two families of null geodesics orthogonal to $\mathcal{F}$ are *converging* at $\mathcal{F}$. The boundary of the union of all trapped regions is called the *apparent horizon* on Σ [6].

This theorem was later complemented with other similar results into what is now known collectively as the singularity theorems [22]. Penrose's theorem shows that singularities can form generically. Clearly, its usefulness mostly hinges on how easily trapped surfaces can be created. A first answer to this question can be found in a theorem credited to Schoen and Yau [23]. The theorem establishes that asymptotically flat initial data will contain a trapped surface if the energy density of matter is sufficiently large in a small enough region. The main drawback of the proof is that the trapped surface is assumed to exist already in Σ. The proof therefore only makes use of the constraint equations of general relativity. Recently, Christodoulou [24] has proved that trapped surfaces can form *dynamically*, even in the absence of matter and without any symmetry assumptions.

Since a trapped surface generally lies inside the event horizon [6], black holes can be seen as a genuine prediction of general relativity. As a result, assuming that general relativity is correct at least at macroscopic scales, one should be able to observe them in our universe! It is remarkable how the detection of black holes have only recently become routine; see Refs [10–13]. Of course, in reality, one does not expect singularities to actually exist in Nature. The classical description of singularity formation in gravitational collapse is an artifact of taking a purely classical point of view. In particular, as the star shrinks to smaller and smaller sizes, new degrees of freedom (notably quantum mechanical) enter the picture. The general belief is that these are expected to prevent the star from reaching arbitrarily large densities. The formation of singularities in general relativity is therefore to be viewed as a consequence of the fact that the theory of general relativity was applied beyond its domain of validity.

At first, this might seem to imply that we would need to know something about quantum gravity to answer astrophysical questions. However, due to the existence of black holes, this

is not the case. For this reason, black holes can be seen as a saving grace of the predictive power of general relativity: Heuristically, trapped surfaces, which lie inside the event horizons [6], generally appear well before the collapse has reached its final destination, such as in the Oppenheimer-Snyder model; see again the left picture of Fig. 1.1. Because of this, the "true nature" of those singularities can be roundly ignored astrophysically as they will not affect the dynamics outside.

It should be noted that, strictly speaking, while Penrose's singularity theorem does show that formation of singularities are generic features of general relativity, it says nothing about whether this singularity is hidden inside a black hole. In particular, it does not tell us which of the singularity or the trapped surface, if any at all [25], appears first! The reader might then raise an important question that was tacitly assumed until now: are the singularities produced by gravitational collapse always hidden inside a black hole? A "stronger" question would be: is it possible for null geodesics from the singularity to reach any (not necessarily far-away) timelike observer? The *cosmic censorship conjectures*, presented in the next section, lie at the heart of such questions.

1.2 The cosmic censorship conjectures

Before presenting the weak and strong cosmic censorships, it is worthwhile to make an important distinction between timelike and spacelike singularities.

In Schwarzschild-Kruskal spacetime, the singularity is spacelike. At first, one might think that this signals catastrophic consequences, but the spacelike nature of the singularity implies that it cannot be "seen" by any observer. This is illustrated in Fig. 1.2. On the left, a spacelike singularity, such as the one in a Schwarzschild black hole, is shown. Sometimes, one hears about "falling into" singularities inside Schwarzschild black holes, but this is a misconception. One does not fall into a spacelike singularity like one would fall into the bottom of a pit. The singularity is not a "spatial location" one simply approaches. Instead, it is approached in time, much like one "approaches" the next day as time passes. So, one cannot be affected by a spacelike singularity until it has actually occurred (this would otherwise amount to traveling backwards in time). On the other hand, for a timelike singularity (right plot), an observer can be affected and "see" the singularity.

Additionally, when discussing singularities, one needs to make a distinction between *locally* and *globally naked* singularities. A singularity is said to be globally naked if there exist outgoing null trajectories from it that can reach null infinity. On the other hand, a singularity is said to be locally naked if it is not globally naked, but there exist outgoing null trajectories from it that can reach some timelike observer in spacetime. A simple (and equally unphysical) example of a globally naked singularity is that of a Schwarzschild black hole with negative mass. On the other hand, the singularity in a Kerr or Reissner-Nordstörm black hole would correspond to a locally naked singularity. This is because an observer can interact with the singularity, provided they have dived into the black hole.

Penrose [20] developed the idea that globally naked singularities should generally not occur. This conjecture is called the *weak cosmic censorship*. A modern formulation [27] is (see

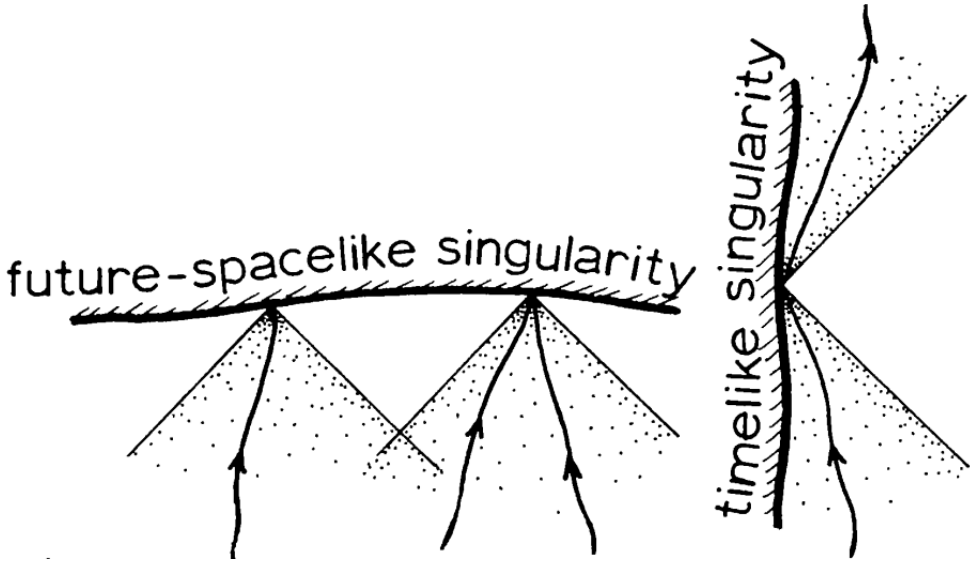

FIGURE 1.2: Illustration of spacelike vs timelike singularities. Arrowed curves show the world-line of an observer. Also drawn are the lightcones at some points from the singularity. Image credit: [26].

also [28]):

Weak cosmic censorship conjecture*: Take some nonsingular, asymptotically flat initial data on a Cauchy surface. Suppose the matter content obeys a reasonable equation of state. Then, generically, the maximal Cauchy development of this initial data is an asymptotically flat spacetime with complete future null infinite.*

Note that the weak cosmic censorship is only referring to the region of spacetime which can be uniquely determined from data on the Cauchy surface, called the maximal Cauchy development [21]. In principle, it is possible for the maximal Cauchy development to be extendible. That is, it is isometric to a proper subset of a "larger" spacetime. From the point of view of this larger spacetime, the boundary of the maximal Cauchy development is called the Cauchy horizon [29]. From a physical standpoint, one cannot predict the physics beyond the Cauchy horizon, since doing so would require novel information. For this reason, the singularity in a Kerr or Reissner-Nordstörm black hole is not relevant for the weak cosmic censorship. In the conjecture, the singularity is prohibited to be visible from infinity by requiring null infinity to be "complete". If there are outgoing null geodesics from the singularity to null infinity, then the physics beyond the future lightcone of the singularity is not determined. The future lightcone of the singularity then acts as a Cauchy horizon. Since this surface stretches all the way to infinity, one can think of null infinity as being "truncated". Intuitively, an observer traveling "near" null infinity along one of its null generators will eventually reach the Cauchy horizon in finite affine time and enter unknown territory. One therefore says that null infinity is not complete. (See standard textbooks such as [6, 29] for a rigorous discussion of null infinity completeness).

Similarly, the naked singularity of a white hole in Kruskal spacetime or the big bang singularity in cosmological models are also not problematic for the weak cosmic censorship [30]. This is because, as long as one can define some regular initial data on some Cauchy surface which produce a complete, asymptotically flat future null infinity, then the weak cosmic censorship is not violated. The fact that some geodesics, which intersect this Cauchy surface, can also approach the white hole/ big bang singularity in the past arbitrarily closely, is not relevant.

The above formulation of the weak cosmic censorship is imprecise for several reasons. First, one does not specify what it means for an equation of state to be reasonable. Obviously, without specifying any sort of constraints on the matter fields, there is nothing stopping us from writing down some spacetime containing a naked singularity, and call it a solution to the Einstein equations by defining the stress-tensor to be $8\pi T_{ab} := G_{ab}$. Instead, one would want the stress-tensor to satisfy some general "physically reasonable" constraints. One such constraint will undoubtedly revolve around some energy condition. Another obvious constraint is that the Einstein-matter field equations should also admit a well-posed initial value problem [6].

Intuitively though, one can still see that this might not be quite enough. A rather interesting example is the case of a fluid. One can certainly find fluids which satisfy the above two conditions, yet showcase violations of the weak cosmic censorship, even on a Minkowski background. The reason is that, in a fluid, singularities can "easily" be caused by shell crossings (for dust matter) or shocks [31]. These singularities have nothing to do with gravity and are an artifact of the fact that a fluid is just a macroscopic approximation of a more fundamental description. The above singularities correspond to a breakdown of such approximation, rather than a true, physical singularity of gravitational collapse. See Refs [6, 28] for a short discussion on this.

Finally, the term "generically" in the definition of the censorship is needed because, otherwise, there are known counterexamples, as we will see shortly. The reader might note that the term "generic" has not been defined. This constitutes one of the outstanding problem in having a well-defined formulation of the weak cosmic censorship. Genericity is intimately linked with the notion of a measure, but there is no clear way to define this [22]. Furthermore, it is not immediately clear if precisely defining such a measure is even relevant, as stronger versions of the weak cosmic censorship may hold true. For example, it could be true that the set of data forming naked singularities has positive co-dimension in the space of initial data [27].

Finally, we can turn our attention to the case of locally naked singularities. Intuitively, it is plausible to think that it should be irrelevant whether a light ray, emanating from a singularity, can actually escape to infinity or not. In particular, one would expect that it should be equally physically unrealistic that some observer can see the singularity as naked, even if they themselves may be trapped (for example inside a Kerr or Reissner-Nordstörm black hole). This has lead Penrose [32] to formulate the *strong cosmic censorship*.

Strong cosmic censorship conjecture: *The maximal Cauchy development of generic asymptotically flat initial data is inextendible.*

The above formulation is equivalent to saying [21, 33] that spacetime should be globally hyperbolic. That is, spacetime admits a Cauchy surface. There are in reality a few different formulations of the strong cosmic censorship. The different formulations have to do with the inextendibility criteria. Naively, one might wish to say that the Cauchy development is inextendible as a Lorentzian manifold with a C^2 metric. Doing so however is not suitable, since there are generic well-posed initial data which are not even C^2 [34]. One can instead ask for a stronger condition by replacing C^2 with C^0. This is then called the C^0-formulation of the strong cosmic censorship. For the Schwarzschild black hole, it was shown that the singularity is in fact C^0-inextendible [35]. The C^0-formulation of the strong cosmic censorship therefore holds in this case. On the other hand, it was shown in a landmark paper [34] that the C^0-formulation does *not* hold for the Kerr black hole. There are also investigations on the case of charged black holes [36–38] and in de-Sitter space [39]. See also Refs [40, 41] for more discussions on the subject.

Intuitively, the strong cosmic censorship complements Penrose's singularity theorem. Recall that the latter only states that a singularity can occur generically, in the form of geodesic incompleteness. Such incompleteness could simply arise because spacetime is extendible. However, if some version of the strong cosmic censorship is correct, then this will generically not be the case. In other words, assuming that the strong cosmic censorship holds, Penrose's singularity theorem would suggest that the geodesic incompleteness is due to a physical singularity in spacetime.

An important word of warning needs to be given at this stage. From the presentation of the weak and strong cosmic censorships above, the reader might get the impression that a violation of one implies a violation of the other. This however need not be the case. On the one hand, the Kerr and Reissner-Nordstörm black holes are relevant for the strong cosmic censorship and in fact violate some version of it, [34, 36, 37]. On the other hand, this is of no consequence to the weak cosmic censorship since the singularity lies inside the black hole and the outside remains in any circumstance unaffected. Another schematic example of a spacetime that violates the strong but not weak cosmic censorship is given on the left diagram of Fig. 1.3. This diagram looks very similar to a diagram one would draw to illustrate the typical gravitational collapse of some matter into a black hole. The only exception is the existence of a timelike singularity inside the event horizon. The event horizon is then also a Cauchy horizon. Clearly, this spacetime is susceptible to violate at least some version of strong cosmic censorship, while the weak version would remain valid. On the contrary, on the right diagram, spacetime has a singular future lightcone [27]. If we assume that the singularity of this future lightcone is sufficiently "strong" (for example such that the metric cannot be extended even continuously across it), then any reasonable definition of strong cosmic censorship would hold, while the weak cosmic censorship certainly fails. In the next section, we will also give an example of a spacetime that relevant to both censorships.

We can now ask ourselves: how do we go about tackling these censorships? One clear obstacle is that working without any symmetry assumption, without some specific matter field and in a fully dynamical evolution, is far too complicated of an undertaking. While there has

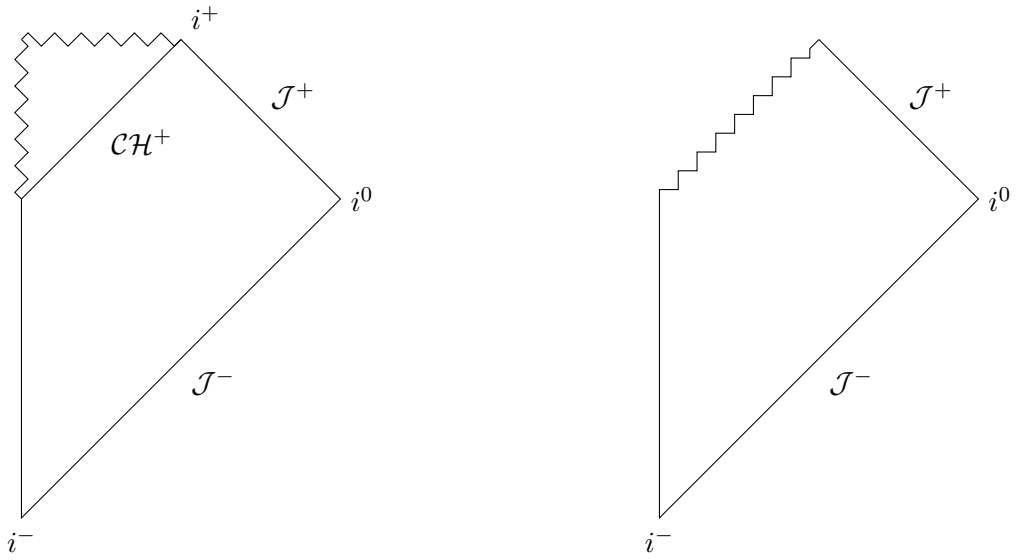

FIGURE 1.3: Left plot: a spacetime diagram where the strong cosmic censorship is violated, but weak cosmic censorship holds. Right plot: a spacetime diagram where the weak cosmic censorship is violated, but the strong cosmic censorship holds.

been good progress in understanding the strong cosmic censorship [34], the same cannot be said for the weak cosmic censorship. For the rest of this section, we will focus our attention on attempts to collect evidence for and against the weak cosmic censorship.

On the theory side, some progress can be made by assuming a simple matter field, and/or adding some symmetry assumptions. The main examples are the works of Christodoulou. In Ref. [33], he investigated the *inhomogeneous* Oppenheimer-Synder dust model and showed that the inhomogeneity can lead to the formation of a naked singularity; see right plot of Fig. 1.1. In parallel, his works on the scalar-field model culminated into showing that the weak cosmic censorship holds for a spherically symmetric massless scalar field; see Refs [24, 42].

Indirect evidence can also be gathered by asking about the stability of black holes. Indeed, if the weak cosmic censorship fails, then gravitational collapse can (generically!) end in a naked singularity rather than a black hole. In other words, this implies that the formation of a black hole is not a generic outcome of collapse. If this is so, one would expect to find some evidence of this by looking at the linear perturbation of the Kerr metric. Specifically, one would expect the event horizon to be unstable. This instability could drive the event horizon to disappear, converting the black hole into a naked singularity. In short, the linear instability of black holes could effectively disprove the weak cosmic censorship, while its linear stability would provide some evidence in support of it. A proof of the nonlinear stability of the Schwarzschild black hole has recently been found [43]. The linear stability of Kerr is much more difficult and has remained an open question. Despite this, there are good reasons to think that it is stable. For one, the formation of rotating black holes are now common in numerical simulations. Furthermore, with the routine observations of black holes in our universe, it is strongly suspected that their event horizon is nonlinearly stable. This stability thus throws some evidence in support of the weak cosmic censorship.

A different approach to tackle the cosmic censorships is to attempt to "overspin" or "overcharge" a near-extremal black hole. As is well-known, black holes are characterized by their mass M, charge Q and spin J. These three parameters satisfy the inequality

$$M^2 \geq Q^2 + \left(\frac{J}{M}\right)^2 . \tag{1.1}$$

In the case of equality, the black hole is said to be *extremal*. If this relation is not satisfied, then the spacetime does not contain a black hole, but instead a naked singularity.

From there, one can attempt to start with an extremal (or near-extremal) black hole, throw in a particle with large enough spin (and/or charge) and small enough mass. The hope is that the black hole would absorb this particle, such that its new parameters violate the above inequality. Such a process is called *overspinning* or *overcharging*. Recently however, Sorce and Wald have shown that black holes cannot be overcharged nor overspun [44].

One can also leave the $3+1$ dimensional setting and see how the situation looks like in higher dimensions. In some sense, black holes in higher dimensions are much more varied: the event horizon is not necessarily spherical [45]. In particular, one can have other types of black holes, with non-compact event horizons like a black string, ring or brane [46]. These more exotic objects are usually unstable under perturbations and so would not be candidates that violate the weak cosmic censorship. More interestingly, there is a new phenomenon that occurs in higher dimensions: under some perturbation, an instability, similar to the Rayleigh-Plateau instability of fluid dynamics, arises. This instability stretches the black hole's event horizon. Eventually, the event horizon pinches off, creating a bead of small satellites which themselves display this instability. This fractal process continues to repeat until, after some finite time, the singularity is naked. This instability is called the Gregory-Laflamme instability [47, 48]. Provided the initial data contain such black holes, which have been shown to be at least numerically stable, generic violations of cosmic censorship can be found [49–51].

Finally, one can start with some (sufficiently) smooth initial data and see if gravitational processes can cause the matter to form a naked singularity. In fact, it was shown rigorously by Christodoulou [27] and numerically by Choptuik [52] that for fine-tuned (i.e. non-generic) regular spherically symmetric initial data, coupled to a massless scalar field, spacetime can develop naked singularities. The solution found by Choptuik lies at the threshold of black-hole formation. This type of phenomena is not unique to the scalar field and the ensemble of such phenomena is dubbed *critical phenomena*. The study of the critical phenomena occurring at the threshold of black-hole formation is called the study of *critical collapse*. The next section is dedicated to giving the reader a brief overview of critical collapse and how it is related to both cosmic censorships.

1.3 Critical collapse and naked singularities

In his pioneering 1993 paper [52], Choptuik shed important insights into the formation of naked singularities. In this paper, Choptuik investigated the evolution of smooth initial data of the

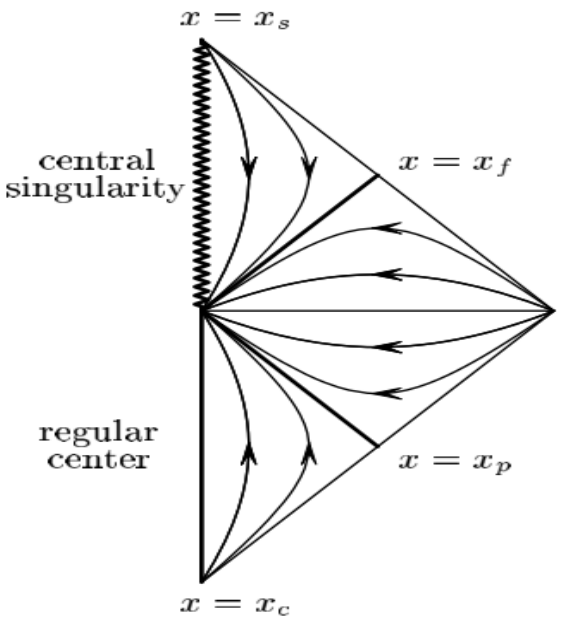

FIGURE 1.4: Conformal diagram of the critical solution for the massless scalar field in spherical symmetry. $x = x_c$ is the regular center, $x = x_p$, the past lightcone of the singularity and $x = x_f$ its future lightcone. It is also a Cauchy horizon. The central singularity is timelike. Image credit: [53].

Einstein-massless scalar system which are "just on the verge" of collapsing into a black hole. Specifically, he considered a one-parameter family of initial data such that for one range of the parameter, the initial data collapse into a black hole, and for another range, they disperse. As one fine-tunes this parameter, one can produce black holes with increasingly smaller masses. Moreover, the evolution of the initial data will, in some intermediary stage, be well approximated by a self-similar solution, the *critical solution*. In a self-similar spacetime, suitable metric and matter variables only depend on the ratio of "radius over time" $R/(t_\star - t)$. At the *accumulation point* $t = t_\star$, the solution will have shrunk to an arbitrarily small length scale at the center. Correspondingly, curvature invariants become arbitrarily large there and spacetime therefore possesses a singularity.

Since Choptuik's initial discovery, the global structure of the critical solution for the massless scalar field has been thoroughly studied in Ref. [53]. We will summarize the main results of this paper in Section 2.5, but we will give here the main qualitative points. In Fig. 1.4, a spacetime diagram of the critical solution is shown. $x = x_c$ denotes the regular center, extending up to the singularity. $x = x_p$ and $x = x_f$ are its past and future lightcone respectively. The latter is also a Cauchy horizon. The metric and scalar field can be extended (none uniquely) beyond it. Furthermore, the central curvature singularity is naked in that any radial null geodesics to the past of the singularity can reach an observer located arbitrarily far away from the singularity. If we were to neglect the condition enforcing the initial data to be generic in the definition of the weak and strong cosmic censorships, the critical solution would then violate them both.

After Choptuik's work, the study of critical collapse was extended to other matter fields. Many properties of the critical solution for the massless scalar field, notably its self-similarity, extend to all other matter systems in $3+1$ and higher dimensions. For example, the gravitational

collapse of self-similar solutions with a perfect fluid matter field was investigated in Refs [54, 55]. There, it is found that the some self-similar solutions can contain a naked singularity. The spacetime structure pertaining to the critical solution is as in Fig. 1.4 up until the Cauchy horizon $x = x_f$. There are different possible continuations beyond it.

The study of critical collapse marks an important milestone in numerical relativity and sheds some light into the weak and strong cosmic censorships. Due to the fact that the critical solution can only be achieved through codimension one (i.e. fine-tuned) initial data, the critical solution has, by definition, at least one growing mode and is therefore not a counterexample to the current definitions of the cosmic censorships.

One can still consider that it violates the weak cosmic censorship in spirit. Critical phenomena provide a way to achieve arbitrarily large curvature, or arbitrarily low black-hole mass, observable from infinity. In particular, once sufficient fine-tuning has been achieved, one expects the general relativistic description to break down as quantum effects are expected to become important. For this reason, critical collapse is also relevant to quantum gravity.

Despite the fact that the study of critical phenomena was initiated nearly thirty years ago, most studies dedicated to it restrict themselves to spherical symmetry. There are numerous reasons for this: First, on the analytical side, the restriction to spherical symmetry means that, by making a self-similar ansatz, the Einstein equations become a system of ordinary differential equations (ODEs), which are relatively tractable. While studying perturbations away from spherical symmetry is still analytically possible, it becomes very difficult to make any progress "far" from spherical symmetry [15, 56]. On the numerics side, due to the fact that the solution is self-similar, a numerical algorithm has to deal with the combination of a highly relativistic regime (arbitrary large curvature), as well as a wide range of length scales (self-similarity). Moreover, when studying critical collapse beyond spherical symmetry, one will have to deal with a competition between the matter field and the gravitational waves. As we will see later, the difficulty is that both of these exhibit critical phenomena on their own! This particular issue is worsened by the fact that the critical phenomena of vacuum are particularly difficult to study and still poorly understood [57]. However, there are two main reasons why it is important to explore critical collapse beyond the spherically symmetric setting. First, some gravitational collapse models, notably gravitational waves, do not exist in spherical symmetry. Second, and more importantly, black holes can carry angular momentum. The full picture of critical collapse therefore requires us to go beyond spherical symmetry.

For this reason, this thesis' main aim is to study the effects of angular momentum on the critical collapse of an ultrarelativistic perfect fluid in $2+1$ dimensions. $2+1$ dimensions serves as a toy model for $3+1$. As will be explained later, its main practical advantage is that the difficulties mentioned above can be simply bypassed. The main drawback is that, in $2+1$ dimensions, black holes cannot form without a negative cosmological constant [58, 59]. In order to study any kind of critical phenomena in this dimension, we therefore need to work with asymptotically anti-de Sitter (adS) spacetimes.

1.4 Overview

Below, we give an outline of the thesis.

In Ch. 2, we give an overview of critical collapse. We start by discussing in detail what critical collapse is through two examples: the spherically symmetric massless and massive scalar field. We show that in the former case, we have type II phenomena: the mass and curvature scale like a power-law as we fine-tune to the black-hole threshold. The critical solution is discretely self-similar. In the latter case, critical phenomena are type I if the size of the initial data is "large" compared to the inverse scalar-field mass. In that case, the mass and curvature do not scale and the critical solution is static. We follow up with a more formal presentation of critical collapse. We show how the power-law scaling in the critical phenomena emerge from simple dimensional analysis. We also discuss in more detail the global structure of the critical solution for the massless scalar field and how it relates to the weak and strong cosmic censorship. The end of the chapter is dedicated to a presentation of a selection of studies on critical phenomena. This list is certainly not exhaustive, but serves to give the reader a better intuition of critical phenomena through examples of various matter fields. We also mention the current difficulties in the research area of critical collapse.

In Ch. 3, we present in detail the critical phenomena associated with the spherically symmetric perfect fluid in $3+1$ dimensions with linear equation of state $P = \kappa\rho$. We present a high-resolution shock-capturing method to simulate the spherically symmetric fluid in $3+1$ dimensions. In spherical symmetry, the numerical code is mostly identical in any spacetime dimensions. Since the main aim of this thesis is to study the same system in $2+1$ dimensions, this also serves as a test that the new numerical algorithm is working. We then proceed to study the critical phenomena of the perfect fluid numerically. We find type II phenomena for $\kappa = 1/3$. The critical solution and the power-laws are numerically extracted. We show how in practice the critical solution is computed analytically by making a self-similar ansatz to rewrite the Einstein-fluid equations into an ODE system. This system is then solved as an eigenvalue problem. Similarly, we solve its linear perturbations and show that it has a unique spherical growing mode. We end this chapter by discussing the case of arbitrary κ and the effect of angular momentum.

The first half of Ch. 4 is dedicated to giving a review of adS space. We will present several useful coordinate systems to parametrize adS, each of which helps highlight a particular feature of this space. Notably, we will show that conformal infinity is *timelike* (instead of null). Furthermore, we will study the null and timelike geodesic motion. and show that the null geodesics can reach the conformal boundary in *finite* proper time. In the second half of this chapter, we give a review of the adS Kerr solution analogue in $2+1$ dimensions, called the BTZ solution. It *cannot* be attained by a small deformation from adS. However, we will show that it can be obtained through a non-trivial identification of adS under a precise isometry. We will also present and discuss its conformal diagram.

In Ch. 5, we proceed to thoroughly analyze the rigidly axisymmetric rotating fluid stars in $2+1$ dimensions for arbitrary equation of state $p = p(\rho)$. These solutions will later play an important role in the critical collapse of a perfect fluid in $2+1$ dimensions. Interestingly, it

turns out that these solutions can be written down *explicitly* in a suitable coordinate system. We show that, assuming regularity at the center, they form a two-parameter family of solutions. We give an explicit condition in terms of the equation of state for when the star has a surface at some finite radius. The causal structure is investigated by analyzing the full parameter space of solutions. We show that the parameter space splits into three regions. Exterior solutions are of BTZ-type and can describe either a black hole, a point particle or a naked singularity.

In the first half of Ch. 6, we present a novel numerical code to solve the axisymmetric Einstein-fluid equations in $2+1$ dimensions. We have a fully constrained scheme for solving the Einstein equations: the matter is evolved by solving the stress-energy conservation, written as balance laws, and the metric coefficients are updated by solving the Einstein equations. Typical finite volume method methods are used: we first only discretize in space (method of lines). At the interface between two neighboring points, the flux is computed by solving a Riemann problem. The novelty is that in $2+1$ dimensions, it turns out that one can generalize the Misner-Sharp quasilocal mass in axisymmetry (in higher dimensions, it only exists in spherical symmetry). This was previously not known. The numerical algorithm takes advantage of this by ensuring that the mass is conserved during the evolution. In the second half of this chapter, we discuss in detail the pointwise and ℓ^2-norm convergence of the code. Furthermore, we explore the stability of the stationary solutions presented in the previous chapter.

In Ch. 7, we study the critical collapse of a spherically symmetric perfect fluid in $2+1$ dimensions with equation of state $P=\kappa\rho$. Unlike for its $3+1$ analogue, the critical phenomena strongly depend on the value of κ. Specifically, we give strong numerical evidence that the phenomena are of type I if $\kappa \lesssim 0.42$, while they are of type II for $\kappa \gtrsim 0.43$. In the former case, the critical solution is shown to be static. In the latter case, the critical solution is not self-similar (as in $3+1$ dimensions). Instead it is *quasistatic*. That is, the profile of the solution goes through an adiabatic sequence of static solutions whose size shrinks to zero. "Far-away" from the center, the solution is shown to be well-approximated as an outgoing static test fluid. We also develop an incomplete theoretical framework that explains some of these numerical results. Notably, assuming that the critical solution for type II is quasistatic, we give an argument that correctly predicts the observed power-law scaling between the mass and curvature.

In Ch. 8, we generalize the results in the previous chapter to rotating axisymmetric initial data. For $\kappa \lesssim 0.42$, the critical phenomena are type I and the critical solution is stationary. The picture for $\kappa \gtrsim 0.43$ is more delicate: for small angular momenta, the critical phenomena are type II and the critical solution is quasistationary. Interestingly, the spin-to-mass ratio of the critical solution *increases* as it contracts, and hence so does that of the black hole created at the end as we fine-tune to the black-hole threshold. As extremality is approached, the contraction of the critical solution smoothly ends, preventing extremal black holes to be created.

In Ch. 9, we summarize the main results of this present thesis. We also give a brief synopsis of questions that emerged from the research conducted in this thesis and which have remained unresolved.

Chapter 2

Critical collapse

2.1 Introduction

Broadly speaking, gravitational collapse is interested in the final fate of a massive star that, after exhausting its internal nuclear fuel, undergoes a contraction under its own gravitation force. The study of gravitational collapse in general relativity can be traced back to the pioneering 1939 paper of Oppenheimer and Snyder [14]. They showed that a spherically symmetric, homogeneous dust collapses on itself, leading, in finite time, that its entire energy density gets compressed to a single point. This showed for the first time that black holes can be dynamically created even from simple matter fields.

In what follows, it will be useful to view general relativity as an infinite-dimensional continuous dynamical system, called the phase space. Each point on this phase space corresponds to some initial data set: the 3-metric (in four spacetime dimensions), the extrinsic curvature and suitable matter fields satisfying the constraint equations [22, 60]. For a given point in the phase space, the Einstein equations dictate a unique curve (once the gauge has been fixed and ignoring subtleties relevant to the strong cosmic censorship) that passes through that point.

In general, any initial data can end up in three different stable states: collapse into a black hole, a stationary or periodic configuration (star), or complete dispersion. Critical collapse can be described as the study of the phenomena that occur at the threshold between initial data that disperse, and those that collapse and form a black hole. Consider a one-parameter family of initial data with parameter p. The parameter p is chosen such that there exists a *critical value* $p = p_\star$, such that for $p < p_\star$, the initial data disperse (called *weak* or *subcritical* data), while for $p > p_\star$, they collapse (called *strong* or *supercritical* data). The *critical surface* at $p = p_\star$ defines the boundary between those two different end-states; see Fig. 2.1 for an illustration. Intuitively, the critical surface has "one dimension less" than the full phase space. More precisely, it is of codimension one.

An attracting fixed point (if any) on this critical surface is called a *critical point*. It follows that this critical point is itself an attractor of codimension one in the full phase space. That is, it has a single growing mode. At $p = p_\star$, the initial data stay on the critical surface by definition. They will be driven towards the critical point. This can be seen as a sign of universality: it does

not matter where one starts on the critical surface, since the dynamical evolution will always drive the initial data towards the critical point.

Of course, in practice, it is not possible to prepare initial data *exactly* on the critical surface. However, one can get arbitrary close to it via bisection. Specifically, one considers a family of initial data with parameter p as described above. One then specifies some criteria to distinguish those initial data that disperse and those that form a black hole , or at least when the black-hole formation is deemed to be unavoidable. A typical choice for the latter is when an apparent horizon has formed. In spherical symmetry for example, this occurs when $\nabla_a R \nabla^a R = 0$, where R denotes the area radius [61]. One could then monitor this quantity and declare that the formation of a black hole is unavoidable and imminent once $\nabla_a R \nabla^a R$ is sufficiently small. For the former case, one can define as a criteria that the initial data are weak when the evolution has run for a sufficiently long time, spacetime on the numerical grid is sufficiently close to Minkowski or, for matter fields, when most of the stress-energy has left the numerical grid. This then allows us to define a $p = p_{\text{weak}}$ and a $p = p_{\text{strong}}$, such that the initial data disperse for the former and collapse for the latter respectively. By continuity, $p_{\text{weak}} < p_\star < p_{\text{strong}}$. One can then bisect to find $p_\star$ to arbitrary precision.

It is worth giving a word of caution here. The appearance of an apparent horizon only guarantees the existence of an event horizon assuming the weak cosmic censorship holds true in the first place [6, 29]! This means that monitoring apparent horizons makes us blind to potential violations of the weak cosmic censorship. Furthermore, it is also possible to find peculiar foliations for which there are no apparent horizon, even if there exists an event horizon [25].

If one starts close, but not on, the critical surface (however not necessarily close to the critical point), then the solution can be roughly subdivided into two different phases: during the first phase, the solution will "stay close" to the critical surface, and move towards the critical point. As it approaches the critical point, the evolution slows down and eventually (phase two) the solution moves away from the critical surface, driven by the growing mode of the critical point and towards one of its two possible end-states (depending on which side to the critical surface the initial data started from). At the critical point, spacetime possesses a naked singularity. Critical collapse is therefore relevant to the cosmic censorships, as illustrated in Sec. 1.3.

The study of critical collapse emerged after the now famous work of Choptuik [52]. In this paper, Choptuik considers the evolution of different one-parameter families of spherically symmetric massless scalar field. By fine-tuning to the black-hole threshold, he observed several intriguing phenomena, which now form the cornerstone of what is called *critical phenomena*:

1) For near-critical initial data, $p \simeq p_\star$, during some intermediary stage, the solution is well-approximated, in the strong-field region, by a *critical solution*. 2) This critical solution is (discretely) self-similar: the profile of the solution is the same at discrete time intervals, after rescaling the radius coordinate by an appropriate factor. Furthermore, the critical solution is *universal*, in the sense that it does not depend on the initial data. 3) The mass of the black hole (for initial data that collapse) scales like a power law of the distance to the critical surface,

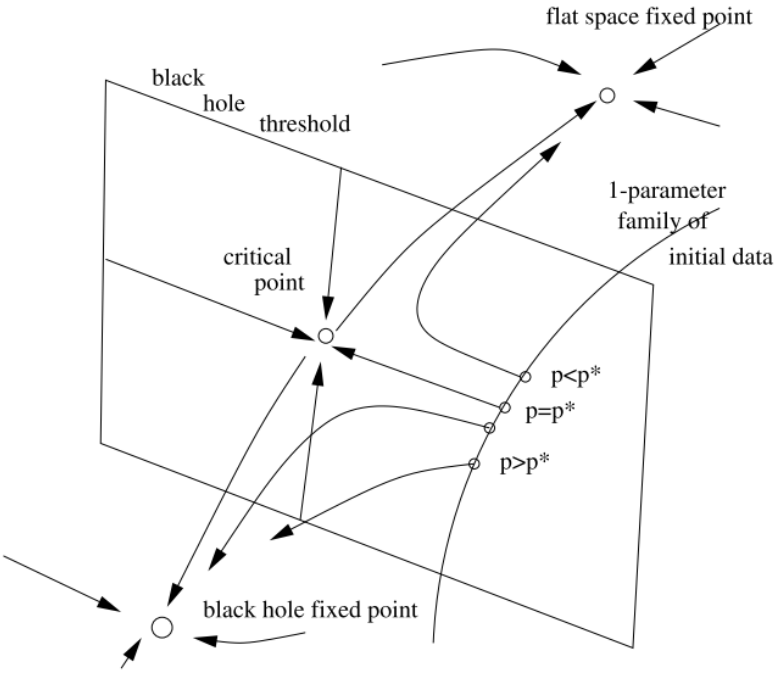

FIGURE 2.1: A simplified picture of the infinite-dimensional phase space as a three-dimensional system. The critical surface splits the phase space in two halves. If a one-parameter family of initial data, parametrized by p, crosses the critical surface exactly once, then it will have as end-state a black hole, if $p > p_\star$, or flat space, if $p < p_\star$. For $p = p_\star$, the initial data are on the critical surface and the solution moves towards the critical point. Initial data close but not on the critical surface (but not necessarily close to the critical point) will first stay close to the critical surface and move towards the critical point, before driving away from it, in the direction of the unique growing mode. Image credit: [56].

$M_{\rm BH} \sim (p - p_\star)^\delta$, where δ is a (positive) constant. This exponent is also independent of the family of initial data.

The above critical phenomena are not specific to the massless scalar field, but similar behavior were later found in a plethora of other matter fields, such as: scalar fields (massless and massive) [62–64], perfect fluid $P = \kappa\rho$ [54, 65–68], Yang-Mills [69–72], in dimensions other than $3+1$ [73–78], or in modified theories of gravity or quantum-gravity inspired models [79–82]. Some studies also extend the investigation beyond spherical symmetry, such as: scalar fields [83–87], perfect fluid [88–92], vacuum [93–96], and electromagnetic waves [57, 97]. See also [56] and references therein.

The study of critical collapse is however not solely limited to the investigation of the cosmic censorships. The self-similar behavior of the critical solution in critical collapse may play an important role in understanding the broader self-similarity hypothesis [98–101]. Furthermore, self-similar models are common when studying primordial black-hole formation in the early universe [102, 103]. Critical collapse is also a useful tool to probe the adS/CFT correspondence. Indeed, the correspondence stipulates that an n-dimensional gravitational theory is related to a $n-1$ CFT at the boundary [104]. This means that the critical behavior in critical collapse should have a specific holographic interpretation. This may provide further insight on the adS/CFT correspondence, as well as understand the phenomena related to critical collapse from an holographic point of view; see Refs [76, 77, 105, 106]. Finally, another obvious use of critical

collapse concerns testing and benchmarking new codes which solve the Einstein equations [67]. This is because critical collapse typically involves the combination of both dynamical flows at different scales and strong gravitational fields.

In this chapter, we will present Choptuik's famous paper in more details. We will follow up by presenting a theoretical discussion of the emergence of the mass power-law scaling. We will discuss a varied selection of studies where critical collapse of other matter fields were considered. This chapter serves to present to the reader the typical properties of the phenomena near the black-hole threshold and highlights some of the current obstacles encountered in this research area. This will help the reader better frame the results that form the core part of this work (presented in Ch. 7 and Ch. 8). As a result, none of the contents in this chapter is original work.

2.2 The notion of mass in spherical symmetry

First, it is helpful to discuss the notion of "mass" in general relativity. From our newtonian intuition, one can give some generally accepted properties that a suitable definition of a *quasilocal mass function* (mass defined on regions/patches of spacetime instead at single points) should have [107]: 1) The mass function is non-negative. 2) When the radius of a two-sphere shrinks to a point, that point must have zero mass. 3) any region in Minkowski spacetime should have zero mass. 4) In asymptotically flat spacetime, the mass function should agree with the ADM and Bondi masses at spacelike and null infinity. 5) In any untrapped region, if a two-sphere S is completely contained inside another two-sphere S', then the mass in S' should be equal to or greater than the mass in S. For a general spacetime, there is no generally accepted notion of mass which satisfies all these properties; see Ref. [108] for a review on the subject.

However, in spherical symmetry, one *can* find such a mass function. A general spherically symmetric spacetime (in any dimension) can be written as

$$\mathrm{d}s^2 = g_{AB}\mathrm{d}x^A\mathrm{d}x^B + R^2\mathrm{d}\Omega^2, \tag{2.1}$$

where $d\Omega^2$ is the usual metric on the unit sphere and g_{AB} is a non-singular Lorentzian metric. R is the area radius of the sphere. By far the most widely accepted mass function in spherical symmetry is called the *Misner-Sharp* mass, first discovered in 1964 [109]:

$$M(t,R) := \frac{R}{2}\left(1 - \nabla_a R \nabla^a R\right). \tag{2.2}$$

This mass function holds in any spherically symmetric spacetime and with any matter field.

Where does this mass function comes from? It originates from the existence of a very special vector field, which is only defined in spherical symmetry:

$$K^a := \epsilon^{ab}\nabla_b R, \tag{2.3}$$

where ϵ^{ab} is the volume form associated with the metric g_{AB}. This vector field is called the *Kodama vector field* [110, 111]. The Kodama vector field is divergence free, $\nabla_a K^a = 0$. Moreover,

it has the crucial property that the associated vector field

$$J^a := G^{ab}K_b, \tag{2.4}$$

where G^{ab} is the Einstein tensor, is also divergence free, $\nabla_a J^a = 0!$ J_a is then a locally conserved energy flux vector field. From the above, the reader might be wondering if K^a is in fact a Killing vector as all the above are straightforward properties of Killing vectors. It is to be emphasized that this is *not* the case in general. Spacetime can be completely dynamical and the only assumption needed was the assumption of spherical symmetry. This is often called the "Kodama miracle". However, if spacetime is also stationary, then K^a is parallel to the timelike Killing vector [110, 111]!

As a result of the conserved current, there is an associated *quasilocal conserved charge*. Since the vector K^a is asymptotically timelike, one can interpret the associated charge as a mass function. This mass function then reduces to the Misner-Sharp mass [112].

2.3 The discovery of critical collapse: the scalar field case

2.3.1 The massless scalar field

We will now discuss the pioneering 1993 paper by Choptuik [52], which first highlighted the critical phenomena that occur at the threshold of black-hole formation.

In this paper, Choptuik considers a single spherically symmetric massless scalar field, ϕ. A natural gauge to consider is the *polar-radial* gauge: The four-dimensional spacetime is split into a product of a two-dimensional spacetime (called the reduced manifold) and a round two-sphere of area $4\pi R^2$. The time coordinate t is chosen to be orthogonal to R. That is, $\left(\frac{\partial}{\partial t}\right)_a \left(\frac{\partial}{\partial R}\right)^a = g_{tR} = 0$. The metric then takes the form

$$\mathrm{d}s^2 = -\alpha^2 \mathrm{d}t^2 + a^2 \mathrm{d}R^2 + R^2 \mathrm{d}\Omega^2, \tag{2.5}$$

where $\mathrm{d}\Omega^2 \equiv \mathrm{d}\theta^2 + \sin^2\theta \mathrm{d}\phi^2$ is the metric on the unit two-sphere. Due to spherical symmetry, α and a are functions of t and R only. There still remains a gauge freedom associated with an arbitrary rescaling of the time coordinate $t \to t(\tilde{t})$. This is fixed by imposing $\alpha(t, 0) \equiv 1$. That is, the coordinate time t is chosen to be the proper time of a central observer. Apart from this gauge freedom, one also needs to ensure that spacetime does not have a conical singularity. This is prevented by enforcing the regularity condition $a(t, 0) \equiv 1$.

The Einstein-scalar system of equations are

$$G_{ab} = 8\pi \left(\nabla_a\phi\nabla_b\phi - \frac{1}{2} g_{ab} \nabla_c\phi\nabla^c\phi \right), \quad \nabla_a\nabla^a\phi = 0. \tag{2.6}$$

We have all in all three unknown variables to solve for: the two metric variables, α and a, and the scalar field, ϕ. For convenience, introduce the auxiliary variables

$$\Phi := \phi', \quad \Pi := \frac{a}{\alpha}\dot{\phi}, \tag{2.7}$$

where primes and dots denote derivatives with respect to R and t respectively.

In terms of these variables, the second-order Klein Gordon equation can be rewritten as a system of two first-order partial differential equations (PDEs) for Φ and Π,

$$\dot{\Phi} = \left(\frac{\alpha}{a}\Pi\right)', \tag{2.8}$$

$$\dot{\Pi} = \frac{1}{R^2}\left(R^2\frac{\alpha}{a}\Phi\right)'. \tag{2.9}$$

In spherical symmetry, the Einstein equations give four algebraically independent equations. Making use of the Bianchi identities, one of these can be expressed as a linear combination of the other equations (and their derivatives). The remaining three equations are first-order equations for $\dot{a}$, a' and α', given by

$$\frac{\alpha'}{\alpha} - \frac{a'}{a} + \frac{1-a^2}{R} = 0, \tag{2.10}$$

$$\frac{a'}{a} + \frac{a^2-1}{2R} = 2\pi R\left(\Pi^2 + \Phi^2\right), \tag{2.11}$$

$$\dot{a} = 4\pi\alpha R\Phi\Pi. \tag{2.12}$$

Altogether, we have a system of five equations for four variables, Φ, Π, α and a. Note that the dynamics are driven by the presence of the scalar field. This is because if $\Phi = \Pi = 0$, then (2.8- 2.9) are immediately verified, while, from (2.12), a is time independent. It then follows from (2.10) that α (with our gauge choice) is time independent. This is a direct consequence of Birkhoff's theorem: any spherically symmetric vacuum solution is static.

In the numerical simulations, the initial data for the scalar field are then evolved in time via (2.8-2.9). At any fixed time t, the metric variables can be updated via integration of (2.10-2.11). (2.12) is ignored in this fully constrained evolution scheme.

One notes that the above system of equations is scale invariant under the simultaneous rescaling $t \to ct$, $R \to cR$. This scale invariance is not surprising since spacetime has no intrinsic length scale (recall that the scalar field is massless). Under this transformation, the matter variables Φ, Π, change as $\Pi \to \Pi/c$, $\Phi \to \Phi/c$. It is therefore useful to consider scale-invariant quantities, such as

$$X(t,R) := \frac{\sqrt{2\pi}}{a}R\Phi, \tag{2.13}$$

$$Y(t,R) := \frac{\sqrt{2\pi}}{a}R\Pi. \tag{2.14}$$

The initial data on the matter fields are specified with $\Pi(0,R)$ and $\Phi(0,R)$. Choptuik considers different families of initial data, but a typical one consists of time-symmetric Gaussian data, where $\Pi(0,R) \sim \dot{\phi} \equiv 0$ (no initial velocity) and where Φ is a Gaussian. All but one of the initial parameters are fixed. This reduces the situation to a one-parameter family of initial data, labeled by the remaining free parameter, p. In order to study the behavior between dispersion and collapse, the only requirement is that the parameter p is chosen so that for one range of p, the initial data disperse, while for another range of p, they collapse. In some sense, the

parameter p characterizes the "strength" of the gravitational self-interaction of the scalar field. For this reason, one typically chooses p to be the amplitude of the initial data. In this case, for sufficiently small values of p, the scalar field will first implode at $R = 0$ due to its gravitational self-interaction. It then reaches a peak density, before exploding and dispersing to infinity, leaving flat space behind. On the other hand, for sufficiently large values of p, the scalar field will promptly collapse into a black hole.

Since we are in polar-radial coordinates, a black hole will never actually form in finite coordinate time, since an apparent horizon forms in spherical symmetry if [61],

$$\nabla_a R \nabla^a R = \frac{1}{a^2} = 0. \tag{2.15}$$

For this reason, polar-radial gauge avoids regions of trapped surfaces in spherical symmetry [113, 114]. In practice, for our gauge choice, what happens is that the timesteps become arbitrarily small as one approaches the onset of black-hole formation. When using polar-radial coordinates, the formation of a black hole is then decided once $1/a$ and/or the timestep have decreased below some specified threshold. The location where $1/a$ is minimal is then taken to be a good approximation for the location of the apparent horizon $R_{\rm AH}$. We note that, in asymptotically flat spacetime, much of the matter that does not initially contribute to the formation of the black hole is usually radiated away to infinity. As a consequence, the location and mass of the apparent horizon are also good approximation to the corresponding values at the event horizon. For our purposes, most properties concerning the black-hole mass that will be described in the following hold equally well irrespective of whether it concerns its value at the apparent or event horizon. In this work, we will not be working with null coordinates. All the simulations are carried out using Cauchy evolutions. We refer the reader to Ref. [115] and references therein for a discussion of the use characteristic evolutions in the study of critical phenomena.

For initial data close to criticality, $p \simeq p_\star$, Choptuik notes that scale-invariant quantities, which we generically label as Z (such as the dimensionless variables X, Y or M/R), become *discretely self-similar* near the center. Specifically, define the logarithmic time and radius coordinates

$$\rho := \ln\left(\frac{R}{R_0}\right), \quad \tau := \ln\left(\frac{t_\star - t}{R_0}\right). \tag{2.16}$$

where the critical time $t_\star$ is defined shortly. R_0 is dependent on the 1-parameter family of initial data and is used to normalize the overall scale of the solution; see Fig. 2.3.

Then, for sufficiently large τ and ρ (i.e. t sufficiently close to $t_\star$ and R to the center), we find the approximate relation,

$$Z(\tau, \rho) \simeq Z(\tau - \Delta_\tau, \rho - \Delta_\rho), \tag{2.17}$$

where Δ_ρ and Δ_τ are (positive) constants. This is illustrated in Fig. 2.2, where X is plotted at two different times in τ, separated by the above echoing periods. This plot shows that actually $\Delta_\tau = \Delta_\rho =: \Delta \simeq 3.44$. As will be explained in more details in the next section, this property of course only holds during some *critical regime*, when the solution is "close" to the critical

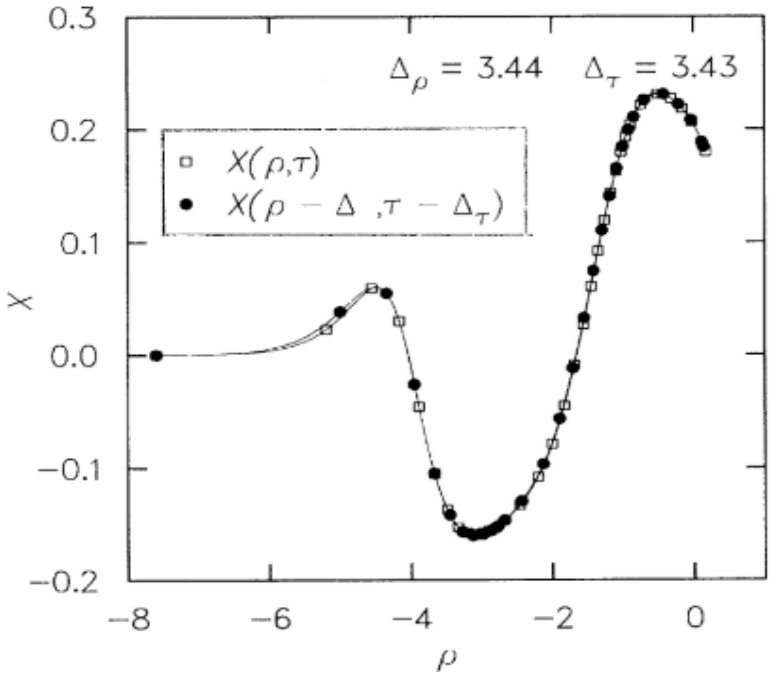

FIGURE 2.2: Illustration of the claimed echoing property (2.17). Here, the variable X is plotted at two different instances in "time" τ, separated by a constant echoing period Δ. Image credit: [52].

point. The more the initial data are fine-tuned to the black-hole threshold $p \simeq p_\star$, the longer this regime persists. In terms of the coordinates t and R, this means that, during this critical regime, if one looks at the profile of scale-invariant quantities Z near the center, the profile is the same at a time $e^{-\Delta}t$ later and on a length scale $e^{-\Delta}R$ smaller.

From there, one can entertain the following thought: if we start with *exactly* $p = p_\star$, the evolution would be characterized by an *infinite amount* of *echoes*, as one approaches $t \to t_\star$. These echoes occur on ever smaller spacetime intervals (by a scale factor $e^{-\Delta}$). One can then easily guess that at $t = t_\star$, spacetime will be singular. The above defines the accumulation point $t_\star$. In practice, we always start slightly off from the exact $p = p_\star$ configuration. We will therefore only get a finite amount of these echoes, before the initial data eventually disperse to infinity or collapse to a black hole. $t_\star$ is in practice found through fitting: one fits $t_\star$ so that (2.17) holds for the largest range in τ.

In the above, the echoing period Δ was introduced as a constant. The reader might wonder how it is affected by making a different choice of initial data and/or parameter p. For different choices of initial data and/or different choices of parameter p (and in fact even for different numerical quantities such as the temporal or spatial resolution), the critical value $p_\star$ is different. In terms of dynamical evolution however, only the *difference* $p - p_\star$ is relevant. In all cases, as we approach the critical point, not only is this discrete self-similarity observed, but the profile of the solution and the echoing period Δ, are *independent* of the initial data! Since the solution takes on some *universal* profile, it deserves a special name: the *critical solution*. The above can then be restated to say that the critical solution and the echoing period Δ are *universal*. This property of universality is one of the hallmarks of critical collapse and is illustrated in Fig. 2.3.

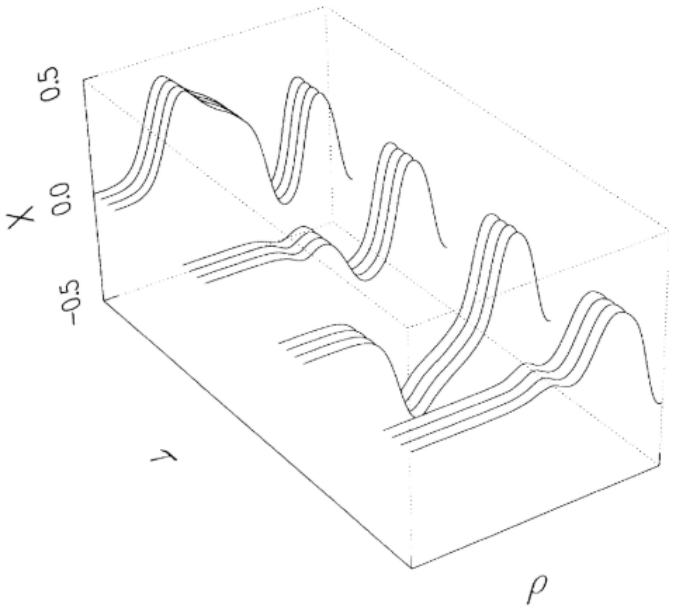

FIGURE 2.3: This plot illustrates the conjecture that the critical solution is independent of the initial data (universality): at different times τ, we have a group composed of three profiles, each corresponding to the evolution of a different fine-tuned family of initial data. For each family, the scale R_0 was chosen so that the different profiles align. The echoing phenomenon is not apparent on this plot as the shown interval in τ corresponds to less than one period. Image credit: [52].

In this plot, a 3D plot of X is shown as a function of ρ and τ, plotted during the critical regime. The plots are subdivided into four triplets of curves. Each curve within a triplet is obtained via a different family of initial data. The alignment of the curves within each triplet for different values of τ then exemplifies this property of universality described above.

We said before that, for exactly critical initial data $p = p_\star$, spacetime will develop some kind of singularity at $t = t_\star$. We can give more perspective to this by noting another remarkable result that emerged from Choptuik's study. If we consider supercritical data, $p \gtrsim p_\star$, one observes that the mass of the ensuing black hole also scales with the initial "distance" from the critical surface $p = p_\star$. Specifically, one observes that the mass of the initial black hole exhibits a power law,

$$M_{BH} \propto (p - p_\star)^\delta \,. \tag{2.18}$$

It turns out that the constant $\delta \simeq 0.37$ *is also independent* of the initial data! This is yet another instance of universality; see Fig. 2.4. We remark there that, strictly speaking, the relation (2.18) is not correct. As it has been later spelled out [70], the discrete self-similarity of the critical solution gives rise to a periodic wiggle in the power-law. In the plot Fig. 2.4 however, those wiggles were not picked up in the numerical evolution; see Refs [62, 116].

To summarize, in the exact case of $p = p_\star$, the solution exhibits, in *finite* central proper time, an infinite series of echoes, that occur on ever smaller spacetime scales, by a factor $e^{-\Delta}$. From the above scaling relation, it is also quite suggestive to say, since the critical point can be approached arbitrarily close from "the left or right", $p \to p_\star$, that it lies right at the boundary

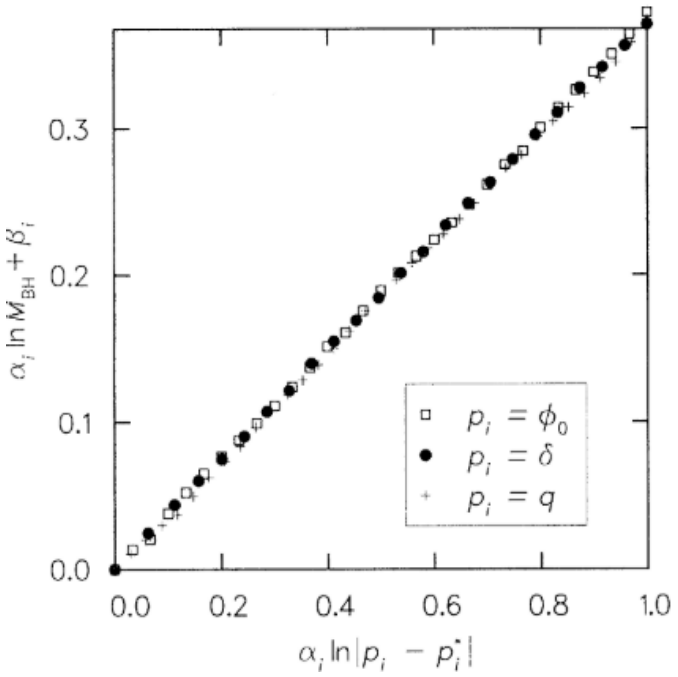

FIGURE 2.4: Evidence of the power law (2.18). The parameters α_i, β_i are used to scale/shift the range of the abscissa and align the plots (the proportionality constant implied in (2.18) does depend on the initial data). Note that there are three different plots, labeled by square, dot and cross, corresponding to a different fine-tuned parameter within the same family of initial data. Image credit: [52].

between a black hole with vanishing mass (and hence vanishing horizon radius) and diverging curvature (due to the self-similarity). The corresponding spacetime would then contain a singularity. Since it also happens that the lapse α stays bounded during the critical regime, it would seem that this singularity is *naked*. This gives a clear indication that the end-state is relevant to the cosmic censorships.

One of the remarkable consequences of Choptuik's discovery of the scaling phenomena in gravitational collapse is that, at least with a massless scalar field, it is possible to create a black hole with an arbitrarily small mass (and thus radius). On the subcritical side, is there a similar scaling behavior? For slightly subcritical initial data, the solution first starts to contract due to its own gravitational attraction. For a while the solution displays the familiar critical phenomena as it would for supercritical data. In particular, the solution contracts to smaller and smaller scales in a self-similar manner. One would therefore expect curvature invariants to diverge. Eventually, the unique growing mode of the critical solution has sufficiently grown and the solution then veers towards dispersion. The maximum of any curvature invariant (say the Ricci scalar Ric) then takes some maximum value, $\mathrm{Ric}_{\mathrm{max}}$, when the solution is "maximally contracted". Clearly, as we fine-tune more and more to the critical value $p = p_\star$, the growing mode is progressively suppressed and, as a consequence, the critical behavior subsists for longer and longer times. In Ref. [117], Garfinkle and Duncan showed that for the massless scalar field, the maximum of curvature $\mathrm{Ric}_{\mathrm{max}}$ then scales as

$$\mathrm{Ric}_{\mathrm{max}} \propto (p_\star - p)^{-2\gamma}, \tag{2.19}$$

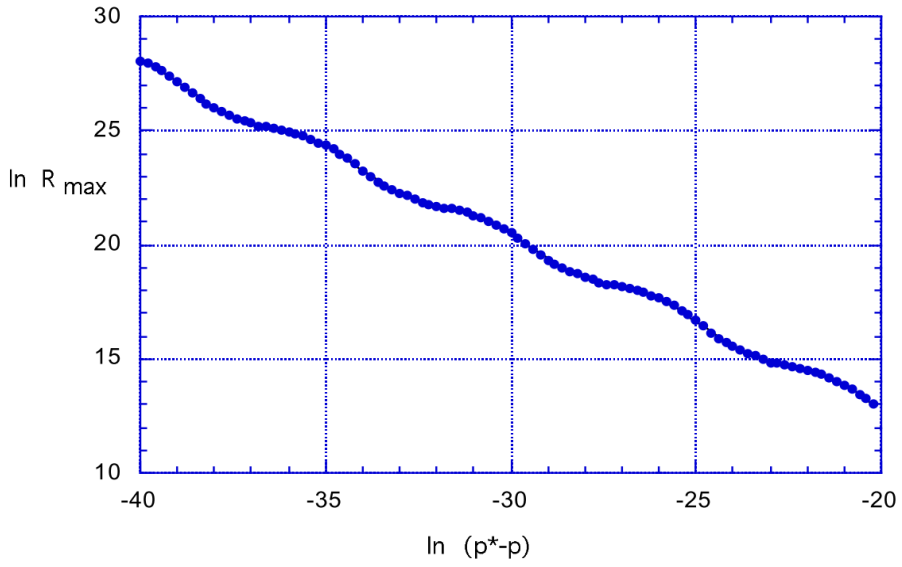

FIGURE 2.5: Power-law scaling of the maximum of the Ricci scalar against $p_\star - p$. Image credit: [117].

for some $\gamma > 0$. This is shown in Fig. 2.5. As we hinted before, the periodic wiggle is *not* a numerical error, but instead is a consequence of the periodic nature of the critical solution. The period is $\Delta/(2\gamma)$, inline with the theoretical prediction; see Refs [117, 118].

It turns out that $\delta = \gamma$. The theoretical reason will be explained in the next section, but this result is expected from naive dimensional analysis: The black hole has dimension [length] (in $3+1$ dimensions). On the other hand, the Ricci scalar has dimension [length]$^{-2}$. One would then expect the product $M_{AH}^2 \mathrm{Ric}_{\mathrm{max}}$ to be a constant.

2.3.2 The massive scalar field

The critical solution for the massless scalar field case is (discretely) self-similar. One might wonder what happens in the case of a *massive* scalar field with mass m. The mass of the scalar field m introduces a natural length scale, m^{-1}, destroying the scale invariance of the Einstein-matter equations. A direct consequence of this is that the system does not allow for *exact* self-similar solutions any more. Since no "massive self-similar" solutions can exist, what does this mean in the present case? Does this mean that the critical solution is of a completely different nature or that critical phenomena are outright excluded?

This situation was studied in Ref. [64]. They considered several gaussian-like family of initial data, each time parametrizing the family by the amplitude $p \equiv \phi_0$. Apart from p, the evolution now also depends on a dimensionless number that quantifies the size of the initial data with respect to to scalar field mass: λm. λ, of dimension [length], is a "radial extent" parameter, quantifying the size of the initial data. For example, for a typical gaussian initial data profile of the form

$$\phi(0, R) = \phi_0 e^{\frac{-(R-R_0)^2}{\sigma^2}}, \tag{2.20}$$

a typical choice would be to take $\lambda = \sigma$.

One finds two different kind of phenomena:

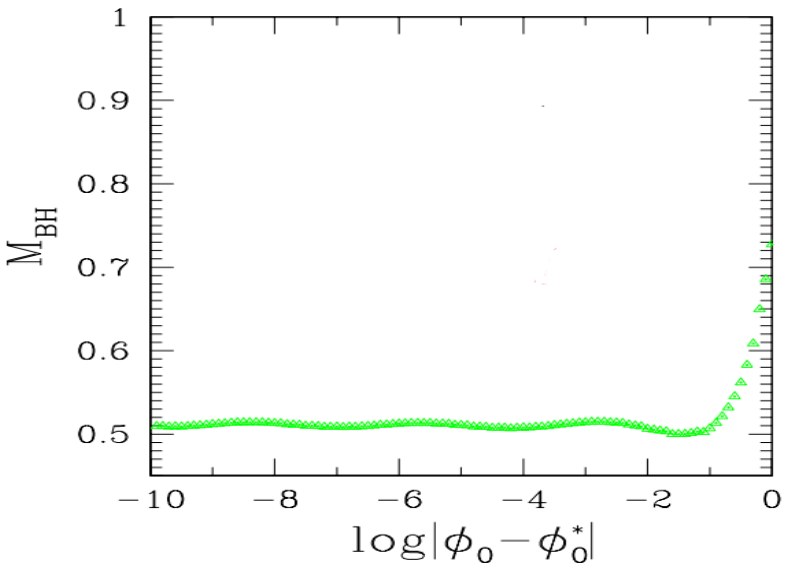

FIGURE 2.6: Plot showing the mass gap in $M_{\rm BH}$ as a function of $p - p_\star$, for $\lambda m \simeq 10$. Image credit: [64].

- In the "massless regime" $\lambda m \ll 1$, the black-hole mass and curvature scale like a power law with the same exponent as for the massless scalar field and the solution approaches the Choptuik (massless) discretely self-similar solution. The reason is that, for the critical solution to be self-similar, it is not necessary for the underlying system to be exactly scale invariant. Instead, it only needs to be scale invariant asymptotically. That is, as the solution shrinks to smaller and smaller spacetime scales, the dynamical effects of the scale introduced by the scalar mass become irrelevant. The underlying equations then become approximately that of the massless scalar field.

- In the"adiabatic regime" $\lambda m \gg 1$, the black-hole mass and curvature *do not* scale. Instead, there is a *mass gap* at the threshold of black-hole formation, where the mass and curvature approach some (family dependent) constant value; see Fig. 2.6. In particular, the critical solution is not self-similar. Instead, it approaches a marginally stable stationary configuration.

2.4 Type I and II phenomena and scalings

2.4.1 Self-similarity

From the scalar field studies described above, we can extract three main properties of critical collapse:

- Universality: the critical solution does not depend on the initial data.

- Either:

  - Power-law scalings: Near-critical solutions exhibit a scaling law for the mass (in case of strong data) and for the maximum of curvature (in case of weak data).

- The critical solution is self similar.

Or

- There is a mass gap.
- The critical solution is stationary/time-periodic.

In the case where there is a power-law scaling, the transition from no-black-hole to black-hole spacetimes may be viewed as a continuous phase transition [56] with the black-hole mass playing the role of order parameter. In analogy to phase transition in statistical mechanics, this type of behavior is called *type II critical phenomena*. For every matter field in $3+1$ dimensions which displayed type II behavior, the critical solution was always found to be self similar.

In the second case, the mass and curvature do not scale. This type of behavior can be observed if the Einstein-matter system admits stationary or time-periodic solutions, as well as a natural length scale, such as the mass of the scalar field, which becomes dynamically relevant during the evolution. The corresponding critical solution is not self-similar, but instead stationary or time-periodic. In that sense, it can be thought of as a metastable star [56]. Again, in analogy with phase transitions in statistical mechanics, such behavior is referred to as *type I critical phenomena*.

One can then describe the critical phenomena for the scalar field as follows: in the massless case, the scalar field exhibits typical type II critical phenomena. In the massive case, it exhibits both type I and II phenomena, depending on the size of the initial data compared to the mass of the scalar field.

As we noted before, the critical solution of the massless scalar field is of type II and the critical solution is discretely self similar. This property of self-similarity turns out to generalize to other matter systems. For example, in the spherically symmetric perfect fluid case (see Ch. 3), the critical solution turns out to be *continuously* self-similar (as opposed to discretely). Geometrically, a spacetime is continuously self similar (CSS) if it admits a homothetic vector-field ξ [119, 120],

$$\mathcal{L}_\xi g_{ab} = -2g_{ab}. \tag{2.21}$$

In order to gain some intuition into (2.21), let us choose coordinates $x^\mu = (\tau, x^i)$ adapted to the self-similarity. Specifically, we will choose the coordinate τ to be aligned with the integral flow of the homothetic vector ξ . That is, we choose

$$\xi \equiv \frac{\partial}{\partial \tau}. \tag{2.22}$$

It is then easy to see that (2.21) is satisfied if the metric takes the form

$$g_{\mu\nu}(\tau, x^i) = e^{-2\tau}\tilde{g}_{\mu\nu}(x^i). \tag{2.23}$$

In the case of discrete self-similarity (DSS), the vector field ξ demotes from a continuous to a discrete conformal isometry [121], where we instead require

$$g_{\mu\nu}(\tau, x^i) = e^{-2\tau}\tilde{g}_{\mu\nu}(\tau, x^i), \tag{2.24}$$

where $\tilde{g}_{\mu\nu}(\tau, x^i)$ is periodic in τ with some period Δ. In other words,

$$\tilde{g}_{\mu\nu}(\tau, x^i) = \tilde{g}_{\mu\nu}(\tau + \Delta, x^i), \quad \forall \tau, x^i. \tag{2.25}$$

If we choose the surfaces of constant τ to be spacelike, then τ plays both the role of a time coordinate and of the logarithm of spacetime scale. This latter fact can be seen from (2.23). Taking $\tau =: -\ln T$, then $g_{\mu\nu} \sim T^2$ and so T plays the role of a length scale.

In order to connect the above concept of self-similarity to the more intuitive, newtonian definition, it is helpful to view the situation in spherical symmetry. One can then write the metric in polar-radial gauge as in (2.5). It turns out that polar-radial gauge is actually well suited to self-similarity, because the metric can easily be recast into the form (2.23), by defining

$$x := -\frac{R}{t}, \qquad \tau := -\ln(-t). \tag{2.26}$$

Then, (2.5) becomes

$$\mathrm{d}s^2 = e^{-2\tau}\left((a^2x^2 - \alpha^2)\mathrm{d}\tau^2 - 2xa^2\mathrm{d}x\mathrm{d}\tau + a^2\mathrm{d}x^2 + x^2\mathrm{d}\Omega^2\right). \tag{2.27}$$

Therefore, the metric is self similar provided that α and a only dependent on x. This connects with our intuition from non-relativistic physics.

2.4.2 Linear perturbations and scaling laws

We noted above that, for type II phenomena, the mass and curvature follow a power-law behavior. In type I phenomena, the mass and curvature are instead non-zero constants, as the black-hole threshold is approached. In the latter case, there is another dimensionful quantity that scales: the duration during which the solution is (approximately) stationary [56]. We will now show how these scalings follow from a simple dimensional analysis. For simplicity, we will also assume that the type II critical solution is CSS. We refer the reader to [62, 116] for a discussion in the case of DSS.

Let Z correspond to a set of first-order dynamical variables and $Z = Z_\star$ the critical solution. For type I, typical choices of Z would be time-independent variable. For type II, suitable choices would be scale-invariant quantities such as the conformal metric $\tilde{g}_{\mu\nu}$, α, or a.

We can write the type I and II critical solution plus its linear perturbations as

$$Z(t, R) = Z_\star(x) + \sum_{n=0}^{\infty} C_n L(t) Z_n(x), \tag{2.28}$$

where we defined the variable

$$x := \frac{R}{s(t)}. \tag{2.29}$$

The function $s(t)$ is subject to the condition

$$\dot{s} = s_0, \tag{2.30}$$

where s_0 is some constant. This reduces to type I if $s_0 = 0$ and type II if $s_0 \neq 0$. Viewing x as the new "radial" coordinate, the function $L(t)$ encodes the time-dependence of the linear perturbation. As we will see shortly, $L(t)$ can either take a polynomial or exponential form, depending on the precise functional form of $s(t)$, and thus of x.

Now, note that for the linear perturbations, we have

$$\frac{\partial}{\partial t}(LZ_n) = \dot{L}Z_n - L\frac{s_0}{s}xZ_n', \tag{2.31}$$

$$\frac{\partial}{\partial R}(LZ_n) = \frac{L}{s}Z_n'. \tag{2.32}$$

In order to proceed further, we consider the cases $s_0 = 0$ and $s_0 \neq 0$ separately.

2.4.2.1 Type II mass and curvature scalings

If $s_0 \neq 0$, then $s(t) = s_0(t - t_\star)$. This means that $x \sim R/t$ and the critical solution is CSS. Additionally, the linear perturbations give a consistent set of equations if all the terms explicitly depending on t are all proportional to each other. From (2.31-2.32), this implies that

$$\dot{L} \propto \frac{L}{s} \iff L(t) \propto (t_\star - t)^{-\lambda}, \tag{2.33}$$

where λ is some constant. In terms of the logarithm of time, $\tau = -\ln(t_\star - t)$, this means that $L \propto e^{\lambda\tau}$. Then, the linear perturbation of the CSS critical solution (2.28) becomes

$$Z(t, R) \simeq Z_\star(x) + \sum_{n=0}^{\infty} C_n(p)e^{\lambda_n\tau}Z_n(x). \tag{2.34}$$

The amplitudes $C_i(p)$ depend on the initial data and thus on p. By definition, the critical solution is assumed to have a single growing mode, say λ_0. At $p = p_\star$, $\lim_{\tau\to\infty} Z = Z_\star$ by definition, which requires $C_0(p_\star) = 0$.

Clearly, the linear perturbation ansatz (2.34) will cease to be valid for large τ due to the growing mode. This means that there exists some $\tau = \tau_\star$ where the term in (2.34) involving the growing mode dominates the perturbation. At that time $\tau = \tau_\star$, we can then make the following approximation

$$Z(t, R)|_{\tau=\tau_\star} \simeq Z_\star(x) + \epsilon Z_0(x), \tag{2.35}$$

where we defined

$$\epsilon := \left.\frac{\mathrm{d}C_0}{\mathrm{d}p}\right|_{p_\star}(p - p_\star)e^{\lambda_0\tau_\star} \tag{2.36}$$

Because of self-similarity, the data at $\tau_\star$ are the same, up to an overall scale $\sim e^{-\tau_\star}$ as it is the only length scale of the system. In particular, once the solution has collapsed, the black-hole mass, of dimension [length]$^{d-2}$ (in $d+1$ spacetime dimensions), depends on the initial data once the critical regime stops, when $\epsilon \sim \mathcal{O}(1)$. Making use of (2.36), the mass then scales as

$$M_{\rm BH} \propto e^{-(d-2)\tau_\star} \propto (p - p_\star)^\delta \,, \tag{2.37}$$

where we defined [56, 99],

$$\delta := \frac{d-2}{\lambda_0}. \tag{2.38}$$

Similarly, the maximum of the Ricci scalar $\mathrm{Ric}_{\rm max}$ has dimension [length]$^{-2}$, so that

$$\mathrm{Ric}_{\rm max} \propto e^{2\tau_\star} \propto (p_\star - p)^{-2\gamma} \,, \tag{2.39}$$

where

$$\gamma := \frac{1}{\lambda_0}. \tag{2.40}$$

In particular, we have the following relation between the exponents

$$\delta = \gamma(d-2), \tag{2.41}$$

for $d \geq 3$. This relation does not hold for $d = 2$, since, in this spacetime dimension, the mass is dimensionless.

2.4.2.2 Type I lifetime scaling

If $s_0 = 0$, then $s(t)$ is a constant and the variable x effectively plays the role of a normalized radius coordinate R. The critical solution $Z_\star(x)$ is then static. Additionally, the second term in (2.31) drops out and the consistency of the linear perturbation equations requires that

$$\frac{\dot{L}}{L} = \lambda \implies L \propto e^{\lambda t}. \tag{2.42}$$

We can then follow the same dimensional analysis that has led us to (2.36), where $\tau_\star$ now replaced with t_p, parametrizing the *lifetime* of the intermediary state when the solution is approximately static. This lifetime then scales as

$$t_p = -\frac{1}{\lambda_0} \ln|p - p_\star| + \text{constant}. \tag{2.43}$$

2.5 Global structure of Choptuik's critical solution

From our discussion of critical phenomena so far, it is intuitively clear that type II critical collapse is of relevance for the cosmic censorships. On the one hand, for strong initial data, the mass of the black hole becomes vanishingly small as we fine-tune to the black-hole threshold. On the other hand, for weak data, it is the maximum of curvature that becomes arbitrarily

large, as the black-hole threshold is approached. Naively, one is then tempted to combine both of these results to say that for perfectly fine-tuned initial data, the critical point (see Fig. 2.1 again) corresponds to a "zero-mass black hole" (and correspondingly zero radius) and infinite curvature at its center. Such a spacetime could then possible run into conflict with either or both cosmic censorships!

While the last sentence is in fact true as we will see, it is important to realize that the critical point is not a "zero-mass black hole". Instead, *the critical point is the critical solution itself.* This fact is clear from the dynamical point-of-view. The critical surface has a fixed point, the critical point. It is an attractor within the critical surface and a repeller in the direction perpendicular to the critical surface. The critical point has therefore a single growing mode and the critical surface is of codimension one. Initial data close, but not on the critical surface, $p \simeq p_\star$, will first move in the direction tangent to the critical surface, towards the critical point. Close to that critical point, the solution is then well approximated by the critical solution.

In what way is then the critical solution connected to the weak and strong cosmic censorship? We will now answer this question by analyzing the global structure of the critical solution for the massless scalar field, as it is laid out in Ref. [53], and argue why it is relevant for both cosmic censorships.

Recall that a spherically symmetric metric has, in adapted coordinates, a conformal factor $\sim e^{-2\tau}$; see again Eq. (2.23). Spacetime is then discretely self-similar if the conformal metric is periodic in τ with some period Δ. It is CSS if it is independent of τ.

Solely due to this conformal factor, it already follows that this spacetime has a curvature singularity at $\tau = \infty$. This kind of singularity is a direct product of self-similarity and not linked to gravity. Even in newtonian or fluid mechanics, self-similar variables only depend on the ratio "$R/(t_\star - t)$". The initial data is given at $t = 0$ say, and the *accumulation point* $t = t_\star$ corresponds to the time where the matter has shrunk to an infinitely small size. The main difference in general relativity is that this self-similar behavior also causes the curvature of spacetime to blow up, by virtue of the Einstein equations.

The spacetime of the critical solution is illustrated in Fig. 2.7. The curvature singularity is a point located at $\tau = \infty$. $x = x_c$ is the regular center, $x = x_p$ the past light-cone from the singularity and $x = x_f$ its future light-cone. Inside the past lightcone, x and τ are defined as in (2.26). τ can then play the role of a time coordinate as explained before. Note that the surfaces of constant x become null at both light-cones. In the "outer region", $x_p < x < x_f$, a different, more convenient gauge choice is being made, where surfaces of constant τ are now timelike and surfaces of constant x spacelike. The coordinates are chosen so that they are continuous across the lightcones.

In practice, how is the critical solution constructed? Making a spherically symmetric DSS ansatz, the resulting ODE system is singular at the center and at the past lightcone. Imposing analyticity there defines a boundary value-problem. It turns out that there are at most a countable set of such solutions, one of which having a single growing mode. In other words, the spherically symmetric DSS ansatz, together with the requirement for the solution to be analytic everywhere in the causal past of the singularity, and possessing a single growing mode

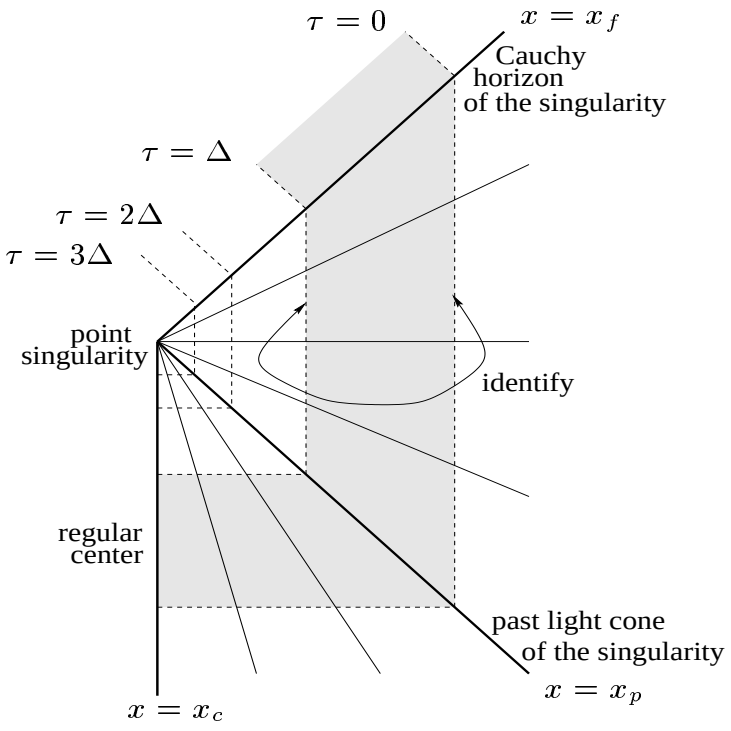

FIGURE 2.7: (Uncompactified) diagram of a discretely self-similar spacetime. The singularity is a single point at $\tau = \infty$. $x = x_c$ is the regular center, to the past of the singularity and $x = x_p$, the past lightcone. $x = x_f$ is the future lightcone from the singularity and also acts as a Cauchy horizon. From the regular center to the Cauchy horizon, the solution is unique, assuming spherical symmetry, DSS, analyticity and assuming it has a single growing mode. Image credit: [53].

singles out a unique solution. This unique solution agrees perfectly with the critical solution found in the numerical simulations.

In practice, however, this solution cannot be obtained explicitly. Instead, one considers a Taylor expansion at the center and past lightcone. The requirement of analyticity then materializes into algebraic conditions. The solution inside the past lightcone is then found via the shooting method: we shoot "to the right" from $x = x_c$ and "to the left" from $x = x_p$. The mismatch from both shootings is resolved at some midpoint and fixes the remaining freely specifiable data at the center and lightcone. Once the critical solution is obtained inside the past lightcone, one can then, again via shooting, analytically extend the solution outside the lightcone, up to the future lightcone of the singularity. See Ch. 3 for an illustration of this procedure in the case of a perfect fluid.

As the future lightcone is approached, the scalar field oscillates an infinite number of times, but the amplitude of the oscillations goes to zero. Furthermore, the curvature invariants, such as the Ricci scalar, are finite as the future lightcone is approached (they diverge if one approaches the singularity). In particular, despite the presence of the singularity, it is possible to assign regular null data on the future lightcone $x = x_f$.

With this assumption, one can consider an expansion around $x = x_f$. One can show that, to leading order in $y := x - x_f$, the Ricci scalar, to the past of the future lightcone, is of the

form

$$\mathrm{Ric}(\tau, y) = \mathrm{Ric}_{\mathrm{reg}}(\tau) + |y|^{\epsilon}\mathrm{Ric}_{\mathrm{sing}}(\tau) + \cdots , \tag{2.44}$$

where $\mathrm{Ric}_{\mathrm{reg}}(\tau)$ and $\mathrm{Ric}_{\mathrm{sing}}(\tau)$ are periodic with period Δ. It is shown numerically that $\epsilon < 1$ (in fact $\epsilon \sim 10^{-6}$). In particular, the Ricci scalar is C^0 at the Cauchy horizon. It follows that the scalar field is C^1 there, since $\mathrm{Ric} \propto (\nabla\phi)^2$.

What happens as we try to cross the future lightcone $x = x_f$? Assuming that the solution is still DSS, the expansion, slightly to the future of the future lightcone, is also of the form (2.44). The main point to note, however, is that there is no reason why $\mathrm{Ric}_{\mathrm{sing}}$ should be the same on both sides of $x = x_f$ (making such a choice does not improve the differentiability of the solution). The solution in the causal future of the singularity is fixed by the regular null data at the future lightcone (found for example from the shooting method described before), as well as some *arbitrary* periodic function. This function can be thought to encode the information that come out of the singularity. The future lightcone is therefore a Cauchy horizon.

Moreover, in polar-radial coordinates (2.5), α and a are bounded above and below. As a consequence, the redshift measured by two observers located "far-away" from the singularity is also finite. In other words, a point of arbitrarily large curvature (arbitrarily close to the singularity) can be observed from a point with arbitrarily low curvature (far-away observer): the singularity is naked.

We remark here that the critical solution is not asymptotically flat. This is not a contradiction from the fact that the critical solution can be approached arbitrarily closely by fine-tuning asymptotically flat initial data. For near-critical data, the solution is well approximated by the critical solution only for some interval of time, within some bounded spacelike hypersurface near the center. The conformal diagram for an exact critical initial data, as it approaches the critical point would then resemble that of the critical solution, but truncated by a null slice, sufficiently far away from the center. Beyond, the solution is matched to some asymptotically flat spacetime. This is illustrated in Fig. 2.8.

2.6 Critical phenomena in other matter systems

2.6.1 Charge scaling

So far, we have only dealt with initial data with zero charge and zero angular momentum. Due to the no-hair theorem of the Einstein-Maxwell system, black holes are uniquely characterized by their mass M, charge Q and angular momentum J [5]. It follows that a complete picture of critical phenomena in gravitational collapse requires us to move to a more generic situation, which allows for initial data to carry charge and angular momentum. Of the two, the addition of charge is probably the simplest, because one can investigate its effects while still staying in spherical symmetry.

For this reason, it is natural to consider the critical phenomena of a charged scalar field ϕ, with charge q, coupled to electromagnetism. This is precisely what was considered in Refs [63, 118].

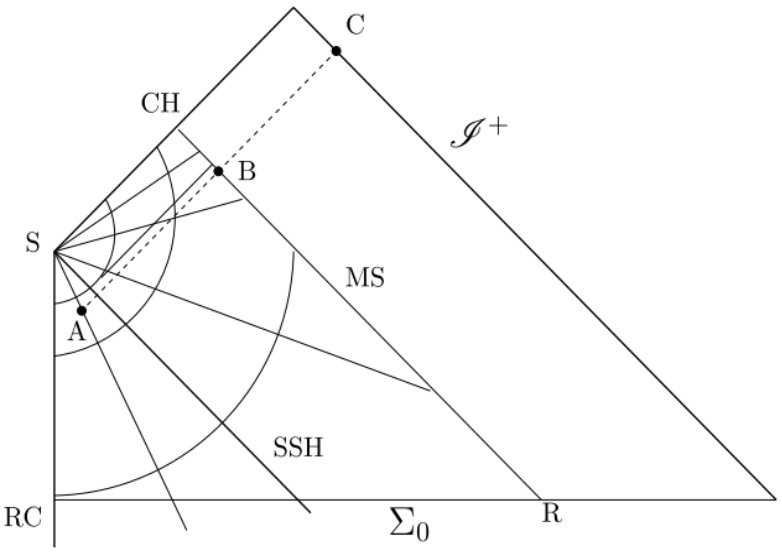

FIGURE 2.8: Conformal diagram of the critical solution matched to an asymptotically flat one. Σ_0 is the initial timeslice, RC the regular center, SSH the self-similarity horizon $x = x_p$, S the singularity and CH the Cauchy horizon. The self-similar initial data is prepared on the initial slice Σ_0, from RC, up to a point R. Beyond this point, we smoothly glue any asymptotically flat initial data. MS marks the null boundary between the critical region and the asymptotically flat one. The only restriction to R is that the asymptotically flat initial data are not causally connected to S. Spacetime cannot be uniquely continued beyond CH. In parallel, the redshift between A and B is finite by self-similarity. It remains finite from B to C by asymptotic flatness. Image credit: [53].

A first important point to remark is that the coupling with electromagnetism causes the Einstein-scalar-Maxwell equations to be not scale invariant anymore. Physically, this is expected, because the scale invariance of the underlying equations reflect the fact that the physical system does not have any "natural" or intrinsic length scale. This is the case for the *massless, uncharged* scalar field. However, the coupling to electromagnetism introduces a scale q^{-1}, which breaks the scale invariance, similarly as it does for the massive scalar field.

One might wonder if the net effect will then be similar to the massive scalar field discussed in Sec. 2.3.2. It turns out that the critical solution still exactly corresponds to the one found by Choptuik, which is a solution to the (complex) scalar field coupled only to gravity (also called free complex scalar field and is obtained by setting $q = 0$ in the field equations)! For the exact free complex scalar field, the critical solution is the real DSS solution found by Choptuik [62].

Taking Z to stand for any suitably rescaled variable, the solution then takes the following form near the black-hole threshold

$$Z(t, R) = Z_\star(\tau, x) + \delta Z_{\text{real}} + \delta Z_{\text{imaginary}}. \tag{2.45}$$

The first term is the usual critical solution, periodic in τ. The second and third terms correspond to its "real" and "imaginary" perturbations. Here, real perturbations correspond to those perturbations where δZ and $\delta\phi$ are purely real. while imaginary those which come from complex conjugate pairs. The perturbation spectrum of the real perturbations, $\{\lambda_i\}$, is then the same as for the real scalar field. In particular, it has a unique growing mode $\lambda_0 \simeq 2.674$. On the other

hand, the perturbations of the imaginary perturbations, $\{\mu_i\}$, turn out to be all decaying. We denote the slowest decaying mode by $\mu_0 \simeq -0.362$. In Ref. [118], a detailed analysis shows that the black-hole mass scales just as for the uncharged case,

$$M_{\rm BH} \sim (p - p_\star)^{\frac{1}{\lambda_0}}, \tag{2.46}$$

where λ_0 is the unique growing mode of the critical solution. The proportionality constant is family dependent. On the other hand, the charge scales as

$$Q_{\rm BH} \sim (p - p_\star)^{\frac{(2-\mu_0)}{\lambda_0}}. \tag{2.47}$$

A direct consequence of this is that the charge-to-mass ratio scales as

$$\frac{Q_{\rm BH}}{M_{\rm BH}} \sim (p - p_\star)^{\frac{(1-\mu_0)}{\lambda_0}}, \tag{2.48}$$

so that, in the limit of fine-tuning $Q_{\rm BH}/M_{\rm BH} \to 0$. Thus the charge of the resulting black-hole becomes increasingly suppressed as we fine-tune to the black-hole threshold. In that sense, the introduction of a charge in the scalar field does not modify the picture of critical phenomena. This also gives some intuition as to why the critical solution for the scalar field coupled to electromagnetism is still the same as for the uncharged case.

2.6.2 Spin scaling

We can complete the picture by now considering the effects of nonspherical initial data. The scalar field case is a little more subtle, in part because the critical solution is DSS and also because angular momentum only enters the picture at *second*-order [83]. To simplify the analysis, we will instead consider the critical solution of a different matter field: the perfect fluid. As will be thoroughly presented in Ch. 3, the corresponding critical solution turns out to be CSS and we can consider the usual linear perturbation analysis. We will summarize the key derivations given in Refs [91, 122].

Recall that in the neighborhood of the critical solution, there exists a regime $\tau \simeq \tau_\star$ where the unique growing mode dominates the linear perturbation (2.34)

$$Z(\tau_\star, x, \theta, \phi) \simeq Z_\star(x) + \epsilon Z_1(x) \equiv Z_0(x), \tag{2.49}$$

where

$$\epsilon \propto (p - p_\star) e^{\lambda_0 \tau_\star}, \tag{2.50}$$

and θ, ϕ are the usual spherical coordinates on the unit sphere.

Now suppose that we add a small correction carrying some angular momentum. For the ensuing critical solution to still be critical, we assume that all the nonspherical modes are decaying (or else the critical surface would not be of codimension one anymore).

For small angular momentum, the $l = 1$ modes dominate over the other modes in the sense that it is the slowest decaying mode [122]. A fairly intuitive way to understand this is to note

that the Kerr black hole, for small spin J, can be viewed as a perturbation of the Schwarzschild black hole. The $l = 1$ mode is the only first-order metric perturbation when one considers an expansion in powers of J. Retaining the effect of this mode only, a small nonspherical perturbation of Z_0 is then

$$Z(\tau_\star, x, \theta, \phi) \simeq Z_0(x) + e^{\mathrm{Re}\,\lambda'\tau_\star}\delta Z_0(\tau_\star, x, \theta, \phi), \tag{2.51}$$

where we kept the dominant $l = 1$ axial mode, $\mathrm{Re}\,\lambda' < 0$.

Since the effects of angular momentum is controlled by the second term, it follows, within the linear approximation, that the angular momentum of the final black hole, has to be proportional to $e^{\mathrm{Re}\lambda'\tau_\star}$. Since this scale is dimensionless while J has dimension [length]^2, we require, from dimensional analysis, that

$$\frac{J_{\rm BH}}{M_{\rm BH}^2} \sim e^{\mathrm{Re}\,\lambda'\tau_\star}. \tag{2.52}$$

It then follows that J also follows a power law of the form

$$J_{\rm BH} \sim (p - p_\star)^{\gamma_J}, \tag{2.53}$$

where the critical exponent is related to the mass exponent δ as

$$\gamma_J = (2 - \mathrm{Re}\,\lambda')\delta. \tag{2.54}$$

As a corollary, we find that, in the limit of fine-tuning, the black hole is nonspinning.

The above argument relied on the linear perturbation around a CSS solution. In the case of a scalar field, the above argument does not directly apply because black-hole angular momentum only appears at *second-order*. For the scalar field, one can show that all the nonspherical linear perturbations decay [123]. Since the linear perturbations enter the second-order equations as a source term, the associated slowest decaying mode will then contribute *twice* to the angular momentum scaling. The critical exponent for the scalar field is then

$$\gamma_{J,scalar} = (2 - 2\mathrm{Re}\,\lambda')\delta. \tag{2.55}$$

We still find that the angular momentum decreases more rapidly than the square of the mass, so that, in the limit of fine-tuning, the black hole is once again nonspinning.

2.6.3 Rotating scalar field

An important assumption of the above is that we only considered perturbations beyond spherical symmetry. What happens for "strong" deviation from spherical symmetry?

This case was investigated in Ref. [84], restricting to axisymmetry. Axisymmetry is the maximal symmetry for which rotating black holes can form. This then makes it the "strongest" symmetry assumption for which rotating collapse can be studied. In axisymmetry, the corresponding Killing vector $\xi = \partial/\partial\phi$, generates a conserved current: $j^a := T^a_b\xi^b$. The associated

conserved quantity, the angular momentum J, is [85]

$$J := \int_\Sigma \omega \sqrt{h} d^3x, \tag{2.56}$$

where $\omega := -j^a n_a = -T^{ab} n_a K_b$ is the angular momentum density per unit volume. Σ is a spacelike hypersurface (usually corresponding to $t =$ constant), h the induced metric and n^ν is the vector normal to Σ. For a scalar field Ψ in cylindrical coordinates (t, R, z, ϕ), the angular momentum reads

$$J = -\int_\Sigma \left(\Psi_{,\phi} \nabla_\nu \bar{\Psi} + \bar{\Psi}_{,\phi} \nabla_\nu \Psi \right) n^\nu \sqrt{h} d^3x. \tag{2.57}$$

So, if we wish for the scalar field to carry angular momentum, it needs have an angular dependence. Said differently, an axisymmetric massless scalar field cannot carry angular momentum. Therefore, in Ref. [84], the angular momentum is zero.

The authors do find, even for strong deviations from spherically symmetric initial data, that the solution, at least during an intermediary stage, approaches the spherically symmetric critical solution. However, they also find indications for a second slowly growing $l = 2$ mode, albeit the growth rate is much slower than the spherical one, hence the need for good fine-tuning. The simulations suggest that this mode will eventually cause the near-critical solution to split into two spherical regions, each again approaching the spherically symmetric critical solution. There is evidence that is branching occurs again with increased fine-tuning. In principle, this suggests that for arbitrary fine-tuning, this bifurcation behavior will repeat indefinitely. This type of branching behavior was also recently discovered for gravitational [124] and electromagnetic waves [97]; see next section.

The nonspherical growing mode is in conflict with the perturbative calculations in [123], which shows that all the nonspherical perturbations of the massless scalar field are decaying. The numerical results are however not conclusive since the authors cannot rule out that this observed growing mode is a numerical artifact.

In Ref. [86], Healy and Laguna attempted to investigate this case again, but beyond axisymmetry where the deformation was proportional to the real part of the spherical harmonic Y_{21}. They find the same black-hole mass scaling as in spherical symmetry. Their simulations also confirm that the unstable spherical mode dominates during the onset of black-hole formation. They find some hints that the critical solution is discretely self-similar, although the echoing period is slightly smaller than in spherical symmetry. Their critical initial data are however fairly far from the black-hole threshold, so they cannot confidently claim that this period is the echoing period of the critical solution. For the same reason, they were not able to reject or confirm the results concerning the bifurcation of the critical solution found in Ref. [84].

In Ref. [85], the authors considered instead a *complex* scalar field in axisymmetry. This is a known "trick" to allow for a scalar field to carry angular momentum even in axisymmetry. To see this, note that if we take Ψ to be complex, we can then introduce the angular dependence purely as a phase:

$$\Psi = e^{im\phi} \Phi, \tag{2.58}$$

where Φ is axisymmetric. The resulting stress-energy tensor is then also axisymmetric! From the Einstein equations, imposing regularity at the center $R = 0$, requires that $\Phi \sim R^m$, so that m is an integer. This trick does have a price to pay: this ansatz introduces a pseudo-centrifugal potential $2m/R$ into the wave equation for Φ. This term is however not to be attributed to the centrifugal force due to rotation, since it is non-zero even if the angular momentum current vanishes identically. For all the initial data they considered, the critical solution is discretely self-similar with period $\Delta = 0.42$ and scaling exponent $\gamma = 0.11$ in the Ricci scalar. The critical solution is confirmed to not being spherically symmetric and therefore cannot correspond to the spherically symmetric critical solution. Finally, they find that, close to the black-hole threshold, the angular momentum scales as $J_{\rm BH} \sim M_{\rm BH}^6$. In the limit of fine-tuning the black-hole is therefore nonspinning.

2.6.4 Vacuum collapse

When studying critical collapse beyond spherical symmetry, the study of the collapse of pure gravitational waves stands out for several reasons: First, gravitational waves do not exist in spherical symmetry (at least in $3 + 1$ dimensions since Birkhoff's theorem can be evaded in higher dimensions [95]). This means that the critical solution, if it exists, cannot be spherically symmetric. Second, it is useful to see if critical phenomena are a by-product of the coupling of gravity to matter models, or if it is more intrinsically linked with gravity. Finally, not only do gravitational waves exist beyond spherical symmetry, but they are also unavoidable products of time evolution. In particular, if gravitational waves can show critical phenomena, it follows that, when studying the critical collapse of some matter model, we will find a competition between the critical solution due to the gravitational waves and the one due to the matter field. This of course substantially increases the dynamics and complexity of such systems.

For all these reasons, it is perhaps not surprising that, following Choptuik's discovery of critical phenomena with a spherically symmetric massless scalar field, the collapse of axisymmetric wave packets was historically the *second* study to investigate critical phenomena. In their famous papers [93, 94], Abraham and Evans considered Teukolsky-type initial data [125] and found that pure gravity does exhibit critical phenomena.

In the first paper, they focused their attention on ingoing gravitational-wave packets. They find that the critical solution is discretely self-similar, with critical mass exponent $\delta \simeq 0.37$ and echoing period $\Delta \simeq 0.59$. At that time, since the massless scalar field case was the only other matter field studied so far, the remarkable closeness of the critical exponent between this system and the scalar field model was attributed as evidence that the exponent might be universal even across matter fields. This is now known not to be the case. In the second paper, they investigated the critical phenomena using a second family of initial data and found evidence that the critical solution, the critical exponent and the echoing period are universal.

It is striking that, despite both of these papers being written in the early 90s, and despite having now access to much better computational resources, these results have not yet been independently reproduced. In Refs [126] and [124] this issue was re-investigated. In the former, Brill-type initial data [127] were used and the authors found *another* critical solution for

which a bifurcation, reminiscent of the rotating scalar case considered above, was identified. The scaling and echoing period are found to be independent of the initial data. The bifurcation behavior was also confirmed in Ref. [96]. In the latter, both Brill and Teukolsky-like initial data were considered. They observe a universal profile of echo patches forming during the critical regime. The profiles of the echoes, occurring at irregular periods and scales, are only approximate copies of some universal template. Finally, the critical exponent and echoing period all seem to depend on the choice of family of initial data.

As one can see, the critical phenomena in the case of vacuum are still quite poorly understood. This constitutes the biggest obstacle in the current research in critical collapse.

2.6.5 Scalar field in $2+1$ dimensions

We have seen that that there are two major obstacles in studying critical collapse beyond spherical symmetry in $3+1$ dimensions: First, in spherical symmetry, all variables only depend on "time" and "radius". The critical solution can then be treated largely analytically, since a self-similar ansatz reduced the Einstein-matter equations into a system of ODEs. Generalizing spherically symmetric initial data to, say, axisymmetric ones causes all the variables to be dependent on an additional coordinate. Second, one will have to deal with gravitational waves. As we have seen above, pure vacuum can by itself display critical phenomena. As a result, when one wishes to consider the critical behavior of some matter beyond spherical symmetry, one will have to deal with a competition between the matter field and the gravitational waves, each of which can separately display critical phenomena. It then becomes difficult to disentangle the contribution from the matter field and from the gravitational waves.

A tempting way to circumvent both of these problems is to consider the problem in $2+1$ spacetime dimensions. In $2+1$ dimensions, gravitational waves do not exist. Furthermore, in axisymmetry, all the variables are still only functions of time and radius. This makes the generalization from spherical symmetry to axisymmetry much more tractable.

In parallel, an interesting peculiarity in $2+1$ dimensions is that the formation of black holes requires a negative cosmological constant Λ [58, 59]. This fact seemingly causes a paradox: On the one hand, a cosmological constant is required for black holes to form and thus for the possibility of critical phenomena to occur. On the other hand, one expects, for type II phenomena, the cosmological constant to become dynamically irrelevant as the solution shrinks to arbitrarily small length scales.

Independently, a complication comes with the introduction of a negative cosmological constant: conformal infinity is timelike; see Ch. 4. In particular, the evolution depends on the boundary conditions one wishes to impose there. The most common and natural boundary condition is to require the boundary to be totally reflecting. This however creates an even bigger problem: some matter fields are subject to a turbulent instability. Specifically, it was shown in Ref. [128] that even arbitrarily small and smooth massless scalar perturbation of anti-de Sitter will achieve arbitrarily large curvature as the scalar field bounces back and forth between the center and the boundary. This back and forth movement causes the scalar field to transmit energy to higher and higher frequency modes. In the case where the total mass of the system

is non-positive (in $2+1$ dimensions, the black hole spectrum $M > 0$ is separated from anti-de Sitter, $M = -1$ by a unit mass gap), this cascading effect continues indefinitely and so spacetime attains higher and higher curvature. In particular, this shows that spacetime will not settle to anti-de Sitter (adS). This gives strong evidence that adS is not nonlinearly stable [129]. If the total mass of the system is positive, this turbulence is eventually cut off by the formation of a black hole. This in turn raises the question as to how one would then define weak data.

In Ref. [74], Pretorius and Choptuik studied for the first time, the critical collapse of a spherically symmetric massless scalar field case in $2 + 1$ dimensions. Due to the turbulent behavior, they only investigated "prompt collapse". That is, one makes a distinction between those initial data which "immediately" collapse into a black hole (without any reflection from the boundary), and those initial data that require one or several reflections before collapsing into a black hole.

There are a few similarities and differences as compared to the $3+1$ setting. First, the scalar field displays typical type II behavior: the apparent horizon mass and maximum curvature scale like a power law. The curvature scaling exponent turns out to be $\gamma \simeq 1.2$ (right plot of Fig. 2.9). Compare this with its value in $3 + 1$ dimensions ($\gamma \simeq 0.74$). Furthermore, they claimed that the mass and curvature exponents are related by $\delta = 2\gamma$. Pretorius and Choptuik justified this relation from the expression of the mass function in $2 + 1$ dimensions; see (6.34). At the apparent horizon (in spherical symmetry), we have that $M_{AH} = -\Lambda R_{AH}^2$. The argument then goes that one would expect M_{AH} to behave as if it had dimensions [length]^2. However, their plot, showing the mass against $p - p_\star$, correctly suggests instead that $0 < \delta < 1$ (left plot of Fig. 2.9). This shows that naive dimensional analysis does not work here. Second, the critical solution is *approximately continuously* self-similar, as opposed to its $3 + 1$ counterpart which is discretely self-similar; see Fig. 2.10.

The reason why we used the word "approximately" is because in $2+1$ dimensions, the cosmological constant is required for black holes to form. Its effects can therefore not be purely perturbative. Nonetheless, as the solution shrinks to smaller length scales, the cosmological constant becomes dynamically irrelevant over these short length scales and spacetime is approximately scale invariant there. One would however expect its effects to be large (and essential) on larger length scales only, but this was not discussed in this paper.

Later, the system was revisited in much more depth in Ref. [78]. The authors confirmed that the critical solution was approximately self-similar near the center. Specifically, on the grounds that at sufficiently small length scales, the solution should be approximately self-similar, Garfinkle [130] found all the exact CSS solutions with $\Lambda = 0$ which are analytic between the center and the past lightcone of the singularity. These solutions only depend on the ratio $x := R/t$ of radius over proper time and form a one-parameter family of solutions, labeled by $n = 1, 2, 3, \cdots$. By inspection, it turns out that the $n = 4$ member is in good agreement with the numerical data inside the past lightcone.

Despite those encouraging results, there are multiple unsatisfactory facts. First, in the family of CSS solutions, the lightcone is actually an apparent horizon. Naively attempting to analytically extend the solution beyond the lightcone also shows that every surface of constant x is

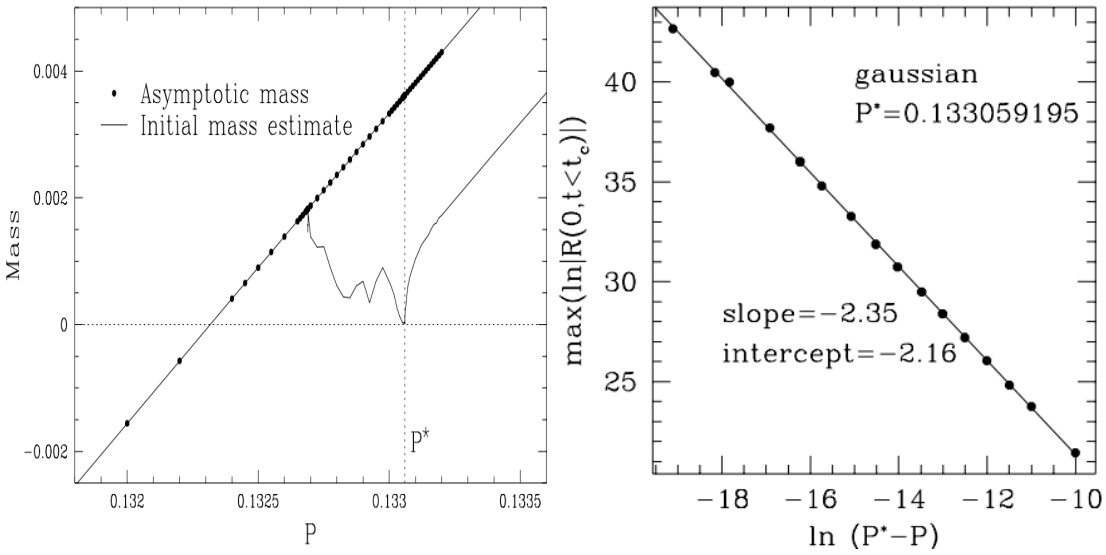

FIGURE 2.9: Left plot: Power-law scaling of the apparent-horizon mass as a function of p, close to $p_\star$. Note that by eye $\delta < 1$. The mass estimate to the left of $p_\star$ is due to data collapsing after the initial implosion, due to the turbulent instability. Right plot: maximum of curvature power-law scaling showing that $\gamma \simeq 1.2$. Image credit: [74].

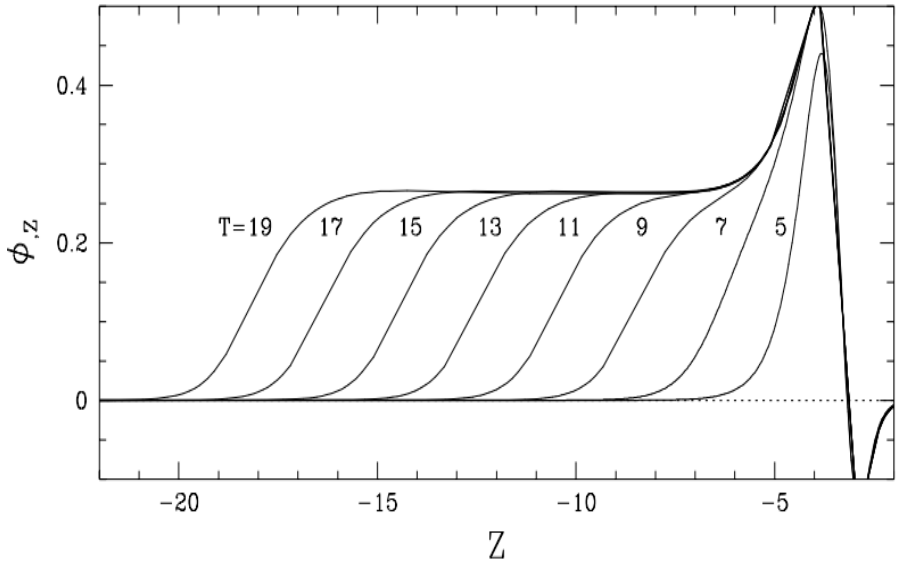

FIGURE 2.10: Plot of the scale-invariant function $\phi_{,Z}$ (this function is similar to the function X (2.13) in the $3+1$ case) during the critical regime at different time intervals T. T and Z were defined to be the logarithm of proper time t and radius R. The $2+1$ massless scalar field critical solution can be seen to be *continuously* self-similar. Image credit: [74].

a trapped surface, with a spacelike central curvature singularity inside. In that respect, the CSS solutions are more akin to "self-similar black-holes" than genuine candidates to be the critical solution. One can instead consider a different continuation, called the null continuation. This continuation is in better agreement with the numerical results outside the lightcone, although each layer of constant x is still a trapped surface. Furthermore, the continuation is not analytic and is instead C^3. Finally, ignoring these problems, linear perturbation analysis shows that the CSS solution with parameter n has $n-1$ growing mode [131]. By definition, since the critical solution has a single growing mode, this would mean that the $n=2$ solution should be the appropriate candidate, instead of the $n=4$. However, it is clear that the $n=2$ solution does not fit the numerical data, while the $n=4$ solution does, despite the fact of having *three* growing mode. How are all these facts explained? The authors of the paper do not have a satisfactory resolution of these problems, but it is clear that the above issues are symptoms of the fact that the above CSS solutions do not take the effects of Λ into account. This was further corroborated by numerical simulations, where perturbations of the $n=4$ solution, matched outside its lightcone to asymptotically adS data, were considered as initial data. Only the top (i.e. largest) growing mode can be identified. In parallel, by adding Λ perturbatively to the null continuation, one can show that $(\nabla R)^2 > 0$ everywhere, which then gets rid of trapped surfaces at and beyond the lightcone. Since Λ is added perturbatively however, this does not change the number of growing modes of the solution.

The authors also find an heuristic explanation for the power-law scaling of the mass and curvature. The curvature scaling is rather straightforward since curvature has the same dimension in any spacetime dimension. Assuming that the critical solution is well-approximated by the $n=4$ CSS solution and that only the top growing mode subsists in the presence of a negative cosmological constant, the exponent is found to be $\gamma = 8/7$, consistent with the numerical results. For the mass scaling, the argument is more subtle and makes use of the cosmological constant. They find $\delta = 16/23$, again consistent with the numerical results.

A last point investigated in the paper is the turbulent cascading effect that the scalar field is subject to. Recall that, starting with any scalar field initial data so that the asymptotic mass is positive, a black hole will always eventually form. One can then make a distinction between initial data that collapse after zero, one, two, etc reflections from the boundary. In this way, one can define a sequence of critical parameters: $p_{\star 0}$, $p_{\star 1}$, $p_{\star 2}$, $\cdots$, defined in the following way: $p_{\star 0}$ is such that for $p < p_{\star 0}$, the initial data will need at least one reflection from the boundary to collapse, while for $p > p_{\star 0}$, it will promptly collapse. For $p < p_{\star 1}$, the data will need at least two reflection before collapsing, while for $p_{\star 0} > p > p_{\star 1}$, it will collapse after exactly one reflection, and so on.

In this fashion, one can separately analyze the phenomena close to each of these parameters. Near $p_{\star 1}$, they again find type II critical behavior, but with a significantly different value for the critical exponents. Nonetheless, the authors note that the scaling is very noisy and they cannot dismiss the possibility that this might be a numerical error.

2.6.6 Rotating scalar field in $2+1$ dimensions

In Ref. [87], Jałmużna and Gundlach generalized the above study to the axisymmetric case. As was done previously [84] in $3+1$ (see again Sec. 2.6.3), they considered a complex scalar field, where the angular dependence appears only as a phase in the scalar field. They focused on the critical phenomena for prompt collapse. As a consequence, they chose several families of initial data which are "ingoing" ($\phi_{,t} \sim \phi_{,R}$), to reduce as much as possible the effect of reflection from the boundary.

For $m > 0$, the angular momentum shows no scaling at all. Furthermore, for some initial data, there is some evidence for mass scaling, but no curvature scaling, while for other initial data, the opposite is true. For some but not all initial data, the black hole becomes extremal as we fine-tune to the black-hole threshold. Because of this, for initial data where we observe mass scaling, this scaling only lasts up to a certain level of fine-tuning. The curvature and mass scalings (if they exist) are also heavily family dependent.

On top of this, and very surprisingly, the critical threshold for curvature and mass scaling (when we do find them) are *not the same*. In other words, the parameter $p_\star$, controlling the scaling of $M_{\rm BH}$ and $\mathrm{Ric}_{\rm max}$ is not the same for $m > 0$. This is of course different in spherical symmetry and for any other matter fields in higher dimension. Similarly, the mass and curvature exponents heavily depend on the family of initial data. All this seems to rule out the possibility of a unique critical solution, controlling both the Ricci and mass scaling.

To date, there is no satisfactory explanation for these results. The authors note that a possible explanation is that the critical solution is only asymptotically CSS, having more than one unstable mode and sensitive to the initial data. In particular, the critical solution may be unique, up to fixing the total angular momentum and mass of the initial data. The different growing modes also could explain why the power-law scaling only lasts for a certain fine-tuning and why the critical solution heavily depends on the family of initial data.

Chapter 3

3+1 collapse of a spherically symmetric perfect fluid

3.1 Introduction

In the preceding chapter, we have refrained from talking about the critical phenomena pertaining to a perfect fluid. Historically, the first two models for which critical phenomena were studied were the massless scalar field and pure vacuum. On hindsight, these two choices, albeit very natural, were also rather unfortunate. This is because the critical solution for both systems turns out to be discretely self-similar. Furthermore, the critical exponent for the mass and curvature were also very close to each other. This had, momentarily, led researchers to postulate incorrectly that the discrete self-similarity and the value of the critical exponent were universal across matter models. A theoretical explanation was then sought to explain these phenomena. The discrete self-similarity was, however, an analytical obstacle. Clearly, if a critical solution was found to be locally (i.e. continuously) self-similar, this would significantly ease the theoretical undertaking. For this reason, the third type of model that was studied was the spherically symmetric perfect fluid by Evans and Coleman [65] and later by Maison [66] and Hara et al [132]. Since continuously self-similar solutions of perfect fluids were known, this made it a natural choice. Furthermore, the claim that the critical exponent is universal across models can also be easily tested in this case, since the fluid model needs an *equation of state* to close the system of equations.

In this chapter, we will analyze the critical phenomena of the spherically symmetric perfect fluid in $3+1$ dimensions both numerically and theoretically. The numerical algorithm for a spherically symmetric fluid is largely identical in any dimensions. This therefore serves as a good test for the validity of our code, before applying it to the unknown $2+1$ case.

We will show numerically how the power-law scaling for the mass and curvature come about and how the continuous self-similarity of the critical solution can be identified. This is then compared to the above existing literature.

We will then compute the critical solution semi-analytically. This is done by imposing the self-similarity ansatz, transforming the PDE system into an ODE system and solving it as an eigenvalue problem. In a similar way, the linear perturbations of the critical solution are

calculated, from which the critical exponent can be extracted by the analysis of Sec. 2.4.2. The results, obtained semi-analytically in this fashion, are then compared to the numerical results.

At the end of this chapter, we will summarize the results for the case beyond spherical symmetry.

3.2 Description in polar-radial coordinates

We consider a 4-dimensional spherically symmetric metric in generalized polar-radial coordinates,

$$g = -\alpha^2(t,r)\mathrm{d}t^2 + a^2(t,r)R'^2\mathrm{d}r^2 + R^2\mathrm{d}\Omega^2. \tag{3.1}$$

$R = R(r)$ is an odd function of r, satisfying $R(0) = 0$ and $R'(0) = 1$.

On the matter side, we consider a perfect fluid

$$T^{\mu\nu} = (P+\rho)u^\mu u^\nu + Pg^{\mu\nu}, \tag{3.2}$$

where P is the pressure and ρ the density of the fluid. We restrict our attention to the linear equation of state $P = \kappa\rho$, where $0 < \kappa < 1$ is a constant.

In spherical symmetry, the 4-velocity of the fluid u^μ has only two non-trivial components, namely

$$u^\mu = \left(u^t, u^r, 0, 0\right)^\mu. \tag{3.3}$$

We will be following the Valencia formulation [133, 134], where we split the 4-velocity u^a into its parts perpendicular and tangent to the spacelike slices

$$u^a =: \Gamma\left(n^a + v^a\right), \tag{3.4}$$

$$\Gamma := -n_a u^a, \tag{3.5}$$

$$v^a n_a := 0. \tag{3.6}$$

We choose the unit normal vector, $n_\mu = (-\alpha, 0, 0, 0)$ and the normalization $u^a u_a \equiv -1$. Then, we have

$$v^\mu = \left(0, \frac{v}{aR'}, 0, 0\right), \tag{3.7}$$

$$u^\mu = \Gamma\left(\frac{1}{\alpha}, \frac{v}{aR'}, 0, 0\right), \tag{3.8}$$

$$\Gamma^2 := \frac{1}{1-v^2}. \tag{3.9}$$

Note that v is the physical 3-velocity of the fluid, defined by

$$v := -\frac{u^a\nabla_a R}{u^b n_b ||\nabla_c R||} = \frac{aR'u^r}{\alpha u^t}, \tag{3.10}$$

where $||X_a|| := \sqrt{X^a X_a}$ is the length of the covector X_a. Note that we require

$$v^2 < 1. \tag{3.11}$$

The lightcone corresponds to the collection of points where $v = \pm 1$.

The variables $\mathbf{u} := (\rho, v)$ will be referred to as the *primitive variables*.

Note that the coordinate system has a residual gauge freedom $t \to t(\tilde{t})$. This gauge freedom allows us to choose $\alpha(t, r_0)$ for any r_0. For our numerical code, we choose to fix it so that t corresponds to central proper time, $\alpha(t, 0) \equiv 1$.

3.3 The field equations

First, we rewrite the stress-energy conservation $\nabla_a T^{ab} = 0$ as a balance law. Contracting the equation with a vector V^a, we find

$$V_a \nabla_b T^{ab} = 0, \tag{3.12}$$

$$\iff \nabla_a \left(V_b T^{ab} \right) = T^{ab} \nabla_{(a} V_{b)}, \tag{3.13}$$

$$\iff \nabla_a j^a_{(i)} = s_{(i)}, \tag{3.14}$$

$$\iff \left(\sqrt{-g} V_\mu T^{t\mu} \right)_{,t} + \left(\sqrt{-g} V_\mu T^{r\mu} \right)_{,r} = \sqrt{-g} s_{(i)}, \tag{3.15}$$

where in the last line, we made use of the well-known relation

$$\nabla_a V^a = \frac{1}{\sqrt{-g}} \partial_a \left(\sqrt{-g} V^a \right). \tag{3.16}$$

We finally abbreviate this as

$$\dot{\mathbf{q}} + \mathbf{f}' = \mathbf{s}, \tag{3.17}$$

where $\mathbf{q}, \mathbf{f}, \mathbf{s}$ are the *conserved variables, fluxes* and *sources* respectively. Dots and primes stand for derivatives with respect to t and r respectively.

In spherical symmetry, it is easy to see that the stress-energy conservation equation has only two non-trivial equations, coming from the "t" and "r" components. It therefore suffices to find two linearly independent vectors $V^a_{(i)}$, $i = 1, 2$. In spherically symmetry, the existence of the Misner-Sharp mass

$$M := \frac{R}{2} \left(1 - \frac{1}{a^2} \right) \tag{3.18}$$

allows us to choose one vector so that the corresponding source vanishes.

The second vector is fixed by requiring the resulting balance law to be well-balanced. Specifically, we required that, if we consider a fluid with constant density at rest in flat space, its flux should be proportional to the pressure (and thus constant), while the source should vanish.

The set of vectors satisfying the above are

$$V_{(X)\mu} := \left(\frac{\alpha}{a\sin\theta}, 0, 0, 0\right), \tag{3.19}$$

$$V_{(Y)\mu} := \left(0, \frac{R'}{R^2\sin\theta}, 0, 0\right). \tag{3.20}$$

It is then straightforward to show that the conserved quantities

$$\mathbf{q} := (X, Y), \tag{3.21}$$

are given by

$$X = R'R^2\tau, \tag{3.22}$$

$$Y = R'v\sigma, \tag{3.23}$$

where, for convenience, we defined

$$\sigma := \Gamma^2(1+\kappa)\rho, \tag{3.24}$$

$$\tau := \sigma - P. \tag{3.25}$$

The fluxes read

$$f_{(X)} = \frac{\alpha}{a}R^2 v\sigma, \tag{3.26}$$

$$f_{(Y)} = \frac{\alpha}{a}\left(P + v^2\sigma\right), \tag{3.27}$$

with the corresponding sources

$$s_{(X)} = 0, \tag{3.28}$$

$$s_{(Y)} = -\frac{1}{a}\left(2v^2\sigma\alpha\frac{R'}{R} + \tau\alpha' + \frac{\alpha}{a}\left(P + v^2\sigma\right)a' + 2v\sigma R'\dot{a}\right). \tag{3.29}$$

Finally, out of the six algebraically independent Einstein equations, three can be solved for $\dot{a}, a', \alpha'$,

$$\dot{M} = 4\pi X, \tag{3.30}$$

$$M' = -4\pi f_X, \tag{3.31}$$

$$(\ln(a\alpha))' = 4\pi a^2(1+v^2)RR'\sigma. \tag{3.32}$$

In addition to the primitive and conserved variables, we will consider yet another set of fluid variables, dubbed as *generic*,

$$\mathbf{w} := (\omega, \eta) := \left(\frac{X}{R'R^2}, \frac{Y}{R'R}\right) = \left(\tau, \frac{v\sigma}{R}\right). \tag{3.33}$$

The generic variables $\mathbf{w}$, unlike the conserved variables $\mathbf{q}$, do not generically vanish at the center $r = 0$. These variables are therefore more convenient when it comes to cell reconstruction, floor imposition (see below) and dealing with the ghost points for the inner and outer boundaries of our grid.

From the generic variables, we can recover the primitive variables by inverting (3.33),

$$\rho = \frac{\tau}{\Gamma^2(1+\kappa) - \kappa}, \tag{3.34}$$

$$v = \frac{R\eta}{\Gamma^2(1+\kappa)\rho}, \tag{3.35}$$

where Γ is given in terms of the generic variables as

$$\Gamma^2 = \frac{1 - 2\kappa(1+\kappa)U + \sqrt{1-4\kappa U}}{2\left(1-(1+\kappa)^2 U\right)}, \qquad U := \frac{R^2\eta^2}{(1+\kappa)^2\tau^2} = \frac{\Gamma^2(\Gamma^2-1)}{\left(\Gamma^2(1+\kappa)-\kappa\right)^2}. \tag{3.36}$$

In the above, we have chosen the "positive" root for Γ^2, so that $\Gamma^2|_{v=0} = 1$, in accordance with its definition from the primitive variable v.

Note that U is bounded above, which implies the inequality

$$U < \frac{1}{(1+\kappa)^2} \iff R^2\eta^2 < \tau^2. \tag{3.37}$$

This inequality also ensures that Γ is real.

3.4 Numerical method

3.4.1 Fluid and metric evolution

The balance laws (3.17) will be solved using standard finite-volume methods [135, 136].

Specifically, we will follow the method outlined in Ref. [67] and we will first discretize the radius coordinate r. We denote by $r_{i\pm1/2}$ the cell faces and by r_i the cell centers. In general, we allow for cells to have different widths, but the cell centers are always located at

$$r_i := \frac{\Delta_i r}{2}, \qquad \Delta_i r := r_{i+1/2} - r_{i-1/2}. \tag{3.38}$$

By definition, we set the center $r = 0$ to correspond to $i = 1/2$.

We can choose R so that r corresponds to a compactified coordinate. However, in the following, we will always take $R = r$, since we are only interested in the critical collapse in an asymptotically flat spacetime.

Two grid types that were commonly used were the uniform and exponential grids

$$r^{\text{uniform}}_{i+1/2} = \frac{i}{N} r_{\max}, \tag{3.39}$$

$$r^{\text{sinh}}_{i+1/2} = \frac{\sinh\left(\frac{ci}{N}\right)}{\sinh(c)} r_{\max}, \tag{3.40}$$

where $c > 0$ is a free parameter, N denotes the number of grid points and $r_{\max} := r_{N+1/2}$ is the radius at the numerical outer boundary. Typical values are $c = 8$, $N = 800$ and $r_{\max} = 1.5$.

For the exponential grid, we use the function $\sinh$, because it causes the extrapolated grid to be odd near the center. Also, we can recover the uniform grid by choosing a small value for c and using that $\sinh(x) \simeq x$ for small x.

The time increments Δt are computed in such a way that the Courant-Friedrichs-Lewy (CFL) condition is satisfied at each timestep [136]. Specifically, the CFL condition gives as a necessary condition for the stability for our numerical scheme that at each cell, the numerical grid is wider than the lightcone,

$$\frac{\mathrm{d}r}{\mathrm{d}t} \geq \frac{\alpha}{aR'} \tag{3.41}$$

Consequently, we take

$$\Delta t := c_{\mathrm{CFL}} \min_i (\Delta_i r) \min_{i, i-\frac{1}{2}} \left(\frac{aR'}{\alpha} \right), \tag{3.42}$$

where $0 < c_{\mathrm{CFL}} < 1$ is a free parameter, usually called the CFL parameter. A typical value is $c_{\mathrm{CFL}} = 0.5$. This ensures that the above defined timestep satisfies (3.41) at all cell centers and faces.

Within a grid cell $\left(r_{i-1/2}, r_{i+1/2}\right)$, we first compute the average value of the conserved variables

$$\bar{\mathbf{q}}_i := \frac{1}{\Delta_i r} \int_{r_{i-1/2}}^{r_{i+1/2}} \mathbf{q}(t, r) dr. \tag{3.43}$$

Integrating the balance laws between the above two grid faces yields,

$$\frac{\mathrm{d}\bar{\mathbf{q}}_i}{\mathrm{d}t} = \frac{1}{\Delta_i r} \left(\mathbf{f}_{i-1/2} - \mathbf{f}_{i+1/2} \right) + \bar{\mathbf{s}}_i. \tag{3.44}$$

The evolution is conservative in the sense that $\sum_i \frac{\mathrm{d}\bar{\mathbf{q}}_i}{\mathrm{d}t} \Delta_i r$ only depends (up to the source terms) on the fluxes at the inner and outer ghost points.

To find the fluxes $f_{i\pm1/2}$ at the cell faces, we first approximate the reconstruction of the generic variables as constant within each grid cell.

$$\mathbf{w}(t, r_i) =: \mathbf{w}_i \simeq \bar{\mathbf{w}}_i. \tag{3.45}$$

Integrating (3.33) and making use of the above approximation, we see that

$$\omega_i = \frac{3\Delta_i r}{\Delta_i R^3} \bar{X}_i, \tag{3.46}$$

$$\eta_i = \frac{2\Delta_i r}{\Delta_i R^2} \bar{Y}_i. \tag{3.47}$$

Of course, the reconstructed variables are in general not continuous across grid faces and similarly for the associated fluxes. This is resolved by solving the resulting Riemann problem. Specifically, one considers the Riemann problem for the flux at each cell face $r_{i+1/2}$. An

important property of the Riemann problem is that the solution is self-similar,

$$q_{\text{Riemann}}(t, r) = \tilde{q}\left(\frac{r - r_{i+1/2}}{t}\right). \tag{3.48}$$

In general, finding an exact solution to the Riemann problem is computationally expensive. Since we are only interested in the fluxes at the cell faces, we see from the above that $q_{\text{Riemann}}(t, r_{i+1/2})$ is in fact time-independent and therefore so is the associated flux. It suffices to solve the Riemann problem only approximately to find the flux only at that point. For our purposes, it is sufficient to consider the simple HLL approximate Riemann solver [136]. The solution is approximated as a left and right shock solution with shock characteristic speed parametrized by λ_{HLL}. In terms of the left and right values of the conserved variables at the cell face $i + 1/2$, which will be denoted by $\mathbf{q}_i^R$ and $\mathbf{q}_{i+1}^L$ respectively, we have

$$\mathbf{f}_{i+1/2} = \frac{1}{2}\left(\mathbf{f}(\mathbf{q}_i^R) + \mathbf{f}(\mathbf{q}_{i+1}^L) + \lambda_{HLL}\left(\mathbf{q}_i^R - \mathbf{q}_{i+1}^L\right)\right). \tag{3.49}$$

For the value of λ_{HLL}, we choose to take the coordinate speed of radial light rays, given by $\frac{\mathrm{d}r}{\mathrm{d}t} = \frac{\alpha}{aR'}$. This choice is a rather sharp upper limit for the matter's characteristic speed.

Note that, from the expression of the source (3.29), we see that near the center, $s_Y = RR'f$, where f is some generic even function. Integrating over the ith cell and making the approximation $f_i \simeq \bar{f}_i$, we find the relation,

$$\bar{s}_{Y_i} = \frac{s_{Y_i}}{R_i R_i'} \frac{\Delta_i R^2}{2\Delta_i r}. \tag{3.50}$$

We can recover the metric variable a by making use of (3.31). By integrating this equation, we get

$$\Delta_i M = 4\pi \bar{X}_i \Delta r_i. \tag{3.51}$$

This expression is by definition exact. Notice that, since $s_X = 0$ by construction, X is then conserved in our scheme and therefore so is M. From M, we can compute a using (3.18) at the cell faces. Since a is a generic even function, its cell-center values are obtained by averaging adjacent cell faces,

$$a_i := \frac{1}{2}\left(a_{i+1/2} + a_{i-1/2}\right). \tag{3.52}$$

Finally, we can then make use of (3.18) and (3.32) to find $\alpha_{i+1/2}$ and subsequently its cell-center values using the same averaging as for a.

3.4.2 Boundary conditions, ghost points and floor imposition

Recall that we require $a(t, 0) = 1$ to avoid conical singularities and we gauge-fixed t to be central proper time $\alpha(t, 0) = 1$.

The inner ghost points (effectively at points corresponding to $r < 0$), are fixed by making use of the fact that all the variables are either even or odd near the center,

$$a(t,-r) := a(t,r), \tag{3.53}$$
$$\alpha(t,-r) := \alpha(t,r), \tag{3.54}$$
$$M(t,-r) := -M(t,r), \tag{3.55}$$
$$X(t,-r) := X(t,r), \tag{3.56}$$
$$Y(t,-r) := -Y(t,r). \tag{3.57}$$

At all times, the fluid is subject to the condition (3.37). Numerical error and ultrarelativistic speeds $v^2 \lesssim 1$ can easily conspire for this inequality to be violated. Each time when the generic variables are calculated from the conserved variables, we therefore impose a slightly more restrictive condition at each physical cells. Namely

$$\omega_i - |R_i \eta_i| > \bar{\delta}, \tag{3.58}$$

where $\bar{\delta} \ll 1$.

The floor is imposed by splitting the solution into "ingoing" and "outgoing" parts. In other words, we define

$$c_+ = \max_i(\omega_i + R_i\eta_i, \bar{\delta}), \tag{3.59}$$
$$c_- = \max_i(\omega_i - R_i\eta_i, \bar{\delta}). \tag{3.60}$$

We then recompute the new generic variables as

$$\omega_i := \frac{1}{2}\left(c_+ + c_-\right), \tag{3.61}$$
$$\eta_i := \frac{1}{2R_i}\left(c_+ - c_-\right). \tag{3.62}$$

The value of $\bar{\delta}$ is fixed dynamically, in response to the size of the data. Fixing an absolute value $\bar{\delta} = \bar{\delta}_{\text{abs}}$ can cause unexpected results. Specifically, if (3.58) is violated and $\omega_i + |R_i\eta_i|$ is sufficiently "large", the update for $\mathbf{w}_i$ will go unnoticed, as c_+ will be too large comparatively to c_-. In order to alleviate this problem we instead opt for a relative floor, defined by

$$\delta = \max_i(\bar{\delta}_{\text{abs}}, \bar{\delta}_{\text{rel}}(\omega_i + |R_i\eta_i|)). \tag{3.63}$$

This choice of $\bar{\delta}$ is essentially the same as the above in the case of "small" density. On the other hand, in region of "large" density, the scheme rather opts for a value of $\bar{\delta}$ that is considered "small" relative to the density. In practice, we choose $\bar{\delta}_{\text{abs}} = \bar{\delta}_{\text{rel}} = 10^{-10}$.

In the following, we are interested in initial data where $p \simeq p_\star$ and we refer to "sub$n$" data as subcritical data for which $\log_{10}(p_\star - p) \simeq -n$, and to "super$n$" as supercritical data with $\log_{10}(p - p_\star) \simeq -n$. By "best" subcritical and supercritical data, we will always mean the sub$n$

1.	$\mathbf{w}_i$	(3.58)
2.	$\mathbf{u}_i$, $\bar{\mathbf{q}}_i$ (floored)	(3.34), (3.35), (3.46), (3.47)
3.	$M_{i+1/2}$	(3.51)
4.	$a_{i+1/2}$, a_i	(3.18), averaging
5.	$\alpha_{i+1/2}$, α_i	(3.32), averaging
6.	$\bar{s}_{(Y)i}$ via $s_{(Y)i}$	(3.29), (3.50)
7.	$\mathbf{f}_{i-1/2}$ via $\mathbf{q}_i^L$, $\mathbf{q}_{i-1}^R$.	(3.26), (3.27), (3.49)
8.	$d\bar{\mathbf{q}}_\mathbf{i}/dt$	(3.44)

TABLE 3.1: Overview of how $d\bar{\mathbf{q}}/dt$ is calculated.

and super$n$ data with largest n. That is, the data with the highest level of fine-tuning to the black-hole threshold.

3.4.3 Time evolution algorithm

The evolution scheme can be divided in multiple steps, visualized in Table. 3.1.

1. Start with some initial data given in terms of the generic variables, $\mathbf{w}_i$ and impose the floor (3.58).
2. Compute $\mathbf{u}_i$ from $\mathbf{w}_i$ via (3.34, 3.35) and cell averages $\bar{\mathbf{q}}_i$ by inverting (3.46,3.47).
3. Compute $M_{i+1/2}$ using (3.51).
4. Compute $a_{i+1/2}$ using (3.18), as well as a_i by averaging (3.52).
5. Compute $\alpha_{i+1/2}$ using (3.32), as well as α_i by averaging (3.52).
6. Compute source $\mathbf{s}_Y$ using (3.29) and thus $\bar{\mathbf{s}}_Y$ via (3.50).
7. Compute fluxes at cell centers, using (3.26, 3.27). Find their cell faces values using (3.49).
8. Update $\bar{\mathbf{q}}_i$ via (3.44) at the next timestep, using a forth-order Runge-Kutta method. Between each substep of Runge-Kutta, we make sure that the newly computed conserved variables satisfy (3.58).

3.4.4 Results

We initialize the generic variables $\mathbf{w}$ as double Gaussians in terms of the area radius R. Recall that we choose $R = r$, so, in this case, this is equivalent to initializing them in terms of the coordinate r),

$$\omega(0,R) = \frac{p_\omega}{2}\left(e^{-\left(\frac{R-R_\omega}{\sigma_\omega}\right)^2} + e^{-\left(\frac{R+R_\omega}{\sigma_\omega}\right)^2}\right), \tag{3.64}$$

$$\eta(0,R) = \frac{p_\eta}{2}\left(e^{-\left(\frac{R-R_\eta}{\sigma_\eta}\right)^2} + e^{-\left(\frac{R+R_\eta}{\sigma_\eta}\right)^2}\right). \tag{3.65}$$

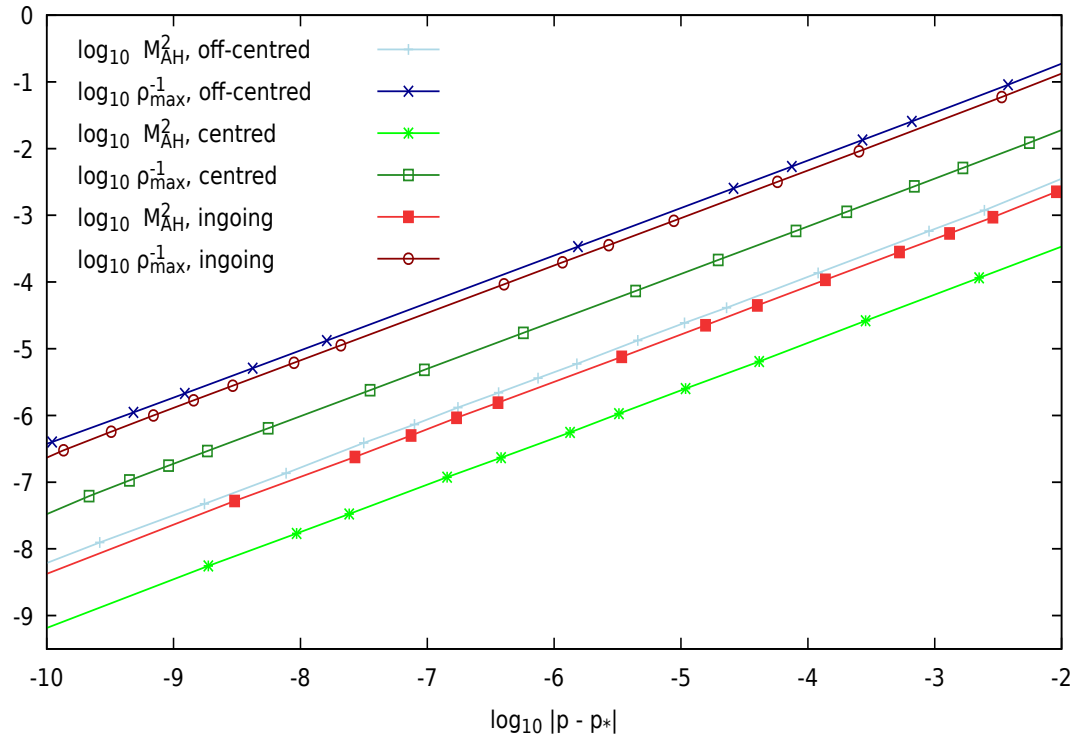

FIGURE 3.1: Log-log power-law scaling of mass $M^2_{\rm AH}$ and $1/\rho_{\rm max}$ for the ingoing, centered and off-centered initial data. In all cases, we considered radiation fluid, $\kappa = 1/3$.

Here, p_ω and p_η are the magnitudes, R_ω and R_η the displacements from the center, and σ_ω and σ_η the widths of the Gaussians. Note that p_ω has dimension $[\text{length}]^{-2}$, while p_η is dimensionless.

In the following, we fix $\sigma_\omega = 0.2$, $R_\eta = 0.5$ and $\sigma_\eta = 0.2$. In order to investigate the property of universality of the critical solution, we consider three types of initial data:

1) time-symmetric off-centered: $p_\eta = 0$, $R_\omega = 0.5$,

2) time-symmetric centered: $p_\eta = 0$, $R_\omega = 0$, and

3) initially ingoing off-centered: $p_\eta = -0.1$, $R_\omega = R_\eta = 0.5$.

In all cases, the remaining parameter $p := p_\omega$ is to be fine-tuned to the black-hole threshold.

In Fig. 3.1, we show a log-log plot of $M^2_{\rm AH}$ and the maximum of density $\rho_{\rm max} \sim {\rm Ric}_{\rm max}$ against $|p - p_\star|$, with $\kappa = 1/3$. Thanks to the sinh grid, we observe scaling up until sub10 and super10 data. This plot establishes two results: First, we have that the apparent horizon mass and maximum curvature scale as power laws

$$M_{\rm AH} = |p - p_\star|^\delta, \tag{3.66}$$

$$\rho_{\rm max} = |p - p_\star|^{-2\gamma}, \tag{3.67}$$

with $\delta = \gamma$, as expected from dimensional analysis; see Sec. 2.3.1. In particular, this implies that the product $M^2_{\rm AH}\rho_{\rm max}$ is constant. Second, the critical exponents, δ and γ, do not depend on the initial data, giving evidence for universality.

κ	δ	γ
0.1	0.197	0.200
0.2	0.265	0.271
1/3	0.356	0.356
0.4	0.404	0.403
0.5	0.479	0.476
0.6	0.555	0.553
0.7	0.633	0.635
0.8	0.701	0.719
0.9	0.805	0.831

TABLE 3.2: The scaling exponents δ and γ for different values of κ.

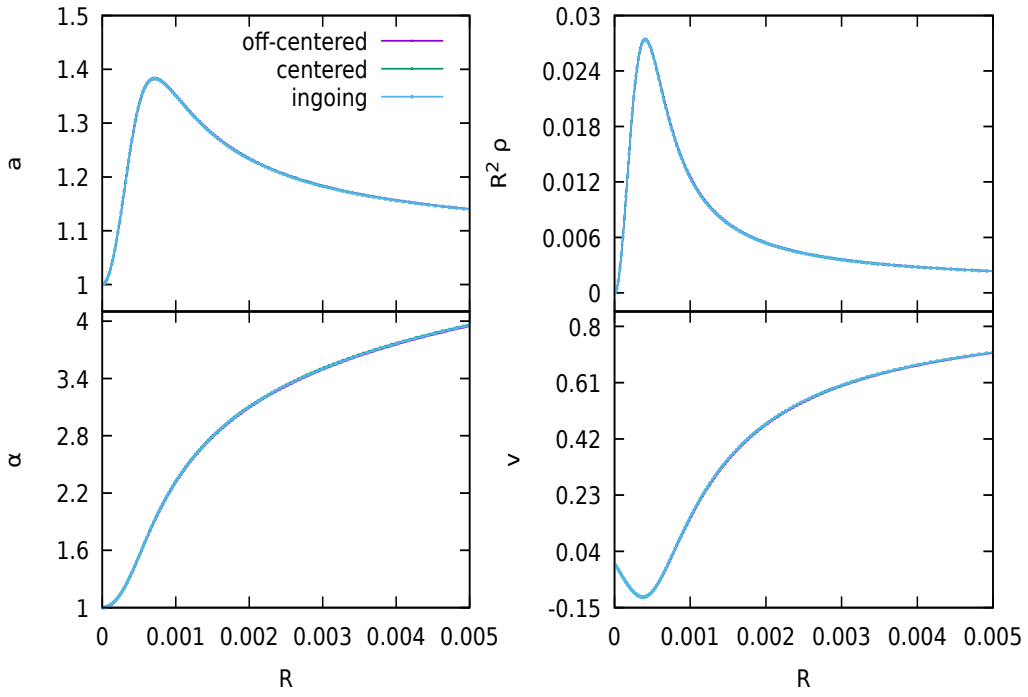

FIGURE 3.2: The profiles of M, $R^2\rho$, α and v during the critical regime, for three different sub10 initial data with $\kappa = 1/3$, giving some evidence for universality. The data have been plotted at different times, chosen so that the profiles are aligned.

We ran the simulation for different values of κ and recorded the respective values for δ and γ in Table 3.2. This shows that the critical exponent is *dependent* on the equation of state, and therefore on the matter field under consideration. The values we find are consistent with those reported in the literature; see for example [66, 132].

In Fig. 3.2, we plot, again for radiation fluid $\kappa = 1/3$, our best subcritical data for the three different initial data at a moment in time during the critical regime. This time is different for different initial data, chosen so that the plots align. This gives further evidence for universality.

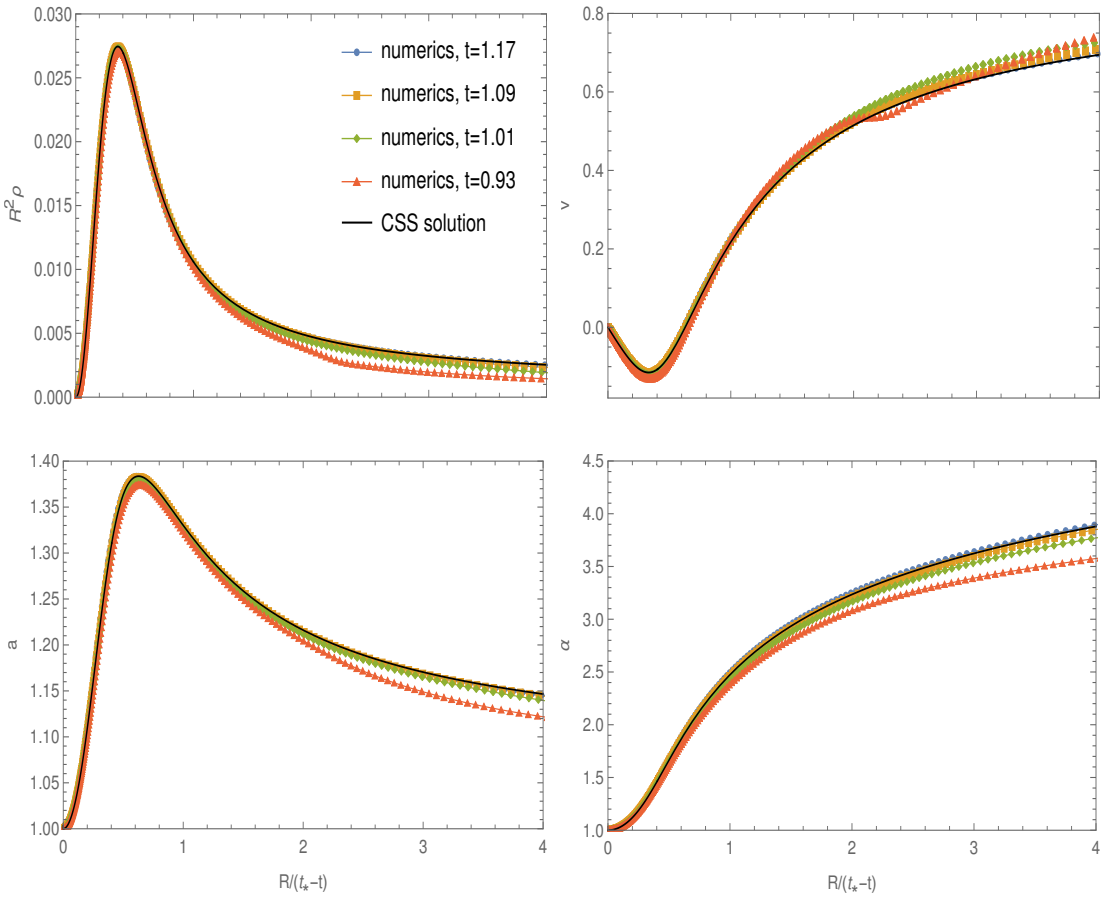

FIGURE 3.3: Numerical solution (coloured lines) for $R^2\rho$, v, a and α plotted against $R/(t_\star - t)$, at different times during the critical regime. This is compared with the exact CSS solution (black).

In Fig. 3.3, we compare the numerical evolution of our best subcritical off-centered initial data (colored lines) at different times during the critical regime, against the exact CSS solution (black). This exact solution will be semi-analytically derived in the next section. The time $t_\star \simeq 1.17$ roughly marks the time before the growing perturbation takes over, causing the solution to disperse. Note that, close to the center, we find a good match between the analytical prediction and the numerical solution. Further away, this matching becomes increasingly better as we approach $t = t_\star$. The reason is that for fixed R, as $t \to t_\star$, the range in $R/(t_\star - t)$, where the critical solution is valid, increases.

Finally, in Fig. 3.4, we compare the unique growing perturbation of the CSS solution, (black) against the difference between the numerical solution at time slightly after $t_\star$ and the CSS solution (blue). Note that the latter contains all the modes (both growing and decaying). However, at $t \simeq t_\star$, the decaying modes have been sufficiently suppressed so that the unique growing perturbation dominates. We remark that for the perturbation of α, we had to further rescale the perturbation (black curve) by a factor $\simeq 0.88$ to make the plots match. The reason for this additional rescaling is unclear but is attributed to the fact that in the derivation of the unique growing perturbation, we employ a different gauge condition for t than we do in the numerical simulations.

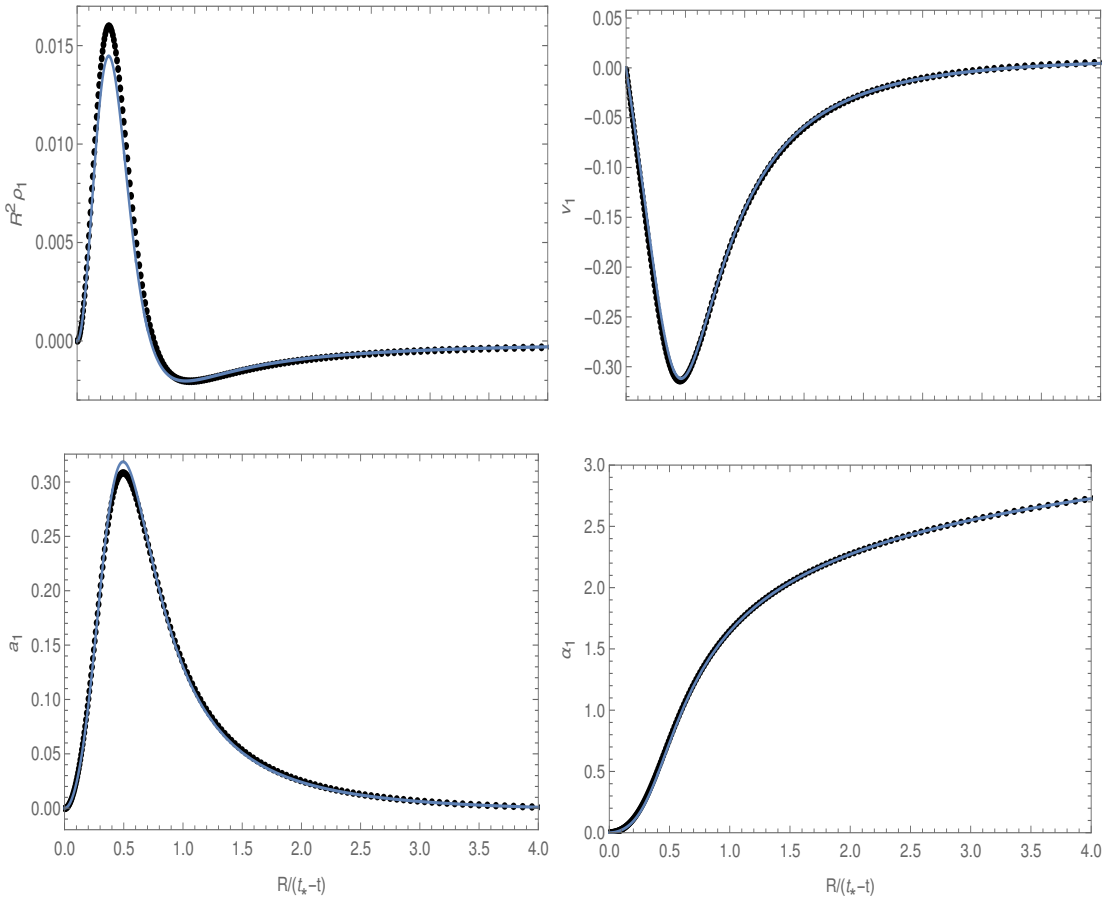

FIGURE 3.4: Comparing the unique growing perturbation (black), obtained in the next section, against the difference between the numerical solution and the CSS solution (blue) slightly after the critical time $t \simeq t_\star$.

3.5 The critical solution

3.5.1 Einstein equations

In this section, we will obtain the critical solution by making a continuous self-similarity ansatz and solving the resulting Einstein equations as an eigenvalue problem. Specifically, we start by considering the coordinates (τ, x), adapted to self-similarity, given in (2.26).

In addition to using henceforth the above coordinate system, we will also follow the convention in Ref. [132] and work with the following dimensionless variables

$$N := \frac{\alpha}{ax}, \qquad A := a^2, \qquad \omega := 4\pi R^2 a^2 \rho. \tag{3.68}$$

Note that the above-defined ω is not the same as the one defined in our numerical scheme. Rewritten in this new coordinate system and in terms of the above variables, the Einstein equations take an autonomous form: there is no explicit τ dependence, except for derivative terms.

We now assume the self-similarity ansatz: the variables (N, A, ω, v) are all functions of x only. This turns the PDE system into an ODE system. In particular, the $\partial_\tau A$ equation transforms into an algebraic equation. We can solve this equation algebraically for one of the fields,

say A. The ODE system can then be rewritten as a system of three equations for the remaining fields, $X := (N, \omega, v)$. Schematically, we have

$$X' = F_X(X) = \frac{N_X}{D_X}, \tag{3.69}$$

$$A = A_{\text{alg}}(X). \tag{3.70}$$

In the last equality of (3.69), we decomposed F_X into its numerator and denominator.

The explicit equations are

$$(\ln N)'(x) = \frac{v^2(\kappa\omega + \omega + 1) + 2(\kappa+1)Nv\omega + \kappa\omega + \omega - 1}{(1-v^2)\,x}, \tag{3.71}$$

$$(\ln \omega)'(x) = N\frac{\begin{array}{c}(1+\kappa)\omega\left(3N^2v^3 - N^2v + \kappa(N+v)\left(N\left(v^2-3\right)v - v^2 - 1\right)\right.\\ \left. +Nv^4 + 4Nv^2 - N + v^3 + v\right) + 2\kappa(1-v^2)\left(Nv^2 + N + 2v\right)\end{array}}{(1-v^2)\,x\left(\kappa(N+v)^2 - (Nv+1)^2\right)}, \tag{3.72}$$

$$v'(x) = N\frac{2\kappa\left(1-v^2\right)\left(\kappa v(N+v) + Nv + 1\right) - (1+\kappa)^2\omega\left((Nv+1)^2 - \kappa v^2(N+v)^2\right)}{(1+\kappa)x\left(\kappa(N+v)^2 - (Nv+1)^2\right)}, \tag{3.73}$$

$$(A-1)\left(1-v^2\right) = 2v\omega\kappa(N+v) + 2\omega(Nv+1). \tag{3.74}$$

3.5.2 Regularity conditions

As we are searching for regular solutions, we need to ensure that the ODE system (3.69) is well defined everywhere. By inspection, we see that two points require some care: first at the center $x = 0$, second at the sonic point $x = x_s$, which is defined to be the point where $D_X = 0$.

Since a,α and ρ are scalars, they must have an even expansion in R and thus in x. This is because $x \sim R$ is not an analytic function of its Cartesian coordinates at the center, whereas x^2 is. This then means that A, ω and xN will have an even expansion in x. Finally, v has an odd expansion in x. This is because the component u^r in spherical coordinates can be written in terms of Cartesian coordinates x_i as

$$u^r r\partial_r = x_1 u^{x_1}\partial_{x_1} + x_2 u^{x_2}\partial_{x_2} + x_3 u^{x_3}\partial_{x_3}. \tag{3.75}$$

Assuming that the RHS is smooth everywhere, including at the center, then it follows that u^r has an odd expansion in r.

To summarize, near the center, the leading-order term of each variable is

$$xN \sim \mathcal{O}(1), \quad A \sim \mathcal{O}(1), \quad \omega \sim \mathcal{O}(x^2), \quad v \sim \mathcal{O}(x), \tag{3.76}$$

We fix $A(0) \equiv 1$ to avoid a conical singularity at the center. One can check explicitly that the equations are regular at the center, provided that

$$\lim_{x\to 0} Nv = -\frac{2}{3(1+\kappa)}. \tag{3.77}$$

In order to regularize the ODE system at the sonic point, we need to impose the numerator of F_X to vanish at that point as well. We then *define* the evaluation of the matter fields and their derivatives at that singular point as

$$\omega(x_s) := \lim_{x\to x_s} \omega(x), \tag{3.78}$$

$$v(x_s) := \lim_{x\to x_s} v(x) \tag{3.79}$$

and similarly for their derivatives.

Since $D_\omega \propto D_v$, the sonic point gives a single algebraic equation between N, ω and v. In the following, we solve it for $N(x_s)$. Using this constraint, both numerators of F_ω and F_v are then proportional to each other. Setting them to zero gives yet another algebraic equation at the sonic point, which we use to fix $\omega(x_s)$. Finally, the algebraic equation $A = A_{\text{alg}}$ fixes $A(x_s)$. We are therefore left with a single free parameter: $v(x_s)$. Altogether, the regularity conditions at the sonic point read

$$A(x_s) = -\frac{8\kappa^{3/2}v(x_s) + \left(3\kappa^2 - 2\kappa - 1\right)v(x_s)^2 + \kappa^2 + 6\kappa + 1}{(1+\kappa)^2\left(1 - v(x_s)^2\right)}, \tag{3.80}$$

$$\omega(x_s) = \frac{2\sqrt{\kappa}\left(\sqrt{\kappa} - v(x_s)\right)\left(1 + \sqrt{\kappa}v(x_s)\right)}{(1+\kappa)^2\left(1 - v(x_s)^2\right)}, \tag{3.81}$$

$$N(x_s) = \frac{1 - \sqrt{\kappa}v(x_s)}{\sqrt{\kappa} - v(x_s)}. \tag{3.82}$$

Note that (3.82) restricts the allowed range of $v(x_s)$ to

$$-1 < v(x_s) < \sqrt{\kappa}. \tag{3.83}$$

To simplify the analysis at the sonic point later, we will henceforth choose a different gauge than in the numerical simulations, where we chose t to be central proper time. Here, we instead fix the sonic point to occur at $x_s \equiv 1$.

3.5.3 Power-series solution

3.5.3.1 Power series near the center

As explained in the previous section, the power-series expansion near the center takes the following form,

$$N(x) = \frac{N^c_{-1}}{x} + N^c_1 x + N^c_3 x^3 + \cdots, \tag{3.84}$$

$$A(x) = 1 + A^c_2 x^2 + A^c_4 x^4 + \cdots, \tag{3.85}$$

$$\omega(x) = \omega^c_2 x^2 + \omega^c_4 x^4 + \cdots, \tag{3.86}$$

$$v(x) = v^c_1 x + v^c_3 x^3 + \cdots. \tag{3.87}$$

$$\tag{3.88}$$

The product of N^c_{-1} and v^c_1 satisfies (3.77) and the solution will therefore be expressed in terms of two free parameters. We will choose them to be $\check{N} := N^c_{-1}$ and $\check{\omega} := \omega^c_1$.

Substituting the above ansatz into the Einstein equations and solving up to fourth order gives

$$N^c_1 = \frac{1}{6}\left(-1+3\kappa\right)\check{N}\check{\omega}, \tag{3.89}$$

$$N^c_3 = \frac{\left(-3-14\kappa+45\kappa^2\right)\check{\omega}}{180\kappa\left(1+\kappa\right)\check{N}} + \frac{\left(3-\kappa\right)\left(1+\kappa\right)\check{N}\check{\omega}^2}{120\kappa}, \tag{3.90}$$

$$A^c_2 = \frac{2\check{\omega}}{3}, \tag{3.91}$$

$$A^c_4 = \frac{2\left(1+13\kappa\right)\check{\omega}}{45\kappa\left(1+\kappa\right)\check{N}^2} - \frac{\left(3-8\kappa+9\kappa^2\right)\check{\omega}^2}{45\kappa}, \tag{3.92}$$

$$\omega^c_4 = \frac{\left(1+9\kappa\right)\check{\omega}}{9\kappa\left(1+\kappa\right)\check{N}^2} - \frac{\left(1+3\kappa^2\right)\check{\omega}^2}{6\kappa}, \tag{3.93}$$

$$v^c_1 = -\frac{2}{3\left(1+\kappa\right)\check{N}}, \tag{3.94}$$

$$v^c_3 = -\frac{2\left(1+14\kappa+33\kappa^2\right)}{135\kappa\left(1+\kappa\right)^3\check{N}^3} + \frac{\left(1-\kappa+18\kappa^2\right)\check{\omega}}{45\kappa\check{N}(1+\kappa)}. \tag{3.95}$$

3.5.3.2 Power series near the sonic point

We consider the following regular power-series expansion

$$\mathrm{X} = \mathrm{X}^s_0 + (x-1)\mathrm{X}^s_1 + (x-1)^2\mathrm{X}^s_2 + \cdots . \tag{3.96}$$

Regularity at the sonic point imposes three algebraic constraints, (3.80)-(3.82) and, as a consequence, the power-series solution has a single free parameter, $v(x_s) =: \check{v}$.

Solving the ODE system order by order, we obtain a three-fold degeneracy for the linear coefficients of the matter fields; see Fig. 3.5. This is a direct consequence of the regularity constraint at the sonic point and is explained in Appendix A.

The explicit power series is somewhat complicated and will therefore not be given here. In order to distinguish the different solutions, we shall denote them by an additional subscript: $X^s_{1,i}$, $i = 1, 2, 3$.

It turns out that the $X^s_{1,1}$ solution is unphysical as the resulting power-series solution will not be consistent with the A' equation. This singular behavior can be understood from the fact that the ODE system (3.69) is solved in the form $D_X = X' N_X$. The $i = 1$ solution then corresponds to having $D_X = 0 = N_X$ at each order. It should therefore be discarded.

In order to find which of the two remaining solutions is the physically relevant one, let us analyze the sonic point more closely. Just like the lightcone, the sonic cone is characterized by its two tangent vectors $S^a_\pm$, which satisfy

$$g_{ab}S^a_\pm S^b_\pm = -1, \tag{3.97}$$

$$g_{ab}u^a S^b_\pm = -\frac{1}{\sqrt{1-\kappa}}. \tag{3.98}$$

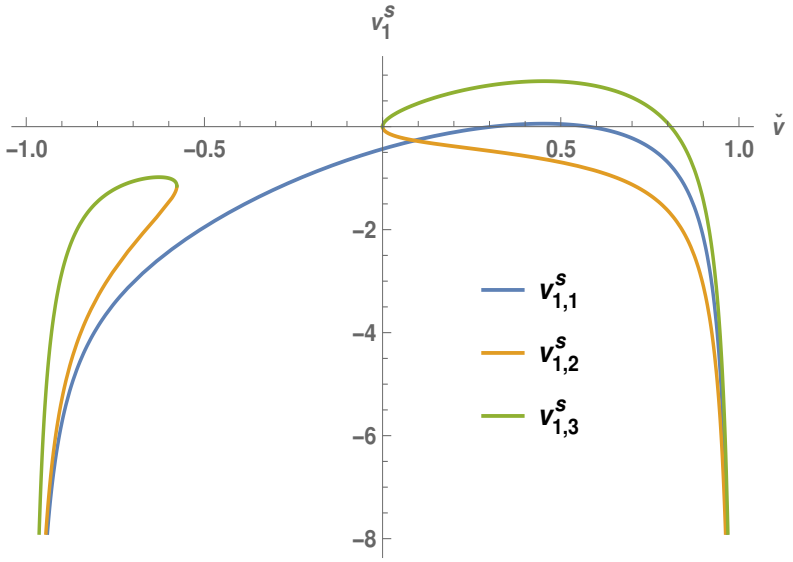

FIGURE 3.5: Linear coefficient in the expansion of $v(x)$, against its leading coefficient. Due to the regularity condition, there are three possible solutions. For this plot, we considered the radiation fluid $\kappa = 1/3$.

For convenience, let us also define

$$S_\pm := \frac{S^x_\pm}{S^\tau_\pm} \tag{3.99}$$

The above system of equations imply the following condition on $S_\pm$:

$$(Nx(\sqrt{\kappa} - v) + (-1 + v\sqrt{\kappa})(x - S_\pm))(Nx(\sqrt{\kappa} + v) + (1 + v\sqrt{\kappa})(x - S_\pm)) = 0. \tag{3.100}$$

Now, the sonic point occurs when

$$S^a_- \propto \left(\frac{\partial}{\partial\tau}\right)^a, \tag{3.101}$$

or equivalently when $S_-(x_s) = 0$; see Fig. 3.6. At the sonic point, we then have the condition

$$\left[Nx(\sqrt{\kappa} - v) + (-1 + v\sqrt{\kappa})x\right]\left[Nx(\sqrt{\kappa} + v) + (1 + v\sqrt{\kappa})x\right]\Big|_{x_s} = 0. \tag{3.102}$$

This is equivalent to the condition that D_ω and D_v vanish. The above argument holds in any spacetime dimension, assuming spherical symmetry.

The correct power-series solution should preserve the property (3.101). In particular, we must have that

$$\left.\frac{\mathrm{d}S_-}{\mathrm{d}x}\right|_{x_s} = \left.\left(\frac{S'^x_-}{S^\tau_-} - S_-\frac{S'^\tau_-}{S^\tau_-}\right)\right|_{x_s} = \left.\frac{S'^x_-}{S^\tau_-}\right|_{x_s} > 0. \tag{3.103}$$

Substituting the two remaining power-series solutions to linear order, one finds the values of $\check{v}$ as a function of κ for the $i = 2$ (red) and $i = 3$ (blue) solutions, which satisfy this inequality; see Fig. 3.7. The colored region corresponds to those points $(\check{v}, \kappa)$ for which (3.103) is satisfied. The prohibited region, where $\check{v} < 0$ for both $i = 2$ and $i = 3$, is due to the fact that $v^s_{1,2}$ and $v^s_{1,3}$ are not real there. Apart from this region, and recalling the allowed range for $\check{v}$ (3.83), the

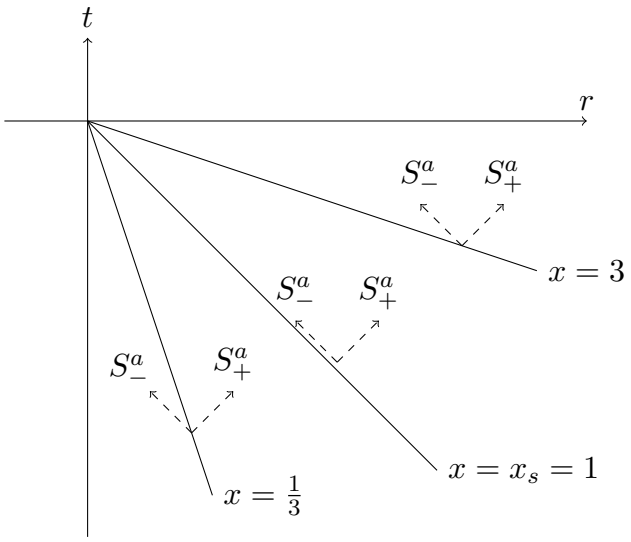

FIGURE 3.6: The two sonic limit $S^a_\pm$ on lines of constant x. The line $x = x_s$ on which $S^a_- \sim \left(\frac{\partial}{\partial\tau}\right)^a$ characterizes the sonic point.

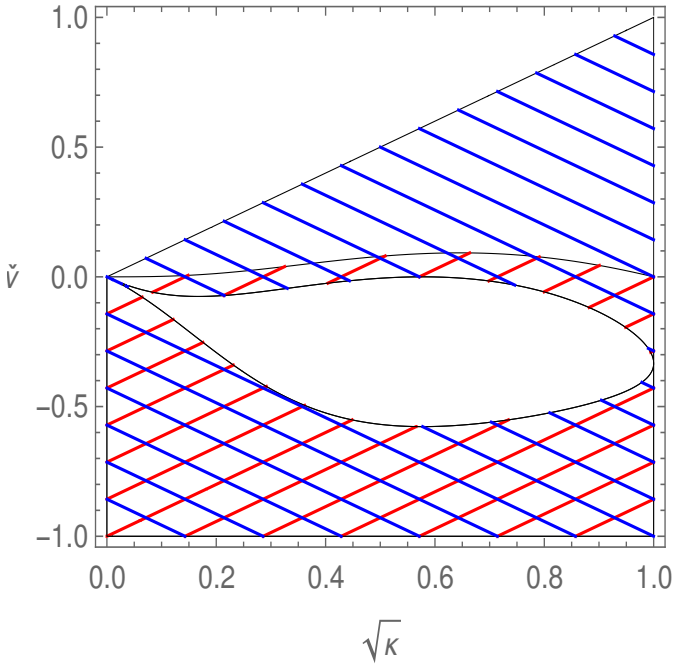

FIGURE 3.7: The allowed values of $\check{v}$ satisfying $\left.\frac{\mathrm{d}S_-}{\mathrm{d}x}\right|_{x_s} > 0$, in terms of κ for $i = 2$ (red) and $i = 3$ (blue).

$i = 3$ solution always verifies the condition (3.103). The $i = 2$ solution on the other hand does not. The $i = 2$ solution is therefore discarded as well.

3.5.4 The CSS solution

From the previous section, we found a power-series solution near the center with free parameters $\check{N}$ and $\check{\omega}$ and a power-series solution near the sonic point, with free parameter $\check{v}$.

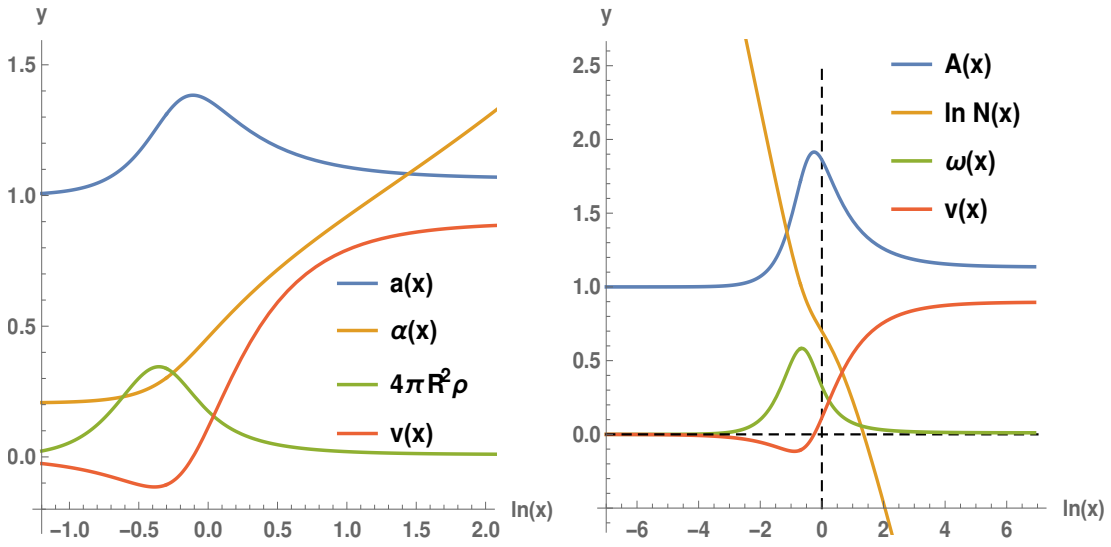

FIGURE 3.8: The CSS solution. The left and right plots can be immediately compared to those found in Refs [65] and [132] respectively.

Assuming that both power-series hold within a small enough radius δ, we can then consider shooting from δ and $1-\delta$ to, say the midpoint $x = 0.5$. We then impose that the solution from both shootings coincides there.

This condition gives rise to a highly nonlinear system of three equations. They are then solved by appropriately fixing the value of our parameters $\check{N}$, $\check{\omega}$ and $\check{v}$. Using Mathematica's NSolve function as a black box, the mismatch at $x = 0.5$ can be easily reduced to $\sim \mathcal{O}(10^{-15})$. The free parameters are then fixed as

$$\check{N} \simeq 1.23660, \qquad \check{\omega} \simeq 5.82098, \qquad \check{v} \simeq 0.11244. \tag{3.104}$$

The resulting plots are shown in Fig. 3.8. These can be compared with the results found in Refs [65, 132]. For the right plot, note that the ω between the one displayed in Ref. [132] and our plot do not agree. This is due to an error in Ref. [132] as their ω visibly does not satisfy the regularity condition (3.81) for ω at the sonic point $x = 1$, whereas it does in our plots. For the left plot, α (and thus N) was rescaled to obtain the exact plot as in Ref. [65]. This is due to the fact that in Ref. [65], a different gauge was used.

We remark here that it is well-known that the spherically symmetric CSS fluid solution, together with the requirement of analyticity at the center and sonic point, actually admits a countable family of solutions [55, 132]. The above solution we find using the Mathematica software is singled out during the matching. An intuitive reason for this is that the above solution, as we will show, has a single growing mode. The other solutions possess more than one growing mode and are therefore not picked up without the use of fine-tuning or other, more rigorous, approaches.

3.6 Linear perturbation of the critical solution

3.6.1 The perturbed equations

We now proceed to calculate the linear perturbations of the CSS solution. As for the background solution, we will follow the notation introduced in Ref. [132]. Specifically, we will work with the logarithms of N, A and ω. In order to avoid cluttering, we introduce the notation

$$\bar{N} := \ln N, \tag{3.105}$$

and similarly for $\bar{A}$ and $\bar{\omega}$, so that any quantity with a bar corresponds to the logarithm of that quantity. For compactness, we then define

$$\bar{X} := \{\bar{N}, \bar{\omega}, v\}. \tag{3.106}$$

Note that v is the only variable for which we do not consider its logarithm.

We are seeking eigenmode solutions of the linear perturbation, with Lyapunov exponent λ_0. We then consider the linear perturbations of the form

$$\bar{X}(t, R) = \bar{X}_0(x) + \epsilon e^{\lambda_0 \tau} \bar{X}_1(x), \tag{3.107}$$

$$\bar{A}(t, R) = \bar{A}_0(x) + \epsilon e^{\lambda_0 \tau} \bar{A}_1(x), \tag{3.108}$$

where $\bar{X}_0$ and $\bar{A}_0$ correspond to the background CSS solution.

It is easy to find the relationship between the linear perturbation of a bar and unbarred quantity,

$$\bar{N}_1 = \frac{N_1}{N_0}, \tag{3.109}$$

and so on. Therefore, we can think of $\bar{N}_1$ as measuring the size of the perturbation N_1, relative to the size of the background N_0. We will call $\bar{X}_1$ and $\bar{A}_1$ the eigenmodes.

The eigenmodes $\bar{N}_1$, $\bar{A}_1$ and $\bar{\omega}_1$ are related to the eigenmodes α_1, a_1 and ρ_1 as

$$\alpha_1 = x\sqrt{A_0} N_0 \left(\bar{N}_1 + \frac{1}{2} \bar{A}_1 \right), \tag{3.110}$$

$$a_1 = \frac{1}{2} \sqrt{A_0} \bar{A}_1, \tag{3.111}$$

$$R^2 \rho_1 = \frac{\omega_0}{4\pi A_0} \left(\bar{\omega}_1 - \bar{A}_1 \right). \tag{3.112}$$

Substituting this ansatz into the Einstein equations, the leading-order term vanishes by assumption and at linear order, reminiscent of the CSS equations, we obtain one ODE equation for each of the four variables, as well as an algebraic equation. As before, we can solve this algebraic equation for $\bar{A}_1$, and reduce the ODE system into a system of three ODE equations for $\bar{N}, \bar{\omega}, v$. We then consider a power-series expansion near the center and sonic point, and resolve the mismatch between these two expansions via the method of shooting.

For the metric variables, it is straightforward to find the first-order equations. For the fluid's variables, a bit more care needs to be taken. As for the case for the background variables, we

will need to regularize the equations at the sonic point x_s. Recall that, for example, the ODE for ω can be written as

$$\bar{\omega}' = \frac{N_\omega}{D_\omega}. \tag{3.113}$$

We can then apply our ansätze (3.107) and (3.108). It follows that the numerator and denominator can be expanded as $N_\omega = N_{\omega,0} + \epsilon e^{\lambda_0 \tau} N_{\omega,1}$, and so on. The resulting system of ODE can be written as

$$\bar{\omega}_0' = \frac{N_{\omega,0}}{D_{\omega,0}}, \tag{3.114}$$

$$\bar{\omega}_1' = \frac{D_{\omega,0}\, N_{\omega,1} - N_{\omega,0}\, D_{\omega,1}}{D_{\omega,0}^2}. \tag{3.115}$$

The first equation, corresponding to the zeroth-order equation, is of course just the CSS equation we have solved previously. Turning our attention to the new second equation, we see that we have a $D_{\omega,0}^2$ in the denominator. In this form, regularizing the equation at the sonic point is a bit tricky. So, we first make use of (3.114) and rewrite the linear equation as

$$\bar{\omega}_1' = \frac{N_{\omega,1} - \bar{\omega}_0'\, D_{\omega,1}}{D_{\omega,0}}, \tag{3.116}$$

and similarly for v_1'. $\bar{\omega}_0'$ is assumed to be known, at least as a power-series near the center and sonic point.

3.6.2 Regularity conditions and gauge fix

At the center, we need to ensure that our spacetime remains free of conical singularities after the introduction of the linear perturbations. This requires

$$\bar{A}_1(0) = 0. \tag{3.117}$$

Moreover, since the velocity is an odd function of x, we need

$$v_1(0) = 0. \tag{3.118}$$

It then follows, as in the background case, that the power-series solution around the center is described by two parameters, $\check{\bar{N}}_1 := \bar{N}_1(0)$ and $\check{\bar{\omega}}_1 := \bar{\omega}_1(0)$.

Note that the linear perturbations produce a remaining gauge freedom corresponding to a coordinate transformation of t of order ϵ, $t \to t + \epsilon f(t)$. This allows us to fix the value of $\bar{N}_1$ at any point x. For convenience, we will choose to fix it such that

$$\bar{N}_1(x_s) = 0. \tag{3.119}$$

Since the denominator in the ODE system for the fluid variables only depends on the background variables, it follows that the location of the sonic point is still located at $x_s = 1$. Regularization there requires, $N_{\omega,1} = \bar{\omega}_0'\, D_{\omega,1}$ and similarly for v. This would give us naively two

constraints. However, as in the background case, both numerators are proportional to each other at the sonic point. Regularity therefore fixes two out of the three degrees of freedom (recall that we gauge-fixed the freedom on N) of the system. Here, we will take the remaining free parameter to be $A_1(1) =: \check{\bar{A}}_1$.

3.6.3 Power-series solution

3.6.3.1 Power series near the center

We expand both the known background variables and perturbed variables around $x = 0$. The latter reads,

$$\bar{N}_1 = \sum_{n=0}^{\infty} \bar{N}^c_{1,n} x^n, \tag{3.120}$$

and similarly for the other variables.

For similar reasons as in the derivation of the CSS solution, we may assume $\bar{A}_1$, $\bar{\omega}_1$ and $\bar{N}_1$ to be even, while v_1 is odd. The reason the barred quantities are all even can be understood from Eq. (3.109). The barred quantities are ratios between the unbarred and background quantities. The latter two are either both even (as for A and ω), or odd (as for N). As a result, the expansion of the barred quantities are even in either cases.

Substituting this ansatz and solving up to second order in the power series gives

$$\bar{N}^c_{1,2} = \frac{1}{6}(-1+3\kappa)\check{\bar{\omega}}_1\check{\omega}, \tag{3.121}$$

$$\bar{A}^c_{1,2} = \frac{2}{3}\check{\bar{\omega}}_1\check{\omega}, \tag{3.122}$$

$$\bar{\omega}^c_{1,2} = \frac{\begin{array}{r}-2\left(2+3\lambda_0+3\kappa(6+\lambda_0)\right)\check{\bar{N}}_1 + \check{\bar{\omega}}_1\left(\left(-1+15\kappa\right)\lambda_0 + 3\left(1+\kappa\right)\lambda_0^2\right. \\ \left.-3\left(1+\kappa+3\kappa^2+3\kappa^3\right)\check{N}^2\check{\omega}\right)\end{array}}{18\kappa\left(1+\kappa\right)\check{N}^2}, \tag{3.123}$$

$$v^c_{1,1} = \frac{2\check{\bar{N}}_1 - \lambda_0\check{\bar{\omega}}_1}{3\check{N}(1+\kappa)}. \tag{3.124}$$

3.6.3.2 Power series near sonic point

Again, we expand both the known background and perturbed variables. The latter reads

$$\bar{N}_1 = \sum_{n=0}^{\infty} \bar{N}^s_{1,n}(x-1)^n \tag{3.125}$$

and so on. Recall that in the above, we gauge-fixed $\bar{N}_1(1) = \bar{N}^s_{1,0} = 0$.

The power-series solution is rather complicated and will not be given here.

3.6.4 The eigenmode solution and critical exponent

As in the background case, we will shoot from the origin "to the right" (i.e. towards increasing R) and shoot from the sonic point "to the left" (i.e. towards the center). The mismatch between

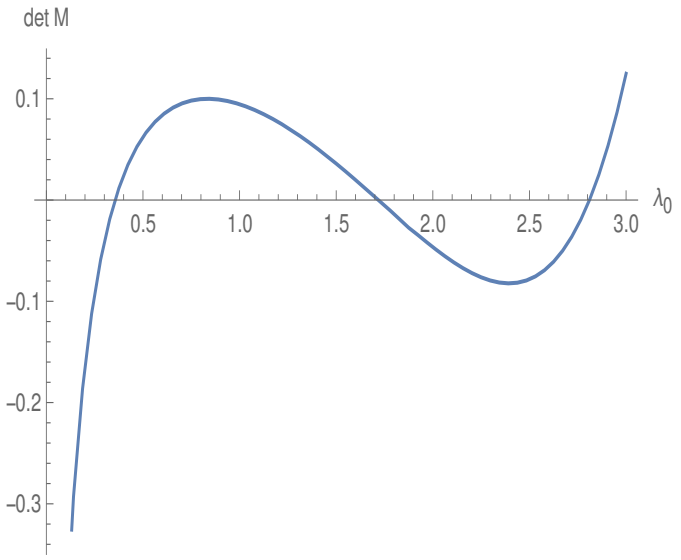

FIGURE 3.9: Plot of $\det M$ for $\kappa = 1/3$. This shows that only discrete values of λ_0 are permissible.

the two shootings will be resolved at the midpoint $x = 0.5$. This gives a system of three equations, which will be solved for the three free parameters from the power expansion as well as the Lyapunov exponent λ_0. At first glance, this system thus looks under-determined. However, we will see that only discrete values of λ_0 are allowed. Once we have resolved the mismatch, we can further extend the shooting to the "right" of the sonic point.

In order to resolve the mismatch we note that, due to linearity, the mismatch function must itself have a linear form. In particular, we may write the mismatch function as

$$\mathcal{M} := M(\lambda_0)w, \tag{3.126}$$

where $M(\lambda_0)$ is a 3×3 matrix depending (nonlinearly) on λ_0 and $w = (\check{\tilde{N}}_1, \check{\tilde{\omega}}_1, \check{\tilde{A}}_1)$. Solving for the mismatch means to choose a suitable w such that $\mathcal{M} = 0$.

In order to find a non-trivial solution, we require $\det M = 0$. This produces a nonlinear equation to be solved for λ_0.

In Fig. 3.9, we plot $\det M$ for $\kappa = 1/3$. The rightmost root gives

$$\lambda_0 \simeq 2.81055250, \tag{3.127}$$

with corresponding eigenvector

$$w \simeq (-0.569469, 0.769713, 0.288524). \tag{3.128}$$

This Lyapunov exponent can be checked to agree well with the existing literature [65, 67, 132].

The reader may be wondering why there seems to be three distinct positive roots in Fig. 3.9 instead of only one. The rightmost root corresponds to the unique physical growing mode of the critical solution. The leftmost root instead corresponds to a gauge mode. Recall that we

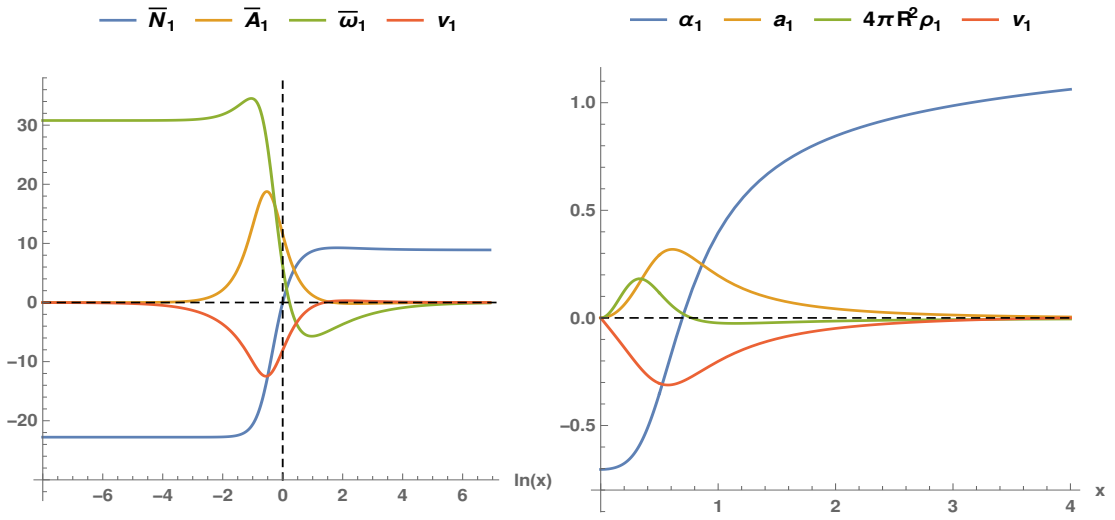

FIGURE 3.10: Eigenmode solution of the linear perturbations for $\lambda_0 \simeq 2.81$ and $\kappa = 1/3$.

gauge-fixed $\bar{N}_1(1) = 0$. This induces a gauge mode [132] equal to $-N_0'(1) \simeq 0.3557$. This comes from the fact that the perturbation that we are considering may be a critical solution viewed from a different coordinate system through a coordinate transformation. Finally, upon inspection, the solution corresponding to the middle root is only C^0 at the point where the mismatch is resolved. This can be further inspected by changing the location of where the mismatch is evaluated at. In this case, the middle root also drastically changes location. As we only wish to retain physical, smooth solutions, we are therefore left with a single root. The critical solution has therefore one growing mode.

The resulting eigenmodes are then plotted in Fig. 3.10. The left plot can be compared with Ref. [132]. In this paper, there is a small error as they plot A_1, instead of $\bar{A}_1$. See also Ref. [137].

3.6.5 The case $\kappa \neq 1/3$

Up until this point, we have thoroughly presented the critical phenomena for radiation fluid, $\kappa = 1/3$. What about other values of κ? In Refs [66, 67, 132], the critical phenomena for the perfect fluid were investigated for the full range of κ. One still finds the same qualitative picture as for $\kappa = 1/3$. Namely: critical behavior is type II (mass and curvature scaling) and the critical solution is (continuously) self-similar. The critical solution and the scaling exponents are universal.

By definition, the self-similar solution characterizing the critical solution has a single unstable mode. One can turn the problem around and ask if other kind of self-similar solutions, besides the critical solution, exists? In newtonian mechanics, this line of research was first investigated by Larson and Penston in 1969, [17, 18]. Their studies gave rise to what is now called the Larson-Penston solution. It describes coherent/pure collapse of a shell of fluid to a singularity (physical velocity never changes sign). A more complete picture was given by Hunter [138]. He found a discrete family of self-similar solutions. One member of such family

corresponds to the Larson-Penston solution discussed above. All the other ones are then usually labeled at Hunter (a), (b), etc, solutions. These latter solutions describe oscillative collapse, the indexing (a), (b), etc, labeling the number of zeroes in the velocity field.

In the general-relativistic setting, Ori and Piran [54, 139], made a thorough investigation of collapse scenarios in self-similar spacetimes. They showed that in the limit $\kappa \to 0$, a given relativistic solution is well approximated by some newtonian solution. As a consequence of this, they find the general-relativistic counterpart of the Larson-Penston solution, which exists for $0 < \kappa \lesssim 0.036$. Interestingly, it was shown that for this solution, if $\kappa \lesssim 0.0105$, spacetime develops a naked singularity. Numerical and analytical evidences [140, 141] have shown that this solution is stable under spherical perturbation. This makes it a direct violation of weak cosmic censorship in spherical symmetry.

The relativistic counterpart of the Hunter (a) and (b) solutions were also found and investigated in Refs [139, 140]. One finds that they have, respectively, one and two growing spherical modes. The fact that the relativistic Hunter (a) solution is a self-similar solution with a single growing mode is actually not a coincidence, as this solution actually corresponds to the critical solution.

The above relativistic results were anticipated in Ref. [142], where linear perturbation analysis was performed for the Larson-Penston and Hunter family of solution in the newtonian regime. They found that the former has no growing modes while the latter has the number of growing modes equal to the number of zeroes in its velocity profile (so Hunter (a) has one growing mode, Hunter (b) has two, etc). Later, the Hunter (a) solution was also confirmed to be the analogue of a critical solution in newtonian mechanics [143].

3.6.6 The effect of angular momentum

In Ref. [88], the effect of the linear perturbations (both spherical and nonspherical) of the CSS solution were investigated for the full range $0 < \kappa < 1$. The CSS solution has one growing mode for a given κ. The situation for the nonspherical modes depends on κ:

For "soft" equation of state, $0 < \kappa < 1/9$, the CSS solution gains three further growing modes, corresponding to the $l = 1$ axial mode (with $m = -1,0,1$). This was in part numerically confirmed in Ref. [92]. Due to the existence of these additional growing modes, the critical solution can only approached by fine-tuning several parameters instead of one. One would therefore expect the usual power scaling for the mass and curvature to breakdown below some scale. However, the $l = 1$ unstable mode grows much more slowly than its spherically symmetric one. To compensate for this, one would require very high fine-tuning to the black-hole threshold, which is currently difficult to achieve numerically.

For an "intermediate" equation of state, $1/9 < \kappa \lesssim 0.49$, the CSS solution has no nonspherical growing mode. The CSS solution is therefore still a critical solution, at least when slightly perturbed from spherical symmetry. For this range, the angular momentum also scales like a power-law as was discussed in Sec. 2.6.2. The values of the critical exponent for the mass and curvature are not affected by the presence of (small) angular momentum and so are the same as in the spherically symmetric case. In particular, we do find, in the limit of fine-tuning,

that the final black hole for supercritical data is nonspinning; see again Sec. 2.6.2. These results were confirmed in Refs [89–91] in fully non-linear numerical simulations for radiation fluid $\kappa = 1/3$.

Finally, for "stiff" equation of state, $0.49 \lesssim \kappa < 1$, the CSS solution has several nonspherical growing modes, including at least the $l = 2$ polar mode. This $l = 2$ polar instability was much later confirmed in a full numerical simulation; see Ref. [144].

3.7 Conclusion

We have investigated the critical behavior of a perfect fluid with linear barotropic equation of state $P = \kappa\rho$ in $3 + 1$ dimensions.

We have shown that the critical phenomena are of type II, for all values of κ. The critical exponents satisfy the relation $\delta = \gamma$, in line with the dimensional analysis in Sec. 2.4. The critical solution is continuously self-similar. Both the critical solution and the critical exponents are universal. It is worthwhile for the reader to keep these general results in mind once we study the critical phenomena for the same system but in $2 + 1$ dimensions.

The numerical results agree well with the existing literature [65, 67, 132]. This gives a first test that the numerical algorithm manages to correctly capture the main features (critical exponent and critical solution) in the critical collapse of a perfect fluid, using a simple method of lines technique and without using adaptive mesh refinements.

An interesting check, which to the best of my knowledge has not been done thus far, is to slightly extend the code to include the effects of a cosmological constant. This can provide evidence for the intuition that the cosmological constant should become dynamically irrelevant during the strong-field regime [145]. As a result, neither the critical solution nor the critical exponents should be affected.

Chapter 4

The anti-de Sitter and BTZ solutions

4.1 Introduction

Very few studies have studied critical phenomena beyond spherical symmetry. One reason is that in spherical symmetry, the critical solution can be largely studied analytically. This is done by making a self-similarity ansatz, thereby transforming the Einstein-matter system into a simple system of ODEs. This is not so beyond spherical symmetry. Furthermore, gravitational waves exist beyond spherical symmetry. Since they can, by themselves, display critical phenomena, the analysis (numerical or theoretical) of any matter field is therefore substantially more complicated.

A way to circumvent all of these issues is to consider critical collapse in $2+1$ spacetime dimensions. In $2+1$ dimensions, many mathematical problems become more tractable. One enlightening example of this is that in $2+1$ dimensions, gravitational waves do not exist. A direct consequence of this is that the vacuum exterior of any rotating body is given by the BTZ metric [58] (the Kerr equivalent in $2+1$ dimensions). This is clearly not true in $3+1$ dimensions. Also, in axisymmetry, all variables (metric and matter) still only depend on time and radius, as they would in spherical symmetry. This means that generalizing spherically symmetric initial data to axisymmetric ones is a relatively harmless process in $2+1$ dimensions. This comes however with a large drawback: black holes cannot exist in $2+1$ dimensions [59], except with a negative cosmological constant [58].

AdS is a very bizarre space. It has the merit of being one of the simplest and most symmetric solutions of the Einstein field equations. On the other hand, it is also somewhat notorious for having many counter-intuitive properties. Nonetheless, in these past few decades, it has received a strong renewed attention. This is principally due to the fact that it is an essential ingredient to the adS/CFT correspondence [104]. We will not touch on the correspondence here. Instead, in the first half of this chapter, we will review most of the basic properties of adS: notably the geodesic motion and its conformal structure. In the second half, we will review the basic properties of the BTZ black hole.

The first section closely follows the references [146, 147]. The second section is based on [147–150]. As a result, none of the contents in this chapter is original work.

4.2 Anti-de Sitter space

4.2.1 Coordinates

4.2.1.1 Embedding coordinates

Consider an $n+1$ dimensional space $\mathbb{R}^{2,n-1}$, with coordinates, X_μ, where $\mu = 0, \cdots, n$. These coordinates will be referred to as *embedding coordinates*. The space is equipped with a flat metric with signature $\text{diag}(-1, 1, \cdots, 1, -1)$, given by

$$\mathrm{d}s^2 = \mathrm{d}X_\mu \mathrm{d}X^\mu = -\mathrm{d}X_0^2 - \mathrm{d}X_n^2 + \sum_{i=1}^{n-1} \mathrm{d}X_i^2. \tag{4.1}$$

Intuitively, this space has 2 time coordinates, X_0 and X_n, and $n-1$ spatial coordinates, $\{X_i\}_{i=1}^{n-1}$. AdS is then defined as the n-dimensional hypersurface in $\mathbb{R}^{2,n-1}$ given by

$$X^\mu X_\mu = -X_0^2 - X_n^2 + \sum_{i=1}^{n-1} X_i^2 = -\ell^2. \tag{4.2}$$

As is clear from the above, ℓ has dimension length and sets the length scale of adS.

AdS space is the collection of points which are equidistant (in the above metric) to the origin, in the embedding coordinates. This identification can be made explicit if we switch to "imaginary times" $X_0 \to iX_0$ and $X_n \to iX_n$. It is for this reason that adS is also referred to as a pseudo- or quasisphere. For $n = 2$, the equation $-X_0^2 - X_2^2 + X_1^2 = -\ell^2$ precisely represents a one-sheeted hyperboloid. By analogy, the general case is also called an hyperboloid.

In the embedding coordinates, it is easy to see that adS is maximally symmetric: the defining relation (4.2) has $SO(2, n-1)$ as its symmetry group. Its Lie algebra has $n(n+1)/2$ generators, which is the maximum amount of isometries that an n-dimensional manifold may have [6].

As we will see, the embedding coordinates are advantageous to get an overview of some geometrical properties of adS (like geodesics). For calculation purposes however, it is useful to employ coordinates which are directly defined on the pseudosphere.

4.2.1.2 Hyperbolic coordinates

Consider Cartesian coordinates $\{\tilde{X}_i\}$ in $\mathbb{R}^m$. Recall that the embedded unit sphere S^{m-1} in $\mathbb{R}^m$ is defined in terms of the Cartesian coordinates by $\tilde{X}_1^2 + \cdots + \tilde{X}_m^2 = 1$. The sphere can be more naturally defined in spherical coordinates $(\theta, \phi_1, \cdots, \phi_{m-2})$, defined by

$$\tilde{X}_1 = \cos(\theta), \tag{4.3}$$
$$\tilde{X}_2 = \sin(\theta)\cos(\phi_1), \tag{4.4}$$
$$\tilde{X}_3 = \sin(\theta)\sin(\phi_1)\cos(\phi_2), \tag{4.5}$$
$$\vdots$$
$$\tilde{X}_m = \sin(\theta)\sin(\phi_1)\cdots\sin(\phi_{m-2}). \tag{4.6}$$

We can then consider *spherical coordinates* $(t, r, \theta, \phi_1, \cdots, \phi_{n-3})$,

$$X_0 =: \ell \sin\left(\frac{t}{\ell}\right) \cosh\left(\frac{r}{\ell}\right), \quad X_n =: \ell \cos\left(\frac{t}{\ell}\right) \cosh\left(\frac{r}{\ell}\right), \quad X_i =: \ell \sinh\left(\frac{r}{\ell}\right) \tilde{X}_i. \tag{4.7}$$

Note that the range of the variable t is $-\pi\ell < t \leq \pi\ell$. Furthermore, the times $t = \pm\pi\ell$ correspond to the same point on the manifold. Time t is therefore periodic. One can check that (4.2) is identically verified. The pullback of the metric takes the form

$$\mathrm{d}s^2 = -\cosh^2\left(\frac{r}{\ell}\right) \mathrm{d}t^2 + \mathrm{d}r^2 + \ell^2 \sinh^2\left(\frac{r}{\ell}\right) \mathrm{d}\Omega_{n-2}^2, \tag{4.8}$$

where $\mathrm{d}\Omega_{n-2}^2$ is the metric of the unit $(n-2)$-sphere.

The surface $t =$ constant is called hyperbolic space H^{n-1} [151]. This is why these coordinates are also sometimes referred to as *hyperbolic coordinates*.

From (4.8), r is to be interpreted as a radial coordinate. Of course, r is not uniquely defined as any other coordinate $\bar{r} = \bar{r}(r)$ would be a legitimate radial coordinate.

4.2.1.3 Standard coordinates

A useful alternative radial coordinate to the one used above is given by $R := \ell \sinh(r/\ell)$. In this case, the metric takes the *standard form*

$$\mathrm{d}s^2 = -(1 + R^2/\ell^2)\mathrm{d}t^2 + \frac{\mathrm{d}R^2}{1 + R^2/\ell^2} + R^2 \mathrm{d}\Omega_{n-2}^2. \tag{4.9}$$

In this coordinate system, it is easy to verify again that adS is maximally symmetric, since

$$R_{abcd} = -\frac{1}{\ell^2}\left(g_{ac}g_{bd} - g_{ad}g_{bc}\right). \tag{4.10}$$

The Ricci scalar then reads,

$$\mathrm{Ric} = -\frac{n(n-1)}{\ell^2}. \tag{4.11}$$

This coordinate system also makes it particularly easy to see that we recover Minkoswki spacetime by taking the limit $\ell \to \infty$.

4.2.1.4 Conformal coordinates

In the hyperbolic coordinates given previously, the boundary of adS is located at $r = \infty$. In Sec. 4.2.2, we will more closely analyze this boundary. As in Minkowski, it is however useful to work with a more convenient radial coordinate ψ which puts the boundary at some finite value of ψ. Such a coordinate is said to be *compact*, or *conformal*. One common definition of ψ is $\tan\psi := \sinh(r/\ell)$. Note that the range of ψ is then $0 \leq \psi < \pi/2$, where infinity is now located at $\psi = \pi/2$. The metric takes the form

$$\mathrm{d}s^2 = \frac{1}{\cos^2\psi}\left(-\mathrm{d}t^2 + \ell^2\mathrm{d}\psi^2 + \ell^2 \sin^2\psi \mathrm{d}\Omega_{n-2}^2\right). \tag{4.12}$$

This coordinate system, as the two previous coordinates defined before, cover the entire manifold, apart from the coordinate singularities at the origin $r = 0 = \psi$ and the boundary $\psi = \pi/2$.

4.2.1.5 Poincaré coordinates

The *Poincaré coordinates* $x_{\bar{\mu}}$ are defined in terms of the embedding coordinates as

$$X_i =: \frac{\ell x_i}{x_{n-1}}, \quad i = 0, \cdots, n-2, \tag{4.13}$$

$$X_{n-1} =: \frac{1}{2x_{n-1}} \left(x^{\bar{\mu}} x_{\bar{\mu}} - \ell^2 \right), \tag{4.14}$$

$$X_n =: \frac{1}{2x_{n-1}} \left(x^{\bar{\mu}} x_{\bar{\mu}} + \ell^2 \right), \tag{4.15}$$

where $x^{\bar{\mu}} x_{\bar{\mu}} = -x_0^2 + x_1^2 + \cdots + x_{n-1}^2$. The metric then takes the simple form

$$\mathrm{d}s^2 = \frac{\ell^2}{x_{n-1}^2} \mathrm{d}x^{\bar{\mu}} \mathrm{d}x_{\bar{\mu}}. \tag{4.16}$$

Note that the metric has a coordinate singularity at $x_{n-1} = 0$. Thus, we have two distinct patches, depending on whether one chooses to consider $x_{n-1} > 0$ or $x_{n-1} < 0$. Because adS is maximally symmetric, we may without loss of generality consider $x_{n-1} > 0$. The Poincaré coordinates most explicitly show that half of adS is conformal to the flat-space metric.

4.2.1.6 Comoving coordinates

Finally, consider the *comoving coordinates* $(\tau, \chi, \theta, \phi_i)$,

$$X_0 =: \ell \cos\left(\frac{\tau}{\ell}\right), \tag{4.17}$$

$$X_n =: \ell \sin\left(\frac{\tau}{\ell}\right) \cosh\chi, \tag{4.18}$$

$$X_i =: \ell \sin\left(\frac{\tau}{\ell}\right) \sinh\chi \tilde{X}_i, \tag{4.19}$$

where the functions $\tilde{X}_i$ were defined in Sec. 4.2.1.2.

We have again a periodic time coordinate $0 \leq \tau < \pi\ell$ and radial coordinate $\chi > 0$. The metric is

$$\mathrm{d}s^2 = -\mathrm{d}\tau^2 + \ell^2 \sin^2\frac{\tau}{\ell} \left(\mathrm{d}\chi^2 + \sinh^2\chi \mathrm{d}\Omega_{n-2}^2 \right). \tag{4.20}$$

Again, these coordinates do not cover the whole manifold, since we need to restrict $-\ell < X_0 < \ell$ and $X_n > 0$. In these coordinates, it is not obvious at first sight that adS is stationary but their advantage is that they are comoving with a free-falling (test) particle, as will be made clear shortly.

4.2.2 Global properties and conformal structure

In the hyperbolic coordinates introduced, the time coordinate t is periodic, so that points $(-\pi\ell, r, \theta, \phi_i)$ and $(\pi\ell, r, \theta, \phi_i)$ are identified. In other words, the one-dimensional manifold, $r, \theta, \phi_i =$ constant has topology S^1. On the other hand, the hyperbolic space H^{n-1} has topology $\cong \mathbb{R}^{n-1}$. AdS has therefore the product topology,

$$\text{adS} \cong S^1 \times \mathbb{R}^{n-1}. \tag{4.21}$$

The periodicity of time introduces closed timelike curves. For example, consider the parametrized curve in the coordinates (4.7)

$$X_0 = \ell \cos\left(\frac{t}{\ell}\right), \qquad X_n = \ell \sin\left(\frac{t}{\ell}\right), \qquad X_i = 0. \tag{4.22}$$

This curve's tangent vector is clearly $\partial/\partial t$, which has norm -1. The curve is then timelike, but periodicity of time causes it to be closed at both endpoints $t = -\pi\ell$ and $t = \pi\ell$.

The existence of closed timelike curves can be avoided by "unwrapping" the time coordinate t. This means that we consider its range to be $-\infty < t < \infty$ and we *do not* identify points $t = \pi\ell k$, $k \in \mathbb{Z}$. From the point of view of the ambient $(n+1)$-pseudosphere, we are then running an infinite amount of times around the pseudosphere. In order to avoid making this periodic identification on the pseudosphere, the idea is to simply throw away the definition of adS in terms of the higher-dimensional pseudosphere (4.2.1.1). Instead, one *defines* adS as the manifold equipped with the metric (4.8), where the time coordinate t now has the range $-\infty < t < \infty$. Note that the periodicity of time is now completely absent in this case. In particular, this "enhanced" adS now has global topology $\mathbb{R}^n$. One therefore wishes to distinguish this new manifold from the definition of adS in terms of pseudosphere. This manifold is then called the *universal covering space of adS*, or CadS.

In what follows, we will typically be dealing with CadS, although often times it will be useful to temporarily revert back to the pseudosphere analogy to understand certain results more intuitively. Most of the time, going back and forth between adS and CadS is harmless, principally because the only difference between these two spaces is *global*: any local features of adS is preserved in CadS and vice versa. For example, CadS is also maximally symmetric, as isometries are local features of the geometry. This is also the reason why sometimes in the literature, adS and CadS are used synonymously.

An important global property of any spacetime is its structure at infinity. As already advertised, the conformal coordinates (see Sec. 4.2.1.4) are most useful to studying the conformal structure of CadS. Clearly, the metric is conformal to

$$\mathrm{d}\bar{s}^2 = -\mathrm{d}t^2 + \ell^2\left(\mathrm{d}\psi^2 + \sin^2\psi \mathrm{d}\Omega^2\right). \tag{4.23}$$

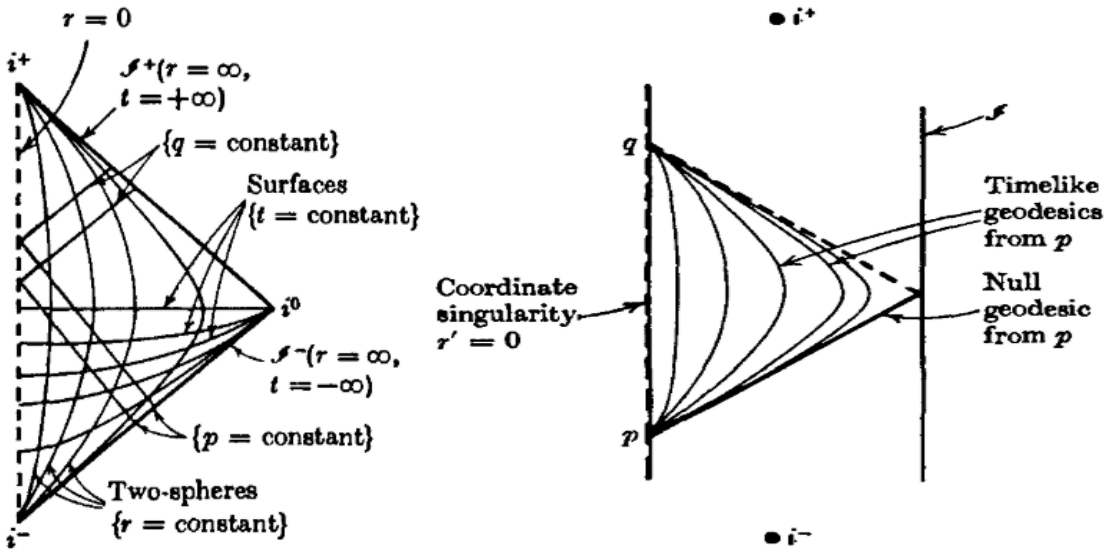

FIGURE 4.1: Penrose diagram of Minkowski (left) and adS (right). Image credit: [22].

This conformal metric is "larger" than the physical metric in that this metric is regular at $\psi = \pi/2$. The metric at the boundary $\mathcal{J}$ reads

$$\mathrm{d}\bar{s}^2_{\partial} = -\mathrm{d}t^2 + \ell^2 \mathrm{d}\Omega^2. \tag{4.24}$$

The normal vector to this hypersurface is given by

$$n_a := (d\psi)_a|_{\psi=\pi/2} = (0, 1, 0, \cdots, 0). \tag{4.25}$$

This has norm $n_a n^a = g^{\psi\psi} = 1/\ell^2 > 0$. The normal vector is spacelike and therefore conformal infinity $\mathcal{J}$ is a timelike hypersurface. This is for example in contrast to Minkowski spacetime where, by simply taking $\ell \to \infty$, the normal vector is null and therefore conformal infinity is also null.

We can take a shortcut in drawing the conformal diagram of CadS. First, recall CadS is conformally flat (recall Sec. 4.2.1.5). So, the lightcones in CadS can be drawn the same as those in Minkowski. The only difference is the conformal infinity, as it is timelike in CadS. See Fig. 4.1 for a Penrose diagram of Minkowski and CadS, where the angular dimensions have been suppressed.

Since $\mathcal{J}$ is timelike, it is inherently impossible to predict the "far future" in CadS. In order to understand this, let us first discuss the situation in Minkowski spacetime. Suppose that we are being given some initial data on some (spacelike) surface S at $t = t_{\text{initial}}$. Making use of the Einstein field equations, we can evolve this initial data at some later time. If the initial surface S is, for example bounded, then so is its domain of dependence D. We can predict further into the future by simply making the initial surface S larger. In particular, if we pick the initial surface to be the entire hypersurface $t = t_{\text{initial}}$, then we can, assuming the validity of the strong cosmic censorship, predict the entire future (and past) of spacetime. This is possible

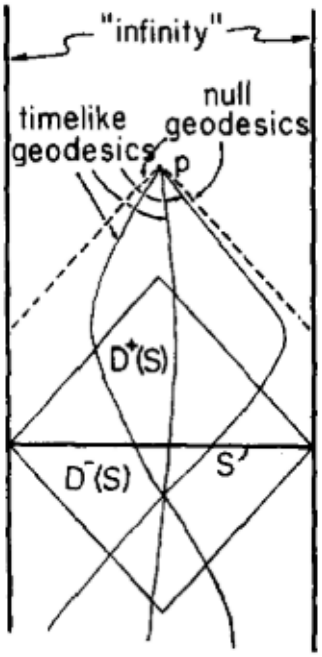

FIGURE 4.2: Penrose diagram of CadS where the domain of dependence is highlighted. Unlike in Minkowski, curves emanating from the adS boundary (and thus not intersecting S) can affect the evolution. The boundary of the domain of dependence of S is therefore a Cauchy horizon. Image credit: [21].

in Minkowski, because conformal infinity consists of two null cones and therefore no signal from $\mathcal{J}$ can affect the interior.

For CadS, the situation is different, since there are timelike geodesics connecting points inside spacetime to points at infinity. These geodesics can be made to never intersect the initial surface. This is made particularly clear from the spacetime diagram, where conformal infinity is drawn as a straight vertical line; see Fig. 4.1 and Fig. 4.2.

This can also be understood by noting that null geodesics, as will be shown in the next section, can actually reach infinity in *finite* proper time. In reverse, this also means that data originating from infinity can eventually interact with data only specified "inside". So, in CadS, if some initial data are specified on some spacelike hypersurface $t = t_{\text{initial}}$, there will still be a limit to how much one can predict. Thus CadS (and therefore also adS) is not globally hyperbolic [21, 29].

In order to say something beyond the domain of dependence of the initial data, one needs to impose boundary conditions at infinity. In typical numerical studies, one chooses "reflective" boundary condition at the boundary, so that nothing can neither escape nor enter spacetime. These boundary conditions are however not the only possible choices [152, 153].

4.2.3 Geodesics

4.2.3.1 Null geodesics

The geodesic equation may be written as

$$\frac{\mathrm{d}}{\mathrm{d}\lambda}\left(g_{\alpha\beta}\frac{\mathrm{d}x^\beta}{\mathrm{d}\lambda}\right) - \frac{1}{2}g_{\mu\nu,\alpha}\frac{\mathrm{d}x^\mu}{\mathrm{d}\lambda}\frac{\mathrm{d}x^\nu}{\mathrm{d}\lambda} = 0, \tag{4.26}$$

where λ is some affine parameter.

The null geodesics can be immediately computed in the Poincaré coordinates. In these coordinates, (half of) adS is conformal to Minkowski spacetime and one can immediately deduce that the null geodesics are straight lines.

It is however more useful to directly solve the geodesic equation in the conformal coordinate system instead. This also has the advantage that we can probe the properties of geodesics at the boundary. For simplicity, consider radial geodesics, with tangent vector $\dot{x}^\alpha = (\dot{t}, \dot{\psi}, \mathbf{0})$, where from now on, dots indicate derivative with respect to λ.

In the geodesic equation (4.26), only the $\alpha = t$ and $\alpha = \psi$ equations are non-trivial. The latter equation will be a second-order equation for ψ. Since we only consider null geodesics, we can discard this equation and instead replace it with the null constraint, $\dot{x}^\alpha \dot{x}_\alpha = 0$.

Assuming that the geodesics start at $\psi = \psi_0$ for $\lambda = 0$, $\dot{\psi} > 0$ (outgoing) and $\dot{t} > 0$ (this is without loss of generality), the system of equations reads

$$\dot{t} = E\ell\cos^2\psi, \tag{4.27}$$

$$\dot{t} = \ell\dot{\psi}. \tag{4.28}$$

The constant E can be interpreted as the energy of the particle. One way to see this is that the metric has the timelike Killing vector $\partial/\partial t$ in those coordinates and the induced conserved quantity [154] gives rise to the above first equation. The system can be integrated to give

$$\tan\psi = E\lambda + \tan\psi_0, \tag{4.29}$$

$$t - t_0 = \ell(\psi - \psi_0). \tag{4.30}$$

It follows that the lightcone consists of straight $45°$ lines in the $(t, \ell\psi)$ variables. However, a notable difference from Minkowksi is that the travel time from $\psi = \psi_0$ to any other radial point is *finite* in coordinate time t. In particular, traveling from an arbitrary radial location $\psi = \psi_0$ to the conformal infinity $\mathcal{J}$, takes $\Delta_{\mathcal{J}} t = \ell(\pi/2 - \psi_0)$. The largest travel time corresponds to a particle starting at $\psi_0 = 0$, and is $\pi\ell/2$. This is however not simply an effect tied to the coordinate system. In terms of the proper time, we have

$$\mathrm{d}\tau = \frac{\mathrm{d}t}{\cos\psi_0} \implies \Delta_{\mathcal{J}}\tau = \frac{\Delta_{\mathcal{J}} t}{\cos\psi_0}. \tag{4.31}$$

This is always finite and ranges from a maximum of $\pi\ell/2$, for $\psi_0 = 0$, to ℓ, for $\psi_0 \to \pi/2$. Of course, by definition, we formally have that $\Delta_{\mathcal{J}}\tau = 0$ if $\psi_0 = \pi/2$.

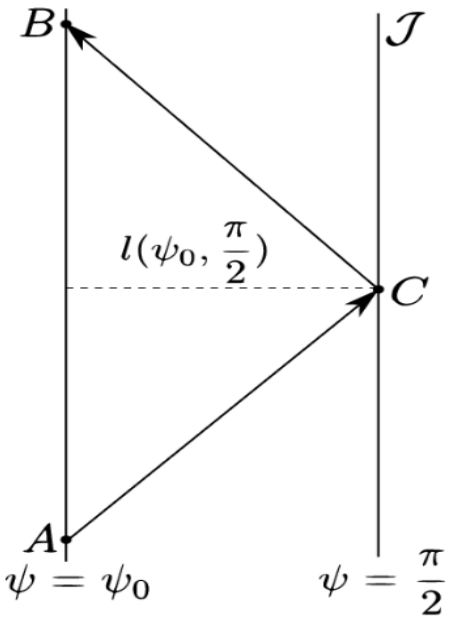

FIGURE 4.3: A particle (say a photon) emitted at a point A at radial coordinate $\psi = \psi_0$ travels to the CadS boundary $\mathcal{J}$ at C in some finite proper time τ, before traveling back to point B at the same spatial location as A. Note that while the time of travel is finite, the spatial distance $l(\psi_0, \pi/2)$ traveled from A to C and C to B is infinite. Image credit: [146].

This should be contrasted with the distance traveled. In fact, measuring the distance along $\partial/\partial\psi$, we find

$$l(\psi_0, \pi/2) := \int_{\psi_0}^{\pi/2} \mathrm{d}s = \ell \int_{\psi_0}^{\pi/2} \frac{\mathrm{d}\psi}{\cos\psi}, \tag{4.32}$$

which diverges for $\psi_0 < \pi/2$; see Fig. 4.3.

Complementary to radial geodesics, let us mention circular null geodesics. In CadS, it is easy to see that circular null geodesics do not exist, except at the boundary. Precisely, the geodesic equation (4.26), together with the null condition $\dot{x}^\alpha \dot{x}_\alpha = 0$ is consistent with the ansatz $\psi = \psi_0$ only if $\psi_0 = \pi/2$. This can be most easily checked in hyperbolic coordinates (4.7) where the radial component of the geodesics equation $\alpha = r$, together with the null condition $\dot{x}^a \dot{x}_a = 0$, require $\sinh r_0 = \cosh r_0$, which is only true for $r_0 = \infty$.

The properties of null geodesics are in some extent related to the question of stability. In Minkowski, it was proven that Minkowski is nonlinearly stable [27]. The main reason for the stability is the ability of small perturbation to radiate off their energy to infinity. In CadS however, since $\mathcal{J}$ is timelike, energy can enter (or leave) spacetime from the boundary. In order to correctly analyze the stability of CadS, one first needs to choose appropriate boundary conditions. In many cases, one chooses reflective boundary conditions. Then, no energy can leave nor enter and the boundary effectively acts like a mirror, at which radiation "bounces off". However, such a boundary condition of course immediately poses a potential problem: energy, which travels on null geodesics, will perpetually travel to and away from the boundary. In some sense, CadS is analogous to a closed system, with material "walls" delimiting the boundary. From this point of view, it should come as no surprise that CadS has been found to

be nonlinearly unstable for suitable matter systems which can exploit this feature [128, 129, 155–158].

4.2.3.2 Timelike geodesics

Consider a massive test particle moving in CadS space. An adapted reference frame to study the motion of the test particle is to choose a comoving reference frame, which means that the particle has constant spatial coordinates. The tangent vector of a comoving particle is then by definition $\dot{x}^a = (\partial/\partial\tau)^a$. Although the particle is at rest in this frame, it is the relative distances that instead vary in time. The comoving coordinates introduced in Sec. 4.2.1.6 are precisely the comoving coordinates in CadS.

Usually, one would like to make a distinction between different kinds of geodesics, such as radial or circular ones. It turns out that all timelike geodesics in adS can be represented as a circular geodesic on an appropriate two-plane [159]. In order to explain this, it is useful to momentarily return to the the higher-dimensional point of view. Geodesics in adS are curves in the embedded space. The curve can be described in the coordinates $X_\mu(s)$ and parametrized by the proper length s. Of course, this curve will *not* be a geodesic in the higher space. (i.e. a "straight line" with respect to the metric of the higher-dimensional space). In fact, the geodesic equation of adS can be written from the point of view of the ambient space, via the Lagrange multipliers method [159], and gives

$$\ddot{X}_\mu + \frac{1}{\ell^2} X_\mu = 0. \tag{4.33}$$

The solution to this equation is further subject to two conditions:

1) normalization of the velocity vector $\dot{X}^\mu \dot{X}_\mu = -1$,

2) X^μ satisfies the defining relation of adS (4.2).

The solution of the geodesic equation is then

$$X_\mu(s) = q_\mu \sin\left(\frac{s}{\ell} + c\right) + p_\mu \cos\left(\frac{s}{\ell} + c\right). \tag{4.34}$$

c is a constant and the constant vectors q_μ, p_μ are subject to the three conditions

$$q^\mu q_\mu = p^\mu p_\mu = -\ell^2, \quad q^\mu p_\mu = 0. \tag{4.35}$$

Together, they satisfy the defining relation (4.2) and properly normalize the tangent vector. In particular, a general timelike vector is described by an ellipse. However, we can say more.

For simplicity, we take $c = 0$ as this is simply a shift of the parameter s. We shall make full use of the fact that adS is maximally symmetric. Let $X_\mu(0)$ be a point on this curve. First, one can "boost" to a frame where $X_\mu(0) = (0, \ell, 0, \cdots, 0)$. Second, on can "rotate" so that the tangent vector $\dot{X}_\mu(0) = (1, 0, \cdots, 0)$. Both conditions make up $2n$ constraints (recall that X_μ and $\dot{X}_\mu$ need to satisfy the constraint (4.2) and $\dot{X}^\mu \dot{X}_\mu = -1$). For $n \geq 3$, $SO(2, n-1)$ has enough generators to make this transformation. These two conditions fix q_μ and p_μ, and the

curve simplifies to

$$X_0(s) = \ell \sin\left(\frac{s}{\ell}\right), \quad X_n = \ell \cos\left(\frac{s}{\ell}\right), \quad X_i = 0. \tag{4.36}$$

Therefore, a generic timelike geodesic in adS can be described, in the ambient $R^{2,n-1}$ space, as a circle of radius ℓ! The geodesics are periodic, with period $2\pi\ell$. As a result, any two timelike geodesics, which intersect at any point in adS, will first diverge, and inevitably converge back to the same point again after a distance $\Delta s = 2\pi\ell$. In fact, before then, they already converge at the antipodal point $\Delta s = \pi\ell$ [159]. Geometrically, this is because the two geodesics are circles lying on two different planes and they intersect both at the initial and antipodal points.

Note that the $X_\mu(s)$ are always bounded. A direct consequence of this is that the timelike geodesics cannot reach the boundary. This is most readily seen in the hyperbolic coordinates (4.7), where the coordinates X_μ are unbounded as $r \to \infty$. Finally, and more dramatically, this also implies that, fixing any point P_0 in adS, it is easy to find a second point P_1, in the causal future of P_0, which cannot be connected by a causal geodesic [22].

4.3 The BTZ black hole

4.3.1 Metric and parameter space

We now restrict our attention to $2+1$ dimensions. The vacuum Einstein equations have a black-hole solution, found by Bañados, Teitelboim and Zanelli [58]

$$\mathrm{d}s^2 = -N^2\mathrm{d}t^2 + N^{-2}\mathrm{d}r^2 + r^2\left(N^\phi \mathrm{d}t + \mathrm{d}\phi\right)^2, \tag{4.37}$$

where the lapse N and shift N^ϕ are functions of the radius r only and given by

$$N^2 = -M + \frac{r^2}{\ell^2} + \frac{J^2}{4r^2}, \quad N^\phi = -\frac{J}{2r^2}. \tag{4.38}$$

The range of the coordinates are $-\infty < t < \infty$, $0 < r < \infty$, $0 \le \phi < 2\pi$. M and J are constants and, as their notation suggests, represent the conserved (ADM) mass and angular momentum, due to the Killing vectors $\partial/\partial t$ and $\partial/\partial\phi$ [147]. This black-hole solution is referred to as the BTZ solution.

The existence of the BTZ solution is quite surprising. Black holes generally produce gravitational waves during gravitational collapse. Since gravitational waves do not exist in $2+1$ dimensions, this naively seems to imply that black holes should not exist either. A second reason as to why the existence of the BTZ solution is surprising, is that in $2+1$ dimensions, the metric is locally flat. This in turn implies that a black hole in $2+1$ dimensions should have no curvature singularities in its interior.

One can show that black holes cannot form in $2+1$ dimensions without a cosmological constant [59] and from the above, we can have a first intuition as to why this is so. In $2+1$ dimensions, the mass M is dimensionless and since all of the coordinates' variables have dimension length, we require a length scale in order to construct a dimensionless quantity.

Furthermore, from (4.38), taking $r \to \infty$, it is easy to see that the presence of a negative cosmological constant serves to keep N^2 positive at infinity.

The BTZ solution shares many similarities with its $3+1$ (Kerr) counterpart. First, notice that the lapse function vanishes for

$$r_{\pm}^2 = \frac{M\ell^2}{2}\left(1 \pm \sqrt{1 - \left(\frac{J}{M\ell}\right)^2}\right). \tag{4.39}$$

Inverting, we can also write M and J in terms of $r_{\pm}$

$$M = \frac{r_+^2 + r_-^2}{\ell^2}, \qquad |J| = \frac{2r_+r_-}{\ell}. \tag{4.40}$$

r_- is the Cauchy horizon of the black hole, while r_+ is the event horizon. Second, the norm of the Killing vector $\partial/\partial t$ is null at

$$r_{\text{erg}} := lM^{\frac{1}{2}}, \tag{4.41}$$

where r_{erg} is the ergosurface. It is easy to check that these three values satisfy

$$r_- \leq r_+ \leq r_{\text{erg}}. \tag{4.42}$$

The existence of an event horizon imposes some upper and lower bounds on the parameters,

$$M > 0, \quad |J| \leq M\ell. \tag{4.43}$$

The BTZ black hole is extremal when $|J| = M\ell$. In that case, the Cauchy and event horizon coincide, $r_-^2 = r_+^2 = \frac{M\ell^2}{2}$.

It is interesting to see what happens for infinitesimal black holes, namely for $M \to 0^+$. We then also need $|J| \to 0^+$ and the line element becomes

$$\mathrm{d}s^2 = -\frac{r^2}{\ell^2}\mathrm{d}t^2 + \frac{\ell^2}{r^2}\mathrm{d}r^2 + r^2\mathrm{d}\phi^2. \tag{4.44}$$

Unlike what might have been expected at first, this metric does *not* correspond to adS, except asymptotically. Instead, for negative values of the mass, $M < 0$ and $J = 0$, the metric is

$$-(|M| + (r/\ell)^2)dt^2 + (|M| + (r/\ell)^2)^{-1}dr^2 + r^2d\phi^2. \tag{4.45}$$

We can then redefine $t \to t/\sqrt{|M|}$, $r \to \sqrt{|M|}r, \phi \to \phi/\sqrt{|M|}$ to recast the metric in standard adS form (4.2.1.3). The only difference is that the angular coordinate has the range $\phi \in [0, 2\pi\sqrt{|M|}]$. This exactly coincides with the adS metric for the special value $M = -1$. We obtain an angular deficit/excess for any other values of $M < 0$. These solutions correspond to naked singularities. For $-1 < M < 0$, they can also be interpreted as point particles [160]. In particular, this means that adS3 space, corresponding to $M = -1$, is separated from the smallest black-hole solution, $M = 0$, by a (unit) mass gap. Therefore, one cannot continuously deform one solution into the other, without passing through a sequence of naked singularities;

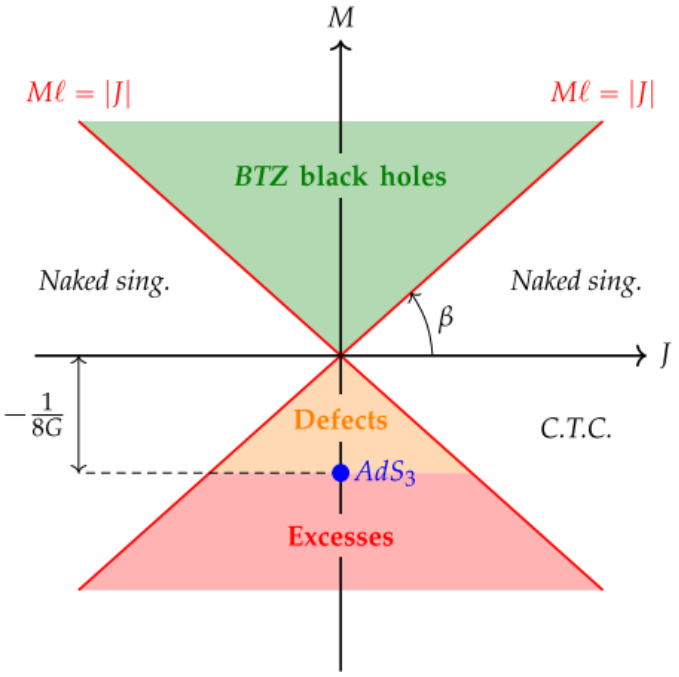

FIGURE 4.4: The BTZ metric in the (J, M) plane. The adS metric is separated from the black-hole solutions by a gap. Image credit: [147].

see Fig. 4.4. Nonetheless, there is a deep geometric link between adS space and the BTZ black hole, which we will discuss in the next section.

4.3.2 Isometries of adS3

AdS3 space has as isometry group $SO(2,2)$. The Killing vectors spanning it can be arranged as [148]

$$J_{\mu\nu} := X_\mu \frac{\partial}{\partial X^\nu} - X_\nu \frac{\partial}{\partial X^\mu}, \tag{4.46}$$

where X_μ are the embedding coordinates. A general Killing vector is then an arbitrary linear combination of the above,

$$\xi := \frac{1}{2}\omega^{ab} J_{ab}. \tag{4.47}$$

Without loss of generality, we may assume ω^{ab} to be antisymmetric. We can take this arbitrary Killing vector and consider a one-parameter subgroup of isometries. This subgroup maps a point p to a point p' according to [161]

$$p \to p' := \exp(t\xi)(p) = \exp_p(t\xi). \tag{4.48}$$

Let $t \in I$, where $I \subseteq \mathbb{R}$. Suppose we wish to identify the points p and p'. Specifically, consider the equivalence relation

$$p \sim q \iff \exists t \in I, \quad q = \exp_p(t\xi). \tag{4.49}$$

We then wish to consider the quotient manifold $\mathrm{N} := \mathrm{adS3}/\sim$. In order for the resulting quotient manifold to be well-defined, we need the map $\exp(t\xi) : \mathrm{adS3} \to \mathrm{adS3}$ to be properly discontinuous. That is, we need it to fulfill the following two conditions [22],

- $\exists \mathcal{U} \subseteq \mathrm{adS3}$ such that $\exp_{\mathcal{U}}(t\xi) \cap \mathcal{U} = \emptyset$ (which implies that N is a manifold).
- If $p \nsim q$, then there exist neighborhoods $p \in \mathcal{U}_p$, $q \in \mathcal{U}_q$, such that $\nexists t$ with $\exp_{\mathcal{U}_p}(t\xi) \cap \mathcal{U}_q \neq \emptyset$ (which implies that N is Hausdorff).

Both of these conditions are satisfied if $I \cong \mathbb{N}$. By convention, one in fact chooses to discretize t as

$$t = 2\pi k, \qquad k \in \mathbb{Z}. \tag{4.50}$$

In other words, we choose to identify the points $p, \exp_p(\pm 2\pi\xi), \exp_p(\pm 4\pi\xi)$, etc and the resulting quotient space is well-defined.

N is still a solution to the Einstein equations because we identified points that belonged to the orbit of an isometry. This can be easily seen by going into coordinates where we choose one of the coordinates, say ϕ, to be aligned with the orbit of the Killing vector ξ, $\xi = \frac{\partial}{\partial\phi}$. In such coordinates, the metric coefficients do not depend on that coordinate and is therefore well-defined upon identifying $p \sim \exp_p(2\pi k \frac{\partial}{\partial\phi})$.

In order to get some intuition as to what N looks like, notice that one of the by-products of the identification process is that any curve joining two distinct points that lie on the same orbit is closed in N. In particular, this means that if the curve is timelike in adS3, it will remain so in N. N therefore contains closed timelike curves. This means that if we wish for N to have an admissible causal structure, we need, before making the identification, to remove the regions in adS3 that will produce closed timelike curves in the quotient space N. A necessary condition to avoid close timelike curves is to consider points for which the Killing vector is spacelike,

$$\xi_a \xi^a > 0. \tag{4.51}$$

In general, this condition is not sufficient, but we will show that it is for a particular Killing vector that will be introduced later. Following the notation of [148], the resulting spacetime will be denoted as (adS3)'. Thus, we consider the quotient space

$$\mathrm{N}' := (\mathrm{adS3})'/\sim . \tag{4.52}$$

In N′, the hypersurface $\xi^a\xi_a = 0$ is a singularity in the causal structure of spacetime as, by definition, analytically extending beyond it (which is the same as simply considering adS3/ $\sim$) introduces closed timelike curves. It is easy to see that N′ is geodesically complete, except for the geodesics that hit the singularity $\xi^a\xi_a = 0$.

Now, we claim that the quotient N′ is equivalent to the BTZ solution when we consider the Killing vector

$$\ell\xi_{\mathrm{BTZ}} := r_- J_{23} + r_+ J_{01} - J_{12} + J_{13}. \tag{4.53}$$

Note that this differs from the form of the expression given in [148]. This is due to a difference in how the coordinates X_μ have been defined. In order to demonstrate that the resulting quotient space gives the BTZ solution, we will first need to compute adS3' and then N'. For simplicity, we will assume from now on the nonextremal case where $r_+ > r_-$, as the extremal case adds some subtleties in the analysis. We refer the reader to [148] for additional details. In the Poincaré coordinates (x_0, x_1, x_2) (Sec. 4.2.1.5), the Killing vector takes the form

$$\xi_{\text{BTZ}} = \frac{r_-}{\ell}\left(x_0\frac{\partial}{\partial x_0} + x_1\frac{\partial}{\partial x_1} + x_2\frac{\partial}{\partial x_2}\right) + \frac{r_+}{\ell}\left(x_0\frac{\partial}{\partial x_1} + x_1\frac{\partial}{\partial x_0}\right) - \frac{\partial}{\partial x_1}. \tag{4.54}$$

In these coordinates, it is easy to see that the shifts

$$x_0 \to x_0 + \frac{\ell r_+}{r_+^2 - r_-^2}, \qquad x_1 \to x_1 - \frac{\ell r_-}{r_+^2 - r_-^2} \tag{4.55}$$

are $SO(2,2)$ isometries and eliminate the last term in (4.54).

Written back into the original coordinates, the Killing vector then takes the simplified form,

$$\xi_{\text{BTZ}} = \frac{r_-}{\ell}J_{23} + \frac{r_+}{\ell}J_{01}. \tag{4.56}$$

Making use of the defining relation (4.2), its norm is

$$||\xi_{\text{BTZ}}||^2 = \frac{r_+^2 - r_-^2}{\ell^2}(X_0^2 - X_1^2) + r_-^2. \tag{4.57}$$

Therefore the admissible region in adS3, where $||\xi_{\text{BTZ}}||^2 > 0$, is

$$-\frac{r_-^2\ell^2}{r_+^2 - r_-^2} < X_0^2 - X_1^2 < \infty. \tag{4.58}$$

The above region can be further subdivided into three distinct regions:

- Region 1: $X_0^2 - X_1^2 > \ell^2$ or $r_+^2 < ||\xi_{\text{BTZ}}||^2 < \infty$.
- Region 2: $0 < X_0^2 - X_1^2 < \ell^2$ or $r_-^2 < ||\xi_{\text{BTZ}}||^2 < r_+^2$.
- Region 3: $-\frac{r_-^2\ell^2}{r_+^2 - r_-^2} < X_0^2 - X_1^2 < 0$ or $0 < ||\xi_{\text{BTZ}}||^2 < r_-^2$.

These regions are separated by the null surfaces $X_0^2 - X_1^2 = 0$ and $X_0^2 - X_1^2 = \ell^2$. They will turn out to be the outer and inner horizons!

The current expression of the Killing vector is not very insightful. In order to make progress, we need to find a more suitable coordinate system. A natural coordinate system would be one where one of the coordinates parametrize the flow along the above Killing vector. In that case, the identification simply dictates to impose a periodicity condition on the corresponding coordinate. Introduce a "polar-radial" coordinate system (t, r, ϕ) in each such region [149].

- Region 1. $r_+ < r$,

$$X_0 = \ell\sqrt{\alpha(r)}\cosh\left(\frac{r_+}{\ell}\phi - \frac{r_-}{\ell^2}t\right), \tag{4.59}$$
$$X_1 = \ell\sqrt{\alpha(r)}\sinh\left(\frac{r_+}{\ell}\phi - \frac{r_-}{\ell^2}t\right), \tag{4.60}$$
$$X_2 = \ell\sqrt{\alpha(r)-1}\cosh\left(\frac{r_+}{\ell^2}t - \frac{r_-}{\ell}\phi\right), \tag{4.61}$$
$$X_3 = \ell\sqrt{\alpha(r)-1}\sinh\left(\frac{r_+}{\ell^2}t - \frac{r_-}{\ell}\phi\right). \tag{4.62}$$
$$\tag{4.63}$$

- Region 2. $r_- < r < r_+$,

$$X_0 = \ell\sqrt{\alpha(r)}\cosh\left(\frac{r_+}{\ell}\phi - \frac{r_-}{\ell^2}t\right), \tag{4.64}$$
$$X_1 = \ell\sqrt{\alpha(r)}\sinh\left(\frac{r_+}{\ell}\phi - \frac{r_-}{\ell^2}t\right), \tag{4.65}$$
$$X_2 = -\ell\sqrt{1-\alpha(r)}\sinh\left(\frac{r_+}{\ell^2}t - \frac{r_-}{\ell}\phi\right), \tag{4.66}$$
$$X_3 = -\ell\sqrt{1-\alpha(r)}\cosh\left(\frac{r_+}{\ell^2}t - \frac{r_-}{\ell}\phi\right). \tag{4.67}$$
$$\tag{4.68}$$

- Region 1. $0 < r < r_-$,

$$X_0 = \ell\sqrt{-\alpha(r)}\sinh\left(\frac{r_+}{\ell}\phi - \frac{r_-}{\ell^2}t\right), \tag{4.69}$$
$$X_1 = \ell\sqrt{-\alpha(r)}\cosh\left(\frac{r_+}{\ell}\phi - \frac{r_-}{\ell^2}t\right), \tag{4.70}$$
$$X_2 = -\ell\sqrt{1-\alpha(r)}\sinh\left(\frac{r_+}{\ell^2}t - \frac{r_-}{\ell}\phi\right), \tag{4.71}$$
$$X_3 = -\ell\sqrt{1-\alpha(r)}\cosh\left(\frac{r_+}{\ell^2}t - \frac{r_-}{\ell}\phi\right), \tag{4.72}$$
$$\tag{4.73}$$

where

$$\alpha(r) := \frac{r^2 - r_-^2}{r_+^2 - r_-^2}, \quad t \in (-\infty, \infty), \quad \phi \in (-\infty, \infty). \tag{4.74}$$

In each region, the adS3 metric (4.1) reduces to the BTZ metric (4.38).

As it stands, the metric is diffeomorphic to adS3 and consequently cannot describe the BTZ solution. The reason is that the coordinate ϕ is not a “proper" angular coordinate, since its range is $-\infty < \phi < \infty$. It will acquire its usual range and periodicity after the identification along the Killing vector ξ_{BTZ}. Indeed, one checks that in the above coordinates, (t, r, ϕ), the Killing vector ξ_{BTZ} reduces to

$$\xi_{\text{BTZ}} = \frac{\partial}{\partial\phi}. \tag{4.75}$$

In those coordinates, the identification then simply imposes that we identify

$$\phi \sim \phi + 2\pi. \tag{4.76}$$

With this identification, ϕ becomes a genuine angular coordinate and the metric is then the BTZ metric.

Recall that, while we ignored the region $\xi^a\xi_a < 0$ as it would contain closed timelike curves upon identification, it does not guarantee that the region $\xi^a\xi_a > 0$ will not contain closed timelike curves after the identification. It turns out that this condition is actually also sufficient in this case. To see this, we consider the adS3 metric, written in the "BTZ coordinates" (4.38) (so, with $-\infty < \phi < \infty$). We need to show that there is no causal curve $\gamma : [0,1] \to \text{adS3}'$ from a a point (t_0, r_0, ϕ_0) to a point $(t_0, r_0, \phi_0 + 2\pi)$. In other words, we need to ensure that $\gamma(1) \neq \exp(2\pi\partial/\partial\phi)\gamma(0)$. Let us show that by contradiction.

Consider a causal curve $\gamma(\lambda) = (t(\lambda), r(\lambda), \phi(\lambda))$ such that its tangent vector, $\mathrm{d}\gamma(\lambda)/\mathrm{d}\lambda$, does not vanish anywhere. From the metric, this curve satisfies

$$-N^2\left(\frac{\mathrm{d}t}{\mathrm{d}\lambda}\right)^2 + N^{-2}\left(\frac{\mathrm{d}r}{\mathrm{d}\lambda}\right)^2 + r^2\left(N^\phi\frac{\mathrm{d}t}{\mathrm{d}\lambda} + \frac{\mathrm{d}\phi}{\mathrm{d}\lambda}\right)^2 \leq 0. \tag{4.77}$$

Assume now that this causal curve connects the two points, $\gamma(0) = (t_0, r_0, \phi_0)$ and $\gamma(1) = (t_0, r_0, \phi_0 + 2\pi)$. This implies the existence of a $\lambda_0 \in [0,1]$ such that $\mathrm{d}t/\mathrm{d}\lambda$ vanishes at $\lambda = \lambda_0$. This is because t is the same between the starting and endpoint. But then, if $N^2 > 0$, this implies that $\mathrm{d}r/\mathrm{d}\lambda = \mathrm{d}\phi/\mathrm{d}\lambda = 0$ at $\lambda = \lambda_0$. This in turn implies that the tangent vector vanishes at that point, a contradiction. Similarly, if $N^2 < 0$, we can instead consider another $\lambda_1 \in [0,1]$ such that $\mathrm{d}r/\mathrm{d}\lambda = 0$ at $\lambda = \lambda_1$ and a similar conclusion follows. So, the region $\xi^a\xi_a > 0$ does not contain any closed timelike curves and so neither does the BTZ solution.

It is worth emphasizing again that $\xi^a\xi_a = 0$ is not a curvature singularity but only a singularity in the causal structure. This should be contrasted with the $3+1$ dimensional black hole (say Schwarzschild) where $r = 0$ is a curvature singularity. In $2+1$, spacetime is locally undistinguishable to adS3 and, in particular, none of the curvature scalars are singular anywhere, as can be for example verified from the expression of the metric (4.38) with $J = 0$.

4.3.3 Penrose diagram

Let us now construct the Penrose diagram for the BTZ black-hole solution. Starting from the form of the metric (4.38) one introduces Kruskal coordinates, (U, V, ϕ) in a neighborhood of the roots $r = r_\pm$. On each patch, one wishes the line element to take the form

$$\mathrm{d}s^2 = \Omega^2\left(\mathrm{d}U^2 - \mathrm{d}V^2\right) + r^2\left(N^\phi\mathrm{d}t + \mathrm{d}\phi\right)^2, \tag{4.78}$$

where Ω, r and t are all functions of (U, V).

To the left and right of the root $r = r_+$ we define the patch K_+ as,

$$r_- < r \leq r_+ : \begin{cases} U_+ = \left(\left(\frac{-r+r_+}{r+r_+} \right) \left(\frac{r+r_-}{r-r_-} \right)^{r_-/r_+} \right)^{1/2} \sinh(a_+ t), \\ V_+ = \left(\left(\frac{-r+r_+}{r+r_+} \right) \left(\frac{r+r_-}{r-r_-} \right)^{r_-/r_+} \right)^{1/2} \cosh(a_+ t) \end{cases} \tag{4.79}$$

$$r_+ \leq r < \infty : \begin{cases} U_+ = \left(\left(\frac{r-r_+}{r+r_+} \right) \left(\frac{r+r_-}{r-r_-} \right)^{r_-/r_+} \right)^{1/2} \cosh(a_+ t), \\ V_+ = \left(\left(\frac{r-r_+}{r+r_+} \right) \left(\frac{r+r_-}{r-r_-} \right)^{r_-/r_+} \right)^{1/2} \sinh(a_+ t), \end{cases} \tag{4.80}$$

where

$$a_+ := \frac{r_+^2 - r_-^2}{\ell^2 r_+}. \tag{4.81}$$

Note that in these coordinates, $t(U, V)$ is singular as $r \to r_+$. We need the above metric to be regular everywhere, including at the horizon. This can be done by fixing the gauge freedom we have to shift ϕ by $\phi \to \phi - N^\phi(r_+)t$. This is equivalent to imposing $N^\phi(r_+) = 0$ and the one-form $N^\phi dt$ will be regular at $r = r_+$.

The metric then takes the wanted form (4.78), with

$$\Omega^2 = \frac{(r^2 - r_-^2)(r + r_+)^2}{a_+^2 r^2 \ell^2} \left(\frac{r - r_-}{r + r_-} \right)^{r_-/r_+}, \quad r_- < r < \infty. \tag{4.82}$$

In the nonrotating case, $J = r_- = 0$ The above patch covers the whole manifold. In the rotating case, we need a second patch K_- to the left and right of r_-,

$$0 < r \leq r_- : \begin{cases} U_- = \left(\left(\frac{-r+r_-}{r+r_-} \right) \left(\frac{r+r_+}{-r+r_+} \right)^{r_+/r_-} \right)^{1/2} \cosh(a_- t), \\ V_- = \left(\left(\frac{-r+r_-}{r+r_-} \right) \left(\frac{r+r_+}{-r+r_+} \right)^{r_+/r_-} \right)^{1/2} \sinh(a_- t). \end{cases} \tag{4.83}$$

$$r_- \leq r < r_+ : \begin{cases} U_- = \left(\left(\frac{r-r_-}{r+r_-} \right) \left(\frac{r+r_+}{-r+r_+} \right)^{r_+/r_-} \right)^{1/2} \sinh(a_- t), \\ V_- = \left(\left(\frac{r-r_-}{r+r_-} \right) \left(\frac{r+r_+}{-r+r_+} \right)^{r_+/r_-} \right)^{1/2} \cosh(a_- t), \end{cases} \tag{4.84}$$

where

$$a_- := \frac{r_-^2 - r_+^2}{\ell^2 r_-}. \tag{4.85}$$

Imposing this time $N^\phi(r_-) = 0$, the metric is regular and takes again the required form (4.78), with

$$\Omega^2 = \frac{(r_+^2 - r^2)(r + r_-)^2}{a_-^2 r^2 \ell^2} \left(\frac{r_+ - r}{r_+ + r} \right)^{r_+/r_-}, \quad 0 < r < r_+. \tag{4.86}$$

As in the $3+1$ case, the geometry can be maximally extended by gluing together an infinite string of patches K_+ and K_- through their nontrivial overlapping region $K_+ \cap K_-$.

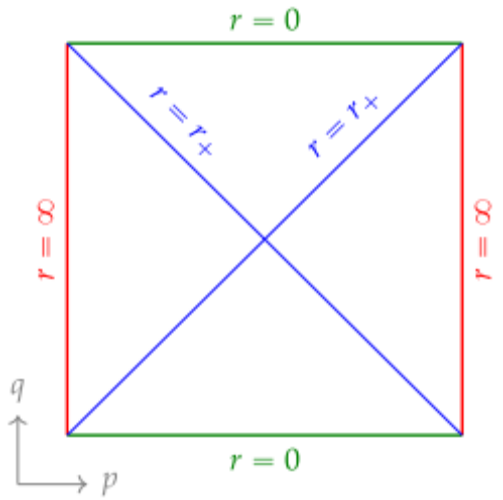

FIGURE 4.5: Penrose diagram for the nonrotating BTZ black hole. Image credit: [147].

Let us now change coordinates again, from (U, V) to a set of compact coordinates p and q. In the nonextremal case, $r_- \neq r_+$, consider the following compactified coordinates,

$$U + V = \tan\left(\frac{p+q}{2}\right), \qquad U - V = \tan\left(\frac{p-q}{2}\right). \tag{4.87}$$

We restrict that ranges to the usual $-\pi \leq p \pm q \leq \pi$.

First, consider the nonrotating case, $J = r_- = 0$. The Penrose diagram is shown in Fig. 4.5. Infinity $r = \infty$ is mapped to $p = \pm\pi/2$ (red vertical lines). The singularity $r = 0$ is instead mapped to $q = \pm\pi/2$ (green horizontal lines), while the horizon $r = r_+$ is mapped to $p = \pm q$ (blue diagonal lines).

For the rotating case, the compactification is performed on each patch, namely on K_- and K_+. The full diagram is then obtained by the usual gluing technique; see Fig. 4.6. Note that the resulting diagram is quite reminiscent to the Kerr black hole in $3 + 1$. The only difference in the causal structure are the conformal infinity and the nature of the singularity.

Let us now briefly turn to the two singular cases. First consider $M = J = 0$ where the BTZ metric takes the simple form (4.44). In this case, one chooses,

$$U = r^\star, \quad V = t, \tag{4.88}$$

where $r^\star$ is the tortoise coordinate defined as,

$$\mathrm{d}r^\star = \frac{\mathrm{d}r}{r^2} \iff r^\star = -\frac{1}{r}. \tag{4.89}$$

The metric is then again of the form (4.78), with $\Omega^2 = \frac{r^2}{\ell^2}$. We can then consider the compact coordinates p and q as given previously (4.87). The Penrose diagram has the shape of a triangle; see Fig. 4.7. The origin is mapped to the line segment $p = -\pi \pm q$ (green diagonal lines). Infinity is mapped to $p = \pi$ (red vertical line).

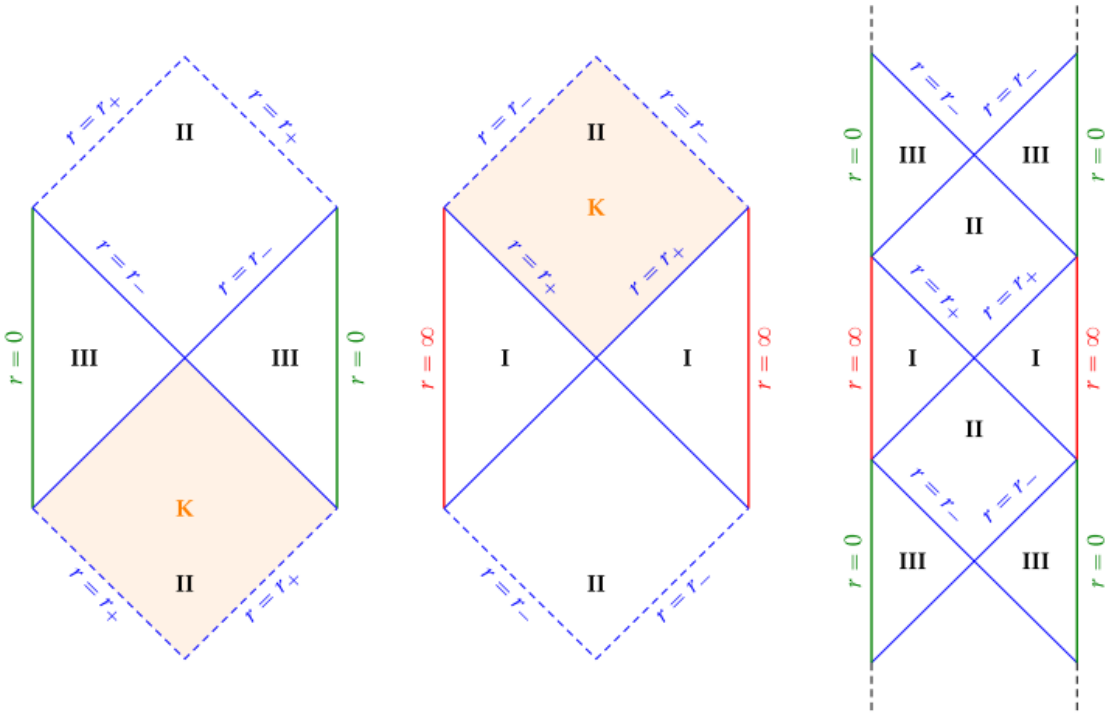

FIGURE 4.6: Penrose diagram for the rotating nonextremal BTZ black hole. The compactification is done on patch K^- (left) and K^+ (middle) separately. The full diagram (right) is then obtained by gluing the diagram across the intersections $K^+ \cap K^-$ (region II). Image credit: [147].

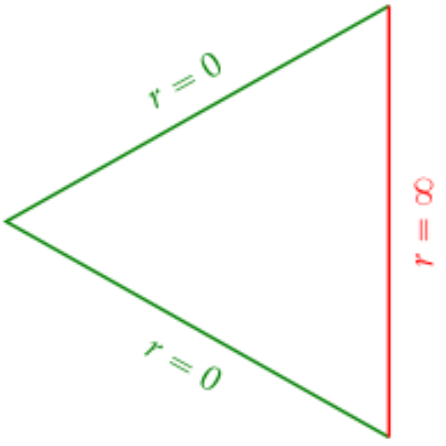

FIGURE 4.7: Penrose diagram for the vacuum BTZ solution ($M = J = 0$). Image credit: [147].

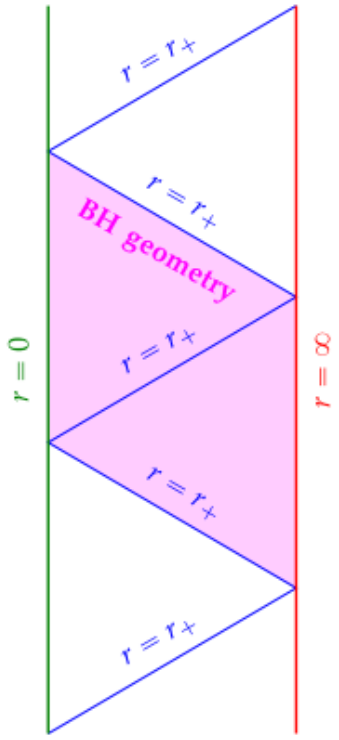

FIGURE 4.8: Penrose diagram for the extremal BTZ black hole ($M\ell = |J|$). Image credit: [147].

Finally, let us turn towards the extremal black hole, where $r_+ = r_-$. In particular, we can parametrize the metric in terms of r_+ only. The lapse is then

$$N^2 = \frac{(r^2 - r_+^2)^2}{r^2\ell^2}. \tag{4.90}$$

We again use U and V as in (4.88), where $r^\star$ is now

$$\mathrm{d}r^\star = N^{-2}\mathrm{d}r \iff r^\star = -\frac{r\ell^2}{2(r^2 - r_+^2)} + \frac{\ell^2}{4r_+}\ln\left|\frac{r - r_+}{r + r_+}\right|. \tag{4.91}$$

The conformal factor is then $\Omega^2 = N^2$. The conformal diagram is shown in Fig. 4.8. The horizon is represented by blue diagonal lines $p = \pi \pm q$ and $p = -\pi \pm q$, while the origin and infinity are represented by $p = \pm\pi$ (green and red vertical lines).

Chapter 5

Rigidly rotating perfect fluid star in $2+1$ dimensions

This chapter is taken from a paper submitted to Phys. Rev. D; see Ref. [1]. In this thesis, Appendix D was added, discussing the linear perturbation of the static solution with $\Lambda = 0$ and no rotation.

Aside from Appendix D, this chapter was written by Carsten Gundlach. The results of Secs 5.2.8.4 and 5.3.1, restricted to spherical symmetry, were independently found by me. I also independently checked all the results in this chapter.

5.1 Introduction

Classical Einstein gravity in $2+1$ spacetime dimensions may appear to be dynamically trivial because in $2+1$ dimensions the Weyl tensor is identically zero. This means that the full Riemann tensor is determined by the Ricci tensor, and so by the stress-energy tensor of the matter. Hence there are no gravitational waves, and the vacuum solution is locally unique: Minkowski in the absence of a cosmological constant Λ, de Sitter for $\Lambda > 0$, and anti-de Sitter for $\Lambda < 0$.

However, in 1992, Bañados, Teitelboim and Zanelli [58] (from now on, BTZ) noticed that $2+1$ dimensional vacuum Einstein gravity with $\Lambda < 0$ admits rotating black hole solutions that are in close analogy with the family of Kerr solutions in $3+1$ dimensions. They can be found easily by solving an axistationary ansatz for the metric, but their existence was unexpected because the metric has to be locally that of the $2+1$-dimensional anti-de Sitter solution (from now on, adS3). In fact, these metrics can be derived as highly non-trivial identifications of adS3 under an isometry [148].

We define the cosmological length scale

$$\ell := (-\Lambda)^{-\frac{1}{2}}. \tag{5.1}$$

and the dimensionless spin

$$\tilde{J} := \frac{J}{\ell}. \tag{5.2}$$

The gravitational mass M is already dimensionless in $2+1$ dimensions. A key difference to axistationary vacuum solutions in $3+1$ dimensions is the existence of a mass gap: while adS3 is given by the BTZ solution with parameters $M=-1$ and $\tilde{J}=0$, only the BTZ solutions with $M>0$ and $|\tilde{J}|<M$ represent black holes. Solutions with $-1<M<0$ and $|\tilde{J}|<-M$ represent point particles, similar to those for $\Lambda=0$ described in Ref. [160]. The status of those with $|\tilde{J}|>|M|$, which we call "overspinning", remains unclear.

The relevance of the BTZ solutions goes beyond vacuum because, roughly speaking, the vacuum exterior of any rotating isolated object must be a BTZ solution, even if the object itself is neither stationary nor axisymmetric.

More precisely, consider a region of spacetime with a timelike world tube removed. We can make this region simply connected by making a cut from the world tube to the outer boundary of the region. In the resulting simply connected region the spacetime must be adS3. However, when we make the region multiply connected again by identifying the two sides of the cut, this identification is parametrized by an isometry of adS3. The isometry group of adS3 is six-dimensional, but it was shown in Ref. [148] that the gauge-invariant part of the identification is characterized by only two parameters $(\tilde{J},M)$, parametrizing precisely the BTZ solutions. A region of spacetime with several world tubes removed requires one identification around each world tube, and so is described by a pair $(\tilde{J}_i,M_i)$ for each world tube representing a compact object.

By contrast, in $3+1$ dimensions, the exterior of a rotating object is not in general the Kerr solution, even if the object is axisymmetric and stationary. The argument we have just given does not apply because in more than $2+1$ dimensions a vacuum spacetime need not be Minkowski even locally. Put more physically, compact objects in $3+1$ dimensions can make not only their mass and spin, but also their internal structure felt in their vacuum exteriors through tidal forces and gravitational waves.

Perhaps the simplest example of axistationary matter solutions are rotating perfect fluid stars. In this chapter we examine if rigidly rotating perfect fluid stars exist in $2+1$ dimensions for reasonable equations of state. Here we define a star to be a perfect fluid solution with a regular center and finite mass and spin. We allow both for stars which have a surface at finite radius and are surrounded by vacuum, and stars which fill all of space but whose density falls off sufficiently rapidly. Given the existence of three different classes of BTZ solutions, we ask if point-particle, black hole and overspinning BTZ solutions can all be realized as exterior or asymptotic spacetimes of rigidly rotating perfect fluid stars.

Hence in this chapter, we solve the Einstein-fluid equations

$$G_{ab}+\Lambda g_{ab}=8\pi T_{ab} \tag{5.3}$$

with $\Lambda\leq 0$ and the perfect-fluid stress-energy tensor

$$T_{ab}=(\rho+p)u_a u_b+p g_{ab}, \tag{5.4}$$

making an ansatz of stationarity and axisymmetry. The vector field u^a is tangential to the fluid worldlines, with $u^a u_a = -1$, and p and ρ are the pressure and total energy density measured in the fluid rest frame. We formally assume a barotropic equation of state $p = p(\rho)$ given a priori. However, as we consider only axistationary solutions, where all variables depend only on the radial coordinate r, any solution with a given barotropic equation of state could also a posteriori be a interpreted as a solution of a two-parameter equation of state $p = p(\rho, s)$ (where s is, for example, the temperature), together with a given stratification $s = s(\rho)$. We set $c = G = 1$ throughout.

Cruz and Zanelli [162] have shown that static perfect fluid solution require a non-positive cosmological constant $\Lambda \leq 0$ and also studied in more detail the case of constant energy-density. The special cases of a polytropic equation of state with and without cosmological constant were also studied in Refs [163, 164]. In Ref. [165], García et al. have derived all static circularly symmetric spacetimes with $\Lambda \leq 0$. Rigidly rotating configurations were also studied [166, 167]. Cataldo [168] has found all axistationary rigidly rotating perfect fluid solutions in $2 + 1$ spacetime dimensions with $\Lambda < 0$. The total energy density ρ is specified a priori as a function of the radial coordinate $\rho(\bar{r})$. The metric and $p(\bar{r})$ are then given explicitly in terms of $\rho(\bar{r})$ and four parameters C, D, E and ω_0. The equation of state $p(\rho)$ is implied only a posteriori by comparing $p(\bar{r})$ and $\rho(\bar{r})$. We summarize these results in Sec. 5.2.1 below, followed by a list of questions that remained open: How does one find the general solution if not $\rho(\bar{r})$ but the equation of state $p(\rho)$ is given a priori? Which solutions have a regular center? Which solutions have a vacuum exterior solution, and what is its form? What are the BTZ mass and angular momentum of such star-like solutions?

To answer these questions, we translate Cataldo's solution into the standard $2 + 1$ form in terms of a lapse, shift and 2-metric, introduce an area radius coordinate, identify Cataldo's radial coordinate $\bar{r}$ with a certain integral over the equation of state, and identify the subset of solutions with a regular center, which as expected have only two free parameters (not four). We give expressions for M and $\tilde{J}$ in terms of these two parameters and certain integrals involving only the equation of state.

Our solutions for a general equation of state are in implicit form. They can be made explicit by evaluating an integral, inverting the resulting function, and evaluating another integral. As already obtained by Cataldo, this can be done for the linear equation of state $p = \kappa\rho$ and the "polytropic" equation of state $p = K\rho^k$. As a further example, we also consider the equation of state $p = \kappa(\rho - \rho_s)$ for $\rho_s > 0$.

5.2 General equation of state

5.2.1 Rigidly rotating axistationary perfect fluid solutions

Cataldo [168] has found axisymmetric, stationary, rigidly rotating perfect fluid solutions of the Einstein equations in comoving coordinates, defined by $u^a \propto (\partial_t)^a$, for a certain choice of

radial coordinate, in the form

$$\mathrm{d}s^2 = -\left(\bar{r}\,\mathrm{d}\bar{t} + \omega \mathrm{d}\theta\right)^2 + h^{-1}\,\mathrm{d}\bar{r}^2 + h\,\mathrm{d}\theta^2, \tag{5.5}$$

where

$$\omega(\bar{r}) := \frac{\omega_0}{\bar{r}} + E\bar{r}, \tag{5.6}$$

$$h(\bar{r}) := C - \Lambda\bar{r}^2 + D\bar{r} + \frac{\omega_0^2}{\bar{r}^2} + 16\pi\bar{f}(\bar{r}), \tag{5.7}$$

$$\bar{f}(\bar{r}) := \int_{\bar{r}_0}^{\bar{r}} \bar{r}'\rho(\bar{r}')\,\mathrm{d}\bar{r}' - \bar{r}\int_{\bar{r}_0}^{\bar{r}} \rho(\bar{r}')\,\mathrm{d}\bar{r}', \tag{5.8}$$

$$p(\bar{r}) := \frac{D}{16\pi\bar{r}} - \frac{1}{\bar{r}}\int_{\bar{r}_0}^{\bar{r}} \rho(\bar{r}')\,\mathrm{d}\bar{r}'. \tag{5.9}$$

Here $\bar{r}_0$ is an arbitrary integration limit. (In solutions with a regular center, we will later choose it to correspond to the center.) These solutions are parametrized by the function $\rho(\bar{r})$ and the constants ω_0, E, C and D. (We denote the time and radial coordinates of [168] by $\bar{t}$ and $\bar{r}$ to distinguish them from rescaled coordinates t and r that we introduce below, and the area radius, which we will denote by R.)

At this point, it appears that the density ρ has to be specified as a function of the radial coordinate $\bar{r}$, which only afterwards implies an equation of state $p(\rho)$ through the expression (5.9) for $p(\bar{r})$. This issue was partly addressed in Ref. [168] by deriving explicit solutions for two simple barotropic equations of state, but it remained unclear if and how solutions can be obtained for an arbitrary equation of state $p(\rho)$ given a priori.

It also remained unclear which solutions have a regular center. This issue was partly addressed in Ref. [168] by giving explicit solutions with a regular center for the above-mentioned equations of state. There was, however, no systematic construction of all solutions with a regular center for an arbitrary given equation of state in terms of precisely two free parameters that control the mass and spin of the star. Also lacking was a criterion on the equation of state for a solution with a regular center to either have a vacuum exterior, or to be asymptotically adS3 with finite BTZ mass M and spin J.

In the remainder of this chapter, we resolve all these questions.

5.2.2 The equation of state

We first clarify the role of the equation of state. Differentiating (5.9), we obtain

$$\bar{r}\frac{\mathrm{d}p}{\mathrm{d}\bar{r}} + p + \rho = 0. \tag{5.10}$$

Solving this separable ODE by integration, we find

$$\ln\frac{\bar{r}}{\bar{r}_0} = -\int_{p_0}^{p(\bar{r})} \frac{\mathrm{d}p}{p+\rho(p)} = -\int_{\rho_0}^{\rho(\bar{r})} \frac{p'(\rho)\,\mathrm{d}\rho}{p(\rho)+\rho}, \tag{5.11}$$

where $\rho_0 := \rho(\bar{r}_0)$ is the density at $\bar{r}_0$ and $p_0 := p(\rho_0)$ the corresponding pressure, given by the equation of state $p(\rho)$. For stars, we will later choose $\bar{r}_0$ as the value of $\bar{r}$ at the regular center, so that p_0 is the central pressure.

Unless stated otherwise, we assume throughout that the equation of state $p(\rho)$ is at least continuous and piecewise continuously differentiable, with $0 \leq p'(\rho) < 1$, and where $p'(\rho) = 0$ is allowed only at $p = 0$. As a consequence, the sound speed $\sqrt{p'(\rho)}$ is real and less than the speed of light, and the inverse equation of state $\rho(p)$ also exists as a continuous function that is piecewise once differentiable for $p > 0$. We allow for the possibility that $p(\rho_s) = 0$ for some $\rho_s \geq 0$.

In obtaining (5.10) by differentiating (5.9) we have lost the constant D. To find its value, we evaluate (5.9) at $\bar{r}_0$, obtaining

$$D = 16\pi \bar{r}_0 p_0. \tag{5.12}$$

5.2.3 Standard form of the metric

For further analysis, we rearrange the metric in the usual $2+1$ form, and with the 2-metric expressed in terms of an area radius R, that is, as

$$\mathrm{d}s^2 = -\bar{\alpha}^2\,\mathrm{d}\bar{t}^2 + a^2\left(\frac{\mathrm{d}R}{\mathrm{d}\bar{r}}\right)^2\mathrm{d}\bar{r}^2 + R^2\,(\mathrm{d}\theta + \bar{\beta}\,\mathrm{d}\bar{t})^2, \tag{5.13}$$

where a, $\bar{\alpha}$, $\bar{\beta}$ and R are all functions of $\bar{r}$. Hence $\bar{\alpha}$ is the lapse, $\bar{\beta}$ the shift in the angular direction, both with respect to the time coordinate $\bar{t}$, $g_{\theta\theta} = R^2$ defines the area radius R as the length of the Killing vector ∂_θ (and hence R is a scalar), and $g_{RR} = a^2$ if we use R as the radial coordinate. We read off

$$\begin{aligned}
R^2 &= h - \omega^2, && (5.14)\\
\bar{\beta} &= -\frac{\bar{r}\omega}{R^2}, && (5.15)\\
\bar{\alpha}^2 &= \bar{r}^2 + R^2\bar{\beta}^2, && (5.16)\\
a^2 &= \frac{1}{\left(\frac{\mathrm{d}R}{\mathrm{d}\bar{r}}\right)^2 h} = \frac{4R^2}{\left(\frac{\mathrm{d}R^2}{\mathrm{d}\bar{r}}\right)^2 h} && (5.17)
\end{aligned}$$

as functions of $\bar{r}$. We see that $\bar{t}$ and $\bar{r}$ have nonstandard dimensions, namely length^{-1} and length^2, respectively. We use $\bar{r}_0$ to define a length scale

$$s := \sqrt{\bar{r}_0}, \tag{5.18}$$

and then define

$$t := s^2\,\bar{t}, \qquad r := \frac{\bar{r}}{s}, \tag{5.19}$$

which have the usual dimension length. We correspondingly rescale the lapse and shift as

$$\alpha := \frac{\bar{\alpha}}{s^2}, \qquad \beta := \frac{\bar{\beta}}{s^2}. \tag{5.20}$$

The metric now takes the form

$$\mathrm{d}s^2 = -\alpha^2\,\mathrm{d}t^2 + a^2\left(\frac{\mathrm{d}R}{\mathrm{d}r}\right)^2\mathrm{d}r^2 + R^2\,(\mathrm{d}\theta + \beta\,\mathrm{d}t)^2. \tag{5.21}$$

We introduce the dimensionless cosmological constant and spin parameters

$$\lambda := s\sqrt{-\Lambda} \geq 0, \tag{5.22}$$
$$\Omega := \frac{\omega_0}{s^3}, \tag{5.23}$$

and their combination

$$\mu := \lambda^2 - \Omega^2. \tag{5.24}$$

Note that $\lambda \ll 1$ corresponds to the length scale s being small compared to the cosmological length scale ℓ, but also, equivalently, to the cumulative effects of the cosmological constant being small over length scales of size s. We will in general consider $\lambda > 0$, but at one point also $\lambda = 0$, interpreted as $\Lambda = 0$. Otherwise, we always express λ in terms of the two independent parameters μ and Ω.

To write all our equations in fully non-dimensional form, we introduce the dimensionless radial coordinate y and dimensionless area radius x defined by

$$y := \frac{r}{s}, \qquad x := \frac{R}{s}. \tag{5.25}$$

For a given equation of state $p(\rho)$ and reference density ρ_0, the relation between the density ρ and the dimensionless radial coordinate y is

$$y(\rho_0;\rho) = \exp\left(-\int_{\rho_0}^{\rho}\frac{p'(\tilde\rho)\,\mathrm{d}\tilde\rho}{p(\tilde\rho)+\tilde\rho}\right), \tag{5.26}$$

or equivalently

$$y(p_0;p) = \exp\left(-\int_{p_0}^{p}\frac{\mathrm{d}\tilde p}{\tilde p + \rho(\tilde p)}\right), \tag{5.27}$$

where ρ_0 and $p_0 = p(\rho_0)$ are the density and pressure at $y = 1$, $p'(\rho) := \mathrm{d}p/\mathrm{d}\rho$, and $\rho(p)$ is the inverse equation of state, compare also Eq. (50) of Ref. [167]. We define the dimensionless function $f(y) := s^{-2}\bar f(\bar r)$, that is

$$f(y) = s^2\left(\int_1^y \rho(\tilde y)\tilde y\,\mathrm{d}\tilde y - y\int_1^y \rho(\tilde y)\,\mathrm{d}\tilde y\right). \tag{5.28}$$

We primarily use s rather than ℓ to adimensionalize all other variables and parameters in order to keep the limit $\Lambda = 0$ regular. However, when we want to compare different solutions with the same $\Lambda < 0$, it is more natural to express the dimensionful quantities R, ρ and p in terms of ℓ, using

$$s = \lambda\ell = \sqrt{\mu+\Omega^2}\,\ell. \tag{5.29}$$

In particular we have

$$R = \ell\sqrt{\mu + \Omega^2}\, x \tag{5.30}$$

and

$$s^2\rho = (\mu + \Omega^2)\ell^2\rho. \tag{5.31}$$

5.2.4 Local mass and angular momentum

For an arbitrary time-dependent axisymmetric spacetime in $2+1$ spacetime dimensions, regardless of matter content, there exist two conserved currents $\nabla_a j^a_{(J)} = 0$ and $\nabla_a j^a_{(M)} = 0$: the conserved current due to the angular Killing vector, and a second, more mysterious, one that generalizes the Misner-Sharp mass that exists for spherical symmetry in any dimension, to a conserved mass that exists for axisymmetry in $2+1$ dimensions only. In terms of the metric (5.21), the corresponding conserved quantities are given by

$$J = \frac{R^3 \frac{\partial\beta}{\partial r}}{\frac{\mathrm{d}R}{\mathrm{d}r} a\alpha}, \tag{5.32}$$

$$M = \frac{R^2}{\ell^2} + \frac{J^2}{4R^2} - \frac{1}{a^2}. \tag{5.33}$$

Note that these expressions hold in the axisymmetric but time-dependent case. In the axistationary case that we consider here, $\partial\beta/\partial r$ simply becomes $d\beta/dr$. In any vacuum region, M and J are constant with values equal to the BTZ parameters of the same name, that is, the Einstein equations give $M_{,r} = M_{,t} = J_{,r} = J_{,t} = 0$. In particular, for constant (J, M), the polar-radial metric (5.21) takes the form

$$c_0^2\alpha^2 = -M + \frac{R^2}{\ell^2} + \frac{J^2}{4R^2}, \tag{5.34}$$

$$a^2 = \frac{1}{c_0^2\alpha^2}, \tag{5.35}$$

$$c_0\beta = -\frac{J}{2R^2} + \beta_0. \tag{5.36}$$

We can further set $c_0 = 1$ by rescaling t by the constant factor c_0, and $\beta_0 = 0$ by a rigid rotation of the coordinate system that corresponds to shifting θ by $\beta_0 t$. The result is the standard form of the BTZ metric first given in [58].

5.2.5 Solutions with a regular center

We now demand that the solution has a regular center at some value of the radial coordinate $\bar{r}$. Without loss of generality we choose the center to be at the reference radius $\bar{r}_0$, so that $R(\bar{r}_0) = 0$ and $\bar{f}(\bar{r}_0) = (\mathrm{d}\bar{f}/\mathrm{d}\bar{r})(\bar{r}_0) = 0$. With these conditions, (5.7) can be solved for the parameter C, which is now replaced as a free parameter by $\bar{r}_0$.

We also demand that there is no conical singularity at the center, $a(\bar{r}_0) = 1$. However, a necessary condition for this limit to be finite, given that $R(\bar{r}_0) = 0$ (by definition) and $(\mathrm{d}R^2/\mathrm{d}\bar{r})(\bar{r}_0) \neq 0$ (by observation) is that $h(\bar{r}_0) = 0$, and hence that $\omega(\bar{r}_0) = 0$. This last

condition can be solved for the parameter E. Applying l'Hôpital's rule, we then have

$$\lim_{\bar{r}\to\bar{r}_0} a = \lim_{\bar{r}\to\bar{r}_0} \frac{4}{\frac{\mathrm{d}R^2}{\mathrm{d}\bar{r}}\frac{\mathrm{d}h}{\mathrm{d}\bar{r}}} = \frac{4}{\frac{\mathrm{d}h}{\mathrm{d}\bar{r}}(\bar{r}_0)^2}, \tag{5.37}$$

and so we need $(\mathrm{d}h/\mathrm{d}\bar{r})(\bar{r}_0) = 2$, which can be solved for D. The result, expressed for brevity in terms of our dimensionless parameters μ and Ω and reference scale s, is

$$E = -\frac{\Omega}{s}, \tag{5.38}$$
$$C = s^2(\mu - 2(1+\Omega^2)), \tag{5.39}$$
$$D = 2(1-\mu). \tag{5.40}$$

For a given barotropic equation of state, the general solution with a regular center now has two dimensionless free parameters μ, Ω, which govern, roughly speaking, the mass and spin of the star. This is the number of free physical parameters one would expect after imposing regularity at the center. Note that, for fixed Λ, s is given in terms of μ and Ω by (5.29), and from (5.12) and (5.40), the central pressure is given in terms of μ by

$$p_0 = \frac{1-\mu}{8\pi s^2}, \tag{5.41}$$

or equivalently

$$p_0 = \frac{1-\mu}{8\pi(\mu+\Omega^2)\ell^2}. \tag{5.42}$$

The expression for the metric coefficients, for an arbitrary equation of state, can be written concisely as

$$x^2 = \mu(y-1)^2 + 2(y-1) + 16\pi f, \tag{5.43}$$
$$\alpha^2 = y^2 + \frac{\Omega^2(y^2-1)^2}{x^2}, \tag{5.44}$$
$$a^2 = \frac{4y^2}{\left(\frac{\mathrm{d}x^2}{\mathrm{d}y}\right)^2 \alpha^2}, \tag{5.45}$$
$$\beta = \frac{\Omega(y^2-1)}{sx^2}. \tag{5.46}$$

where x, a, α and β are all functions of y. Note that $y \geq 1$ with $y = 1$ at the regular center. Recall that $f(y)$ was defined in Eq. (5.28), where $\rho(y)$ is given implicitly by inverting the integral (5.26), with the integration limit $\rho_0 = \rho(p_0)$ defined in terms of our free parameters μ and Ω by Eq. (5.42).

Eqs. (5.26), (5.28), (5.42) and (5.43)-(5.46) together fully specify our solutions, and can be taken as the starting point for the analysis that follows.

For an analytic equation of state, $f(y)$ is analytic with $f(y) = O(y-1)^2$ near the center, and hence

$$x^2 = 2(y-1) + O(y-1)^2, \tag{5.47}$$

$$\beta = \frac{\Omega}{s} + O(y-1) = \frac{\Omega}{\sqrt{\mu + \Omega^2}\,\ell} + O(y-1) \tag{5.48}$$

near the center. We note for later use that, while β is proportional to Ω for small Ω, it remains finite everywhere as $|\Omega| \to \infty$.

We obtain a fully explicit solution in the radial coordinate y if and only if the integral (5.26) can be evaluated for $y(\rho_0; \rho)$, this can then be inverted to give $\rho(\rho_0; y)$, and if the integral (5.28) can then also be evaluated. Furthermore, we obtain a fully explicit solution in terms of the area radius R if and only if Eq. (5.43) can also be inverted to give $y(x)$.

However, we do not need explicit solutions to establish analyticity of the solution in the area radius R. In an open interval of ρ where the equation of state $p(\rho)$ is analytic and $p+\rho > 0$, Eq. (5.26) defines y as a monotonically decreasing analytic function of ρ in this interval of ρ, and so $\rho(y)$ exists and is analytic in the corresponding interval of y. It follows that f is an analytic function of y in this interval. Hence a, α and β are all analytic functions of y at least for $y > 1$. A closer look shows that they are analytic also at $y = 1$, which corresponds to $x = 0$. Moreover, x^2 is an analytic function of y for $y \geq 1$, and so implicitly ρ, p, a, α, β are all analytic functions of x^2. In other words, they are even analytic functions of R for $R \geq 0$. For typical equations of state, analyticity breaks down at the surface of the star where $p = 0$.

By a standard argument, analyticity in R^2 implies that if we rewrite the metric in terms of Cartesian coordinates $X := R\cos\theta$, $Y := R\sin\theta$, all coefficients of the metric in the coordinates (t, X, Y) are analytic functions of X and Y (and independent of t), including at the center $X = Y = 0$.

The expressions for the local mass and angular momentum as functions of y are

$$M = (\mu + 2\Omega^2)x^2 - \frac{1}{4}\left(\frac{\mathrm{d}x^2}{\mathrm{d}y}\right)^2 - \frac{\Omega^2(y^2-1)\frac{\mathrm{d}x^2}{\mathrm{d}y}}{y}, \tag{5.49}$$

$$J = s\Omega\left(2x^2 - \frac{(y^2-1)\frac{\mathrm{d}x^2}{\mathrm{d}y}}{y}\right), \tag{5.50}$$

or equivalently

$$\tilde{J} = \sqrt{\mu + \Omega^2}\,\Omega\left(2x^2 - \frac{(y^2-1)\frac{dx^2}{dy}}{y}\right). \tag{5.51}$$

These are also even analytic functions of R.

5.2.6 The adS3 and test fluid cases

For $\mu = 1$ the central pressure is zero, and so this must correspond to the adS3 solution. Indeed, with $\mu = 1$ the metric takes the form

$$x^2 = y^2 - 1, \tag{5.52}$$
$$\alpha^2 = (1+\Omega^2)y^2 - \Omega^2, \tag{5.53}$$
$$a^2 = \alpha^{-2}, \tag{5.54}$$
$$\beta = s^{-1}\Omega =: \beta_0, \tag{5.55}$$

and we have $M = -1$ and $J = 0$. Hence this is the adS3 solution in a rigidly rotating coordinate system, with constant angular velocity β_0. In the vacuum solution, β_0 has no physical significance, and can be set to zero.

Expanding in $\mu - 1$, to leading order we obtain the test fluid limit, in which a stationary, rigidly rotating, fluid configuration is held together only by the cosmological constant (as well as being pulled apart by rotation), but in which its self-gravity can be ignored. The metric is that of adS3, but in a coordinate system that rotates with the fluid. As in the self-gravitating case, the equation of state and the central density ρ_0 implicitly determine a function $\rho = \rho(\rho_0; y)$ through Eq. (5.26). In the test fluid case, from (5.52), y is given in terms of the area radius R, the cosmological constant Λ and the constant angular velocity β_0 as

$$y^2 = 1 + x^2 = 1 + R^2(-\Lambda - \beta_0^2), \tag{5.56}$$

where we have used (5.22), (5.24) with $\mu = 1$ and (5.55) to eliminate s. Hence we have an implicit expression $\rho(R)$ for any rigidly rotating test fluid solution, for arbitrary central density ρ_0 and arbitrary constant angular velocity β_0 (with respect to the Killing vector ∂_t), given a cosmological constant $\Lambda < 0$ and equation of state.

5.2.7 Star-like solutions

We now look for solutions in which either $p = 0$ occurs at finite radius or $p \to 0$ and $\rho \to 0$ sufficiently rapidly as $R \to \infty$ so that the solution has finite M and J. We shall call such solutions "stars". Without any attempt at rigor, we classify the possibilities by assuming that the fluid is polytropic at low pressure, that is

$$p \sim \rho^k \quad \text{as} \quad p \to 0, \tag{5.57}$$

for some $k \geq 1$. We note that for $k < 1$, the sound speed $\sqrt{p'(\rho)}$ diverges as $\rho \to 0$. We therefore disregard this range as unphysical.

From (5.42), we require $\mu \leq 1$ for the central pressure to be non-negative, and from (5.43) we further require $\mu \geq 0$ for $x(y)$ to be a monotonically increasing function for all y, in particular at large y. Stars therefore exist only with $\Lambda < 0$, and for $0 \leq \mu \leq 1$. Physically, from (5.24), $\mu > 0$ means that the Hubble acceleration is centripetal ($\Lambda < 0$) and larger than the

centrifugal acceleration due to the rigid rotation ($\lambda^2 > \Omega^2$). Both the Hubble and the centrifugal acceleration depend on radius in the same way, and so this is true either for all y or for none.

5.2.7.1 Stars with a surface

From (5.27), we see that the solution has a surface $p(y_\star) = 0$ at some finite coordinate radius $y_\star$ and finite area radius $x_\star$ if and only if the integral

$$y_\star(p_0) := y(p_0; 0) = \exp \int_0^{p_0} \frac{\mathrm{d}p}{p + \rho(p)}. \tag{5.58}$$

converges. Note that in this case $y_\star(0) = 1$. In the approximation (5.57) this is the case for $k > 1$. The limiting case $k = \infty$ can be interpreted as a fluid where $\rho = \rho_s > 0$ is finite at $p = 0$. (One may think of such a perfect fluid as a liquid, rather than a gas).

In the exterior $y > y_\star$, the solution must be equal to a BTZ solution with constant M and J. To verify this, we note that in the exterior, (5.28) reduces to

$$16\pi f = m - 2(1 - \mu)y, \tag{5.59}$$

where we have defined the integrated fluid mass

$$m := 16\pi s^2 \int_1^{y_\star} \rho\, y\, \mathrm{d}y. \tag{5.60}$$

We have identified the coefficient of y in (5.59) as $-D$ by demanding that (5.9) holds in the vacuum region $p = 0$, and have then used (5.40) to eliminate D.

As $y \geq 1$ in the integral in (5.60), we have

$$m \geq 16\pi s^2 \int_1^{y_\star} \rho\, \mathrm{d}y = 2(1 - \mu), \tag{5.61}$$

where to obtain the last equality we have evaluated (5.9) in the vacuum region $p = 0$ and used (5.40).

To clarify what free parameters determine m, we use (5.27) to eliminate y and (5.41) to eliminate s in favor of the central pressure p_0, and then (5.42) to in turn express p_0 in terms our free parameters μ and Ω. We obtain

$$m = 2(1 - \mu)\, I\left(\frac{1 - \mu}{8\pi(\mu + \Omega^2)\ell^2}\right), \tag{5.62}$$

where

$$I(p_0) := \int_0^{p_0} \exp\left(-2\int_{p_0}^{p} \frac{\mathrm{d}\tilde{p}}{\tilde{p} + \rho(\tilde{p})}\right) \frac{\rho(p)}{p_0} \frac{\mathrm{d}p}{p + \rho(p)}. \tag{5.63}$$

So in general m depends on μ and Ω^2, as well as of course on the equation of state. Note that from (5.61), we have $I(p_0) \geq 1$.

To simplify the expressions that follow, we define the auxiliary quantity

$$A(\mu,\Omega) := m(\mu,\Omega) + \mu - 2. \tag{5.64}$$

By definition, $A(1,\Omega) = -1$ in the vacuum or test fluid case, where $m = 0$. From (5.61), we have

$$A + \mu \geq 0. \tag{5.65}$$

With f given by (5.59), the metric coefficients in the vacuum exterior are given by (5.43)-(5.46) as

$$x^2 = \mu y^2 + A, \tag{5.66}$$

$$\alpha^2 = y^2 + \frac{\Omega^2(y^2-1)^2}{\mu y^2 + A}, \tag{5.67}$$

$$a^2 = \frac{1}{\mu^2 \alpha^2}, \tag{5.68}$$

$$\beta = \frac{\Omega(y^2-1)}{s(\mu y^2 + A)}. \tag{5.69}$$

Substituting (5.66) into the expressions (5.49) and (5.50) for M and J, we obtain the constant values

$$M = M_{\rm tot} := A\mu + 2(A+\mu)\Omega^2, \tag{5.70}$$

$$\tilde{J} = \tilde{J}_{\rm tot} := 2\sqrt{\mu + \Omega^2}(A+\mu)\Omega, \tag{5.71}$$

or equivalently

$$J_{\rm tot} = 2s(A+\mu)\Omega. \tag{5.72}$$

It is then easy to verify that the exterior metric (5.66)-(5.69), is (5.34)-(5.36), generally with $c_0 \neq 1$ and $\beta_0 \neq 0$.

5.2.7.2 Stars without a surface

If the integral (5.58) diverges but the integral (5.60) with $y_\star = \infty$ converges to a finite value of m, the star has no surface but finite mass.

Taking the limit of $M(y)$ and $J(y)$ as $y \to \infty$, we again obtain the finite total values given by (5.70) and (5.72). The metric is now asymptotic (rather than strictly equal) to the BTZ metric (5.21),(5.34)-(5.36).

In these stars without a sharp surface, we can nevertheless roughly identify a central region where self-gravity of the star is important and M and $|J|$ still increase, and an outer region, or stellar atmosphere, where M and J are essentially constant and the fluid is essentially a test fluid on the BTZ spacetime with parameters $M_{\rm tot}$ and $J_{\rm tot}$.

In our approximation (5.57) this happens in the marginal case $k = 1$, we need to also specify the constant of proportionality, as the dimensionless parameter κ in

$$p \simeq \kappa\rho \quad \text{as} \quad p \to 0, \tag{5.73}$$

for some $0 < \kappa < 1$. The pressure and density fall off as $\rho \sim p \sim y^{-1-\frac{1}{\kappa}}$, and so once again m is finite, but there is now no surface at finite radius, and the metric is only asymptotically BTZ, with $y_\star = \infty$. The sound speed is also less than the the speed of light for $0 < \kappa < 1$.

5.2.7.3 Non-stars

When not only $y_\star$ but m diverges, $f(y)$ grows faster than y as $y \to \infty$. In the approximation (5.57), this is the case for $1/2 \leq k < 1$, when $\rho \sim y^{-\frac{1}{k}}$ and $f \sim y^{2-(1/k)}$ as $y \to \infty$. However, we have already ruled out $k < 1$ on the grounds that the sound speed $\sqrt{p'(\rho)}$ diverges at the surface. The expressions for $M(y)$ and $J(y)$ also diverge, and so the spacetime is not asymptotically BTZ. Such solutions do not describe stars. Recall again that we have already ruled out $k < 1$ on the grounds of diverging sound speed.

5.2.8 The manifold of solutions

In contrast to $3 + 1$ and higher dimensions, the vacuum exterior metric, or the asymptotic metric at infinity, of a rotating star is given by a BTZ metric. It is therefore of interest what region in the $(\tilde{J}, M)$ plane is covered by possible stellar exterior solutions. Recall that for stars the parameters μ and Ω can take any values in the strip

$$0 < \mu \leq 1, \quad -\infty < \Omega < \infty. \tag{5.74}$$

In the following, we suppress the suffix "tot" for brevity, and for the rest of this section, M and $\tilde{J}$ always denote the total mass and spin of the spacetime, measured at infinity.

The manifold of solutions is uniquely parametrized by (Ω, μ). However, if we are interested more in the values of $(\tilde{J}, M)$, we can present the solution manifold as a hypersurface in $(\tilde{J}, M, \mu)$ space. The case of the linear equation of state $p = \kappa\rho$ is non-generic in that A is a function of μ only, but it, and in particular the value $\kappa = 1/2$, can serve as a concrete illustration of the general considerations presented below. The solution manifold parametrized by (Ω, μ) for the equation of state $p = \rho/2$ is shown in Fig. 5.1. The same solution manifold embedded in $(\tilde{J}, M, \mu)$ space is shown in Fig. 5.2, and the projection of this embedding down into the $(\tilde{J}, M)$ plane in Fig. 5.3. We stress that the following arguments hold for all equations of state that admit star-like solutions, and so these figures apply qualitatively to all equations of state.

5.2.8.1 Boundary $\mu = 1$ of solution space

We have already seen that $\mu = 1$ at finite Ω (the thick black line in Fig. 5.1) corresponds to a rotating test fluid on the adS3 spacetime with $M = -1$ and $\tilde{J} = 0$. However, taking the

simultaneous limit $\mu \to 1_-$, $\Omega \to \pm\infty$ of (5.70) and (5.71) such that

$$\mu = 1 - \frac{\tilde{q}}{\Omega^2} \tag{5.75}$$

for some fixed constant $\tilde{q} > 0$, we have $s \to \infty$ and $p_0 \to 0$ and so, for finite $I(0)$, we obtain

$$m \simeq 2(1-\mu)\, I(0), \tag{5.76}$$

giving

$$A + \mu \simeq \frac{q}{\Omega^2}, \quad q := 2[I(0) - 1]\tilde{q}, \tag{5.77}$$

and hence two one-parameter families of solutions with

$$M = -1 + q, \quad \tilde{J} = \pm q. \tag{5.78}$$

From (5.65), we have that $q \geq 0$. See the blue region in Fig. 5.1 as $\Omega \to \pm\infty$, and the thick dashed black line in Fig. 5.2. In this limit, the fluid is infinitely dilute but infinitely extended. Note that even though $\Omega \to \infty$, the angular velocity β is finite everywhere. The integrated fluid rest mass m vanishes, but $M > -1$. Intuitively, this nontrivial gravitational mass comes from rotational energy.

We now show, assuming an analytic equation of state for small $p > 0$, that $I(0) = 1$ if the star has a surface at finite radius. To see this, we write

$$I(p_0) = \int_0^{p_0} y^2(p_0; p) \frac{\rho}{p_0} \frac{\mathrm{d}p}{p+\rho} \geq 0. \tag{5.79}$$

We can bound $1 \leq y^2 \leq y_\star^2$ in the integrand, and so

$$\frac{1}{p_0}\int_0^{p_0} \frac{\rho}{p+\rho}\mathrm{d}p \leq I(p_0) \leq \frac{y_\star^2}{p_0}\int_0^{p_0} \frac{\rho}{p+\rho}\mathrm{d}p. \tag{5.80}$$

From $y_\star(0) = 1$ (as noted above) and the squeeze theorem, we then have

$$I(0) = \lim_{p_0 \to 0} \frac{1}{p_0}\int_0^{p_0} \frac{\mathrm{d}p}{1 + \frac{p}{\rho}}. \tag{5.81}$$

From causality, p/ρ must remain bounded as $p \to 0$. If in fact $p/\rho \to 0$ as $p \to 0$, we have $I(0) = 1$.

In the other case, where $p/\rho \to \kappa$ remains finite as $p \to 0$, the surface of the star is at infinity and so we cannot rely on (5.81). However, one can see by explicit calculation that $I(0) = 1/(1-\kappa)$ for this case, which is finite, see also (5.109) below.

5.2.8.2 Boundary $\mu = 0$ of solution space

If $A(0, \Omega)$ is finite, the boundary $\mu = 0$ of solution space corresponds to a family of solutions with

$$M = 2A(0,\Omega)\,\Omega^2, \quad \tilde{J} = 2A(0,\Omega)\,|\Omega|\,\Omega, \tag{5.82}$$

Note that $A(0,\Omega) \geq 0$ from (5.65), and so these solutions obey $M \geq 0$ with $|\tilde{J}| = M$. See the thick blue line in Figs. 5.1 and 5.2.

5.2.8.3 Second family of critically spinning solutions

There is a second family of solutions with $|\tilde{J}| = |M|$, over a finite range of M including both positive and negative values of M, namely

$$\Omega = \pm\Omega_c(\mu), \tag{5.83}$$

where $\Omega_c(\mu)$ is defined by solving

$$A^2 = 4(A+\mu)\Omega^2 \tag{5.84}$$

for Ω^2, given μ. Along these curves, parametrized by μ, we have

$$|M| = |\tilde{J}| = A\left(\mu + \frac{A}{2}\right). \tag{5.85}$$

The range $1 > \mu > 0$ corresponds to the range $-1/2 < M < M_0$. Here

$$M_0 := 8\Omega_0^2, \tag{5.86}$$

where Ω_0 is the positive solution of

$$A(0,\Omega_0) = 4\Omega_0^2. \tag{5.87}$$

[Note that therefore $\Omega_0 = \Omega_c(0)$.] See the thick green lines in Figs. 5.1 and 5.2. The two curves intersect at $M = \tilde{J} = 0$, which corresponds to $\mu = \mu_c$ defined by

$$A(\mu_c, 0) = 0. \tag{5.88}$$

This always has a solution in the range $0 \leq \mu_c < 1$ because $A(\mu,\Omega)$ is continuous with $A(0,\Omega) \geq 0$ and $A(1,\Omega) = -1$. [We assume without proof that there is only one solution.] At their upper ends, the two curves are asymptotic to $\mu = 1$ as $\Omega \to \pm\infty$ in the (Ω,μ) strip, but in the $(\tilde{J}, M)$ plane they end at the finite points $M = -1/2$, $\tilde{J} = \pm 1/2$. At their lower ends they intersect $\mu = 0$ at finite $|\Omega| = \Omega_0$, corresponding to $|\tilde{J}| = M = M_0 > 0$.

5.2.8.4 Double cover of a region in the $(\tilde{J}, M)$ plane

As there are two solutions for $M = |\tilde{J}|$ for $0 \leq M < M_0$, by continuity there must be a region of the $(\tilde{J}, M)$ plane that is doubly covered by the manifold of solutions. As the solutions $M = |\tilde{J}|$ corresponding to $\mu = 0$ lie on one boundary of the solution manifold, they also form one boundary of the doubly-covered region [in (Ω,μ) and $(\tilde{J}, M)$, respectively]. The other boundary of the doubly-covered region in the $(\tilde{J}, M)$ plane occurs where the solution

manifold of Fig. 5.2 folds over. This occurs where

$$\left|\frac{\partial(\tilde{J},M)}{\partial(\Omega,\mu)}\right| = 0, \tag{5.89}$$

which is equivalent to

$$2(A+\mu)(\mu A_{,\mu} + A - 4\Omega^2) + (A - 4\Omega^2 - 3\mu)\Omega A_{,\Omega} = 0. \tag{5.90}$$

This implicitly defines a curve

$$\Omega = \pm\Omega_r(\mu), \quad 0 < \mu < \mu_r, \tag{5.91}$$

where μ_r is defined by $\Omega_r(\mu_r) = 0$, giving

$$\mu_r A_{,\mu}(\mu_r, 0) + A(\mu_r, 0) = 0. \tag{5.92}$$

[Note that $\Omega_r(0) = \Omega_0$. We assume without proof that there is only one such curve, that is, the solution manifold is not folded over more than double.]

In fluid parameter space (Ω, μ), the doubly-covered region lies between the curves (5.83) for $0 < \mu < \mu_c$ (the lower part of the two green curves in Fig. 5.1) and the curve $\mu = 0$ for $-\Omega_0 < \Omega < \Omega_0$ (part of the blue line). It is divided into two halves by (5.91) (the red curve). All three curves intersect at the two points $\mu = 0$, $\Omega = \pm\Omega_0$. Pairs of points from those two halves of the doubly-covered region have the same values of M and $\tilde{J}$.

In BTZ parameter space $(\tilde{J}, M)$, the doubly covered region lies between $|\tilde{J}| = M$ for $0 < M < M_0$ (corresponding to both the blue and green curves in Fig. 5.2), and the red curve

$$\Omega = \pm\tilde{\Omega}_r(M), \quad 0 < M < M_0, \tag{5.93}$$

which is given implicitly by (5.70) and (5.71) with (5.91). The double cover becomes clearer by comparing Fig. 5.2 with its top view, Fig. 5.3. The corner points at $\mu = 0$, $\Omega = \pm\Omega_0$ have $M = |\tilde{J}| = M_0$. Hence the maximum possible M for given $|\tilde{J}| < M_0$ is obtained on the red curve. In particular, the maximum possible mass without rotation is given by $\Omega = 0$ and $\mu = \mu_r$, and is

$$M_r := M(\mu_r, 0) = A(\mu_r, 0)\mu_r. \tag{5.94}$$

The red curve (5.91) corresponds to a curve of solutions that have a zero mode, a static linear perturbation that corresponds to an infinitesimal change of (μ, Ω) that leaves $(\tilde{J}, M)$ invariant to linear order. This signals that a linear perturbation mode changes from stable to unstable across the red curve. This is familiar from nonrotating stars in $3+1$ dimensions, where an extremum of the mass as a function of central density signals a separation between stable and unstable stars, with the less dense stars stable and the more dense ones unstable. We conjecture that the solutions in the doubly-covered region with smaller μ (and hence larger central density) are unstable, corresponding to region below the red curve in Fig. 5.1. As their

asymptotic metrics are of black-hole type, it is possible that these unstable solutions collapse to a black hole when perturbed in a suitable way.

We have obtained some evidence for this conjecture by time-evolving the two solutions with the equation of state $p = \rho/2$ represented by the orange and black dots in Fig. 5.1. Adding a small perturbation of the density with either sign to the less dense (orange) solution sets up propagating perturbations that remain small. Adding a small density perturbation to the denser (black) solution results in a highly nonlinear oscillation for one sign of the perturbation, where the central density repeatedly decreases below that of the orange solution, while perturbing the initial density with the opposite sign triggers prompt collapse to a black hole.

5.2.8.5 Summary of $\Lambda < 0$

In summary, the manifold of solutions contains a unique solution with given $(\tilde{J}, M)$ in the chevron-shaped region

$$|\tilde{J}| - 1 < M < |\tilde{J}| \tag{5.95}$$

that is bounded by the curves (5.78) and (5.82), while in a contiguous compact region bounded by $|\tilde{J}| = M$ for $0 < M < M_0$ and the curve (5.91) there are two solutions with the same given $(\tilde{J}, M)$. There are no solutions with $(\tilde{J}, M)$ outside these two regions.

5.2.8.6 The case $\Lambda = 0$

We now consider the limit where the length scale s remains finite but $\Lambda \to 0$. Then $\lambda^2 = \mu + \Omega^2 = 0$, so in this limit $\mu = \Omega = 0$. Therefore, no rigidly rotating stars can exist. Intuitively, only the cosmological contraction due to $\Lambda < 0$ can balance the centrifugal acceleration of rigid rotation, while the curvature generated by stress-energy cannot. Setting $\Omega = 0$, replacing $(\mu + \Omega^2)\ell^2$ with s^2, and then setting $\mu = 0$, we obtain

$$m = 2I\left(\frac{1}{8\pi s^2}\right). \tag{5.96}$$

Eqs. (5.26) and (5.28) still hold, and so do (5.43)-(5.46) and (5.49), reduced to

$$x^2 = 2(y-1) + 16\pi f, \tag{5.97}$$

$$\alpha^2 = y^2, \tag{5.98}$$

$$M = -\frac{1}{a^2} = -\frac{1}{4}\left(\frac{\mathrm{d}x^2}{\mathrm{d}y}\right)^2, \tag{5.99}$$

with $\beta = 0$ and $J = 0$. They define an analytic interior solution for analytic equation of state, with in particular a regular center. However, in the vacuum exterior to this interior solution, (5.97) with (5.59) gives $x^2 = m - 2$, which is constant, so from (5.99) $M = 0$. This means that a diverges at the surface, but the metric expressed in terms of y remains regular, and in the exterior it is

$$\mathrm{d}s^2 = -y^2\,\mathrm{d}t^2 + s^2\left(\frac{\mathrm{d}y^2}{m-2} + (m-2)\,\mathrm{d}\theta^2\right), \tag{5.100}$$

for $y_\star < y < \infty$. The spatial geometry is a cylinder, see also Eq. (79) of Ref. [167]. If $y_\star$ is finite, we do not consider such a solution as a star. In Appendix D, we discuss the linear perturbation of the static solution with $\Lambda = 0$ and no rotation.

5.2.9 Causal structure

If we apply the standard compactification of adS3, namely

$$R = \ell \tan \frac{\psi}{\ell}, \tag{5.101}$$

to the BTZ metric in its standard form, (5.21), (5.34)-(5.36) with $c_0 = 1$ and $\beta_0 = 0$, we obtain

$$\mathrm{d}s^2 = \frac{1}{\cos^2 \frac{\psi}{\ell}} \left[-F\,\mathrm{d}t^2 + G^{-1}\,\mathrm{d}\psi^2 + \ell^2 \sin^2 \frac{\psi}{\ell} \left(\mathrm{d}\theta + H\,\mathrm{d}t\right)^2 \right], \tag{5.102}$$

where $F = G$ and

$$G = 1 - (M+1)\cos^2 \frac{\psi}{\ell} + \frac{J^2 \cos^4 \frac{\psi}{\ell}}{4 \sin^2 \frac{\psi}{\ell}}, \tag{5.103}$$

$$H = \frac{J \cos^2 \frac{\psi}{\ell}}{2 \sin^2 \frac{\psi}{\ell}}. \tag{5.104}$$

This is conformal to a metric (the one in the large square brackets) that is regular everywhere, or in the black-hole case everywhere outside the event horizon, but always including at $\psi/\ell = \pi/2$, which is therefore revealed as a timelike conformal boundary. In our star-like solutions, $F \neq G$ and H are different functions from those given above, but they are finite and non-zero for $0 \leq \psi/\ell \leq \pi/2$.

For the BTZ metrics corresponding to black holes, the familiar Penrose diagram [148] is a different one, being a square that is compact in the time as well as the radial direction. At first sight, this seems to contradict the above conformal picture for a star, in which the conformal metric has an infinite range of t. The apparent contradiction is resolved by noticing that the black hole conformal diagram contains at its top and right corner a point representing timelike infinity where the curve representing the future branch of the event horizon meets the curve representing the timelike conformal boundary. If we now cover up the black hole region with a star, the timelike curve representing the surface of the star and the timelike conformal boundary meet at the same point in the conformal diagram. Both have infinite proper length, and are tangential to the stationary Killing vector. Moreover, a radial light ray reflected at both curves travels between them an infinity number of times before reaching the point in the conformal diagram where they meet. Hence there must be a conformal transformation where these two curves remain parallel and have infinite coordinate length in the resulting Penrose diagram, as derived above.

A second question about the causal structure is if the spacetime admits closed timelike curves. It is obvious that closed timelike curves exist if there is a region where the metric coefficient $g_{\theta\theta} = R^2$ is negative. Conversely, Bañados, Henneaux, Teitelboim and Zanelli [148]

have proved that the BTZ metrics do not contain closed timelike curves if there is no region with $R^2 < 0$, or if such regions are excluded. The proof only relies on the signature of the metric coefficients, not their form, and so generalizes to metrics of the form (5.13), as long as a^2 and α^2 remain positive. Hence, as a^2, α^2 and R^2 are manifestly non-negative in our star-like solutions, they do not contain closed timelike curves. (The examples of solutions with closed timelike curves given by Cataldo [168] can therefore not be star-like, that is, have both a regular center and be asymptotically BTZ.)

5.3 Simple equations of state

5.3.1 Ultrarelativistic linear equation of state $p = \kappa\rho$

In the following, we concentrate on solutions with the ultra-relativistic (linear) equation of state $p = \kappa\rho$, assuming the physical range $0 < \kappa < 1$ of the equation of state parameter, which gives a real speed of sound smaller than the speed of light. (With the value $\kappa = 1/2$ in particular this equation of state can be interpreted as a gas of massless particles without internal degrees of freedom.) We have already seen above that star-like solutions with this equation of state have no surface at finite radius but are asymptotically BTZ. From (5.26) we have

$$\rho(\rho_0; y) = \rho_0 y^{-\frac{1+\kappa}{\kappa}}, \tag{5.105}$$

and hence from (5.28)

$$8\pi f(y) = (1-\mu)\left((1-y) + \frac{\kappa}{1-\kappa}\left(1 - y^{-\frac{1-\kappa}{\kappa}}\right)\right). \tag{5.106}$$

Of the metric coefficients, we here write out only

$$x^2 = \mu(y^2-1) + \frac{2\kappa(1-\mu)}{1-\kappa}\left(1 - y^{-\frac{1-\kappa}{\kappa}}\right). \tag{5.107}$$

The other metric coefficients are given by (5.44)-(5.46).

In the test fluid case $\mu = 1$ we have $x^2 = y^2 - 1$, and so the density in terms of the area radius takes the simple form

$$\rho = \rho_0\left[1 + R^2(-\Lambda - \beta_0^2)\right]^{-\frac{1+\kappa}{2\kappa}}, \tag{5.108}$$

where the central density ρ_0 is arbitrary (but assumed so small that self-gravity can be neglected) and β_0 is the constant angular velocity.

Integrating (5.105), we have

$$m = 2\frac{1-\mu}{1-\kappa} \quad \Leftrightarrow \quad I(p_0) = \frac{1}{1-\kappa}, \tag{5.109}$$

and so

$$A = \frac{2\kappa - (1+\kappa)\mu}{1-\kappa}. \tag{5.110}$$

For this particular equation of state, $I(p_0)$ is constant, and so m and A depend on μ only but (untypically) not on Ω. The total mass and spin at infinity are

$$M_{\rm tot} = \frac{-(1+\kappa)\mu^2 + 2\kappa\mu(1-2\Omega^2) + 4\kappa\Omega^2}{1-\kappa}, \tag{5.111}$$

$$\tilde{J}_{\rm tot} = \frac{4\kappa(1-\mu)\Omega\sqrt{\mu+\Omega^2}}{1-\kappa}. \tag{5.112}$$

The loci of $\tilde{J}_{\rm tot} = \pm M_{\rm tot}$ are the two intersecting critical curves $\Omega = \pm\Omega_c(\mu)$ with

$$\Omega_c(\mu) = \frac{2\kappa - (1+\kappa)\mu}{\sqrt{8\kappa(1-\kappa)(1-\mu)}}. \tag{5.113}$$

They cross at

$$\mu_c = \frac{2\kappa}{1+\kappa}, \tag{5.114}$$

which is inside the strip for all $0 < \kappa < 1$, and they intersect the edge $\mu = 0$ of the strip at

$$\Omega_0 = \sqrt{\frac{\kappa}{2(1-\kappa)}}. \tag{5.115}$$

Hence for all physical values of κ the strip contains regions corresponding to point-particle, black hole and overspinning values of the pair $(\tilde{J}, M)$, as we have already shown in general.

The parameter space $0 < \mu < 1$, $-\infty < \Omega < \infty$ of solutions is shown in Fig. 5.1 for $\kappa = 1/2$, together with contour lines of M and $\tilde{J}$, the lines $|\tilde{J}| = |M|$, color-coding of the asymptotic metric as black-hole, point particle or overspinning, and the curve that divides the black-hole region of parameter space into two halves that cover the corresponding region of $(\tilde{J}, M)$ space twice. This second curve is given by

$$\Omega_r^2(\mu) = \frac{1+\kappa}{2(1-\kappa)}(\mu_r - \mu), \quad \mu_r := \frac{\kappa}{1+\kappa} \tag{5.116}$$

for $0 < \mu < \mu_r$. We can de-parametrize this curve to obtain J^2 as a function of M involving only square roots, but the result is messy.

Solutions of black-hole type exist only for $M < M_0$ with

$$M_0 = 8\Omega_0^4 = \frac{2\kappa^2}{(1-\kappa)^2}. \tag{5.117}$$

The maximum possible mass without rotation is

$$M_r = A(\mu_r)\mu_r = \frac{\kappa^2}{1-\kappa^2}. \tag{5.118}$$

The manifold of solution is shown embedded in $(\tilde{J}, M, \mu)$ space in Fig. 5.2 to show the double cover more clearly, using the same color-coding. A top view, suppressing the μ direction and thus hiding the double cover, is given in Fig. 5.3.

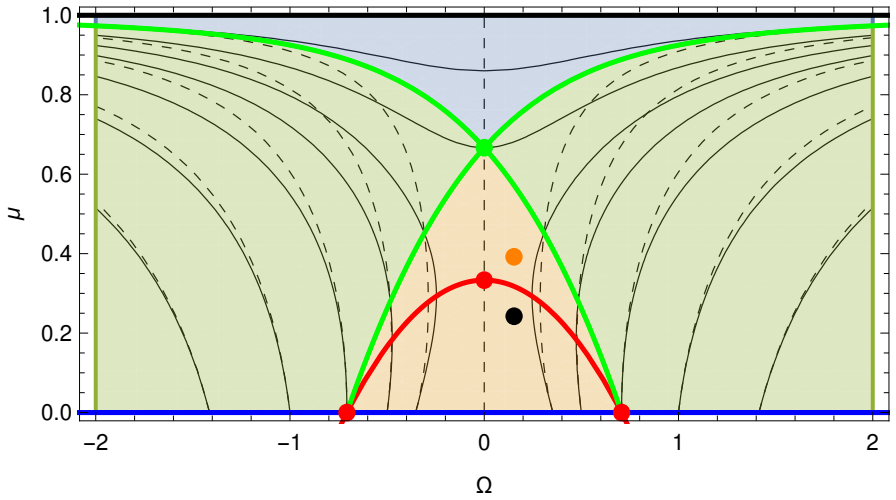

FIGURE 5.1: The nature of the asymptotic metric for star-like solutions with the linear equation of state $p = \rho/2$. All solutions lie in the strip $0 < \mu < 1$, $-\infty < \Omega < \infty$. The asymptotic metric is of black hole type in the orange (bottom) region, of point-particle type in the blue (top) region and of overspinning type in the green (left and right) regions. The parameter values of the two solutions shown in Fig. 5.4, and which have the same $(\tilde{J}, M)$, are indicated by an orange and a black dot. The contours of $M = -1, -1/2, 0, 1/2, 1, 2, 4, 8, 16$ (from top to bottom, solid) and $\tilde{J} = 0, \pm 1/2, \pm 1, \pm 2, \pm 4, \pm 8, \pm 16$ (outward from the center, dashed) are also shown. The crossing green lines indicate $\tilde{J} = \pm M$. The bottom region is split into two regions by the red line, each of which covers the same region in the $(\tilde{J}, M)$ plane. Solutions in the bottom half, such as the one indicated by the black dot, are conjectured to be unstable. The green dot is at $(0, \mu_c)$, and the three red dots are at $(\pm\Omega_0, 0)$ and $(0, \mu_r)$.

In all these figures, we have marked a specific pair of solutions with black-hole class asymptotic metrics, both of which have the same total mass $M = 0.38$ and angular momentum $\tilde{J} = 0.24$, but which have different parameter values $(\Omega, \mu) \simeq (0.154, 0.242)$ and $(0.153, 0.392)$. These solutions themselves are illustrated in Fig. 5.4 by plotting M, $\tilde{J}$ and $\ell^2\rho$ as functions of R/ℓ.

5.3.2 Modified linear equation of state $p = \kappa(\rho - \rho_s)$

A simple equation of state that admits solutions with a surface at finite radius is the inhomogeneous linear one,

$$p = \kappa(\rho - \rho_s), \tag{5.119}$$

for $0 < \kappa < 1$ and $\rho_s \geq 0$. Obviously this reduces to the previous example for $\rho_s = 0$. Proceeding as before, we find

$$\rho = \rho_0\, y^{-\frac{1+\kappa}{\kappa}} + \frac{\kappa\rho_s}{1+\kappa}\left(1 - y^{-\frac{1+\kappa}{\kappa}}\right). \tag{5.120}$$

We then obtain

$$x^2 = \tilde{\mu}(y^2 - 1) + \frac{2\kappa(1-\tilde{\mu})}{1-\kappa}\left(1 - y^{-\frac{1-\kappa}{\kappa}}\right) \tag{5.121}$$

which is just (5.107) again, only with μ replaced by

$$\tilde{\mu} := \mu - \sigma, \tag{5.122}$$

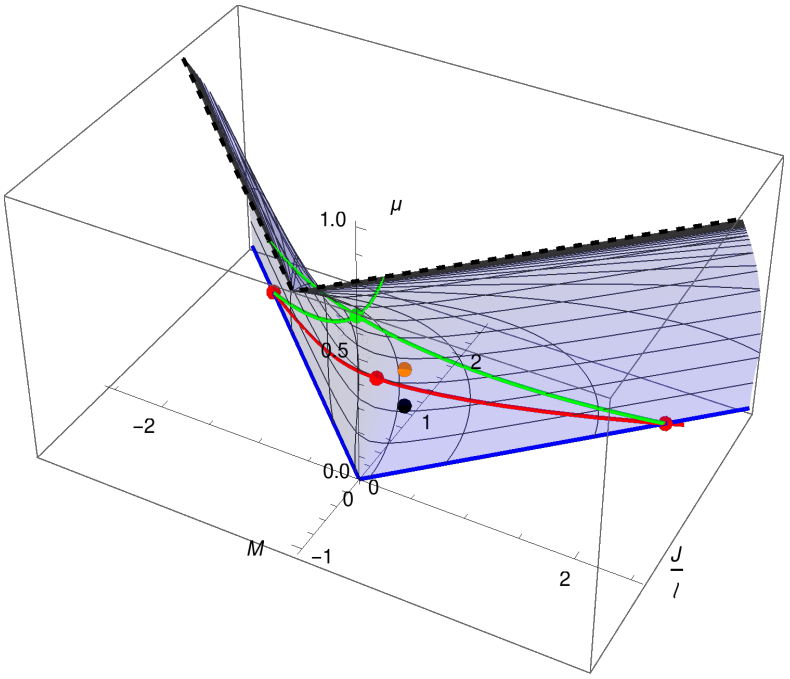

FIGURE 5.2: Parametric plot of $(\tilde{J}, M)$ as a function of (μ, Ω), embedded in three dimensions as $(\tilde{J}, M, \mu)$. All dots and thick curves correspond to those of the same colour in Fig. 5.1. Contours of Ω and μ are shown as thin lines. The thick red line denotes the locus of $|\partial(\tilde{J}, M)/\partial(\mu, \Omega)| = 0$, where the embedded surface is vertical. The intersecting thick green lines denote the loci of $\tilde{J} = \pm M$ at nontrivial values of μ. The bottom edge of the plot, $\mu = 0$, is at $\tilde{J} = \pm M$, for $M > 0$. The top edge of the plot (dashed black line), $\mu = 1$ is at $\tilde{J} = \pm(M+1)$, for $M \geq -1$, with $M = -1$ only at $\mu = 1$. The single point $M = -1$, $\tilde{J} = 0$ in this plot corresponds to a two-parameter family of test fluid solutions. Solutions in the area below the red line are conjectured to be unstable. The orange dot and the black dot represent two solutions with the same M and $\tilde{J}$ that are presumed stable and unstable, respectively. The green dot is at $(0, M_c, \mu_c)$, and the three red dots are at $(\pm M_0, M_0, 0)$ and $(0, 0, \mu_r)$.

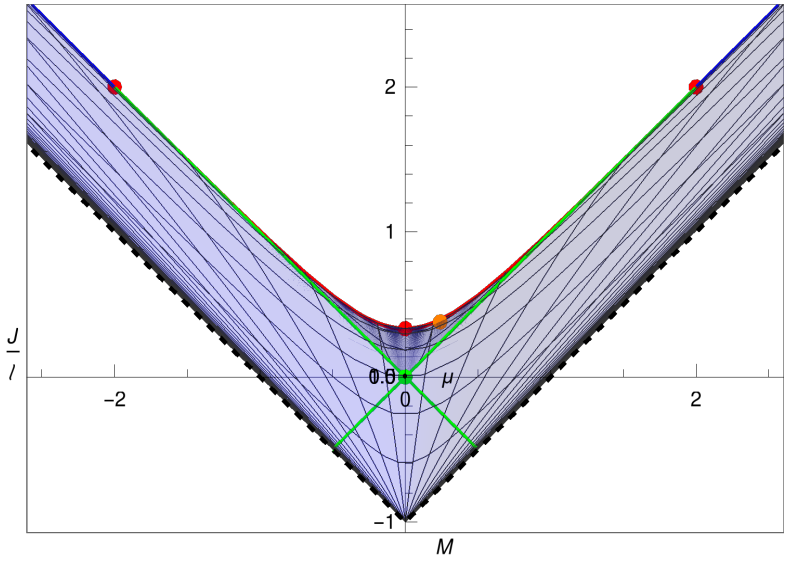

FIGURE 5.3: A top view, suppressing the dimension μ, of the plot in Fig. 5.2. All dots and curves are as described in Fig. 5.2. Note that the orange dot lies on top of, and so hides, the black one.

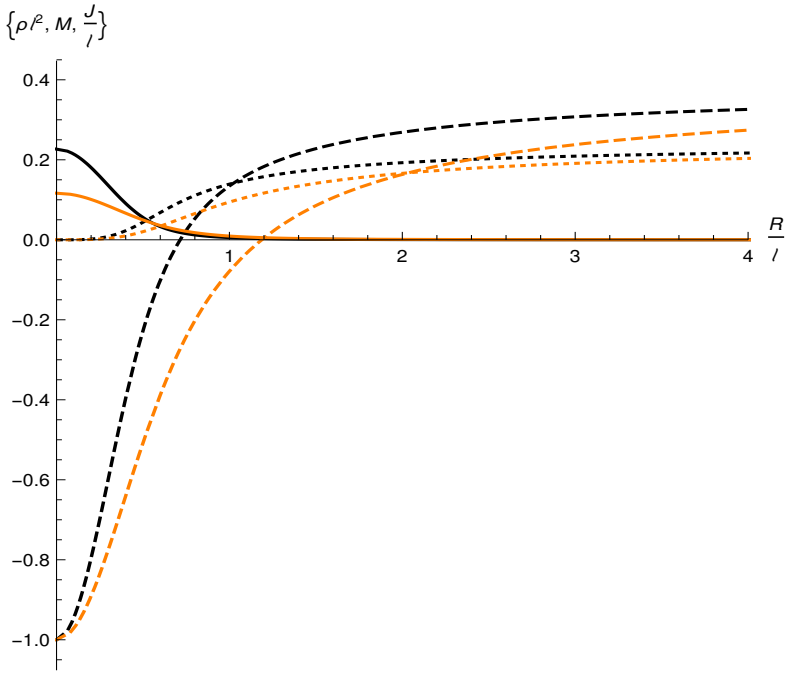

FIGURE 5.4: An example of two star-like solutions with the equation of state $p = \rho/2$. Both have $M = 0.38$ and $\tilde{J} = 0.24$, but different central densities. We plot $\ell^2\rho$ (solid), M (dashed) and $\tilde{J}$ (dotted) against R/ℓ. The less compact solution, with $(\Omega, \mu) \simeq (0.154, 0.242)$ and lower central density, (stable in nonlinear numerical time evolutions) is plotted in orange, and the more compact one with $(\Omega, \mu) \simeq (0.153, 0.392)$ and higher density, (numerically found to be unstable) in blue.

where

$$\sigma := \frac{\kappa}{1+\kappa} 8\pi s^2 \rho_s = \frac{\kappa}{1+\kappa}(\mu + \Omega^2) 8\pi \ell^2 \rho_s. \tag{5.123}$$

The other metric components follow, and we do not give them here. The stellar surface is now at finite radius

$$y_\star(\rho_0) = \left(\frac{(1+\kappa)\rho_0}{\rho_s} - \kappa \right)^{\frac{\kappa}{1+\kappa}}. \tag{5.124}$$

Note that $y_\star(\rho_s) = 1$ as expected. We have

$$m = 2\frac{1-\mu}{1-\kappa} + \frac{1+\kappa}{1-\kappa}\sigma \left(1 - \left(\frac{1-\mu+\sigma}{\sigma} \right)^{\frac{2\kappa}{1+\kappa}} \right), \tag{5.125}$$

which now depends also on Ω through $\sigma(\mu, \Omega)$. We do not write down further expressions, which are complicated and do not add new insight.

5.3.3 Polytropic equation of state $p = K\rho^k$

For

$$p = K\rho^k, \tag{5.126}$$

the star has a surface at finite radius

$$y_\star(\rho_0) = \left(1 + K\rho_0^{k-1}\right)^{\frac{k}{k-1}} \tag{5.127}$$

if and only if $k > 1$, consistent with the analysis in Sec. 5.2.7. We find

$$\rho(\rho_0; y) = K^{-\frac{1}{k-1}} \left(\left(\frac{y}{y_\star(\rho_0)} \right)^{-\frac{k-1}{k}} - 1 \right)^{\frac{1}{k-1}} , \tag{5.128}$$

The functions $f(y)$ and hence $x^2(y)$ can be expressed in closed form in terms of hypergeometric functions, as already noticed in Ref. [168]. The same is true for m, and hence $M_{\rm tot}$ and $J_{\rm tot}$. We do not write down these expressions as they do not give further insight.

5.4 Conclusion

We have constructed rotating perfect fluid star-like solutions in $2+1$-dimensional general relativity with a negative cosmological constant $\Lambda < 0$. We defined these to have a regular center, and finite mass M and spin J at infinity. (We again suppress the suffix "tot" in this Section.) We have found these solutions in standard polar-radial coordinates (t, R, θ), in terms of two free parameters μ and Ω that control their mass and spin, and we have given expressions for the total mass M and spin J in terms of the two free parameters. We have thus established that star-like solutions in $2+1$ dimensions exist for generic equations of state.

Furthermore, we have shown that these solutions are analytic in suitable coordinates, including at the center, for analytic equations of state (except at the surface, if there is a sharp surface). We have also shown that their causal structure is that of the adS3 cylinder, without closed timelike curves.

For any equation of state with $0 < p'(\rho) < 1$ and where either $p \sim \rho^k$ with $k > 1$ as $\rho \to 0$, or $p = 0$ occurs at finite ρ, we have shown that rotating and non-rotating stars with a sharp surface exist. The spacetime in the vacuum exterior is then the BTZ solution. In the limiting case where the equation of state is linear at low density, $p \simeq \kappa\rho$ with $0 < \kappa < 1$ as $\rho \to 0$, the density goes to zero only asymptotically, but sufficiently fast so that the spacetime is asymptotically BTZ with finite M and J.

We stress that the necessary and sufficient criterion for the existence of stars with a surface at finite radius and finite M and J is simply that the integral (5.58) converges at $p = 0$. We have not assumed further constraints on the equation of state except the causality constraint $0 < p'(\rho) < 1$ for all $p > 0$.

We have shown that for a generic equation of state the (Ω, μ) parameter space contains exterior/asymptotic metrics of all three BTZ types: black-hole, point-particle and overspinning, but not for all values $(\tilde{J}, M)$. More precisely, solutions for generic equations of state cover all of the infinite region (5.95) of the $(\tilde{J}, M)$ plane, and a finite region bounded by (5.93). In this second region, there are two solutions for the same values of M and $\tilde{J}$, with the more compact one conjectured to be unstable.

For an arbitrary barotropic equation of state $p = p(\rho)$ our solutions are in implicit form, involving two integrals and one function inversion. The integrals can be solved in closed form for the linear equation of state $p = \kappa\rho$, explicitly constructing the space of solutions, and we have shown that this is possible also for two other simple equations of state in which stars have sharp surfaces.

In spite of the local triviality of gravity, two compact self-gravitating objects in $2 + 1$ dimensions can interact gravitationally through global effects [160] and, for $\Lambda < 0$, even merge to form a black hole; see Ref. [169] for an explicit construction of a spacetime representing the formation of a spinning black hole from two massless point particles colliding with impact parameter. However, because there are no tidal forces or gravitational waves, unless and until the two objects actually touch they do not affect each other's local dynamics. In particular, if they start in an axistationary state they remain so unless and until they touch. This makes axistationary matter solutions even more relevant for representing interacting compact objects than they are in $3 + 1$ dimensions.

Chapter 6

Fully constrained, high-resolution shock-capturing, formulation of the Einstein-fluid equations in $2+1$ dimensions

This chapter is taken from a paper submitted to Phys. Rev. D; see Ref. [2]. In this thesis, Sec. 6.5 was added, describing a way to extend the current code so that the numerical outer boundary is placed at the adS boundary.

Sec 6.1 to Sec. 6.4.3 were written by Carsten Gundlach and Alex Davey. The rest of this chapter was written by me. Furthermore, the numerical code was written by Gundlach and Davey, based on a skeleton code for numerical conservation laws provided by Ian Hawke. At the start of the PhD, it could simulate non-collapse fluid evolution on a fixed Minkowski background. All subsequent improvements of the code, numerical time evolutions and plots were carried out by me. Gundlach suggested investigating the stability of the stationary solutions.

6.1 Introduction

We present a formulation of the Einstein equations with matter and a negative cosmological constant in $2+1$ dimensions, restricted to axisymmetry, that is fully constrained, in the sense that the Einstein equations can be solved by explicit radial integration along time slices to find the metric on that time slice.

We also present a numerical implementation of this formulation where the matter is a perfect fluid with the linear (ultrarelativistic) equation of state $P=\kappa\rho$. We demonstrate convergence of this scheme in a number of test cases with $\kappa=1/2$: rotating collapse, rotating strong field noncollapse, and the time evolution of both stable and unstable rotating stars, perturbed slightly.

In Ch. 7, we shall use this code to investigate critical phenomena at the threshold of prompt collapse in this system.

Our numerical implementation could be generalized straightforwardly to any barotropic or hot perfect fluid equation of state, and our numerical implementation of the Einstein equations to any other matter.

As the starting point for our formulation, we carry out a reduction of the covariant Einstein equations under the axisymmetry, with barred quantities referring here and later to the reduced 2-dimensional spacetime. In axisymmetry in $2+1$ dimensions, there are six independent components of the Einstein equations. Four of these can be written as $\bar{\nabla}_a M = \bar{\epsilon}_{ab}\bar{j}^b_{(M)}$ and $\bar{\nabla}_a J = \bar{\epsilon}_{ab}\bar{j}^b_{(J)}$, where $\bar{\epsilon}_{ab}$ is the 2-dimensional volume form. The left-hand sides are defined in terms of the Killing vector ξ^a of axisymmetry and the "area radius" R defined by the length of the closed symmetry orbits. The right-hand sides are the contraction of the stress-energy tensor with two vectors also made from ξ^a and R.

This tells us two things: $\bar{j}^a_{(M)}$ and $\bar{j}^a_{(J)}$ are conserved matter currents, and M and J are nontrivial quasilocal (local in the reduced spacetime) metric invariants that are constant in vacuum. (They reduce to the constant mass and angular momentum parameters of the same name in the Bãnados-Teitelboim-Zanelli (BTZ family of axistationary metrics [58].)

To stress how unexpected this rich geometrical structure of axisymmetry in $2+1$ dimensions is, we remind the reader what parts of it are known in other situations. The local mass M exists, and is linked to a conserved matter current $j^a_{(M)}$, in spherical symmetry in any dimension, and is then known as the Kodama [110] or generalized Misner-Sharp [107] mass. The current arises as the contraction of the stress-energy tensor with a certain vector field, but this is not a Killing vector field. The conserved angular momentum matter current $j^a_{(J)} = T^{ab}\xi_b$ exists in axisymmetry, also in any dimension. However, the local angular momentum J exists only in $2+1$ dimensions. Moreover, in $2+1$ dimensions only, M and its current exist in axisymmetry even with rotation.

The structure of the chapter is as follows. In Sec. 6.2 we derive the quantities M and J and their underlying currents in the reduction approach. We use these two conservation laws, plus a balance law for radial momentum, to formulate the fluid evolution equations. (To generalize from a barotropic to a hot equation of state, we would only need to add the rest mass conservation law.)

In Sec. 6.3 we then introduce specific coordinates on the reduced spacetime, namely a radial coordinate r linked in a fixed way to the area radius R, and a time coordinate t that is normal to R (polar time slices). The full metric on a time slice can then be obtained from suitable fluid variables on that slice by integration over r (starting from a regular center). In this form, the Einstein equations look quite similar to those in polar-radial coordinates in spherical symmetry (in any dimension).

Sec. 6.4 describes our numerical implementation in detail. In particular, we discretize the integration of the currents to obtain M and J so that the latter are conserved exactly. This is particularly important where $M \simeq 0$ but its sign matters because black holes can form only for $M > 0$ (we use the BTZ convention where its value in vacuum adS3 is -1). Similarly, for rapidly rotating collapse it will matter if J is larger or smaller than M. For the fluid evolution, we use an evolve-reconstruct-limit approach with a simple approximate Riemann solver. In

several details, we follow methods of [67] for ultrarelativistic fluid collapse in spherical symmetry in 3+1 dimensions.

Sec. 6.6 describes numerical tests. To allow black holes to exist in $2+1$ dimensions, we assume a negative cosmological constant throughout. We show that, at least for sufficiently short times and away from the numerical outer boundary, all variables converge pointwise to second order. In some situations, the rate of convergence goes down to first order after numerical error from our "copy" numerical outer boundary condition dominates the error budget. We use five different tests: generic rotating initial data that disperse and collapse respectively, and slightly perturbed stable and unstable rotating stars, the latter perturbed so that they either collapse or begin highly nonlinear oscillations. All regular axistationary solutions with finite M and J ("rotating stars") in $2+1$ dimensions with negative cosmological constants, and for arbitrary barotropic equation of state, and $P = \kappa\rho$ in particular, were classified in Ch. 5, building on earlier work in [168]. Here we give numerical evidence for a conjecture made there, that where there are two stars with the same M and J, the more compact one is unstable and the less compact one stable.

Sec. 6.7 contains our conclusions.

6.2 Geometric description of the model

6.2.1 Axisymmetry in $2+1$ spacetime dimensions

We consider axisymmetric solutions of the Einstein equations in $2+1$ dimensions with negative cosmological constant $\Lambda =: -1/\ell^2$,

$$G_{ab} + \Lambda g_{ab} = 8\pi T_{ab}. \tag{6.1}$$

We set $c = G = 1$ throughout. Let ξ^a be the Killing vector defining the axisymmetry. Its length defines the area radius

$$\xi^a \xi_a =: R^2 \tag{6.2}$$

as a scalar. We define a local angular momentum J geometrically as the twist (a scalar in $2+1$ dimensions) of the Killing vector,

$$J := \epsilon^{abc} \xi_a \nabla_b \xi_c, \tag{6.3}$$

where ϵ_{abc} is the volume form implied by the metric g_{ab}. We define a local mass function M in terms of J and R as

$$M := \frac{R^2}{\ell^2} + \frac{J^2}{4R^2} - (\nabla_a R)(\nabla^a R). \tag{6.4}$$

Following Geroch, we define the metric in the reduced $1+1$-dimensional spacetime of orbits

$$\bar{g}_{ab} := g_{ab} - R^{-2} \xi_a \xi_b, \tag{6.5}$$

so that $\bar{g}_{ab}\xi^b = 0$, the corresponding volume form

$$\bar{\epsilon}_{ab} := R^{-1} \epsilon_{abc} \xi^c, \tag{6.6}$$

and the corresponding covariant derivative operator $\bar{\nabla}_a$ by

$$\bar{\nabla}_a :=\perp \nabla_a \perp \tag{6.7}$$

where $\perp$ stands for contraction with $\bar{g}_a{}^b$ on all indices.

Four linear combinations of components of the Einstein equations can then be written as

$$\bar{\nabla}_a J = -16\pi R\, \bar{\epsilon}_{ab}\, j^b_{(Z)}, \tag{6.8}$$
$$\bar{\nabla}_a M = -16\pi R\, \bar{\epsilon}_{ab}\, j^b_{(\Omega)} \tag{6.9}$$

Clearly the currents $j^a_{(Z)}$ and $j^a_{(\Omega)}$ are conserved in the sense that

$$\bar{\nabla}_a (R\, j^a_{(Z)}) = 0, \tag{6.10}$$
$$\bar{\nabla}_a (R\, j^a_{(\Omega)}) = 0, \tag{6.11}$$

or equivalently

$$\nabla_a j^a_{(Z)} = 0, \tag{6.12}$$
$$\nabla_a j^a_{(\Omega)} = 0. \tag{6.13}$$

The angular momentum and mass currents introduced above are given by

$$j^b_{(Z)} := V_{(Z)a} T^{ab}, \tag{6.14}$$
$$j^b_{(\Omega)} := V_{(\Omega)a} T^{ab}, \tag{6.15}$$

where

$$V^a_{(Z)} := \xi^a \tag{6.16}$$

and

$$V^a_{(\Omega)} := V^a_{(X)} + \frac{J}{2R^2} V^a_{(Z)}, \tag{6.17}$$

with

$$V^a_{(X)} := \bar{\epsilon}^{ab} \nabla_b R, \tag{6.18}$$

or equivalently

$$V^a_{(\Omega)} = R^{-2} \left(\epsilon^{abc} \xi^d + \frac{1}{2} \xi^a \epsilon^{bcd} \right) \xi_b \nabla_c \xi_d. \tag{6.19}$$

The conservation law (6.12) follows directly from the fact that $V^a_{(Z)} := \xi^a$ is a Killing vector, but (6.13) is less obvious. In spherical symmetry, $j^a_{(\Omega)}$ and M are known generalizations of the Kodama conserved current and mass [110] from 3+1 to arbitrary dimensions [107].

While the paper of this chapter was under review, a paper has appeared [170] that independently identifies the same generalized Kodama vector. It is given there in the form

$$V^a_{(\Omega)} = -\frac{1}{2} \epsilon^{abc} \nabla_b \xi_c. \tag{6.20}$$

We had not spotted this simpler form, which is equal to our expression (6.19).

6.2.2 Rotating perfect fluid matter

The stress-energy tensor for a perfect fluid is

$$T_{ab} = (\rho + P)u_a u_b + P g_{ab}, \tag{6.21}$$

where u^a is tangential to the fluid worldlines, with $u^a u_a = -1$, and P and ρ are the pressure and total energy density measured in the fluid frame. In the following, we assume the 1-parameter family of ultrarelativistic fluid equations of state $P = \kappa\rho$, where $0 < \kappa < 1$. In particular, $\kappa = 1/2$ represents a 2-dimensional gas of massless (or ultrarelativistic) particles in thermal equilibrium, where the stress-energy tensor is trace-free. The sound speed is $c_s = \sqrt{\kappa}$. There is no conserved rest mass density.

Following the Valencia formulation [133, 134], we parameterize the 3-velocity u^a in terms of the 2-velocity v^a with respect to a time slicing t as

$$\begin{aligned} u^a &:= \Gamma(n^a + v^a), & (6.22)\\ \Gamma &:= -n_a u^a, & (6.23)\\ v^a n_a &:= 0, & (6.24) \end{aligned}$$

where n^a is the future-pointing unit normal on the time slices. The normalization $u^a u_a = -1$ relates the Lorentz factor Γ to the 2-velocity as

$$\Gamma^{-2} = 1 - v_a v^a. \tag{6.25}$$

Following standard practice in fluid dynamics in curved spacetime, we write the stress-energy conservation equation $\nabla_a T^{ab} = 0$ as a set of three balance laws

$$\nabla_a \left(V_{b(i)} T^{ab} \right) = T^{ab} \nabla_{(a} V_{b)(i)}, \tag{6.26}$$

or

$$\nabla_a j^a_{(i)} = s_{(i)}, \tag{6.27}$$

specified by a choice of three vector fields $V^a_{(i)}$. We have already defined the vector fields $V^a_{(Z)}$ and $V^a_{(\Omega)}$, which give rise to conservation laws (balance laws with zero source term), and so are natural choices.

For the radial momentum (force) balance law we choose

$$V^a_{(Y)} := \nabla^a (\ln R). \tag{6.28}$$

This is the only choice where the resulting balance law is "well-balanced" for a fluid of constant density at rest in Minkowski spacetime, in the sense that the flux term is constant and the source term vanishes. By contrast, a balance-law based on any other choice of $V^a_{(Y)}$ requires

an explicit cancellation of the flux and source terms, which may lead to large and unnecessary numerical error. An equivalent choice for the radial momentum balance law was made in [171] for spherical polar coordinates in $3+1$ dimensions (without restriction to spherical symmetry).

6.3 Description in polar-radial coordinates

6.3.1 Metric and Einstein equations

We now introduce a specific coordinate system, namely the generalized polar-radial coordinates (t, r, θ), in terms of which the axisymmetric metric takes the form

$$\mathrm{d}s^2 = -\alpha^2(t,r)\,\mathrm{d}t^2 + a^2(t,r)R'^2(r)\,\mathrm{d}r^2 + R^2(r)[\mathrm{d}\theta + \beta(t,r)\,\mathrm{d}t]^2. \tag{6.29}$$

Note that our choice $g_{rr} = a^2R'^2$ makes a invariant under a redefinition $r \to \tilde{r}(r)$ of the radial coordinate. The volume forms are given by

$$\epsilon_{tr\theta} = \alpha a R' R, \qquad \bar{\epsilon}_{tr} = \alpha a R', \tag{6.30}$$

where we have made a choice of overall sign.

We assume that the spacetime has a regular central world line $R = 0$, and there we impose the gauge conditions, $\alpha(t,0) = 1$, $\beta(t,0) = 0$, and the regularity condition $a(t,0) = 1$. The gauge is fully specified only after also specifying the strictly increasing function $R(r)$, but we shall always assume that $R(r)$ is an odd analytic function with $R(0) = 0$, $R'(0) = 1$. The Killing vector is

$$\xi^a = \left(\frac{\partial}{\partial\theta}\right)^a \tag{6.31}$$

and R is its length, as above. We define the auxiliary quantity

$$\gamma := \beta_{,r}, \tag{6.32}$$

anticipating that β will not appear undifferentiated in the Einstein or fluid equations, but only in the form of γ and its derivatives, since the form (6.29) of the metric is invariant under the change of angular variable $\theta \to \theta + f(t)$.

Polar-radial coordinates have been used successfully in studying critical collapse in spherical symmetry in $3 + 1$ spacetime dimensions, starting with [52]. Their main advantage is that they allow a fully constrained formulation of the Einstein equations, where at $t = 0$ and each subsequent timestep we solve differential equations for a, α and β that contain only r-derivatives. Their main disadvantage is that they are apparent-horizon avoiding: in spacetime regions where an apparent horizon is about to form, the lapse α collapses near the center compared to its value far out so that the time slicing stops advancing near the center and never reaches the apparent horizon. This means that we cannot look very far into black holes.

In our coordinates, J and M are given by

$$J(t,r) = \frac{R^3\gamma}{R'a\alpha}, \tag{6.33}$$

$$M(t,r) = \frac{R^2}{\ell^2} + \frac{J^2}{4R^2} - \frac{1}{a^2}. \tag{6.34}$$

In an axistationary vacuum ansatz, M and J are constant in space and time with value equal to the BTZ parameters of the same name. The BTZ 2-parameter family of metrics [58] takes the form

$$\alpha^2 = -M + \frac{R^2}{\ell^2} + \frac{J^2}{4R^2}, \tag{6.35}$$

$$a^2 = \frac{1}{\alpha^2}, \tag{6.36}$$

$$\beta = -\frac{J}{2R^2}, \tag{6.37}$$

in all BTZ solutions. The anti-de Sitter solution (from now, adS3) in particular is given by $M = -1$ and $J = 0$. Note that $\alpha a = 1$ in the BTZ solutions.

In contrast to higher dimensions, stationarity actually follows from vacuum axisymmetry locally, intuitively because there are no gravitational waves in $2+1$ dimensions. The situation in $2+1$ axisymmetry is therefore rather more similar to spherical symmetry in higher dimensions, where the vacuum solutions are static and characterized by only a mass parameter.

Each BTZ solution is in fact locally, although not globally, isometric to the adS3 solution [148]. However, this additional symmetry will not be apparent in what follows.

The matter and Einstein equations are simplest in the standard polar-radial coordinates defined by $R(r) = r$. However, in these coordinates the coordinate speed of ingoing and outgoing radial light rays is $\mathrm{d}r/\mathrm{d}t = \pm\lambda_c$, where $\lambda_c := \alpha/(aR')$. This increases rapidly with radius in the BTZ solution, even in adS3. A necessary stability condition for any numerical method for evolving ultrarelativistic fluid matter is the Courant-Friedrichs-Levy (from now on, CFL) condition that the numerical grid be wider than the light cones, that is $\Delta r/\Delta t \geq \lambda_c$, everywhere in spacetime. As we require $R_{\max} \gg \ell$ in situations of physical interest, this makes for a wastefully small Δt.

This problem is easily fixed if we introduce compactified polar-radial coordinates [128]

$$R(r) = \ell \tan(r/\ell), \tag{6.38}$$

where the radial coordinate now has the range $0 \leq r < \ell\pi/2$. In a vacuum region $\rho = 0$, where the metric is BTZ, the light speed then takes the form

$$\lambda_c = 1 - \left(1 + M - \frac{J^2}{4R^2}\right)\cos^2 r/\ell. \tag{6.39}$$

In particular, the light speed is always bounded above and below. In the adS solution, we have $\lambda_c = 1$, and the CFL condition is uniform. Similarly, the coordinate light speed will

remain bounded in asymptotically adS3 solutions. In our numerical simulations we use the compactified coordinates (6.38), with different values of the cosmological scale ℓ, but for clarity we will write R and R' rather than the explicit expressions.

Of the six algebraically independent components of the Einstein equations in generalized polar-radial coordinates, five can be solved for $\gamma_{,r}$, $\gamma_{,t}$, $a_{,r}$, $a_{,t}$ and $\alpha_{,r}$. The undifferentiated shift β does not appear in the Einstein equations or in our formulation of the matter equations. The sixth Einstein equation is a combination of first derivatives of the other ones, and so is redundant modulo stress-energy conservation.

To write the first four Einstein equations (6.8,6.9) in coordinates, we define the current components

$$Z := \sqrt{-g}\, j^t_{(Z)}, \tag{6.40}$$
$$f_{(Z)} := \sqrt{-g}\, j^r_{(Z)}, \tag{6.41}$$
$$\Omega := \sqrt{-g}\, j^t_{(\Omega)}, \tag{6.42}$$
$$f_{(\Omega)} := \sqrt{-g}\, j^r_{(\Omega)}, \tag{6.43}$$

and obtain

$$J_{,r} = 16\pi Z, \tag{6.44}$$
$$J_{,t} = -16\pi f_{(Z)}, \tag{6.45}$$
$$M_{,r} = 16\pi \Omega, \tag{6.46}$$
$$M_{,t} = -16\pi f_{(\Omega)}. \tag{6.47}$$

The resulting conservation laws (6.12,6.13) take the form

$$Z_{,t} + f_{(Z),r} = 0, \tag{6.48}$$
$$\Omega_{,t} + f_{(\Omega),r} = 0. \tag{6.49}$$

A useful choice for the fifth independent Einstein equation, which must contain $\alpha_{,r}$ in order to be independent of (6.44-6.47), is

$$(\ln \alpha a)_{,r} = 8\pi a^2 R R' (1+v^2)\sigma, \tag{6.50}$$

as the right-hand side vanishes in vacuum. The matter quantities v and σ in the right-hand side of this equation will be defined below.

The Einstein equations (6.44-6.47) and (6.50) are all linear combinations of components of the Einstein equations, and so contain the fluid density, pressure and velocity undifferentiated. We have not used the contracted Bianchi identities (stress energy conservation), two of which are separately given as (6.48-6.49).

6.3.2 Balance laws

Rather than working directly with the coordinate components v^r and v^θ of the 2-velocity, we use its frame components in the radial and tangential directions,

$$v := aR'v^r, \qquad w := Rv^\theta. \tag{6.51}$$

We define the 2-velocity to be analytic if in the Cartesian coordinates $x := R\cos\theta$ and $y := R\sin\theta$, its Cartesian components v^x and v^y are analytic functions of x and y. This is the case in axisymmetry if and only if v and w are analytic odd functions of R, and hence of r (as we choose $R(r)$ to be analytic and odd).

In terms of v and w, and with $n_\mu = (-\alpha, 0, 0)$, the 3-velocity (6.22) of the fluid is

$$u^\mu = \{u^t, u^r, u^\theta\} = \Gamma\left\{\frac{1}{\alpha}, \frac{v}{aR'}, \frac{w}{R} - \frac{\beta}{\alpha}\right\}, \tag{6.52}$$

or equivalently

$$u_\mu = \Gamma\left\{-\alpha + Rw\beta, aR'v, Rw\right\}, \tag{6.53}$$

where the Lorentz factor (6.25) is

$$\Gamma^{-2} = 1 - g_{ij}v^iv^j = 1 - (v^2 + w^2). \tag{6.54}$$

In coordinates, the balance laws take the form

$$\left(\sqrt{-g}\,V_{\mu(i)}T^{t\mu}\right)_{,t} + \left(\sqrt{-g}\,V_{\mu(i)}T^{r\mu}\right)_{,r} = \sqrt{-g}s_{(i)}. \tag{6.55}$$

We abbreviate this as

$$\mathbf{q}_{,t} + \mathbf{f}_{,r} = \mathbf{S}. \tag{6.56}$$

Note that the factor $\sqrt{-g} = \alpha a R' R$ is included in our definitions of the conserved quantities $\mathbf{q}$, fluxes $\mathbf{f}$ and sources $\mathbf{S}$, and hence they depend on the choice of coordinates, while the currents $j^a_{(i)}$ and sources $s_{(i)}$ in (6.27) are defined covariantly by (6.26).

The coordinate components of the three vector fields are

$$V^\mu_{(Z)} = \{0, 0, 1\}, \tag{6.57}$$

$$V_{(X)\mu} = \{\frac{\alpha}{a}, 0, 0\}, \tag{6.58}$$

$$V_{(Y)\mu} = \{0, \frac{R'}{R}, 0\}. \tag{6.59}$$

Note these do not all have the index in the same position — we have chosen the simplest form. The corresponding three balance laws have the conserved quantities

$$\mathbf{q} := \{\Omega, Y, Z\} \tag{6.60}$$

given by

$$X = R'R\tau, \tag{6.61}$$
$$Y = R'v\sigma, \tag{6.62}$$
$$Z = aR^2R'w\sigma, \tag{6.63}$$
$$\Omega = X + \frac{JZ}{2R^2}, \tag{6.64}$$

with the corresponding fluxes $\mathbf{f}$ given by

$$f_{(X)} = \frac{\alpha}{a}Rv\sigma, \tag{6.65}$$
$$f_{(Y)} = \frac{\alpha}{a}(P + v^2\sigma), \tag{6.66}$$
$$f_{(Z)} = \alpha R^2 vw\sigma, \tag{6.67}$$
$$f_{(\Omega)} = f_{(X)} + \frac{Jf_{(Z)}}{2R^2}, \tag{6.68}$$

and the corresponding sources $\mathbf{S}$ by

$$S_{(X)} = \frac{1}{a}\Big[-Rv\sigma\alpha(\ln a\alpha)_{,r} + R^2vw\sigma\gamma - RR'(1+v^2)\sigma a_{,t}\Big] \tag{6.69}$$
$$= \frac{1}{a}R^2vw\sigma\gamma = \frac{R'}{R^3}Jf_{(Z)}, \tag{6.70}$$
$$S_{(Y)} = \frac{1}{a}\Big[(w^2-v^2)\sigma\alpha\frac{R'}{R} - \tau\alpha_{,r} - (P+v^2\sigma)\alpha(\ln a)_{,r} + Rw\sigma\gamma - 2v\sigma R'a_{,t}\Big], \tag{6.71}$$
$$S_{(Z)} = 0, \tag{6.72}$$
$$S_{(\Omega)} = 0, \tag{6.73}$$

where we have defined the shorthands

$$\sigma := \Gamma^2(1+\kappa)\rho, \tag{6.74}$$
$$P := \kappa\rho, \tag{6.75}$$
$$\tau := \sigma - P. \tag{6.76}$$

Note that in flat spacetime $S_{(X)}$ vanishes and only the first term in $S_{(Y)}$ is present.

The specific metric derivatives appearing in $S_{(X)}$ and $S_{(Y)}$ are given by the Einstein equations as

$$(\ln\alpha)_{,r} = a^2RR'\left(8\pi(P+v^2\sigma) - \frac{J^2}{4R^4} + \frac{1}{\ell^2}\right), \tag{6.77}$$
$$(\ln a)_{,r} = a^2RR'\left(8\pi\tau + \frac{J^2}{4R^4} - \frac{1}{\ell^2}\right), \tag{6.78}$$
$$a_{,t} = -8\pi\alpha a^2Rv\sigma. \tag{6.79}$$

In (6.70), we have used (6.50) [which itself follows from (6.77) and (6.78)] and (6.79) to

simplify $S_{(X)}$ to something that is proportional to J and so vanishes in spherical symmetry. In (6.73), we have used the Einstein equations (6.44,6.45) as well as the conservation laws for X and Z. By contrast, there is no particular simplification when the Einstein equations are used to express the metric derivatives in $S_{(Y)}$ in terms of the stress-energy.

6.3.3 Characteristic velocities

The coordinate characteristic velocities $\lambda = dr/dt$ of the matter are the eigenvalues of the 3×3 matrix $\partial\mathbf{f}/\partial\mathbf{q}$. It is useful to write the latter as $(\partial\mathbf{q}/\partial\mathbf{u})^{-1}(\partial\mathbf{f}/\partial\mathbf{u})$, where as our primitive variables we choose

$$\mathbf{u} := \{\rho, v, w\}. \tag{6.80}$$

We find the coordinate characteristic velocities

$$\lambda_{0,\pm} = \frac{\alpha}{aR'}\left\{v,\ \frac{v(1-\kappa)\Gamma^2}{(1-\kappa)\Gamma^2+\kappa} \pm \frac{\sqrt{\kappa(1-\kappa)(1-v^2)\Gamma^2+\kappa^2}}{(1-\kappa)\Gamma^2+\kappa}\right\} \tag{6.81}$$

These represent the radial fluid velocity and the velocity of outgoing and ingoing sound waves (in axisymmetry in $2+1$ dimensions, there are only radial sound waves). In the (unphysical) limit $\kappa = 1$, the two sound velocities $\lambda_\pm$ reduce to $\pm\lambda_c$, the coordinate speed of radial light rays. However, the fluid motion will in general become relativistic even for $c_s = \sqrt{\kappa} \ll 1$, and so v will approach ± 1 arbitrarily closely, which then means that one of λ_+ approaches λ_c or λ_- approaches $-\lambda_c$.

6.4 Numerical method

6.4.1 Fluid evolution

We use standard finite-volume methods for the time evolution of the fluid variables. We initially discretize only in r. Time will be discretized at the end, an approach sometimes called the method of lines. We use standard notation where r_i denotes cell centers and $r_{i+1/2}$ denotes cell faces. In principle, each cell is allowed to have a different width, but we always have

$$r_i := \frac{1}{2}(r_{i-1/2} + r_{i+1/2}). \tag{6.82}$$

We define the shorthand

$$\Delta_i(r) := r_{i+\frac{1}{2}} - r_{i-\frac{1}{2}}, \tag{6.83}$$

and similarly for other grid functions.

The numerical values of the conserved variables represent cell averages (denoted by an overbar), that is

$$\bar{\mathbf{q}}_i(t) := \frac{1}{\Delta_i(r)}\int_{r_{i-\frac{1}{2}}}^{r_{i+\frac{1}{2}}} \mathbf{q}(t,r)\,dr \tag{6.84}$$

in terms of notional continuum functions $\mathbf{q}(t,r)$. They are updated by notional fluxes through cell faces plus notional cell averages of the source terms, that is

$$\frac{d\bar{\mathbf{q}}_i}{dt} = \frac{1}{\Delta_i(r)}\left(\mathbf{f}_{i-\frac{1}{2}} - \mathbf{f}_{i+\frac{1}{2}}\right) + \bar{\mathbf{s}}_i. \tag{6.85}$$

This update is conservative by construction when the source terms vanish, simply because the fluxes from adjacent cells cancel in the time derivative of $\int \mathbf{q}\, dr$.

In the numerical code, where array indices must be integers, we label cell i by array index i (obviously) and cell-face $r_{i+1/2}$ by i, so each cell face is labeled by the cell to its left. The physical cells are labeled $i = 1, \ldots N$ and their boundaries $i = 0, \ldots N$, with $r_{1/2} := 0$ labeled as cell face 0.

To find the numerical fluxes, we first reconstruct the fluid variables in each cell in order to find left and right values at the cell faces. In the reconstruction we use a slope limiter such as centered, minmod or van Leer's MC limiter [172]. This takes as its input the cell average of the conserved quantity, as well as some slope information.

For these and other standard reconstruction methods to work well, the functions $\mathbf{w}$ we reconstruct should be "generic" in the sense that if we only have the cell average our best guess for the reconstructed function should be constant over the cell (with value equal to the cell average). However, none of our conserved quantities and not all of our primitive variables are generic in this sense, as they are expected to vary as some power of R near the symmetry boundary $R = 0$. In particular, v and w are odd functions of R (or r). By contrast, the functions we reconstruct are chosen to be even functions of R (or of r) that generically do not vanish at $R = 0$ (or $r = 0$), namely

$$\mathbf{w} := (\omega, \eta, \zeta) := \left\{ \frac{\Omega}{R'R}, \frac{Y}{R'R}, \frac{Z}{R'R^3} \right\} \tag{6.86}$$

$$= \left\{ \tau + \frac{J}{2}\frac{aw\sigma}{R}, \frac{v\sigma}{R}, \frac{aw\sigma}{R} \right\}. \tag{6.87}$$

We now approximate ω, η and ζ as constant in each cell to find their notional cell center values $\mathbf{w}_i$ from the cell averages of the $\mathbf{q}$. For such functions, $\mathbf{w}(r) \simeq \mathbf{w}_i \simeq \bar{\mathbf{w}}_i$ is the best approximation to make inside the ith cell whereas for a function that behaves like a power of R at the center it would not be. For example, from (6.86) we have

$$\omega\, d\left(\frac{R^2}{2}\right) = \Omega\, dr. \tag{6.88}$$

Approximating $\omega(r) = \omega_i$ and integrating over the ith cell, and similarly for η and ζ, we obtain

$$\omega_i = \frac{2\Delta_i(r)}{\Delta_i(R^2)}\bar{\Omega}_i, \tag{6.89}$$

$$\eta_i = \frac{2\Delta_i(r)}{\Delta_i(R^2)}\bar{Y}_i, \tag{6.90}$$

$$\zeta_i = \frac{4\Delta_i(r)}{\Delta_i(R^4)}\bar{Z}_i. \tag{6.91}$$

We use these cell center values $\mathbf{w}_i$ together with notional slopes to reconstruct $\mathbf{w}(r)$ to the cell faces and, independently, the $\mathbf{w}_i$ (only) to compute the source terms at the cell centers.

To find the numerical fluxes $\mathbf{f}_{i+1/2}$, we approximate the reconstruction as constant on each side of a cell face and then solve the resulting Riemann problem. Note that to find the flux through the cell face we do not need the complete solution of the Riemann problem but only the value $\mathbf{q}(r_{i+1/2})$ at the cell face. As the solution of the Riemann problem is self-similar,

$$\mathbf{q}(t,r) = \tilde{\mathbf{q}}\left(\frac{r - r_{i+1/2}}{t - t_n}\right), \tag{6.92}$$

$\mathbf{q}(t, r_{i+1/2})$ is time-independent, and so therefore is $\mathbf{f}_{i+1/2} := \mathbf{f}[\tilde{\mathbf{q}}(0)]$.

In practice, we do not solve the Riemann problem exactly but use an approximate Riemann solver. We use the very simplest one, the HLL approximate Riemann solver [173]. This approximates the solution as a two-shock solution with shock speeds given *a priori* as $\pm\lambda_{\mathrm{HLL}}$. Conservation then forces the middle state to be the average of the left and right state, and the resulting HLL flux is given by

$$\mathbf{f}_{i-\frac{1}{2}} = \frac{\mathbf{f}(\mathbf{q}^R_{i-1}) + \mathbf{f}(\mathbf{q}^L_i) + \lambda_{\mathrm{HLL}}\left(\mathbf{q}^R_{i-1} - \mathbf{q}^L_i\right)}{2}, \tag{6.93}$$

where $\mathbf{q}^R_{i-1}$ and $\mathbf{q}^L_i$ are the right and left reconstructions in the $(i-1)$th and ith cells. λ_{HLL} is an estimate of the absolute value of the largest coordinate characteristic speed. We use the coordinate speed λ_c of radial light rays, which is a (sharp) upper limit for the matter characteristic speeds.

We impose regularity boundary conditions at the center by using ghost points and the fact that all our grid functions are either even or odd in r. We fill the outer ghost cells by extrapolating the $\mathbf{u}$, $\bar{\mathbf{q}}$ or $\mathbf{w}$ as constant functions (copy boundary conditions).

We found some obstacles in extending the numerical outer boundary to infinity. The HLL flux limiter is not positivity preserving, which can lead to unphysical values for the density during the evolution. This is offset by imposing a numerical floor (typically $\sim 10^{-14}$). When extending the numerical grid to infinity, the outer boundary is typically a region of near vacuum, where the density is then set to this floor value. During the RK steps, the numerical flux continuously attempts to reduce the density below the floor value. The density is then replenished back to the floor value, thus continually adding mass to the system. It is possible to circumvent this problem by not imposing a floor on the density. In parallel, one can modify the numerical flux to be positivity preserving by "interpolating" between the HLL flux with some other positivity-preserving flux (such as Lax-Friedrichs); see Sec. 6.5. Doing so however generates shocks near the boundary that quickly grow and travel inwards. We have not attempted to further investigate this issue.

6.4.2 Recovery of primitive variables

To recover the primitive variables $\mathbf{u}$ from the conserved variables $\mathbf{q}$ at one point, we first convert the $\mathbf{q}$ to the $\mathbf{w}$. We then compute

$$\tau = \omega - \frac{J\zeta}{2}. \tag{6.94}$$

Inverting (6.74-6.76, 6.86), we compute

$$\rho = \frac{\tau}{[\Gamma^2(1+\kappa)-\kappa]}, \tag{6.95}$$

$$v = \frac{R\eta}{\Gamma^2(1+\kappa)\rho}, \tag{6.96}$$

$$w = \frac{R\zeta}{a\Gamma^2(1+\kappa)\rho}. \tag{6.97}$$

The Lorentz factor Γ can be written in terms of $\mathbf{w}$, by plugging (6.96, 6.97) into (6.54) and solving for Γ. We find

$$\Gamma^2 = \frac{1-2\kappa(1+\kappa)U+\sqrt{1-4\kappa U}}{2\left(1-(1+\kappa)^2U\right)}, \tag{6.98}$$

where we defined

$$U := \frac{R^2(\eta^2+\frac{\zeta^2}{a^2})}{(1+\kappa)^2\tau^2} = \frac{\Gamma^2\left(\Gamma^2-1\right)}{\left[\Gamma^2(1+\kappa)-\kappa\right]^2}. \tag{6.99}$$

Note that the $\mathbf{w}$ must obey the constraint

$$R^2\left(\eta^2+\frac{\zeta^2}{a^2}\right) < \tau^2 \tag{6.100}$$

for the fluid velocity to be physical (timelike). Numerical error may lead to this condition being violated, in which case (6.98) fails.

6.4.3 Einstein equations, fluxes and sources

We need to already have the metric coefficients J and a (as well as the given functions R and R') to recover the primitive variables from the conserved variables, and in addition we need α to compute the fluxes and sources. Moreover, variables can be represented numerically as cell-center values, cell-face values, or cell averages. Taking all this into account, in our fully constrained evolution scheme we interleave the solution of the Einstein equations at constant t with the recovery of the primitive variables in the following order, see also Table 6.1 for a summary.

0) We start with the cell averages $\bar{\mathbf{q}}_i := (\bar{\Omega}_i, \bar{Y}_i, \bar{Z}_i)$ at some moment of time.

1) We find the cell-center values $\mathbf{w}_i := (\omega_i, \eta_i, \zeta_i)$ using (6.89-6.91).

2) We now come to the first of two blocks of metric calculations. We find J and M at the cell faces by integrating out from $J = 0$ and $M = -1$ at the cell face $r = 0$, using

$$\Delta_i(J) = 16\pi \bar{Z}_i \Delta_i r, \tag{6.101}$$

$$\Delta_i(M) = 16\pi \bar{\Omega}_i \Delta_i r. \tag{6.102}$$

These integrals are exact as $\bar{\Omega}_i$ and $\bar{Z}_i$ represent cell averages. As Ω and Z are conserved exactly by our numerical scheme this discretization also gives us exact conservation of J and M. From J, M and R at the cell faces we find a at the cell faces using (6.34).

a is a generic even function, so using the average of the values at the two cell faces is a reasonable approximation to its value at the cell center,

$$a_i = \frac{1}{2}(a_{i-1/2} + a_{i+1/2}). \tag{6.103}$$

At the same time, we determine τ at the cell centers. This is more subtle, as it involves Z and J, which scale as $Z \sim R^3$ and hence $J \sim R^4$ near the center and so are not generic even functions. We first approximate Z in cell i by assuming that ζ, which is a generic even function, is constant in the cell (at the cell-center value ζ_i, which we found from the cell average $\bar{Z}_i$). This gives the approximation

$$Z_i \simeq \frac{4\Delta_i(r)\bar{Z}_i}{\Delta_i(R^4)} R_i^3 R_i'. \tag{6.104}$$

We also have the exact relation

$$J(r_i) = J_{i-1/2} + 16\pi \int_{r_{i-1/2}}^{r_i} Z(\tilde{r})\, \mathrm{d}\tilde{r} \tag{6.105}$$

and an equivalent expression integrating from $r_{i+1/2}$. Inserting the approximation (6.104), carrying out the integration, and averaging the two resulting expressions for $J(r_i)$, we find the approximation

$$J_i \simeq \frac{\Sigma_i(J)}{2} + 8\pi \Delta_i(r) \bar{Z}_i \frac{2R_i^4 - \Sigma_i(R^4)}{\Delta_i(R^4)}, \tag{6.106}$$

where

$$\Sigma_i(J) := J_{i-1/2} + J_{i+1/2} \tag{6.107}$$

and similarly for other grid functions.

We evaluate the approximation (6.106) at the cell centers to obtain J_i, and hence τ_i.

3) We now have τ_i, η_i and ζ_i and the metric coefficient a_i at the cell centers, and recover the primitive variables $\mathbf{u}_i := (\rho_i, v_i, w_i)$ at the cell centers as described in Sec. 6.4.2.

4) We now come to a second block of metric calculations. We integrate the remaining Einstein equation (6.50) in the approximation

$$\Delta_i \left(\ln(\alpha a)\right) \simeq 4\pi a_i^2 (1 + v_i^2) \sigma_i \Delta_i(R^2) \tag{6.108}$$

to obtain $a\alpha$ and hence α at the cell faces, starting from the gauge condition $\alpha(t, 0) = 1$.

0)	$\bar{\mathbf{q}}_i := (\bar{\Omega}_i, \bar{Y}_i, \bar{Z}_i)$ + floor	(6.61-6.64)
1)	$\mathbf{w}_i := (\omega_i, \eta_i, \zeta_i)$ + floor	(6.86)
2)	$J_{i+1/2}$, $M_{i+1/2}$, $a_{i+1/2}$	(6.44, 6.46, 6.34)
	a_i	average
	J_i, τ_i	(6.106, 6.94)
3)	$\mathbf{u}_i := (\rho_i, v_i, w_i)$ + floor	(6.99, 6.98, 6.95-6.97)
4)	$\alpha_{i+1/2}$	(6.108)
	α_i	average
	γ_i, $\gamma_{i+1/2}$	(6.33)
	$\beta_{i+1/2}$	(6.32)
	β_i	average
5)	$\bar{S}_{(Y)i}$ via $S_{(Y)i}$	(6.71, 6.109)
6)	$\mathbf{f}_{i-1/2}$ via $\mathbf{w}_i^L$, $\mathbf{w}_{i-1}^R$, $\mathbf{u}_i^L$ $\mathbf{u}_{i-1}^R$	(6.65-6.68, 6.93)
7)	$d\bar{\mathbf{q}}_i/dt$	(6.85)

TABLE 6.1: Overview of how $\dot{\mathbf{q}}/\mathrm{d}t$ is calculated. Steps 2 and 4 are not required if the metric is fixed. "+ floor" means that we impose a floor on small quantities at this point.

We interpolate α to the cell centers, as we did for a. From J, a and α we compute γ at the cell faces and cell centers using (6.33). As a diagnostic only, we find β at the cell faces by integration using the trapezoid rule, and then interpolate β to the cell centers. We start the integration of β from the gauge condition $\beta(t, 0) = 0$.

5) We evaluate (6.77-6.79), and hence (6.71) at the cell centers to find the source term $S_{(Y)i}$ at the cell centers. As $S_{(Y)} \sim RR'f$, where f is a generic even function near the center, we integrate the approximation $f_i = \bar{f}_i$ over the i-cell to find

$$\bar{S}_{(Y)i} = \frac{S_{(Y)i}}{R_i R_i'} \frac{\Delta_i(R^2)}{2\Delta_i(r)}. \tag{6.109}$$

6) We use a standard slope-limited method to reconstruct the $\mathbf{w}$ to the cell faces, denoting the value immediately to the left of the cell face at $r_{i-1/2}$ by $\mathbf{w}_{i-1}^R$ and the value immediately to the right by $\mathbf{w}_i^L$. We already have values of J and a at the cell faces (continuous across the cell face). We find τ at both sides of each cell face using (6.94), U from (6.99), then Γ and finally the $\mathbf{u}$. Finally, we use an approximate Riemann solver to find the numerical fluxes $\mathbf{f}$ through the cell faces from the $\mathbf{u}$ on each side.

7) We then have $d\bar{\mathbf{q}}_i/dt$ from (6.85).

6.4.4 Imposition of a floor on small quantities

Recall that the generic variables need to satisfy the constraint (6.100) everywhere at all times. Failure for this condition to be satisfied results in an unphysical value of (6.99) and thus of Γ^2. A primary concern is to ensure that this inequality is satisfied in near-vacuum regions, since

in those regions all three of the variables τ, η, ζ are small. We choose to impose a floor on the generic variables at each physical cell,

$$\tau_i - R_i \sqrt{\eta_i^2 + \frac{\zeta_i^2}{a_i^2}} \geq \delta_{\rm f}. \tag{6.110}$$

If the above condition is not satisfied at any cell i, we proceed as follows: First, τ_i is set to be at least the floor value,

$$\tau_{i,\,\rm new} = \max\left(\delta_{\rm f}, \tau_i\right). \tag{6.111}$$

Then we split the density and momentum variables into an ingoing and an outgoing combination (defined in the spirit of characteristic variables), and impose a floor on each separately,

$$c_\pm := \max\left(\tau_i \pm R_i \sqrt{\eta_i^2 + \frac{\zeta_i^2}{a_i^2}}, \delta_{\rm f}\right). \tag{6.112}$$

Note that necessarily $c_- = \delta_{\rm f}$. The variables τ, η are then updated as,

$$\tau_{i,\rm new} := \frac{c_+ + c_-}{2}, \tag{6.113}$$

$$\eta_{i,\rm new}^2 := \frac{(c_+ - c_-)^2}{4R_i^2} - \frac{\zeta_i^2}{a_i^2}. \tag{6.114}$$

The sign of $\eta_{i,\rm new}$ is chosen so that it has the same sign as η_i. It is possible due to numerical errors that the rhs of (6.114) is negative. In this case, we set

$$\eta_{i,\rm new} = 0 \tag{6.115}$$

and solve (6.114) for $\zeta_i \to \zeta_{i,\rm new}$. The updated value $\zeta_{i,\rm new}$ can be written explicitly as

$$\zeta_{i,\rm new} = 0 \tag{6.116}$$

if $c_+ = c_-$ and

$$|\zeta|_{i,\rm new} = a \left| \frac{2(\tau_i - \delta_{\rm f}) \pm \sqrt{(\tau_i - \delta_{\rm f})^2 + 3R_i^2\eta_i^2}}{3R_i} \right|, \tag{6.117}$$

if $c_+ > c_-$. We select the root that minimizes $||\zeta|_i - |\zeta|_{i,\rm new}|$ and again we choose the sign of $\zeta_{i,\rm new}$ to coincide with the sign of ζ_i.

By construction, the updated values then satisfy (6.110). The floor $\delta_{\rm f}$ itself is computed as the maximum between a relative and absolute floor,

$$\delta_{\rm f} := \max\left(\delta_{\rm abs}, \delta_{\rm rel}\left(\tau_i + R_i\sqrt{\eta_i^2 + \frac{\zeta_i^2}{a_i^2}}\right)\right). \tag{6.118}$$

The addition of this second relative floor is due to the fact that it is possible to encounter a situation for which $c_- < \delta_{\rm f}$, $c_+ > \delta_{\rm f}$ and also $c_+ \gg c_-$. In this case, within numerical precision, the update of the generic variables do not register. The second term in (6.118) ensures

that the floor is never "too small" compared to the data and that the update is therefore always properly applied. Typical values we choose are $\delta_{\text{abs}} = \delta_{\text{rel}} = 10^{-12}$. The floor is applied to the generic variables each time they are computed from the conserved variables. Furthermore, within each Runge-Kutta step, the floor is imposed on the newly computed conserved variables. This is done by first converting $\bar{\mathbf{q}}_\mathbf{i}$ into $\mathbf{w}_\mathbf{i}$ using (6.89)-(6.91), imposing the floor on them as discussed above and then converting back to $\bar{\mathbf{q}}_\mathbf{i}$ by inverting (6.89)-(6.91). We note that each time the floor is applied, the value of τ increases, resulting in the associated conserved variables $\bar{\Omega}_i$ to also increase. Thus, due to the floor, $\bar{\Omega}_i$ is not exactly conserved during the evolution.

6.4.5 Overall time step and initial data

Starting from the conserved quantities $\bar{\mathbf{q}}_i$ at one moment in time we have now recovered the metric and primitive variables, and the time derivative $\mathrm{d}\bar{\mathbf{q}}_i/\mathrm{d}t$. We implement (6.85) in a fourth order Runge-Kutta scheme in t. Note that for high-resolution limiters such as MC or minmod limiters, this scheme will also be total-variation-diminishing [136]. Each time we evaluate $d\bar{\mathbf{q}}_i/dt$ in the substeps of that scheme we also recalculate the metric.

We impose symmetry boundary conditions at $r = 0$, based on the fact that all variables are either even or odd in r. As we start each time step, and each Runge-Kutta timestep, assuming that only the $\bar{\mathbf{q}}_i$ are known, we impose the symmetry boundary conditions on them after each Runge-Kutta substep.

Any initial data in general relativity consist of a part that is freely specified and a part that is obtained by solving the constraints (and perhaps gauge conditions). As we have a fully constrained scheme for solving the Einstein equations, it is natural to prescribe the "matter" and use the Einstein equations to find the metric coefficients, but the meaning of matter is necessarily ambivalent. We specify the generic variables $\mathbf{w}_i$ at the cell centers as our free initial data, from which we can immediately compute the averaged conserved quantities $\bar{\mathbf{q}}_i$ from (6.89)-(6.91). From $\bar{\mathbf{q}}_i$, we can then follow the numerical scheme outlined in Table 6.1 to compute all the other quantities at the initial time step in a consistent way. Note that specifying the $\mathbf{w}$, or equivalently the $\mathbf{q}$, means that we know M and J *a priori*. This would not be the case if we specified the primitive variables $\mathbf{u}$.

6.4.6 Formation of apparent horizon and computation of critical quantities

Since we are not using a horizon penetrating foliation, one cannot observe the formation of an apparent horizon. We instead make use of two simple criteria to determine if a given initial data will collapse or disperse. For our intended application to critical collapse, it is important that this decision can be reliably automated.

First, if during the evolution, the timestep Δt is smaller than some minimum timestep Δt_{min}, then formation of apparent horizon is deemed to be imminent and unavoidable and the corresponding initial data will be judged as being supercritical. The rationale behind this is

that the time steps are computed so that the CFL condition is also satisfied,

$$\Delta t = c_{\text{CFL}} \min_i (\Delta_i r) \min_{i,i-\frac{1}{2}} \left(\frac{aR'}{\alpha} \right), \tag{6.119}$$

where the last minimum is computed from both the cell centers and faces and $0 < c_{\text{CFL}} < 1$. It is well known that in spherical symmetry, the formation of an apparent horizon is easily identified with the vanishing of $(\nabla R)^2 = 1/a^2 = 0$ at some radius $R = R_{AH}$. From the above and (6.77)-(6.78), it follows that the time step $\Delta t \to 0$ outside the horizon. A typical value is $\Delta t_{\text{min}} = 10^{-11}$.

There are also two other criteria that effectively act as fail-safes: if the maximum density ρ_{max} is larger than some threshold density at any point in time, then this will also be deemed as supercritical data. A typical value is $\rho_{\text{threshold}} = 10^{30}$. This criteria is usually never triggered since the time step dt becomes sufficiently small before this happens.

The second criterium is the value of $(\nabla R)^2$ itself. Since on the onset of apparent horizon formation, $(\nabla R)^2 \to 0$, numerical error can conspire to produce unphysical values of $(\nabla R)^2$, namely, $(\nabla R)^2 \lesssim 0$. This will also be a sign that collapse is unavoidable. If a given time evolution does not satisfy any of these criteria and the evolution has run for a sufficiently long time, the initial data will be deemed to be subcritical.

There is a subtlety in the notion of "sufficiently long," in that the negative cosmological constant effectively confines the matter. For perfect fluid matter, this is due to an inward cosmological acceleration. One may conjecture that, given enough time, any initial data with total mass $M > 0$ will form a black hole, and this is well established numerically for scalar field matter [128]. As we impose an unphysical numerical boundary condition at finite R, we are unable to investigate this, and so our criteria are, in some sense, for prompt collapse.

To investigate scaling at the threshold of (prompt) collapse, we need to record the maximum of the density ρ_{max} and the mass and spin of the apparent horizon $M_{\text{AH}}, J_{\text{AH}}$ respectively. The latter are computed using the formulas (6.33) and (6.34) evaluated at the apparent horizon R_{AH}. This is found from the minimum value of $(\nabla R)^2$, $(\nabla R)^2_{\text{min}} := \min_{i,n}(\nabla R)^2_i(t_n)$ from which we then consider the two neighboring points of $(\nabla R)^2_{\text{min}}$ and make a polynomial interpolation. The variables needed in the computation of $M_{\text{AH}}, J_{\text{AH}}$ are then evaluated by linear interpolation from R_{AH}.

6.5 Extending the current code to the adS boundary

One drawback of the code employed in this present work is due to the fact that our numerical grid does not extend all the way to the adS boundary.

We propose here a future modification of the code so that the numerical outer boundary is at the adS boundary, i.e. $r_{N+1/2} = \pi\ell/2$. This modification induces multiple changes to the above description of the code. In this subsection, we explain those changes.

First, note that the relations (6.89-6.91, 6.106, 6.108) and (6.109) are ill-defined at the last cell centre N since they each contain a factor of the form $\sim \Delta_i R^k$ and $\Delta_N R^k = \infty$ since $R_{N+1/2} = \infty$ by construction. We therefore need to address each of those equations separately.

For (6.89-6.91), at $i = N$, we instead use the pointwise relation (6.86), with the pointwise conserved quantities replaced by their cell averages $\mathbf{q_N} \to \bar{\mathbf{q}}_\mathbf{N}$. This change is expected to be consistent, since from (6.46), one requires that $\Omega(t, \pi\ell/2)$ to be finite. In this case, near the adS boundary, one can expect the approximation $\bar{\Omega}_N \simeq \Omega_N$ to hold. For (6.106), J_N is obtained by simple averaging $J_N = \Sigma_N(J)/2$. Note that a consistent alternative would be $J_N = \Sigma_N(J)/2 - 8\pi\Delta_N(r)\bar{Z}_N$. We do not expect the results to strongly depend on this choice since $\bar{Z}_N$ is small. At the outer boundary, $\alpha a = 1$ (recall (4.2.1.3)). Eq. (6.108) will then be approximated to $\ln(\alpha a)_{N+1/2} \simeq \ln(\alpha a)_{N-1/2}$. This is also justified from (6.50). Finally, the source (6.109) will take its pointwise value at the last cell center $\bar{S}_{(Y),N} \simeq S_{(Y),N}$.

Turning to the floor imposition, the floor defined previously causes an unphysical introduction of additional mass near the numerical outer boundary (recall that the total mass should be conserved on the entire spacetime since $S_{(\Omega)} = 0$). This is because the region near the outer boundary is a region of near vacuum (at least for the initial data and thus most of the evolution) where the density is set to the floor value. The numerical flux continuously attempts to reduce the density below the floor and our floor scheme replenishes the density at the floor value, by updating τ and thus $\bar{\Omega}$, thus continually introducing additional mass. This can be circumvented by choosing an alternative scheme which does not modify τ, and thus $\bar{\Omega}$, at all.

In order to understand the new methodology, it is useful to remember that the necessity of (6.100) can be seen to originate from (6.99): if at any point in spacetime, the constraint (6.100) is not satisfied, then this will result in an unphysical value for Γ^2. In order to ensure that U does not take unphysical values, we can therefore impose at every physical point that

$$R_i|\eta_i| \leq (1-\delta)\tau_i, \qquad \delta \ll 1. \tag{6.120}$$

This numerical floor imposition has also the advantage that, failure to satisfy the above numerical floor, only requires to modify (reduce) η_i. Specifically, if the above is not satisfied at some grid cell i, we then modify η_i according to,

$$R_i\eta_{i,\text{new}} = \text{sgn}(\eta_i)(1-\delta)\tau_i, \tag{6.121}$$

where $\text{sgn}(x)$ is the usual sign function. Typical values for the floor is $\delta = 10^{-13}$.

Note that, since it is not $\mathbf{w}$ but $\bar{\mathbf{q}}$ that is updated, there is a risk that the positivity of τ (and thus $\bar{\Omega}$ and ρ) is not guaranteed during the evolution, as the HLL scheme is not positivity preserving [174]. This problem is circumvented by blending the HLL flux-limiter with a positivity-preserving flux scheme which shall be taken to be the Lax-Friedrichs (LF) flux scheme.

Let us focus on the conservation law for $\bar{\Omega}_i$. According to a simple first-order scheme, one can estimate the pointwise value $\bar{\Omega}_i^n$ at the next time step to be [174],

$$\bar{\Omega}_i^{n+1} = \bar{\Omega}_i^n + \frac{\Delta t}{\Delta_i r}\left(f_{i-1/2} - f_{i+1/2}\right), \tag{6.122}$$

$$= \frac{1}{2}\left(\bar{\Omega}_i^+ + \bar{\Omega}_i^-\right), \tag{6.123}$$

where we defined the quantities,

$$\bar{\Omega}_i^\pm := \bar{\Omega}_i^n \pm 2\frac{\Delta t}{\Delta_i r} f_{i\mp 1/2}. \tag{6.124}$$

In the above, we need the fluxes at the cell faces from the cell-centered values. We therefore need a scheme to compute them from the conserved quantities at the cell centers. This is tantamount to defining a functional $\mathcal{F}$, called the numerical-flux function for which [136]

$$f_{i-1/2}^n =: \mathcal{F}(\bar{\Omega}_{i-1}^n, \bar{\Omega}_i^n). \tag{6.125}$$

For a positivity-preserving scheme, we consider the Lax-Friedrichs scheme, defined by

$$f_{i-1/2}^{\mathrm{LF}} = \mathcal{F}^{\mathrm{LF}}(\bar{\Omega}_{i-1}^n, \bar{\Omega}_i^n) := \frac{1}{2}\left(f_i + f_{i-1} - \frac{\Delta_i r}{\Delta t}\left(\bar{\Omega}_i^n - \bar{\Omega}_{i-1}^n\right)\right). \tag{6.126}$$

In particular, (6.124) becomes explicitly,

$$\bar{\Omega}_i^\pm = \bar{\Omega}_{i\mp 1} \pm \frac{\Delta t}{\Delta_i r}\left(f_i + f_{i\mp 1}\right). \tag{6.127}$$

We then consider the flux defined by [174],

$$f_{i+1/2}^{\mathrm{mix}} = \theta f_{i+1/2}^{\mathrm{HLL}} + (1-\theta) f_{i+1/2}^{\mathrm{LF}}, \qquad \theta \in [0,1]. \tag{6.128}$$

Thus, at each grid point, we first compute $\bar{\Omega}_i^{\pm,\mathrm{HLL}}$ using the HLL flux. If $\bar{\Omega}_i^{+,\mathrm{HLL}} + \bar{\Omega}_i^{-,\mathrm{HLL}} \geq 0$, then we continue to use the HLL flux as normal, i.e. we take $\theta = 1$. If it is negative, then there exist a $\theta \in [0,1]$ such that $\bar{\Omega}_i^{+,\mathrm{mix}} + \bar{\Omega}_i^{-,\mathrm{mix}} \geq 0$, since for $\theta = 0$, the numerical flux is the Lax-Friedrich flux which is positivity preserving. We then take the largest such θ.

We have attempted to implement the above modifications. The resulting code allows for far-from-critical dispersion and collapse initial data. In particular, the mass (and angular momentum) at the numerical outer boundary stays constant during the evolution. However, we also note the formation of strong shocks in the density profile, developing from the numerical outer boundary, that quickly grow and travel inwards. These shocks are not present with the code where the numerical outer boundary is set to some finite radius. We have not attempted to investigate further this issue.

6.6 Numerical tests

6.6.1 Convergence testing

In this section, we investigate the pointwise convergence as well as convergence with respect to a norm of our numerical code for different scenarios. Specifically, we examine six cases. First, we consider initial data “far" from the black hole threshold which disperses and collapses. For each of these two cases, we will consider a “slowly" and “rapidly" rotating case. Finally, we also consider initial data corresponding to rotating stars that are presumed stable and unstable.

Let f refer to any quantity of interest. In the following, we will mostly be interested in the conserved variables $\bar{\mathbf{q}}$, as they are used to evolve the data at the next timestep. It should still be emphasized that the primitive and generic variables still indirectly play a role in the evolution, notably during the floor imposition and when computing the fluxes at the cell faces, see Table 6.1. In our numerical code, we consider an approximation to the exact function $f(t,r)$. This approximation depends on the grid resolution $\Delta_i(r)$ and since we always choose a uniform grid spacing in the simulations we may simplify the notation by defining $h := \Delta_i(r)$. The approximation of the exact solution $f(t,r)$ will then be denoted by $F_h(t,r)$. The function $F_h(t,r)$ converges pointwise to the exact solution $f(t,r)$ if at all points we have

$$F_h(t,r) = f(t,r) + C(t,r)h^k + \mathcal{O}(h^{k+1}), \tag{6.129}$$

where $C(t,r)$ is a smooth function which depends on the continuum solution $f(t,r)$ and k is the order of convergence. Typically, the exact solution f is unknown, but this problem can be circumvented by considering instead the difference between two resolutions,

$$\delta F_h(t,r) := F_h(t,r) - F_{\frac{h}{2}}(t,r). \tag{6.130}$$

It follows that our scheme converges to order k if

$$\delta F_h(t,r) = 2^k \delta F_{\frac{h}{2}}(t,r)\left(1+\mathcal{O}(h)\right). \tag{6.131}$$

Besides investigating pointwise convergence, we will also be interested in the convergence in a norm. Consider the ℓ^2-norm, defined at any fixed time t by

$$||F||_2^2(t;h,p) = \frac{h}{2}\sum_{i=1}^{N-p}\left(F_h(t,r_{i-1/2})^2 + F_h(t,r_{i+1/2})^2\right). \tag{6.132}$$

Note that we use the cell faces instead of the cell centers, because the former align exactly when we double the resolution. If F corresponds to fluid variables, such as $\mathbf{u}$, $\bar{\mathbf{q}}$ or $\mathbf{w}$, the cell faces values are computed from the cell centers by linear interpolation.

Recall that the center is located at $r_{1/2} = 0$, while the outer boundary corresponds to $r_{N+1/2} =: r_{\text{max}}$. Note that in the definition of the norm, we also allow the truncation of the last p grid points for reasons that will be explained shortly.

Applying this norm to (6.131), we then find that

$$\mathcal{N}_F(t;h,p) := \log_2\left(\frac{||\delta F||_2(t;h,p)}{||\delta F||_2(t;\frac{h}{2},p)}\right) = k + \mathcal{O}(h). \tag{6.133}$$

By construction, one expects second-order convergence everywhere, except at and near the outer boundary due to the copy boundary conditions. On the other hand, the boundary conditions at the center are expected to not spoil the second-order convergence since they preserve the even/oddness of the functions they are applied to.

In the following, we investigate the following points: First, the correct implementation of the code, which should imply second-order convergence at least at short times everywhere, except possibly near the outer boundary. Second, we wish to investigate how the error that originates from the boundary affects the inside of the numerical grid. This is particularly important for the stationary configurations, since the conserved quantities do *not* vanish at infinity and so one would a priori expect the numerical outer boundary conditions to play a crucial role. Pointwise convergence is useful as it can highlight small numerical oscillations that would otherwise be hidden when looking at the convergence in a norm. On the other hand, convergence in a norm will be used to formalize the idea that the code converges to order k "almost everywhere." Specifically, it is possible that we find that some variables do not converge at all at the boundary, but that these oscillations do not travel inside the numerical grid, or if they do, they do it very slowly. In this case, we then would expect $\mathcal{N}_F(h,0) \ll k$, while for some small p, we would recover $\mathcal{N}_F(h,p) \simeq k$.

In what follows, we always consider the radiation fluid equation of state $\kappa = 1/2$. The numerical grid is equally spaced in the compactified coordinate r, as defined in (6.38) and the Courant factor of (6.119) is set to $c_{\text{CFL}} = 0.5$. The cosmological constant is set to $\Lambda = -\pi^2/4$, which sets the boundary of adS in compactified coordinates to $r_\infty = 1$.

6.6.2 Dispersion and collapse

For both dispersion and collapse, we consider the evolution of five different grid resolutions, with 100×2^n points for n from 1 to 5, so that for the lowest resolution, $h \simeq 0.0035$. The numerical outer boundary is set at $r_{\text{max}} = 0.7$, corresponding to $R_{\text{max}} = \ell \tan(r_{\text{max}}/\ell) \simeq 1.25$, and the copy boundary conditions will be imposed on the conserved variables.

For slowly rotating dispersion and collapse, we will choose the monotonized central-difference limiter (MC limiter) introduced by van Leer [172], while for the rapidly rotating cases, we instead switch to a centered limiter, as the latter is empirically found to be slightly more robust against numerical oscillations. Independently, for rapidly rotating collapse the convergence drops significantly at the onset of collapse. We found that this can be partly offset by imposing no mass to enter the numerical domain from the outer boundary by setting the HLL flux of Ω to be zero if it is negative.

For dispersion, the simulation is stopped when most of the energy has left the numerical domain, while for the case of collapse, we stop at the onset of black hole formation, see Sec. 6.4.6.

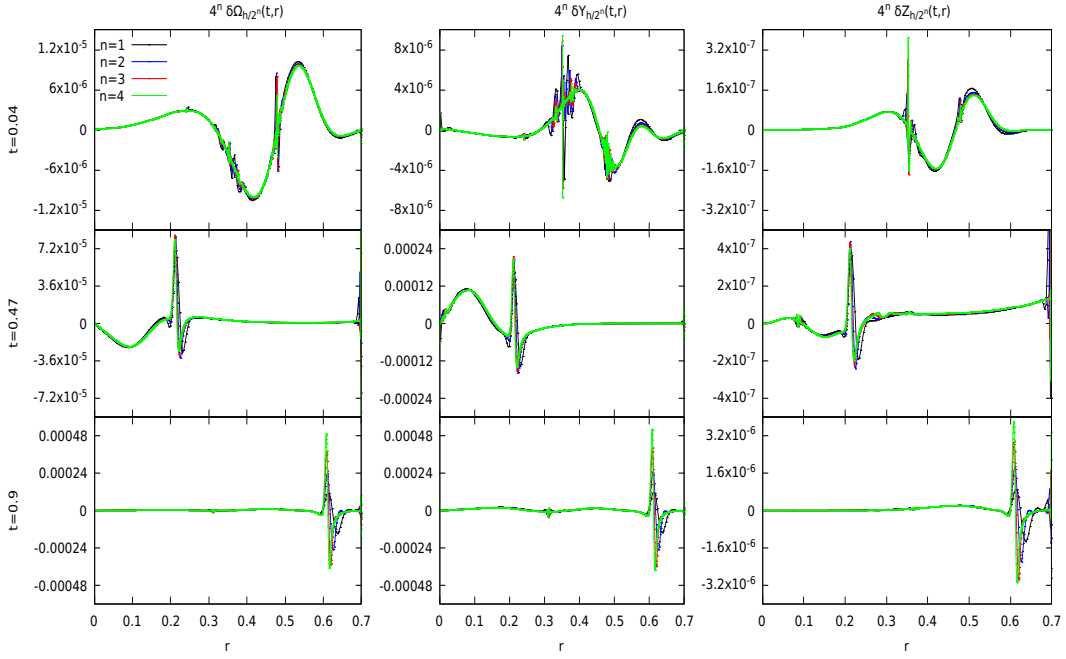

FIGURE 6.1: Dispersion with slow rotation: Plots of $4^n \delta \bar{\mathbf{q}}_{\frac{h}{2^n}}$ against r, at four resolutions $n = 1, 2, 3, 4$. From the left, the columns represent Ω, Y and Z, respectively, while the rows represent the times $t = 0.04$, 0.47 and 0.90, from the top. In each plot, the curves representing different resolutions approximately align, demonstrating pointwise second-order convergence. The unsmooth but convergent features of the error are artifacts of the MC limiter, and do not correspond to any visible unsmoothness of the solution itself. They are absent with the centered limiter.

We choose to initialize the generic fluid variables $\mathbf{w}$ as double Gaussians in the area radius R,

$$\omega(0,R) = \frac{p_\omega}{2}\left(e^{-\left(\frac{R-R_\omega}{\sigma_\omega}\right)^2} + e^{-\left(\frac{R+R_\omega}{\sigma_\omega}\right)^2}\right), \tag{6.134}$$

$$\eta(0,R) = \frac{p_\eta}{2}\left(e^{-\left(\frac{R-R_\eta}{\sigma_\eta}\right)^2} + e^{-\left(\frac{R+R_\eta}{\sigma_\eta}\right)^2}\right), \tag{6.135}$$

$$\zeta(0,R) = \frac{p_\zeta}{2}\left(e^{-\left(\frac{R-R_\zeta}{\sigma_\zeta}\right)^2} + e^{-\left(\frac{R+R_\zeta}{\sigma_\zeta}\right)^2}\right), \tag{6.136}$$

where p_ω, p_η, p_ζ are the magnitudes, R_ω, R_η, R_ζ the displacements from the center and σ_ω, σ_η, σ_ζ the widths of the Gaussians. For all four cases, we set the widths to $\sigma_\omega = 0.2$, $\sigma_\zeta = \sigma_\eta = 0.15$, and the displacements to $R_\omega = R_\eta = R_\zeta = 0.4$. The slowly rotating initial data have $p_\zeta = 0.01$, with $p_\omega = 0.2$ for dispersion and $p_\omega = 0.5$ for collapse. The rapidly rotating data have $p_\omega = 0.3$, $p_\zeta = 0.5$, and $p_\omega = 0.5$ and $p_\zeta = 0.7$ for dispersion and collapse respectively. In the "slowly" and "rapidly" rotating data that collapse, the black hole mass and spin parameter satisfy $J_{\rm AH}/(M_{\rm AH}\ell) \simeq 0.012$ and 0.9 respectively. For all four test cases presented above, the initial data satisfy the inequality (6.100) everywhere.

In Fig. 6.1, we plot $4^n \delta \bar{\mathbf{q}}_{\frac{h}{2^n}}$ (left, middle and right columns for Ω, Y and Z, respectively) at four different resolutions $n = 1, 2, 3, 4$ for initial data that disperses with small angular momentum. The profiles are plotted at three different times (top, middle and bottom rows)

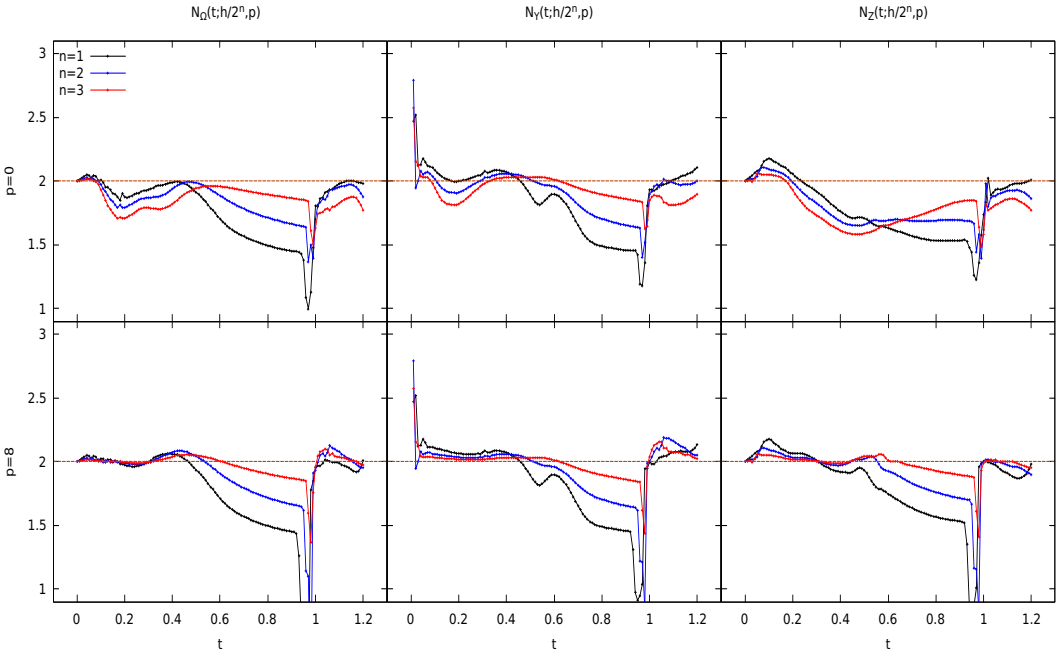

FIGURE 6.2: Dispersion with slow rotation: Plots of the convergence rates in the ℓ^2-norm, $\mathcal{N}_{\bar{\mathbf{q}}}(t;\frac{h}{2^n},0)$ (upper row, all grid points used) and $\mathcal{N}_{\bar{\mathbf{q}}}(t;\frac{h}{n},8)$ (bottom row, last 8 grid points omitted in the norm), for $n=1,2,3$. As in the previous figure the three columns represent Ω, Y and Z, respectively. The dashed horizontal line corresponds to second-order convergence, $\mathcal{N}=2$. When the full grid is taken into account in the computation of the norm, we typically observe less than second-order convergence. On the other hand, second-order convergence is recovered once the last 8 grid points are neglected in the computation of the norm.

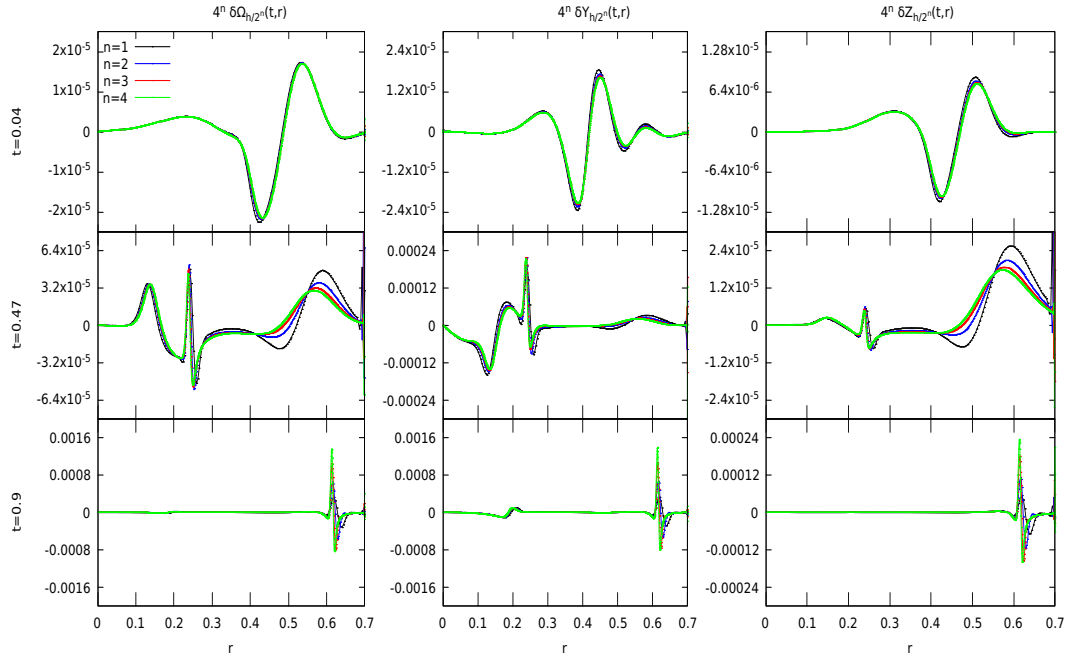

FIGURE 6.3: Dispersion with rapid rotation: Note that the oscillations in Fig. 6.2 at time $t=0.04$ are not present here due to choosing a centered limiter instead of the MC limiter. Otherwise as in Fig. 6.1.

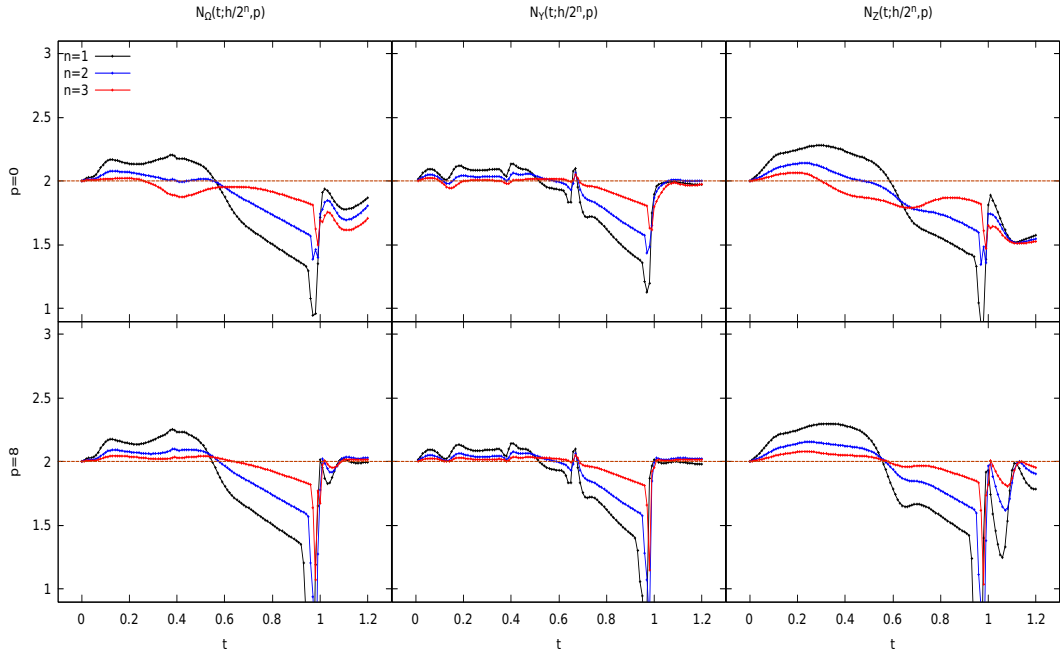

FIGURE 6.4: Dispersion with rapid rotation: Otherwise as in Fig. 6.2.

$t = 0.04, 0.36$ and 0.9. These snapshots represent respectively, the evolution of the error near the initial time, when the energy density reaches a maximum (near the center), and when the matter finally disperses and most of the density is about to leave the numerical domain. During the evolution, the conserved variables remain smooth.

According to (6.131), the approximate alignment of these plots shows that the code converges to second order. One can, however, spot some numerically induced oscillations at isolated points inside the numerical grid. Their frequency increases with resolution, but their amplitudes do not grow with time and in fact converge away rather quickly with increased resolution. These oscillations are a consequence of our choice of limiter as we observed that these oscillations vanish with a centered limiter.

On the other hand, the convergence is mostly unaffected by the choice of imposing copy boundary conditions on the conserved variables instead of the primitive or generic variables. Finally, as anticipated, we lose second-order convergence at and near the outer boundary. The error propagates very slowly inside the numerical domain and so does not spoil the second-order convergence for most of the numerical grid for the period of time the simulation is run.

To illustrate this, in Fig. 6.2 we plot $\mathcal{N}_{\bar{\mathbf{q}}}(t; \frac{h}{2^n}, 0)$ and $\mathcal{N}_{\bar{\mathbf{q}}}(t; \frac{h}{2^n}, 8)$, for $n = 1, 2, 3$. For the former, untruncated case, we find that the order of convergence is typically less than second order. On the other hand, we recover the expected second-order accuracy once the last 8 grid points are ignored in the calculation of the norm. The drop in convergence that can be seen at around $t \simeq 1.0$ corresponds to the energy leaving the numerical grid, see the last row of Fig. 6.1. These type of drops of numerical accuracy are also usually a sign of a zero crossing.

In Figs. 6.3 and 6.4, we demonstrate second-order convergence pointwise and with respect to the ℓ^2-norm for the highly rotating dispersing initial data. As for the slowly rotating case, the conserved variables remain smooth during the evolution.

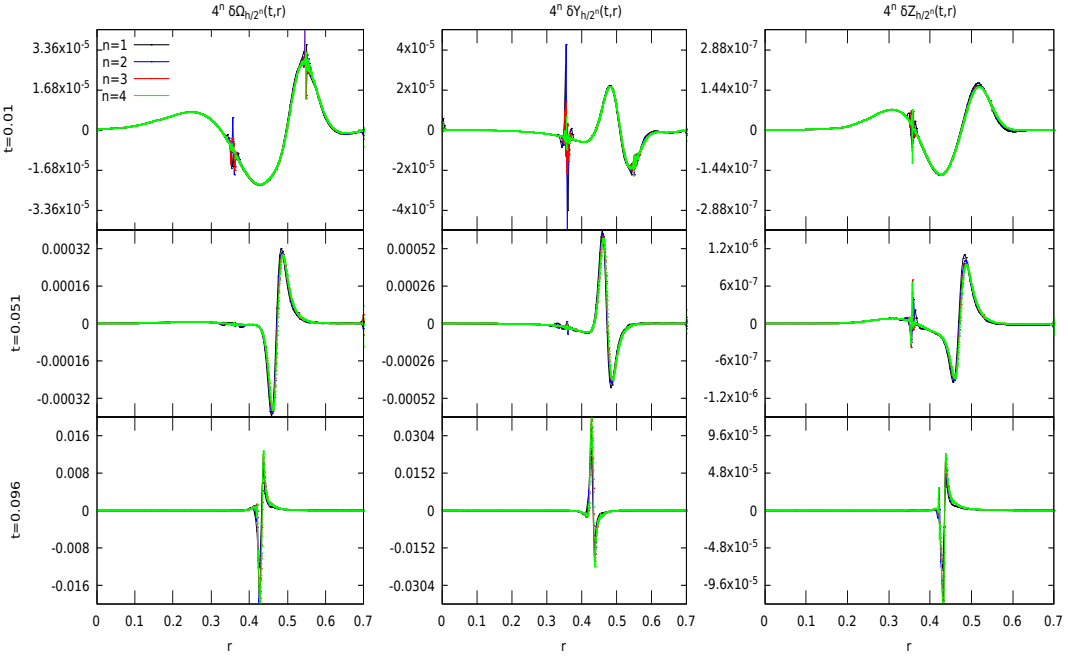

FIGURE 6.5: Collapse with slow rotation: Times are now $t = 0.010$, 0.051 and 0.096 (rows, from top to bottom), otherwise as in Fig. 6.1.

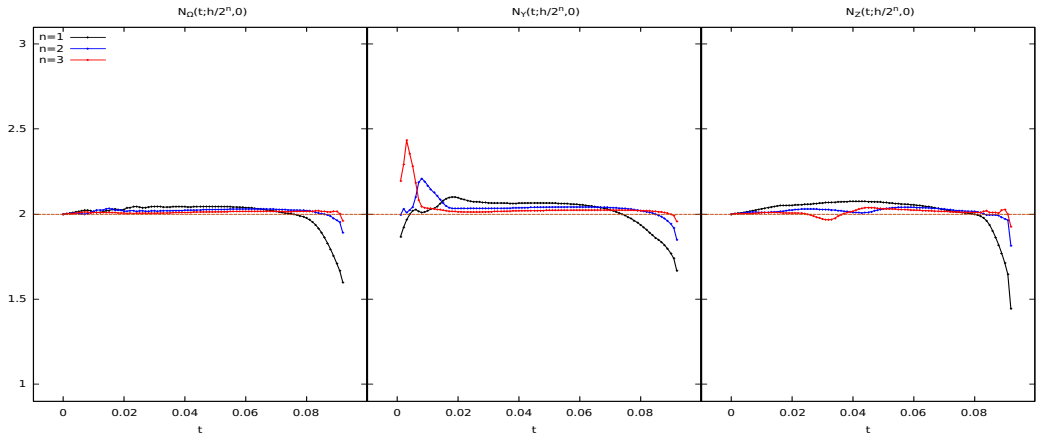

FIGURE 6.6: Collapse with slow rotation: Plots of $\mathcal{N}_{\bar{\mathbf{q}}}(t; \frac{h}{2^n}, 0)$, for $n = 1, 2, 3$. As always, the columns correspond to Ω, Y and Z from left to right. Due to the prompt collapse, second-order convergence is maintained throughout the evolution.

Turning our attention now to the collapse case, in Fig. 6.5 we show $4^n \delta\bar{\mathbf{q}}_{\frac{h}{2^n}}$ at four different resolutions $n = 1, 2, 3, 4$ at times $t = 0.01, 0.051$ and 0.096. We find the same qualitative behavior as for the dispersion case, except that the outer boundary behaves much better.

As a consequence, in Fig. 6.6, we only plot $\mathcal{N}_{\bar{\mathbf{q}}}(t; \frac{h}{2^n}, 0)$ as we have good second-order convergence without the need to truncate the grid. As for dispersion, the choice of limiter and which variables the outer boundary conditions are applied to do not produce any qualitative differences, except for the centered limiter which removes the oscillations already noted in the dispersion case, see Fig. 6.5.

Finally, in Figs. 6.7 and 6.8, we demonstrate second-order convergence for the case of

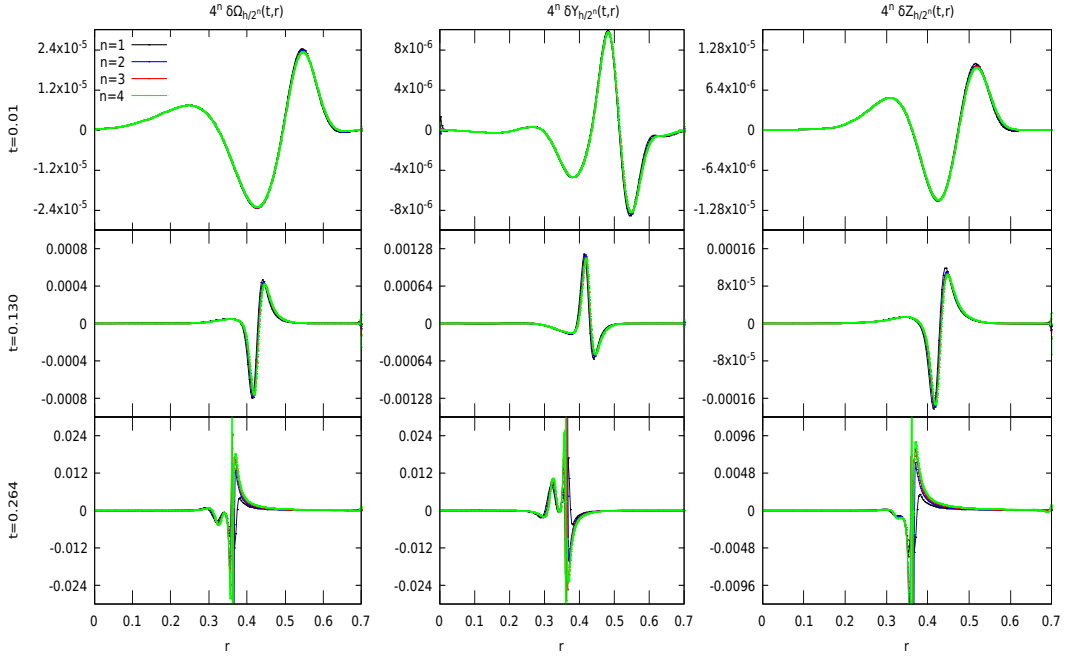

FIGURE 6.7: Collapse with rapid rotation: Times are now $t = 0.010, 0.130$ and 0.264, otherwise as in Fig. 6.5. Note that we lose second-order convergence at the onset of collapse and near the region of black hole formation.

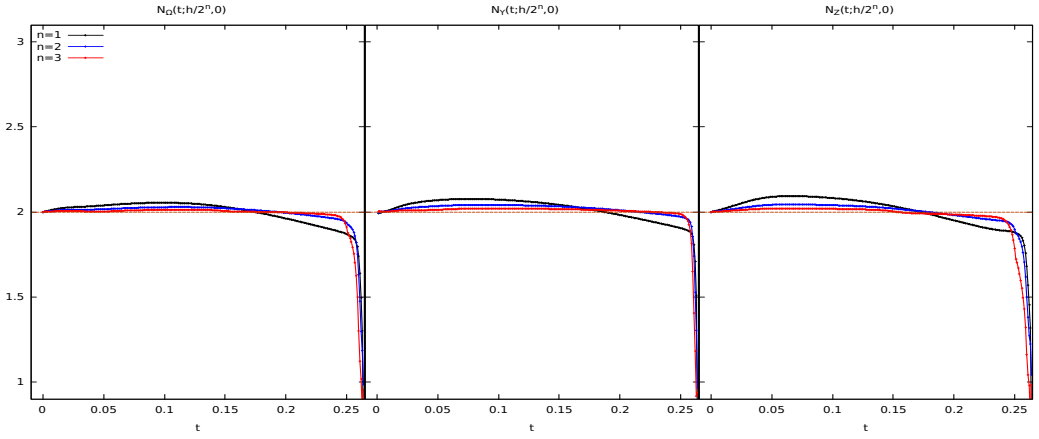

FIGURE 6.8: Collapse with rapid rotation: Otherwise as in Fig. 6.6. Second-order convergence is lost near the onset of collapse, as seen also in the last row (time) of Fig. 6.7.

rapidly rotating collapsing data. As one would expect, the presence of angular momentum delays the time of collapse. Near the onset of collapse the convergence drops to first-order near the region where the horizon forms.

6.6.3 Stable and unstable stars

In Ch. 5, we analyzed in detail the family of stationary solutions parametrized by two dimensionless constants, (Ω_0, μ) or equivalently $(\tilde{J}, M)$, where we defined the dimensionless spin

$$\tilde{J} := \frac{J}{\ell}. \tag{6.137}$$

In the parameter space (Ω_0, μ), it was shown that the set of parameters which result in a solution that is regular everywhere and asymptotes to a BTZ solution with $\tilde{J} \leq M$ is doubly covered for each admissible pair of values $(\tilde{J}, M)$. Both regions are separated by a curve on which solutions have a zero mode, i.e. a static linear perturbation that corresponds to an infinitesimal change in (Ω_0, μ) that leaves $(\tilde{J}, M)$ invariant to linear order.

Such a double cover is familiar in $3+1$ dimensions, where the less dense star is stable and the more dense star unstable. Analogously, it was conjectured that the solution with the smaller μ associated to a given $(\tilde{J}, M)$ is unstable, while the one with the larger μ is stable. We use this opportunity to provide some numerical evidence for this claim. Specifically, consider the pair of solutions with total mass and angular momentum given by $\tilde{J} = 0.24, M = 0.38$, corresponding to $(\Omega_0, \mu) \simeq (0.154, 0.242)$ and $(0.153, 0.392)$. These correspond to the black and orange dots in Fig. 5.1 and therefore to the unstable and stable solutions associated to the above conserved quantities $\tilde{J}, M$.

For both the stable and unstable configuration, we add a small Gaussian perturbation, with plus or minus sign. The Gaussian perturbation is of the form (6.134-6.136), with $|p_\omega| = 0.001$, $p_\eta = p_\zeta = 0$, $R_\omega = 0.4$, $\sigma_\omega = 0.2$. We set $r_{\text{max}} = 0.9$ and consider again five different resolutions, with the lowest resolution now 800 grid points, or $h \simeq 0.00015$. We choose a larger value of r_{max} because that the stationary initial data under consideration do not have a surface at some finite area radius. Consequently, one needs to choose a larger value of r_{max} to fit "most" of the energy density inside the numerical grid. We find that a MC or minmod limiter produces large oscillations in the evolution and that these are mostly tamed with a centered limiter. Furthermore, it is essential to use the primitive variables for the copy boundary conditions. Using the conserved variable instead causes the star to disperse almost immediately due to a perturbation originating from the outer boundary, while using the generic variables produces noticeably larger errors during the evolution. We will therefore restrict to this choice in what follows. Lastly, due to the nonvanishing of the conserved variables at the boundary, it is necessary to impose, as for the highly rotating collapse case, that the flux of Ω be non-negative at the numerical outer boundary. For the stable stationary initial data, we also impose the flux of Z to be positive at the numerical outer boundary. (Note that by construction, Z is non-negative everywhere initially).

Let us first consider the stable stationary solution. In Fig. 6.9, we plot $2^n \delta \bar{\mathbf{q}}_{\frac{h}{2^n}}$ at four different resolutions $n = 1, 2, 3, 4$. These are again plotted at three different times (rows), $t \simeq 0.04$, 1.2, 4.2. We only show the case $p_\omega = -0.001$ as the case where $p_\omega = 0.001$ is qualitatively similar. Note the different power of h from the dispersion/collapse case, due to the fact that we typically get less than second-order convergence. The cause of this is an oscillation originating from the outer boundary propagating inwards. At the time $t \simeq 4.2$, this oscillation has moved to and from the boundary twice. Equivalently, the time for the error originating from the numerical outer boundary to reach the center is $\Delta t \simeq 1.0$. As a consequence, the simulation losses its second-order accuracy everywhere. There is also an oscillation at and near the outer boundary that does not converge at all, but rather is roughly equal at different resolutions.

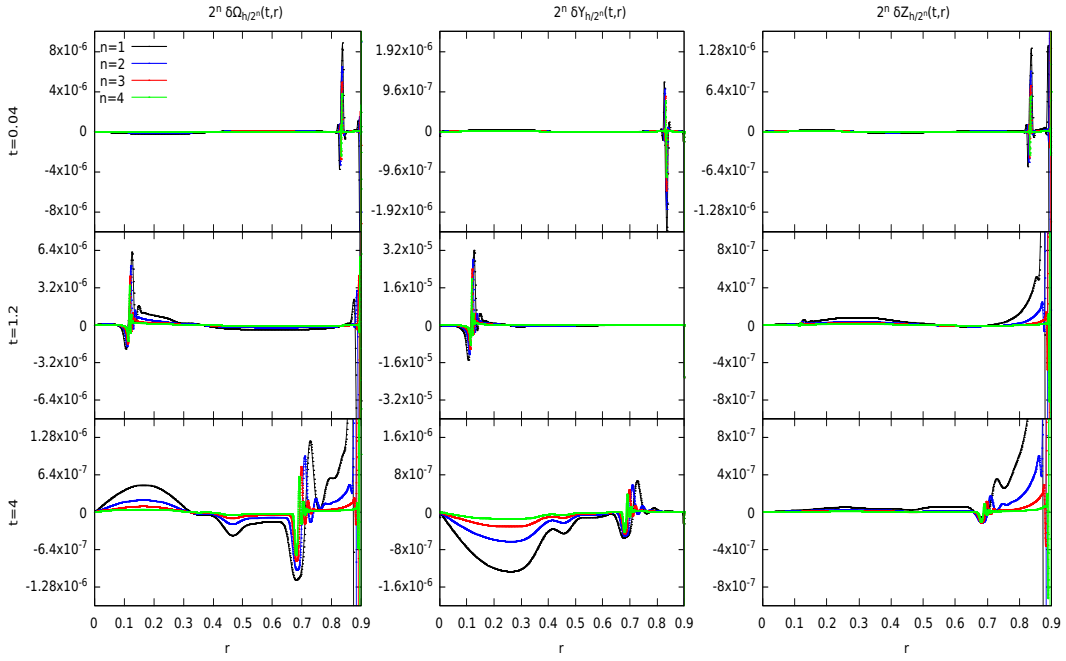

FIGURE 6.9: Stable stationary star: Times are now $t = 0.04$, 1.2 and 4 (rows, from top to bottom). We find $1 < \mathcal{N} < 2$ inside the numerical grid. The numerical error is dominated by the outer boundary. This error does not converge, but travels inward very slowly and its width shrinks with increased resolution.

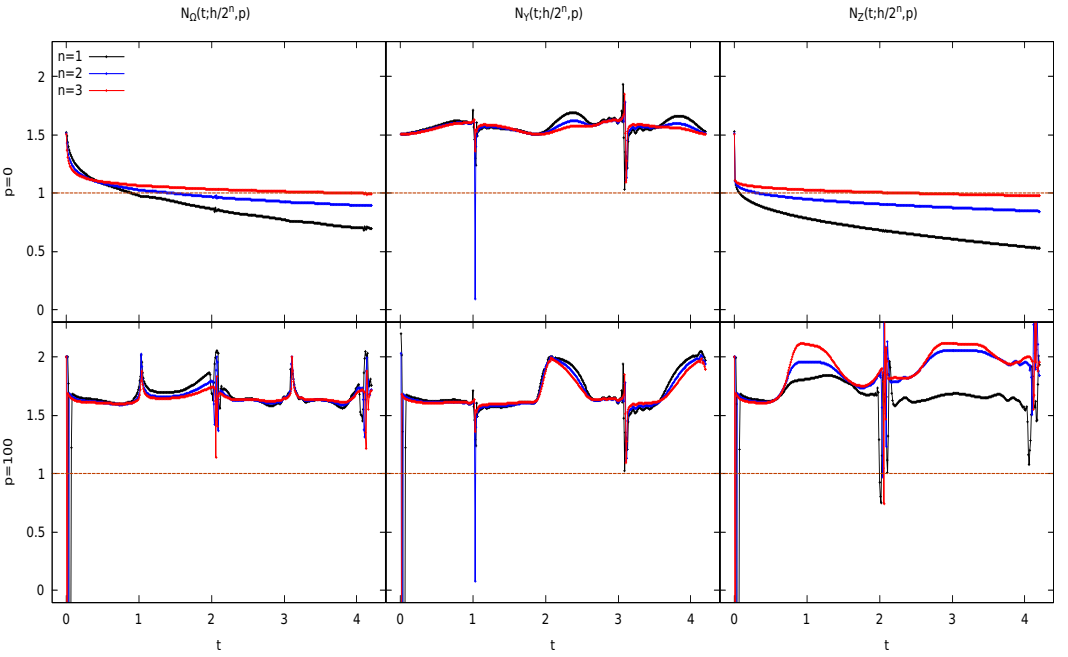

FIGURE 6.10: Stable stationary star: Plots of $\mathcal{N}_{\bar{\mathbf{q}}}(t; \frac{h}{2^n}, 0)$ (upper row) and $\mathcal{N}_{\bar{\mathbf{q}}}(t; \frac{h}{2^n}, 100)$ (bottom row), for $n = 1, 2, 3$. The dashed horizontal line corresponds to first-order convergence $\mathcal{N} = 1$. When the full grid is taken into account in the computation of the norm, we typically observe first-order convergence. On the other hand, by neglecting the last 100 grid points in the computation of the norm, we observe convergence of about $\mathcal{N} \simeq 1.5$ for Ω and Y and $\mathcal{N} \simeq 2$ for Z.

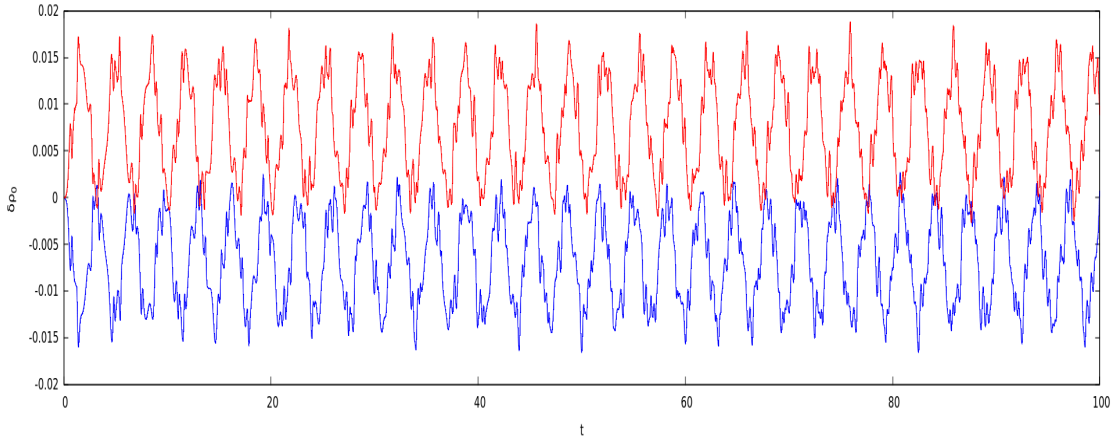

FIGURE 6.11: Stable stationary star: Central density perturbation against time for approximately 30 oscillation periods. Red curve corresponds to the stationary initial data with $p_\omega = 0.001$ and blue curve with $p_\omega = -0.001$.

Nevertheless, as in the case of dispersion, this oscillation propagates into the numerical grid very slowly and its size shrinks with increased resolution.

In Fig. 6.10, we plot the convergence in the norm. Due to the combination of the error originating from the outer boundary and the error near the boundary not converging at all, we find $\mathcal{N}_{\bar{\mathbf{q}}}(t; \frac{h}{2^n}, 0) \simeq 1$. Once the region near the outer boundary is neglected by removing the last 100 grid points, we recover approximate second-order convergence $\mathcal{N}_{\bar{\mathbf{q}}}(t; \frac{h}{2^n}, 100) \simeq 2$.

In Fig. 6.11, we plot the oscillations in the central density, $\delta\rho_0(t) := \rho_0(t) - \rho_0(0)$ for both signs of the perturbation, $p_\omega = \pm 0.001$. The simulation is run with 3200 grid points, for sufficiently long time so that the central density displays approximately 30 cycles. These oscillations maintain constant small amplitude, proportional to the initial perturbations, and we conjecture that they are essentially linear oscillations with constant frequency, as one would expect in a stable star. The central density oscillates about an average that is offset from the unperturbed star, because our perturbation of the initial data changes the total mass of the star. Our unphysical copy outer boundary condition does not seem to destroy this continuum property. It would be interesting to further analysis these oscillations. In particular, applying a fourier transform at different resolutions would allow to differentiate between physical breathing modes and numerical errors.

Note that when checking convergence, we only evolve the initial data up to at most $t = 4$. The reason is that for convergence testing, we consider much higher resolution than we do in Fig. 6.11. Compare for example the highest resolution run ($n = 5$, equivalent to 25600 gridpoints) when testing convergence, with the much lower resolution used to produce Fig. 6.11 ($n = 2$, equivalent to 3200 gridpoints).

Let us now turn to the unstable stationary solution. The convergence tests for both cases are summarized in Figs. 6.12 and 6.13 ($p_\omega = -0.001$) and Figs. 6.15 and 6.16 ($p_\omega = 0.001$).

Recall that for the unstable configuration, we have *not* imposed the positivity of the HLL flux for Z at the outer boundary, as we heuristically find that otherwise a small shock forms during the evolution, which prevents the simulation to converge to the desired order in the

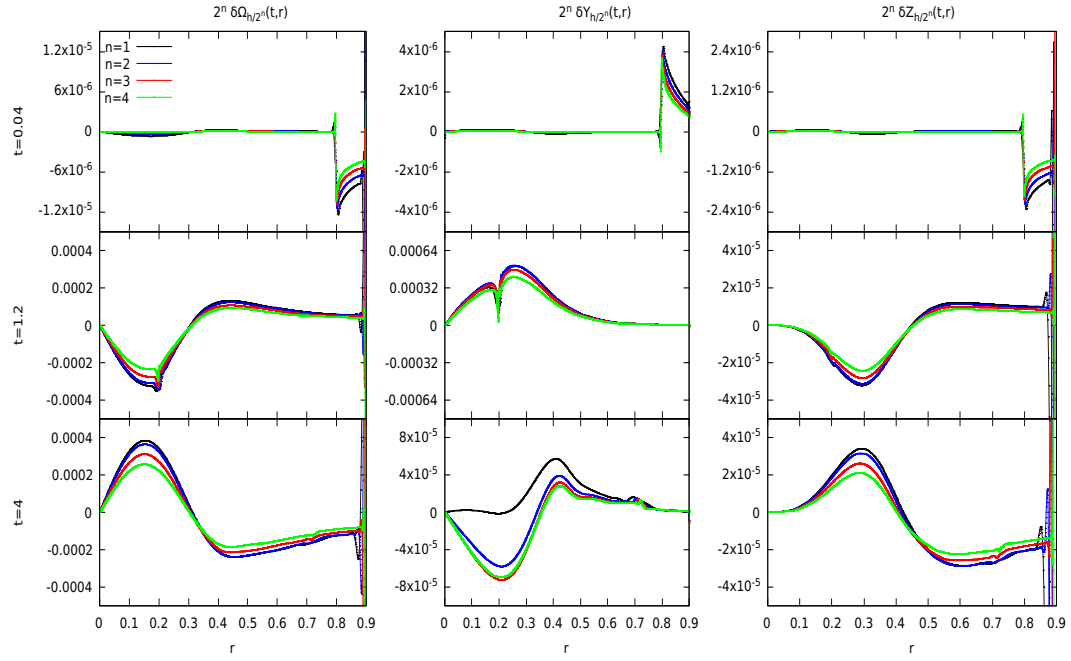

FIGURE 6.12: Unstable stationary star with negative density perturbation: A first-order error originating from the outer boundary travels inward, causing the evolution to converge only to first-order. Otherwise as in Fig. 6.9.

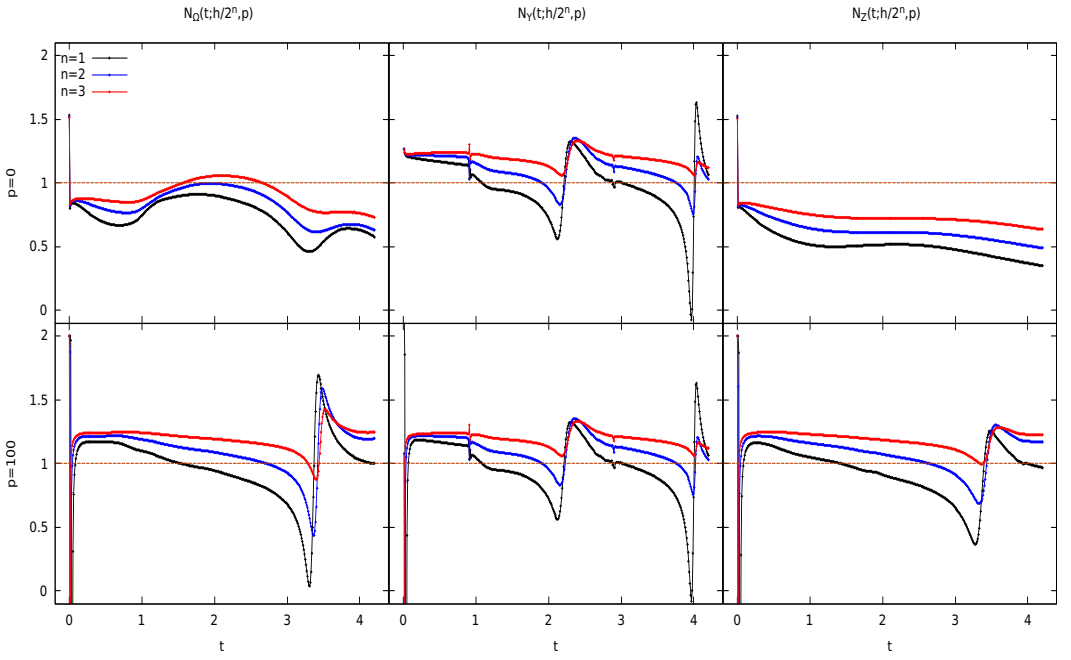

FIGURE 6.13: Unstable stationary star with negative density perturbation: Plots of $\mathcal{N}_{\bar{\mathbf{q}}}(t;\frac{h}{2^n},0)$ (upper row) and $\mathcal{N}_{\bar{\mathbf{q}}}(\frac{h}{2^n},100)$ (bottom row), for $n=1,2,3$. The dashed horizontal line corresponds to first-order convergence, $\mathcal{N}=1$. We find first-order convergence once the last 100 grid points are neglected.

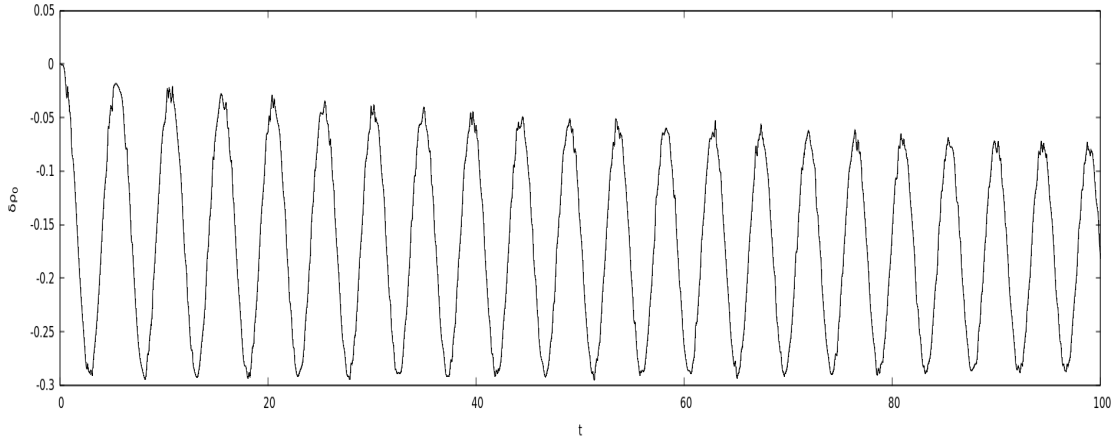

FIGURE 6.14: Unstable stationary star with negative density perturbation: Central density perturbation against time. The star breathes nonlinearly without collapsing. Compare with blue curve in Fig. 6.11.

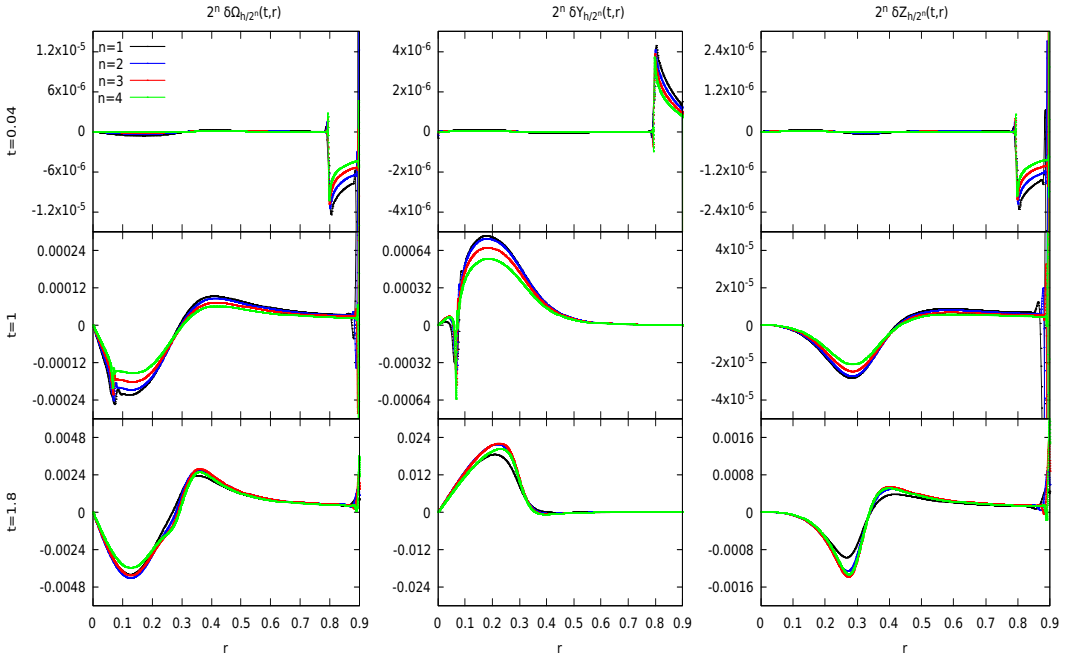

FIGURE 6.15: Unstable stationary star with positive density perturbation: We observe qualitatively similar behavior as for Fig. 6.12.

norm. On the other hand, lifting this constraint on the flux of Z causes a first-order error originating from the outer boundary to propagate inwards. The time for this error to reach the center (for both signs of p_ω) is $\Delta t \simeq 0.9$. The simulation is only about first-order accurate.

As for the stable configuration, there is also an oscillation at and near the outer boundary which does not converge at all, but rather is roughly equal at different resolutions. Nevertheless, this oscillation propagates into the numerical grid very slowly and its size shrinks with increased resolution. Such a behavior can also be noted for the stable configuration discussed above if the constraint on the positivity of the HLL flux of Z is removed there. In particular, a more careful treatment of the boundary conditions at the numerical outer boundary will be

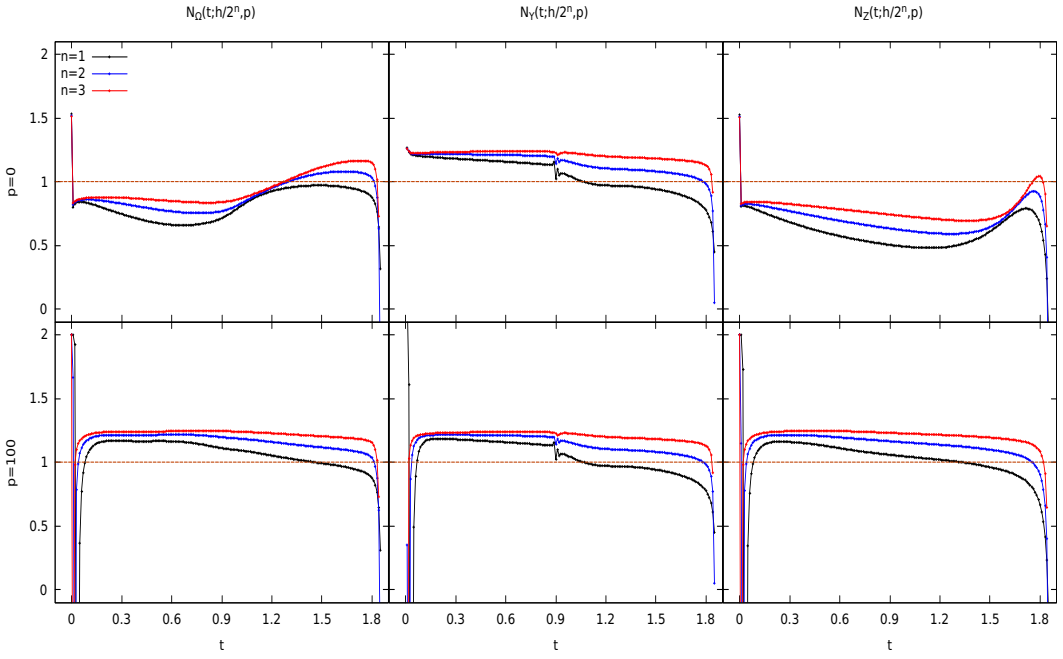

FIGURE 6.16: Unstable stationary star with positive density perturbation: Plots of $\mathcal{N}_{\bar{\mathbf{q}}}(t;\frac{h}{2^n},0)$ (upper row) and $\mathcal{N}_{\bar{\mathbf{q}}}(t;\frac{h}{2^n},100)$ (bottom row), for $n = 1,2,3$. The dashed horizontal line corresponds to first-order convergence. We find here fairly constant convergence of $\mathcal{N}_{\bar{\mathbf{q}}}(t;\frac{h}{2^n},100) \simeq 1.2$ up until the onset of collapse.

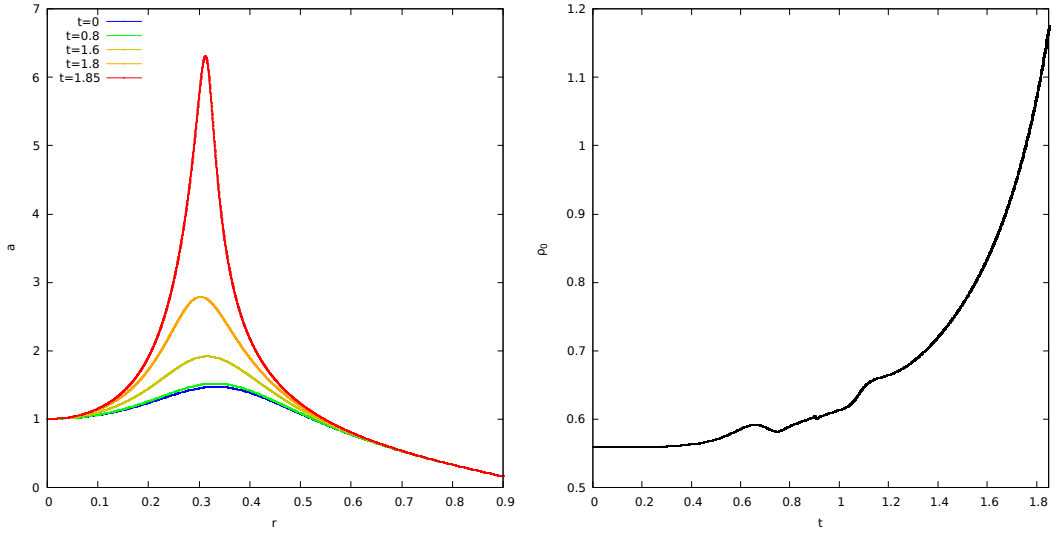

FIGURE 6.17: Unstable stationary star with positive density perturbation: We plot the metric coefficient $a(t_i,r)$ (left) at different times t_i, ranging from the initial time to the onset of collapse, as well as the central density against time (right). For this (positive) sign of the initial density perturbation, the star promptly collapses. Black-hole formation is triggered due to the timestep becoming small ($\Delta t \sim 10^{-10}$).

needed to accurately evolve the stationary solutions.

For a positive sign of the initial density perturbation, the star promptly collapses into a black hole, see Fig. 6.17. On the other hand, for a negative sign, the star does not collapse. Instead, it breathes, i.e. the central density oscillates periodically with very large amplitude, down to about half of the stationary value. This can be seen in Fig. 6.14, where we plot the central density perturbation $\delta\rho_0(t)$ at sufficiently long times for 30 cycles. The simulation is run with 3200 grid points as well. The local maxima stay approximately constant throughout the simulation, and the central density is approximately periodic.

It should be again emphasized that due to the fluctuating numerical convergence for the stable and oscillating unstable cases (see again Figs. 6.10 and 6.13), it is uncertain how much of Fig. 6.11 and Fig. 6.14 is physical or a numerical effect. Nonetheless, we can already observe qualitative differences in the evolution between the stable and unstable stationary initial data even at short times.

6.7 Conclusions

In this chapter, we have presented a new code to simulate the Einstein-fluid equations in axisymmetry in $2+1$ dimensions. We have focused on the ultrarelativistic equation of state $p = \kappa\rho$. However it should be straightforward to adapt the code to an arbitrary barotropic or hot equation of state.

In the case of generic initial data that disperse or collapse both with small and large angular momenta, we have demonstrated that the code converges to second order in resolution both pointwise and in the ℓ^2-norm, except at and near the numerical outer boundary, and near the onset of black hole collapse for highly rotating configurations.

We have also evolved stable and unstable rotating stationary stars. For these, the code converges only to first order. Nevertheless, we can clearly distinguish stable and unstable stars, even at short times. The former remain approximately stationary, with only small oscillations, while the latter show two distinct evolutions depending on the sign of the perturbation that we apply it to, either collapse or very large (but still periodic) oscillations. This provides some evidence in favor of our claim in Ch. 5, where it was suggested that the family of stationary stars with $|J| \leq M\ell$ is divided into two families of stable and unstable solutions.

A fundamental strength of our approach is that we make full use of the existence of two conserved matter currents (unexpectedly, for energy as well as, expectedly, for angular momentum) and related local expressions for the mass M and angular momentum J. As a consequence the metric evolution is fully constrained, and M and J are exactly conserved.

A well-known disadvantage of polar-radial coordinates is that our code stops as an apparent horizon is approached. However, one could in principle make equal use of the two conserved currents and conserved quantities in other coordinates.

The main weakness of our code as presented here is that we have not found a way of extending the outer boundary all the way to the timelike infinity of any asymptotically BTZ spacetime, in a way that is stable and accurate; see Sec. 6.5. This means that we have to impose an unphysical "copy" boundary condition at finite radius R. Fortunately, it turns out that, with

some fine-tuning, this does not prevent us from carrying out long-term (many sound-crossing times) evolutions of stars. Moreover, it also does not seem to be an obstacle in the investigation of critical phenomena at the threshold of (prompt) collapse, which we will investigate in Ch. 7.

Chapter 7

Critical collapse of a spherically symmetric fluid in $2+1$ dimensions

This chapter is taken from a paper submitted to Phys. Rev. D; see Ref. [3]. In this thesis, I added more details and explanations in Appendix G, where the quasistatic solution is derived.

The whole content of this chapter was done by me, with the exception of Appendix H, which was done by Carsten Gundlach.

7.1 Introduction

Since the seminal paper of Choptuik [52], it has become clear that for many simple, typically spherically symmetric, self-gravitating systems, such as a scalar field or perfect fluid, the evolutions of generic initial data close to the threshold of black hole formation exhibit several universal properties, which are now collectively called type II critical phenomena at the threshold of gravitational collapse. These are interesting in particular as a route to the formation of naked singularities from regular initial data; see Ref. [56] for a review.

Consider a one-parameter family of initial data with parameter p. Suppose that there exists a threshold value $p = p_\star$ so that supercritical initial data, $p > p_\star$, eventually collapses into a black hole, while subcritical initial data, $p < p_\star$, instead disperses.

In type II critical phenomena, one observes in the case of supercritical data that the black-hole mass obeys a power law $M \propto (p-p_\star)^\delta$, where the exponent $\delta > 0$ does not depend on the initial data. (It does depend on the type of matter, within certain universality classes). On the other hand, for subcritical data, it is the maximum curvature that scales, $\mathrm{Ric}_{\max} \propto (p_\star - p)^{-2\gamma}$, where $\gamma > 0$ is also independent of the initial data.

In $d+1$ dimensions with $d > 2$, owing to the fact that mass has dimension length^{d-2}, the exponents δ and γ are related to each other via $\delta = (d-2)\gamma$, as can be shown from dimensional analysis. These properties near the black-hole threshold are explained through the existence of a *critical solution*, which has the key properties of being regular, self-similar and having precisely one growing mode. This critical solution appears as an intermediate attractor in the time evolution of any near-critical initial data. As we fine-tune to the black-hole threshold, $p \to p_\star$, the (unique) growing mode is increasingly suppressed, so that the critical solution

persists on arbitrarily small scales and correspondingly large curvature without collapsing and thus without an event horizon forming. A naked singularity then forms at some finite central proper time for exactly critical data $p = p_\star$.

In type I critical phenomena (by contrast to type II), the critical solution is stationary, and instead of mass and curvature scaling, one observes scaling of the lifetime of its appearance as an intermediate attractor, $t_p \propto \ln|p - p_\star|$.

Critical phenomena in spherical symmetry have been observed in numerous matter models. Since black holes are in general characterized by their mass, charge, and angular momentum, the complete picture of critical phenomena necessarily requires investigation beyond spherical symmetry. However, even generalizing spherically symmetric initial data to axisymmetric ones brings substantial numerical and analytical complications in $3+1$ and higher dimensions. As a result, there have been far fewer studies devoted to studying critical phenomena beyond spherical symmetry.

For this reason, it may be helpful to investigate critical collapse in $2+1$ dimensional spacetime as a toy model. In $2+1$ dimensions, all variables are only functions of time and radius for both spherical symmetry and axisymmetry. This avoids much of the additional technical complication of axisymmetry. As in Ref. [87], we call a solution circularly symmetric if it admits a spacelike Killing vector ∂_θ with closed orbits. More specifically, we call it spherically symmetric if there is no rotation, and we call it axisymmetric with rotation.

An interesting peculiarity of $2+1$ is that black holes cannot form without the presence of a negative cosmological constant. This fact seemingly causes a paradox since, on the one hand, a cosmological constant is required for black holes to form, and thus for the possibility of critical phenomena to occur. On the other hand, one expects any type II critical solution to not depend on the cosmological constant, due to the fact that as the critical solution persists on arbitrarily small length scales, the cosmological constant is expected to become dynamically irrelevant, and so the underlying Einstein and fluid equations become approximately scale invariant. That is probably related at a deep level to the fact that in $2+1$ dimensions the mass is dimensionless and it follows that the usual argument to relate the two exponents δ and γ fails.

The only studies that have investigated critical phenomena in $2+1$ dimensions were restricted to the massless nonrotating [74, 78] and rotating [87] scalar fields. An interesting fact that emerged from those studies is that in $2+1$ dimensions, the nonrotating critical solution for the massless scalar field is *continuously* self-similar, as opposed to its $3+1$ version, where it is discretely self-similar. Furthermore, the critical solution is well approximated inside the past light cone of its singularity by exactly self-similar solutions to the $\Lambda = 0$ Einstein equations. Outside the light cone it can be approximated by a different $\Lambda = 0$ exact solution. This patchwork critical solution has three growing modes, but it is conjectured that when Λ is taken into account nonperturbatively, the true critical solution is analytic and retains only the top growing mode. This conjecture is in part supported by the fact that under this assumption, one can find a scaling law for the black-hole mass such that $\delta = 2\gamma/(2\gamma+1)$, consistent with the numerical results.

In this chapter, we study the spherically symmetric collapse of a perfect fluid in $2+1$ in anti-de Sitter (from now, adS) space with the linear (ultrarelativistic) equation of state $P = \kappa\rho$. Although an important motivation for looking at collapse in $2+1$ dimensions is that axisymmetry with rotation is as simple as spherical symmetry, we begin in this chapter with a study of spherically symmetric, nonrotating, collapse.

The structure of the chapter is as follows. In Sec. 7.2, we give a brief description of the equations we solve and their numerical implementation. We refer the reader to Ch. 6 for a complete discussion and details of our numerical implementation. In Sec. 7.3, we present the results of our numerical investigation of the threshold of prompt collapse for a spherically symmetric perfect fluid in $2+1$ dimensions. We show evidence of both type I and type II behavior depending on the value of κ. The type I critical solution is static, describing a metastable star. The type II critical solution shrinks quasistatically, moving adiabatically through the family of static stars. (A slightly different approximation is needed in the thin atmosphere of the star, where the outflow speed is relativistic.) Sec. 7.4 contains our conclusions. In Appendixes E to H, we show that no regular continuously self-similar solution exists, review the static solutions, show how they relate to the quasistatic solution and describe the stationary test fluid solution.

7.2 Einstein and fluid equations in polar-radial coordinates

We refer the reader to Ch. 6 for a complete discussion. We use units where $c = G = 1$.

In spherical symmetry in $2+1$ dimensions, we introduce generalized polar-radial coordinates as

$$\mathrm{d}s^2 = -\alpha^2(t,r)\,\mathrm{d}t^2 + a^2(t,r)R'^2(r)\,\mathrm{d}r^2 + R^2(r)\mathrm{d}\theta^2. \tag{7.1}$$

Note that our choice $g_{rr} = a^2R'^2$ makes a invariant under a redefinition of the radial coordinate, $r \to \tilde{r}(r)$.

We impose the gauge condition $\alpha(t,0) = 1$ (t is proper time at the center), and the regularity condition $a(t,0) = 1$ (no conical singularity at the center). The gauge is fully specified only after specifying the function $R(r)$. In our numerical simulations we use the compactified coordinate

$$R(r) = \ell\tan(r/\ell), \tag{7.2}$$

with different values of the cosmological scale ℓ defined by

$$\ell := \frac{1}{\sqrt{-\Lambda}}, \tag{7.3}$$

but for clarity we write R and R' rather than the explicit expressions.

In our coordinates, the Misner-Sharp mass M is given by

$$M(t,r) \;:=\; \frac{R^2}{\ell^2} - \frac{1}{a^2}. \tag{7.4}$$

The stress-energy tensor for a perfect fluid is

$$T_{ab} = (\rho + P)u_a u_b + P g_{ab}, \tag{7.5}$$

where u^a is tangential to the fluid worldlines, with $u^a u_a = -1$, and P and ρ are the pressure and total energy density measured in the fluid frame. In the following, we assume the one-parameter family of ultrarelativistic fluid equations of state $P = \kappa\rho$, where $0 < \kappa < 1$.

The 3-velocity is decomposed as

$$u^\mu = \{u^t, u^r, u^\theta\} = \Gamma \left\{ \frac{1}{\alpha}, \frac{v}{aR'}, 0 \right\}, \tag{7.6}$$

where v is the physical velocity of the fluid relative to observers at constant R, with $-1 < v < 1$, and

$$\Gamma := \left(1 - v^2\right)^{-1/2} \tag{7.7}$$

is the corresponding Lorentz factor.

The stress-energy conservation law $\nabla_a T^{ab} = 0$, which together with the equation of state governs the fluid evolution, can be written in balance law form

$$\mathbf{q}_{,t} + \mathbf{f}_{,r} = \mathbf{S}, \tag{7.8}$$

where we have defined the conserved quantities

$$\mathbf{q} := \{\Omega, Y\} \tag{7.9}$$

given by

$$\Omega := R' R \tau, \tag{7.10}$$

$$Y := R' v \sigma, \tag{7.11}$$

the corresponding fluxes $\mathbf{f}$ given by

$$f_{(\Omega)} := \frac{\alpha}{a} R v \sigma, \tag{7.12}$$

$$f_{(Y)} := \frac{\alpha}{a}(P + v^2 \sigma), \tag{7.13}$$

the corresponding sources $\mathbf{S}$ given by

$$S_{(\Omega)} := 0, \tag{7.14}$$

$$S_{(Y)} := a\alpha R R' \left[-\frac{v^2 \sigma}{a^2 R^2} + 2P(8\pi P - \Lambda) - \sigma\left(1 - v^2\right)(16\pi P - \Lambda) \right], \tag{7.15}$$

and the shorthands

$$\sigma := \Gamma^2(1+\kappa)\rho, \tag{7.16}$$
$$P := \kappa\rho, \tag{7.17}$$
$$\tau := \sigma - P. \tag{7.18}$$

In Eq. (7.15), we have already used some of the Einstein equations to express metric derivatives in terms of stress-energy terms.

At any given time, the balance laws [Eq. (7.8)] are used to compute time derivatives of the conserved quantities $\mathbf{q}$, using standard high-resolution shock-capturing methods. The $\mathbf{q}$'s are evolved to the next time step via a second-order Runge-Kutta step. At each (sub-)time step, the metric variables are then updated through the Einstein equations

$$(\ln \alpha a)_{,r} = 8\pi a^2 R R'(1+v^2)\sigma, \tag{7.19}$$
$$M_{,r} = 16\pi\Omega. \tag{7.20}$$

Our numerical scheme is totally constrained, in the sense that only the matter is updated through evolution equations. Our numerical scheme exploits this to make Ω and M exactly conserved in the discretized equations.

Another useful Einstein equation, compatible with the above ones via stress-energy conservation, is

$$M_{,t} = -16\pi f_{(\Omega)}. \tag{7.21}$$

7.3 Numerical results

7.3.1 Initial data

The numerical grid is equally spaced in the compactified coordinate r, as defined in Eq. (7.2), with 800 grid points, and for all values of Λ its outer boundary is fixed at the same area radius R. For reasons that will be made clear, we fix, unless otherwise stated, $R_{\max} \simeq 1.25$ for $\kappa \geq 0.43$ and $R_{\max} \simeq 10$ for $\kappa \leq 0.42$.

We choose to initialize the intermediate fluid variables

$$\omega := \frac{\Omega}{R'R}, \qquad \eta := \frac{Y}{R'R} \tag{7.22}$$

as double Gaussians in R,

$$\omega(0,R) = \frac{p_\omega}{2}\left(e^{-\left(\frac{R-R_\omega}{\sigma_\omega}\right)^2} + e^{-\left(\frac{R+R_\omega}{\sigma_\omega}\right)^2}\right), \tag{7.23}$$
$$\eta(0,R) = \frac{p_\eta}{2}\left(e^{-\left(\frac{R-R_\eta}{\sigma_\eta}\right)^2} + e^{-\left(\frac{R+R_\eta}{\sigma_\eta}\right)^2}\right). \tag{7.24}$$

Initial data ($\kappa = 0.5$)	p_-	$p_\star$	p_+
Off-centered, $\tilde{\mu} = 0.01$	0.280	0.309	0.324
Off-centered, $\tilde{\mu} = 0.1$	0.280	0.402	0.612
Centered, $\tilde{\mu} = 0.1$	0.995	1.174	1.354
Ingoing, $\tilde{\mu} = 0.1$	0.280	0.377	0.612
Off-centered, $\tilde{\mu} = 1$	0.280	0.531	3.087
Off-centered, $\tilde{\mu} = 10$	0.280	0.572	27.33

TABLE 7.1: The relation between p_-, $p_\star$, p_+, and the initial data that we are considering in this chapter for $\kappa = 0.5$.

where p_ω and p_η are the magnitudes, R_ω and R_η are the displacements from the center, and σ_ω and σ_η are the widths of the Gaussians. Note that p_ω has dimension length^{-2}, while p_η is dimensionless.

For $\kappa \geq 0.43$, we fix $\sigma_\omega = 0.2$ and $\sigma_\eta = 0.15$ and consider three types of initial data:

1) Time-symmetric off-centered: $p_\eta = 0$, $R_\omega = 0.4$,

2) Time-symmetric centered: $p_\eta = 0$, $R_\omega = 0$, and

3) Initially ingoing off-centered: $p_\eta = -0.2$, $R_\omega = R_\eta = 0.4$.

For $\kappa \leq 0.42$, we consider time-symmetric off-centered and ingoing initial data as given above, and time-symmetric centered $R_\omega = 0$, $\sigma_\omega = 0.05$, $p_\eta = 0$, and $\sigma_\eta = 0.15$.

In all cases, the remaining parameter $p_\omega =: p$ is fine-tuned to the black-hole threshold.

The space of initial data parametrized by p can be subdivided into four regions with boundaries $p_- < p_\star < p_+$ as follows: At $p = p_-$, the total mass is zero, $M_\infty = 0$, while $p = p_\star$ corresponds to the critical value separating subcritical (initially dispersing) from supercritical (promptly collapsing) initial data. Finally, p_+ is defined so that a trapped surface, characterized by $(\nabla R)^2 = 0$, is already present for initial data with $p > p_+$.

In $2+1$, black-hole solutions with $M_\infty > 0$ are separated from the vacuum adS solution $M_\infty = -1$ by a mass gap [58], so that no initial data with $p < p_-$ can collapse into a black hole.

As already stated, in $2+1$ dimensions, a negative cosmological constant is necessary for the formation of black holes, and thus for critical phenomena to occur. Since the cosmological constant introduces a length scale ℓ into the system, we need to consider different sizes of the initial data with respect to ℓ, which can be quantified by considering the dimensionless quantity

$$\tilde{\mu} := -\Lambda \sigma_\omega^2 = \left(\frac{\sigma_\omega}{\ell}\right)^2 . \tag{7.25}$$

σ_ω is kept fixed as given before, while we vary $\tilde{\mu}$ and thus ℓ. For $\kappa \geq 0.43$, we set $\tilde{\mu} = 0.1$. For $\kappa = 0.5$, we in addition study the cases $\tilde{\mu} = 0.01$, 1 and 10, corresponding to a range of values of the cosmological length scale that are "small" to "large" compared to the initial data. For $\kappa \leq 0.42$, we set $\Lambda = -\pi^2/4$ ($\tilde{\mu} \simeq 0.006$).

In Table 7.1, we record the values of p_-, $p_\star$ and p_+ for different families of initial data with $\kappa = 0.5$. Note that, unlike in higher dimensions, $p_- \to p_+$ as $\Lambda \to 0$.

Regularity at the timelike outer boundary of spacetimes with $\Lambda < 0$ does not allow a stress-energy flux through it. For a scalar field, this enforces homogeneous Dirichlet (reflecting) boundary conditions, whereas for perfect fluid matter its energy density needs to vanish at the boundary. Dynamically, this is enforced by an inward Hubble acceleration of the matter, so that any test particles on timelike geodesics, at least, must turn around inwards. Hence, it is *a priori* possible for data to collapse only after being reflected, possibly several times, from the boundary, as was observed for the massless scalar field in Ref. [128]. Since then, many more works were dedicated to studying the adS instability; see Ref. [157] and references therein.

As we impose (unphysical) outer boundary conditions at a finite radius, most of the energy that is outgoing in fact leaves the numerical domain. Thus, we cannot directly investigate the reflective property of adS here. In this sense, we fine-tune to the threshold of prompt collapse.

Independently, because of our polar time slices, our code stops when a trapped surface first appears on a time slice, and so we cannot obtain the final black-hole mass, so in this sense we measure the mass of the apparent horizon when it first touches a polar time slice. (However, it is likely that given enough time, all matter eventually falls into the black hole, so the black-hole mass becomes equal to the total mass M_∞.)

In the following, we are interested in initial data where $p \simeq p_\star$ and we refer to "sub$n$" data as subcritical data for which $\log_{10}(p_\star - p) \simeq -n$, and to "super$n$" as supercritical data with $\log_{10}(p - p_\star) \simeq -n$.

7.3.2 Overview of results

For the equation of state $P = \kappa\rho$ with $\kappa \lesssim 0.42$, we find type I critical phenomena: time evolutions of initial data near the black-hole threshold approach a static solution before either collapsing to a black hole or dispersing, and the time this intermediate attractor is seen for scales as $t_p \sim -\ln|p - p_\star|$. The static type I critical solution is not universal.

For $\kappa \gtrsim 0.43$ we observe scaling of the apparent horizon mass and maximum curvature as powers of distance to the threshold of (prompt) collapse, characteristic of type II critical phenomena. The type II critical solution is universal but not self-similar. It is instead quasistatic, running adiabatically through the one-parameter family of regular static solutions.

7.3.3 $\kappa \lesssim 0.42$: Type I critical collapse

7.3.3.1 Lifetime scaling

In type I critical phenomena, the critical solution is stationary or time-periodic instead of self-similar. Furthermore, there is a nonvanishing mass gap at the black-hole threshold, and so the critical solution is usually thought of as a metastable star.

In Fig. 7.1, we plot the apparent horizon mass M_{AH} against $p - p_\star$ for different values of κ. M_{AH} is computed via Eq. (7.4), evaluated at $R = R_{\text{AH}}$. R_{AH} is defined to be the point where a is maximal. For $\kappa \leq 0.42$, we find the existence of a mass gap, corresponding to type I critical phenomena. Similarly, the maximum curvature is bounded above, but we choose not to show it here in order to avoid cluttering. This plot was obtained using a second-order limiter. With

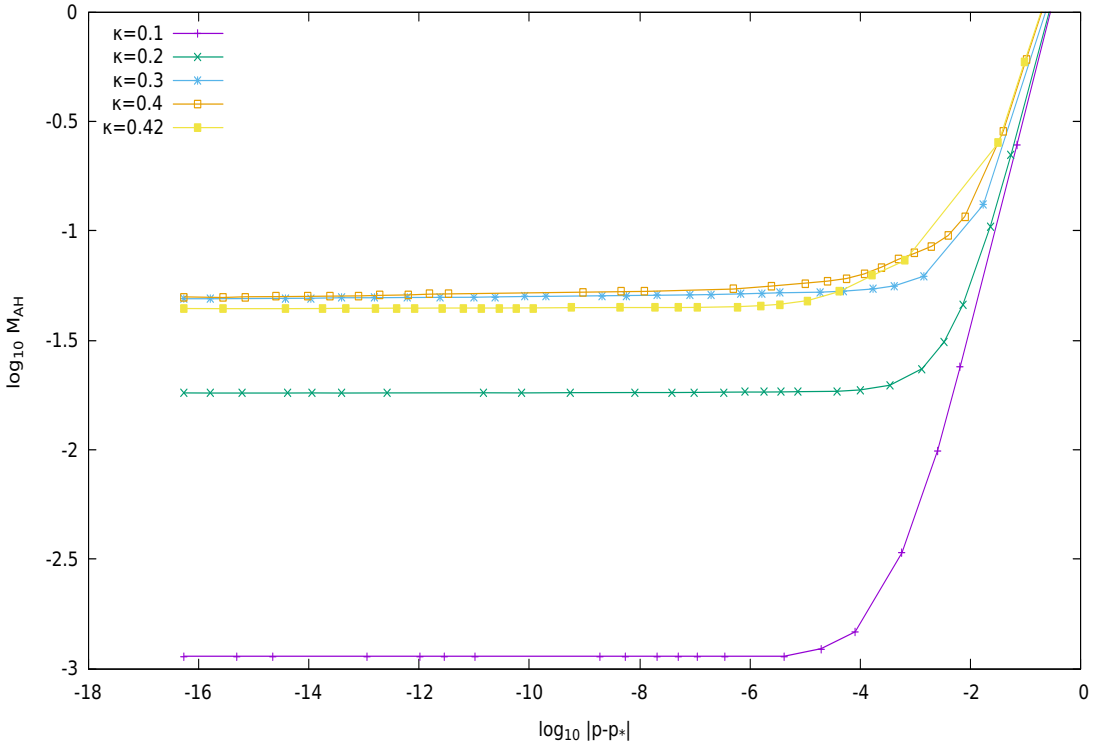

FIGURE 7.1: Apparent horizon mass for different values of $\kappa \leq 0.42$. The mass does not scale, and there is a mass gap at the black-hole threshold instead. We similarly find an upper bound for the maximum curvature.

a first-order (Godunov) flux limiter, the mass scales, but it does so in a step-size manner. We believe that this is an artifact of the Godunov limiter.

To further investigate the type I behavior, we need to define a measure of the length scale of the solution. We can do this by recording, for example, the central density and mass at the outer boundary, defined by

$$\rho_0(t) := \rho(t, 0), \quad M_{\rm OB}(t) := M(t, R_{\rm max}) \tag{7.26}$$

and the radius where the mass vanishes,

$$M(t, R_M(t)) := 0. \tag{7.27}$$

In Fig. 7.2, we plot $\sqrt{\rho_0^{-1}}$, $\sqrt{M_{\rm OB}}$, and R_M for off-centered (left) and centered (right) initial data with $\kappa = 0.4$, evolved with the monotonized central (MC) and Godunov limiters, respectively. Both sets of results are shown at different levels of fine-tuning.

In both cases, we see that R_M and $M_{\rm OB}$ are approximately constant during the critical regime. In the former case, the central density is subject to the apparition of periodic shocks, which cause the periodic structure for R_M and ρ_0. In the latter case, the periodic shocks are not present and the density converges to some finite value. We find that in this case $M_{\rm OB}$ and R_M evolve slightly. This is due to the fact that the Godunov limiter is known to introduce a great

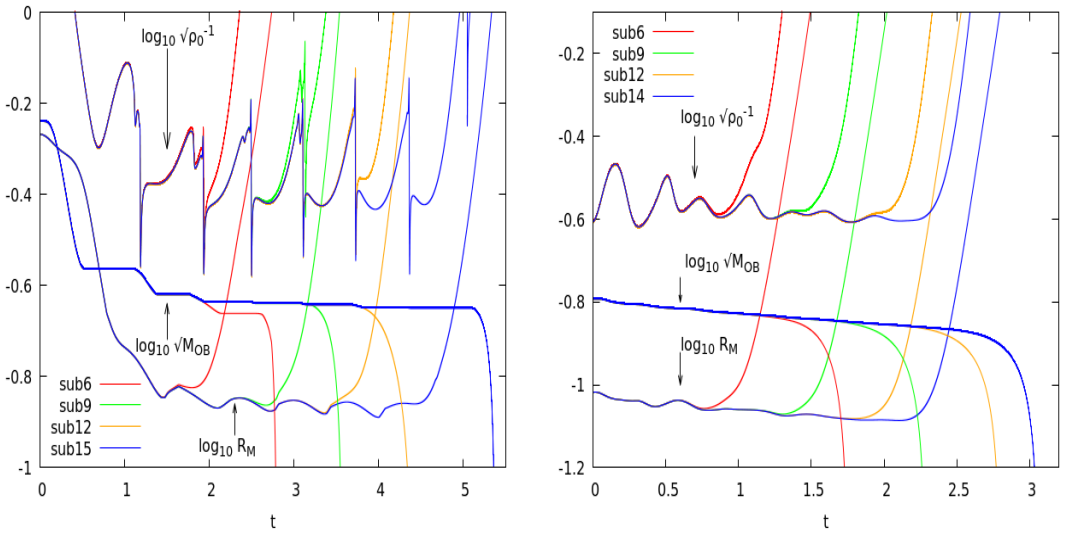

FIGURE 7.2: Linear-log-plot of $R_M(t)$, $\sqrt{\rho_0^{-1}(t)}$, and $\sqrt{M_{\rm OB}(t)}$ for the evolution of sub6-sub15 initial data with $\kappa = 0.4$. The plot on the left shows off-centered initial data, evolved with the MC limiter. The plot on the right shows more compact and centered initial data, evolved with the Godunov limiter.

deal of numerical diffusion [136]. A benefit of this diffusion is that the aforementioned shocks, developing at the outer boundary, are not present, and the density converges to some finite value. In both cases, however, less fine-tuned initial data peel off from the critical behavior faster than more fine-tuned data. This suggests that the critical solution has a single growing mode which is being progressively suppressed as we fine-tune to the black-hole threshold.

The shocks mentioned above in the case of the second-order limiter originate from the unphysical boundary conditions imposed at the numerical outer boundary. Although one might wonder how these shocks interact with the behavior of the critical solution, one can still reasonably believe that the type I phenomena are not a numerical artifact. One reason is that we still find type I phenomena in the second set of simulations described above, where the aforementioned oscillations do not occur.

As the critical solution does not depend on t, for its linear perturbations we can make the ansatz

$$\delta Z(t,x) = \sum_{i=0}^{\infty} C_i(p)\, e^{\sigma_i \frac{t}{\ell}}\, Z_i(x), \tag{7.28}$$

where Z stands for any dimensionless metric or matter variable.

By definition, the critical solution has a single growing mode, $\mathrm{Re}\,\sigma_0 > 0$. Since the solution is exactly critical at $p = p_\star$, this implies that $C_0(p) \sim p - p_\star$.

We define the time $t = t_p$ to be the time where the growing perturbation becomes nonlinear. We can take this to be

$$(p - p_\star) e^{\sigma_0 \frac{t_p}{\ell}} \simeq 1, \tag{7.29}$$

and so

$$t_p = \frac{\ell}{\sigma_0} \ln|p - p_\star| + \text{constant}. \tag{7.30}$$

κ	σ_0
0.30	4.97
0.32	5.54
0.34	5.89
0.36	6.46
0.38	7.19
0.40	8.84
0.42	9.70

TABLE 7.2: The value of σ_0 as a function of κ. We have obtained σ_0 from the lifetime scaling [Eq. (7.30)] of the critical solution.

The exponent σ_0 for $\kappa = 0.4$, for example, can be read off from Fig. 7.2. Specifically, we treat the value of p of our best fine-tuned data as a proxy for $p_\star$. We then record, as a function of $p - p_\star$ from sub8 to sub15 initial data, the time $t = t_p$ where, say R_M, peels off. We similarly compute σ_0 for other values of κ.

In Table 7.2, we show σ_0 for different values of κ and find that σ_0 increases approximately linearly with κ.

7.3.3.2 The critical solution

All spherically symmetric static solutions (and in fact all rigidly rotating axisymmetric stationary solutions) with $\Lambda \leq 0$ were found in Ref. [168], for arbitrary fluid equations of state.

In Ch. 5, we highlighted the existence of a two-parameter family of rigidly rotating static star solutions, for any causal equation of state, which are analytic everywhere including at the center, and have finite total mass M and angular momentum J. In particular, there is a one-parameter family of static solutions with a regular center and finite total mass, parameterized by an overall length scale s, see Appendix F for a summary of the notation and results for the specific equation of state $P = \kappa\rho$.

The equation of state $P = \kappa\rho$ itself is scale invariant, so in the absence of a cosmological constant, the dimensionless quantities

$$Z := \{R^2\rho, M, \alpha\} \tag{7.31}$$

characterizing a static solution can then only depend on R/s. However, the cosmological constant breaks scale invariance and so the family of static solutions instead takes the form

$$Z = \check{Z}\left(\frac{R}{s}, -\Lambda s^2\right), \tag{7.32}$$

where $\check{Z}$ is the corresponding exact static solution.

In what follows, all the quantities referring to the static solution have a check symbol, as in Eq. (7.32).

For $\Lambda < 0$, these stars have finite total mass (and to be a critical solution, the total mass needs to be positive), but the density ρ vanishes only asymptotically at infinity. For small

$\mu := -\Lambda s^2$, the star has an approximate surface [Eq. (F.13)] at $R \simeq s\check{x}_c$, separating the star proper from a thin atmosphere with negligible self-gravity. (We note that in the singular limit $\Lambda = 0$, the atmosphere disappears completely. The exterior solution is now vacuum with $M = 0$, and in particular the spatial geometry is a cylinder of constant radius.)

In Fig. 7.3, we provide some evidence that the critical solution is related to this family of static solution by plotting our best subcritical solution (with the Godunov limiter) at time $t \simeq 2$. This is compared to a member of the static solution, selected to satisfy the condition

$$\Lambda = 8\pi\kappa\rho_0(t) - \frac{1}{s^2(t)}. \tag{7.33}$$

at that time. This ensures that the central density is the same in the numerical and exact static solutions. We find reasonable agreement between the numerical and exact static solutions out to the surface and slightly beyond.

This can also be seen as a further consistency check that the type I phenomena are not a numerical artifact as it is otherwise unlikely that the numerical solution approaches an exact solution to the Einstein equations.

We find that the critical solution has different masses for the off-centered, centered and ingoing families of initial data, so clearly the type I critical solution is not universal.

7.3.4 $\kappa \gtrsim 0.43$: Type II critical collapse

7.3.4.1 Curvature and mass scaling

In type II critical collapse, in a region near the center, curvature becomes arbitrarily large as the solution approaches a critical solution with the following defining properties: it is regular, universal with respect to the initial data, shrinking, and it has precisely one unstable mode.

In spherical symmetry, and assuming a continuous, rather than discrete, scaling symmetry, there exists some adapted coordinate $x = R/s(t)$, for some function $s(t)$, where t is central proper time such that a vector $Z(t, x)$ of suitably scaled variables that characterizes a circularly symmetric solution of the Einstein and matter equations, is only a function of x, $Z(t, x) = Z_\star(x)$.

Since the existence of such a solution is a consequence of the (approximate) scale invariance of the underlying Einstein and matter equations, one would expect any quantity of dimension length^n to scale as $s(t)^n$. In particular, in $d + 1$ spacetime dimensions, one would expect the maximum curvature (say of the Ricci scalar $\mathrm{Ric}_{\max}$), and apparent horizon mass M_{AH} to scale as

$$\mathrm{Ric}_{\max} \sim s(t_\#)^{-2}, \quad M_{\mathrm{AH}} \sim s(t_\#)^{d-2} \tag{7.34}$$

where $s(t_\#)$ is the smallest scale the solution reaches before either dispersing or forming an apparent horizon.

As the critical solution is independent of t, for its linear perturbations we can make the ansatz

$$\delta Z(t, x) = \sum_{i=0}^{\infty} C_i(p)\, s(t)^{-\lambda_i}\, Z_i(x). \tag{7.35}$$

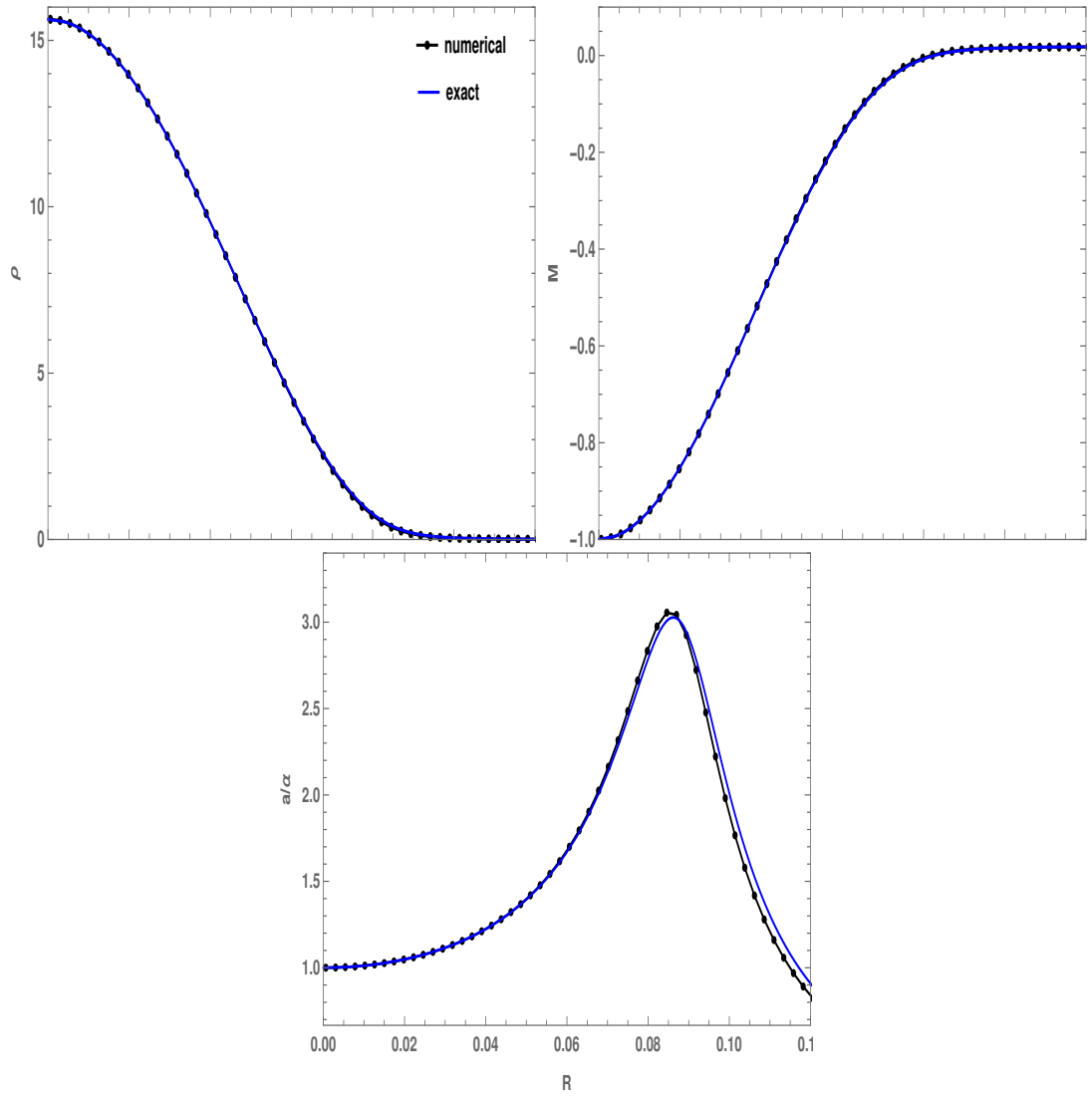

FIGURE 7.3: Plots of M, ρ, and a/α for sub14 centered initial data evolved with the Godunov limiter (black) with $\kappa = 0.4$ at $t \simeq 2$. This is compared with the exact static solution (blue), matched using Eq. (7.33).

We define $t = t_\star$ to be the time where $s(t_\star) = 0$. Since by definition the critical solution has a single growing mode, $\operatorname{Re}\lambda_0 > 0$, near the critical time $t \lesssim t_\star$, all other (decaying, $\operatorname{Re}\lambda_i < 0$) modes are negligible, and we therefore need the fact that $C_0(p) \sim p - p_\star$.

The time $t = t_\#$ when the growing perturbation becomes nonlinear occurs when $(p - p_\star)s(t_\#)^{-\lambda_0} \sim \mathcal{O}(1)$. Together with Eq. (7.34), one then deduces $\rho_{\max}$ and M_{AH} scale according to the power laws

$$M_{\mathrm{AH}} = c_M |p - p_\star|^\delta, \tag{7.36}$$

$$\mathrm{Ric}_{\max} \sim \rho_{\max} = -\Lambda c_\rho |p_\star - p|^{-2\gamma}, \tag{7.37}$$

where c_M and c_ρ are dimensionless constants, $\gamma = 1/\lambda_0$, and in space dimension $d \geq 3$, $\delta = (d-2)\gamma$.

We have here slightly generalized the discussion in Ref. [56], where $s(t) \propto t_\star - t$, with t as the proper time at the origin, because the critical solution is continuously self-similar (homothetic). We will see that the critical solution for type II critical fluid collapse in 2+1 dimensions is not self-similar, but the generalized discussion still applies.

In $d = 2$, the mass scaling and the value of δ cannot be derived by the simple dimensional analysis outlined above. In Ref. [74], Pretorius and Choptuik proposed that from the expression (7.4) for the Misner-Sharp mass, one has $M_{\rm AH} = -\Lambda R_{\rm AH}^2$, and so one would expect $M_{\rm AH} \sim s(t_\#)^2$. Furthermore, from the dimension of the curvature, one also expects $\rho_{\rm max}^{-1} \sim s(t_\#)^2$, which, combined with the previous expression, implies

$$M_{\rm AH} \sim -\Lambda \rho_{\rm max}^{-1}, \tag{7.38}$$

or $\delta = 2\gamma$. Although we will see that such a relation holds in the present case, the explanation should explicitly depend on the matter field under consideration, since a different relation has been shown to hold for the massless scalar field [78], where it was shown that $R_{\rm AH}$ does not scale as suggested by its dimension.

In our numerical investigation of type II critical collapse, we focus on the equation of state with $\kappa = 0.5$, where we have investigated possible critical behavior by bisecting between subcritical and supercritical data. Due to the small values of δ and γ (as compared to critical fluid collapse in 3+1 dimensions [65]), we observe scaling all the way down to $\log_{10}|p - p_\star| \simeq -15$ in double precision, even at fairly low numerical resolution and without mesh refinement, as the range of length scales is not large. We make use of this, or compensate for it, by working in quadruple precision, even at fairly low grid resolution. We can then fine-tune to about $\log_{10}|p - p_\star| \simeq -25$ before we lose resolution (without mesh refinement).

We observe that for $\tilde{\mu} = 0.01$, 0.1, 1, and 10, as we fine-tune to the black-hole threshold, $M_{\rm AH}$ becomes arbitrarily small while $\rho_{\rm max}$ becomes arbitrarily large. Moreover, both quantities scale so that their product is constant,

$$\frac{\rho_{\rm max} M_{\rm AH}}{-\Lambda} \simeq \mathcal{C}, \tag{7.39}$$

where $\mathcal{C}$ is a dimensionless constant independent of Λ.

Furthermore, we empirically observe that for sub15 data onwards, $M_{\rm AH}$ and $\rho_{\rm max}$ are well fitted by power laws (7.36) and (7.37), respectively, where the exponents are related by

$$\delta \simeq 2\gamma. \tag{7.40}$$

Note that from Eq. (7.39), $c_\rho c_M = \mathcal{C}$. The scaling laws are illustrated in Fig. 7.4, which shows $\ln M_{\rm AH}$ and $-\ln \rho_{\rm max}$ against $\ln|p - p_\star|$.

In Table 7.3, we record the values of $\mathcal{C}$, δ, and 2γ for different initial data and $\tilde{\mu}$. We find that the relation in Eq. (7.39) holds independently of the initial data. On the other hand, we cannot exclude that the exponents δ and 2γ depend weakly on $\tilde{\mu}$. Similarly, we find that $\mathcal{C}$ may weakly depend on both the initial data and $\tilde{\mu}$.

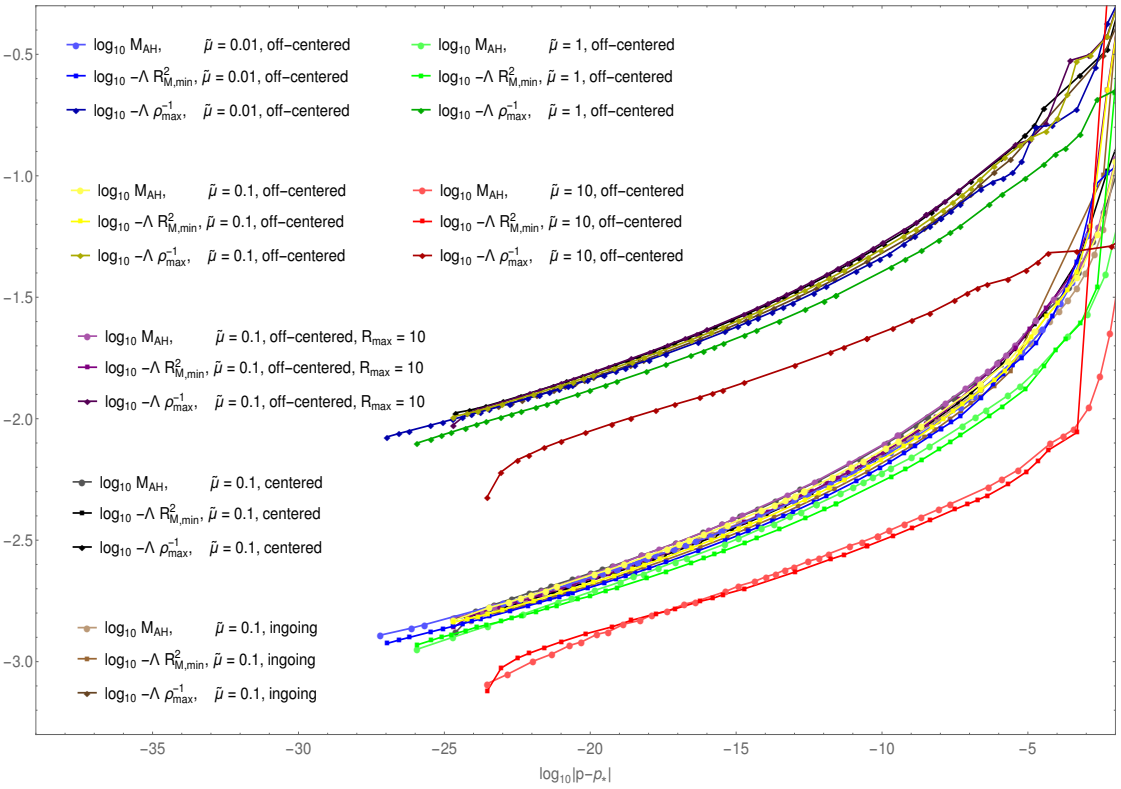

FIGURE 7.4: Log-log plot demonstrating the power-law scaling of $\rho_{\max}$ (upper group of curves), $M_{\rm AH}$ and $R_{M,\min}$ (lower group of curves) for different values of the cosmological constant, different outer boundary locations, and different initial data. The plot gives evidence that the relations $-\Lambda\rho_{\max}^{-1} \sim M_{\rm AH} \simeq -\Lambda R_{M,\min}^2$ hold, are universal, and are independent of the cosmological constant. The constants c_M, c_ρ, and c_R in general depend on the family of initial data and $\tilde{\mu}$, but here are almost universal except for $\tilde{\mu} = 10$ (curves somewhat below each group).

Initial data ($\kappa = 0.5$)	$\mathcal{C}$	δ	2γ
Off-centered, $\tilde{\mu} = 0.01$	0.148	0.0364	0.0371
Off-centered, $\tilde{\mu} = 0.1$	0.151	0.0413	0.0409
Centered, $\tilde{\mu} = 0.1$	0.170	0.0440	0.0410
Ingoing, $\tilde{\mu} = 0.1$	0.156	0.0417	0.0409
Off-centered, $\tilde{\mu} = 1$	0.161	0.0410	0.0389
Off-centered, $\tilde{\mu} = 10$	0.167	0.0427	0.0391

TABLE 7.3: The values of $\mathcal{C}$, δ, and 2γ for different initial data and $\tilde{\mu}$, all for $\kappa = 0.5$. These values are obtained by fitting a straight line to the log-log plots from super/sub15 to super/sub25 data points. (We only go to super/sub22 for $\tilde{\mu} = 10$).

We have checked that our results are not affected by the location of the (unphysical) outer boundary $R = R_{\max}$ by performing a bisection with $R_{\max} \simeq 10$.

7.3.4.2 The critical solution

In $3+1$ dimensions or higher, the critical solution exhibiting type II phenomena has always been found to be either continuously or discretely self-similar, depending on the matter field under consideration. The critical solution then only depends on $x = R/(t_\star - t)$ (in polar-radial

coordinates, with t normalized to be proper time at the center) in the continuous case, while in the discrete case, it also depends on the logarithm of $t_\star - t$, with some period Δ.

In $2+1$ dimensions, the presence of a cosmological constant is required for black holes to exist and thus for the possibility of critical phenomena to occur. Therefore, the Einstein equations are not scale-free, and as a consequence the critical solution cannot be *exactly* continuously or discretely self-similar. However, as the solution contracts to increasingly smaller scales, one expects the effect of the cosmological constant to become dynamically irrelevant. The critical solution could then again be approximated by an expansion in powers of (length scale of the solution)/ℓ, where the zeroth-order term is a self-similar solution of the $\Lambda = 0$ Einstein and matter equations. This is actually the case for the massless scalar field [78], where the critical solution is well approximated near the center by a continuously self-similar solution of the $\Lambda = 0$ field equations, but where the presence of Λ becomes relevant near the light cone.

However, it is shown in Appendix E that a regular self-similar solution does not exist for the perfect fluid with a barotropic equation of state in $2+1$ (in contrast to higher dimensions, where it is the type II critical solution). Given that we have type II critical collapse nevertheless, this raises the question of what form $s(t)$ takes.

In order to quantify $s(t)$, one can consider "candidate" functions $R_M(t)$ [defined previously; see Eq. (7.27)] and $R_v(t)$, defined by

$$v(t, R_v(t)) := 0. \tag{7.41}$$

Both of these functions are expected to be related to the size of the solution $s(t)$. We characterize the minimum size of the solution by $R_{M,\text{min}} := \min_t R_M(t)$. It turns out that this also scales as suggested by its dimension, i.e.,

$$R_{\text{M,min}} = \ell c_R |p - p_\star|^\gamma, \tag{7.42}$$

where c_R is a dimensionless constant; see Fig. 7.4.

In $2+1$ dimensions, the total mass of the spacetime must be positive for black holes to form. It is therefore instructive to see the evolution of the mass in the case of near-critical data. In Fig. 7.5, we plot $M(t_i, R)$ (left panel) and $v(t_i, R)$ (right panel) for sub25 off-centered initial data at times $t_i = 0,\ 0.25,\ 0.5,\ \cdots,\ 2.25,\ 2.37,\ 2.5$. Near the initial time, one part of the initial data shrinks, while the other part leaves the numerical domain, causing the mass at the numerical outer boundary to quickly decrease (green). As the data approaches a critical regime (red), the mass profile shrinks with t for $R \leq R_M(t)$, while for $R \geq R_v(t)$, the mass is approximately constant in R but asymptotes to 0^+ exponentially in t (see inset). The in-between region, $R_M(t) < R < R_v(t)$, is a transition region whose width shrinks with t; see Fig. 7.6. For our best subcritical data, we find $t_\# \simeq 2.1$, after which the mass disperses (blue) and the velocity is a positive function of R and attains values close to 1 (the speed of light).

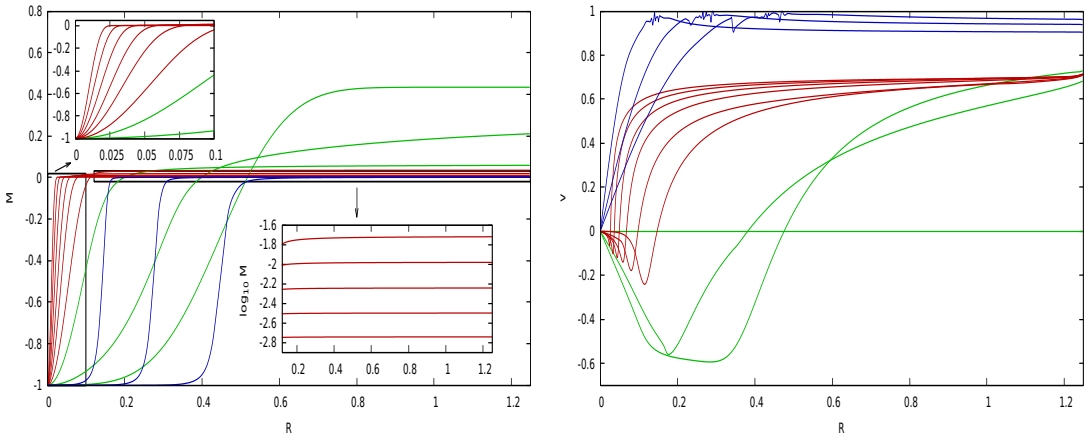

FIGURE 7.5: Plots of $M(t_i, R)$ (left) and $v(t_i, R)$ (right) at different times $t_i \simeq 0., 0.25, 0.5, \cdots, 2.25, 2.37, 2.5$ for our best subcritical data. The density profile shrinks and a large part of the total mass leaves the numerical domain (green). The evolution enters a critical regime (red) before dispersing (blue). In the bottom inset, the logarithm of the mass at large radius is plotted during the critical regime to show that it is almost constant in space and decays exponentially to zero. In the top inset, note that the contraction slows down. During dispersion, the velocity is close to 1 at $R \simeq 0.2$, causing numerical errors.

From dimensional analysis, the quantities $R_M(t)$ and $R_v(t)$, as well as the central proper density $\rho_0(t)$, are expected to be related to $s(t)$ as

$$\rho_0 \sim s(t)^{-2}, \qquad R_M(t) \sim R_v(t) \sim s(t). \tag{7.43}$$

In Fig. 7.6, we plot the logarithms of $R_M(t)$, $R_v(t)$, $\sqrt{\rho_0^{-1}(t)}$, and $\sqrt{M_{\rm OB}(t)}$ for sub5, sub10, sub15, sub20 and sub25 data. We find that these quantities are exponential functions of t, thus suggesting that $s(t)$ should also be an exponential. It should be noted here that for our best subcritical data, the duration of the critical regime, $\Delta t \simeq 1$, is sufficiently long to distinguish an exponential from a power law.

The exponential scaling lasts longer the more fine-tuned the initial data is to the black-hole threshold, while less fine-tuned initial data peel off sooner. This indicates that the critical solution has a single growing mode that is being increasingly suppressed as we fine-tune to the black-hole threshold.

It is useful to compare this plot with the left plot of Fig. 7.2, which was obtained with the same initial data and limiter but with $\kappa = 0.4$. There the proxies for $s(t)$ were approximately constant, while here we see clear exponential shrinking. Note that we do not observe here any numerical oscillation originating from the numerical outer boundary, as we did for $\kappa \leq 0.42$. The reason for this is that for $\kappa = 0.5$, near the numerical outer boundary, all three characteristic speeds of the fluid are positive.

A striking feature implied by the fact that $s(t)$ is exponential instead of polynomial in t is that $t_\star = \infty$. In fact, by the time the solution is entering the critical regime (at $t \simeq 1.1$), the speed of the contraction is small, with $\dot{R}_M, \dot{R}_v \sim \mathcal{O}\left(10^{-2}\right)$, and decreasing exponentially; see Fig. 7.6. In parallel, the maximum absolute value of the velocity in $R < R_v(t)$ also quickly decreases; see Fig. 7.5 (right panel).

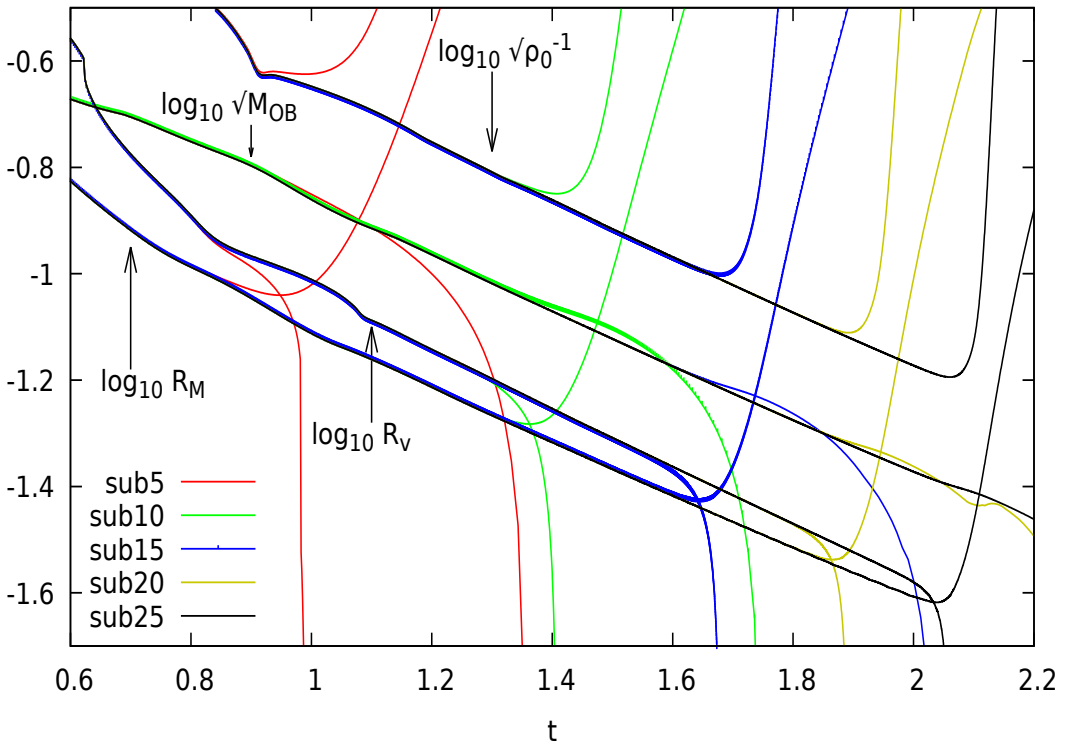

FIGURE 7.6: Log plot of $R_M(t)$, $R_v(t)$, $\sqrt{\rho_0^{-1}(t)}$, and $\sqrt{M_{\rm OB}(t)}$, for sub5 to sub25 off-centered initial data. We observe that as we fine-tune to the black-hole threshold, the solution approaches an intermediate attractor solution in which R_M, R_v, ρ_0^{-1}, and $M_{\rm OB}$ decrease exponentially. Less fine-tuned initial data peel off from this critical line sooner than more fine-tuned data, leading to critical scaling of the maximum density, etc.

As a consequence, if the critical solution is of the form $Z_\star(R/s(t))$, then, as $t \to t_\star = \infty$, the critical solution is essentially static near the center, so that near $t \simeq t_\#$, it can be expanded in powers of $\dot{s}$, and the leading-order term is then the static solution. The critical solution is in this sense *quasistatic*.

To leading order in a formal expansion in $\dot{s}$ (noting that $\dot{s}$ is dimensionless), the quasistatic solutions are then approximated by

$$Z_\star(t,R) \simeq \check{Z}\left(\frac{R}{s(t)}, -\Lambda s(t)^2\right), \tag{7.44}$$

where $s(t)$ is now slowly time dependent. In particular, near the center, $\check{Z}(x,\mu) \simeq Z(x,0)$ as $\mu \to 0$, and so the family of static solutions becomes asymptotically scale invariant as $\mu := -\Lambda s^2 = s^2/l^2 \ll 1$, meaning that the size s of the solution is much smaller than the cosmological length scale.

Since by definition the velocity vanishes for the static solution, one expects the velocity profile for the critical solution to be of the form

$$v_\star(t,R) \simeq \dot{s}(t)\,\check{v}_1\left(\frac{R}{s(t)}, -\Lambda s(t)^2\right), \tag{7.45}$$

to leading order in $\dot{s}$. In Appendix G, we give explicit expressions for $\check{Z}$ and $\check{v}_1$.

Let us therefore model the critical solution as a quasistatic solution, given to leading order by Eqs. (7.44), (7.45), and

$$s(t) \equiv s_0 e^{-\nu \frac{t}{\ell}}, \tag{7.46}$$

where s_0 has dimension length, while ν is dimensionless. These two parameters are fixed by imposing Eq. (7.33) at times $t = 1.1$ and $t = 1.9$, which roughly mark the beginning and end of the critical regime. This gives $s_0 \simeq 0.22$ and $\nu \simeq 0.78$. We find that ν is the same for our three different families of initial data, which gives some evidence that it is universal.

In Fig. 7.7, the critical solution is then compared to the leading-order term of the $\Lambda = 0$ (black dotted) and $\Lambda < 0$ (colored dotted) quasistatic solution in terms of $x := R/s(t)$.

Inside the star, the numerical solution is approximately a function of x only, implying that it is well approximated by the $\Lambda = 0$ family of static solutions. In the atmosphere, this is not true even for small Λ, for two separate reasons.

First, the $\Lambda = 0$ solution breaks down as an approximation to the $\Lambda < 0$ one at $x = x_\star$, where the $\Lambda = 0$ solution has a surface, whereas the $\Lambda < 0$ solutions transition to an atmosphere. Bringing in the explicit Λ dependence through the second argument of $\check{Z}$ then also brings in a dependence on time, as well as x.

Second, and more importantly, the quasistatic approximation still holds out to the beginning of the atmosphere but we notice that in Fig. 7.7, the quasistatic approximation systematically underestimates the falloff rate of the density and the velocity. In other words, the true critical solution achieves the same outgoing mass flux with a thinner atmosphere moving more relativistically than the quasistatic approximation. This means that a different ansatz than the quasistatic one should be made in this regime in order to correctly model the behavior of the solution there, and the two approximations should be matched in a transition region, in a similar spirit as for the massless scalar field case in Ref. [78].

Since the mass in the atmosphere is approximately constant in space, the fluid in the atmosphere can be modeled as a test fluid on a fixed BTZ spacetime, but not assuming that the v is small. An explicit solution under this approximation is given in Appendix H.

In Fig. 7.8, we plot, as in Fig. 7.7, the numerical and quasistatic solutions (dotted and dashed red lines, respectively) for our best subcritical time. In blue, we add the stationary test fluid solution where the mass is approximately constant. We find that the latter is a suitable ansatz for this atmosphere, as it correctly models both the relativistic speed of the fluid and the falloff rate of the density.

In Fig. 7.9, we plot the products $M_{\mathrm{OB}}(t)\rho_0(t)$ and $M_v(t)\rho_0(t)$, where M_v is the mass at $R_v(t)$, at different levels of fine-tuning. The static solution has the property that in the limit where $s \to 0$, the product $\check{M}_\infty \check{\rho}_0$ is a constant; see Eq. (F.21). We then expect the product $M_{\mathrm{OB}}(t)\rho_0(t)$ to approach this constant as the solution contracts, $s(t) \to 0$, where we consider $M_{\mathrm{OB}}(t)$ as a substitute for the total mass of the static solution. We find that during the critical regime, the product $M_{\mathrm{OB}}(t)\rho_0(t)$ is close to this theoretical value, although in our best subcritical data it eventually becomes larger at the end of the critical regime.

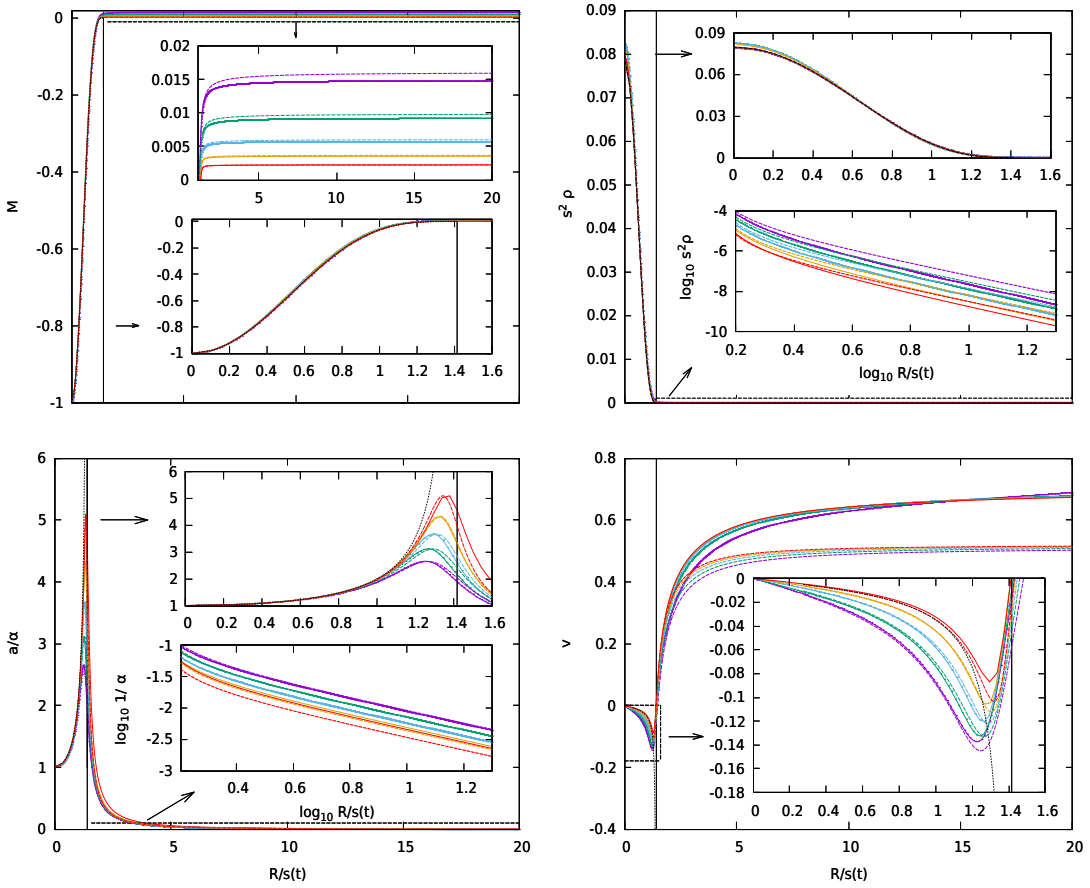

FIGURE 7.7: Numerical solution (solid colored lines) for M, $s^2\rho$, a/α, and v, plotted against $R/(s(t)$, at different times during the critical regime, $t \simeq 1.1, 1.3, 1.5, 1.7$, and 1.9. We have made a fit for s_0 and ν in $s(t) = s_0 e^{-\nu t/\ell}$. For comparison, we plot the leading-order term of the quasistatic $\Lambda = 0$ solution (black dotted line) and the $\Lambda < 0$ solution (colored dotted lines). The vertical black line corresponds to the location of the surface in the $\Lambda = 0$ exact static solution. For $\Lambda < 0$, there is no sharp surface.

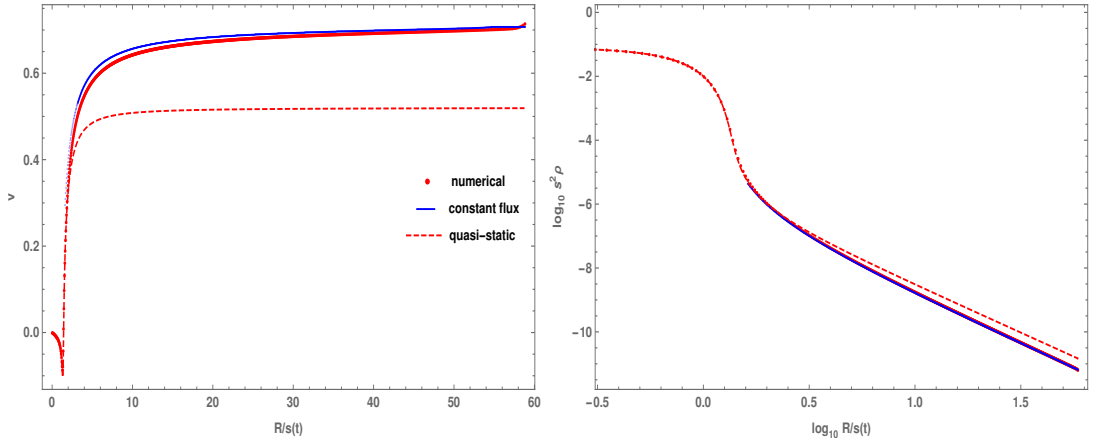

FIGURE 7.8: We compare the agreement between the numerical solution for our best subcritical data at $t = 1.9$ (red line), the quasistatic solution (dashed line), and the test fluid solution (blue line) on the entire numerical grid. The quasistatic solution underestimates the asymptotic value of the velocity, as well as the rate of decay of the density, (see also Fig. 7.7), while the constant flux solution correctly predicts these. The small upturn in v just inside the numerical outer boundary is believed to be an effect of the unphysical outer boundary condition.

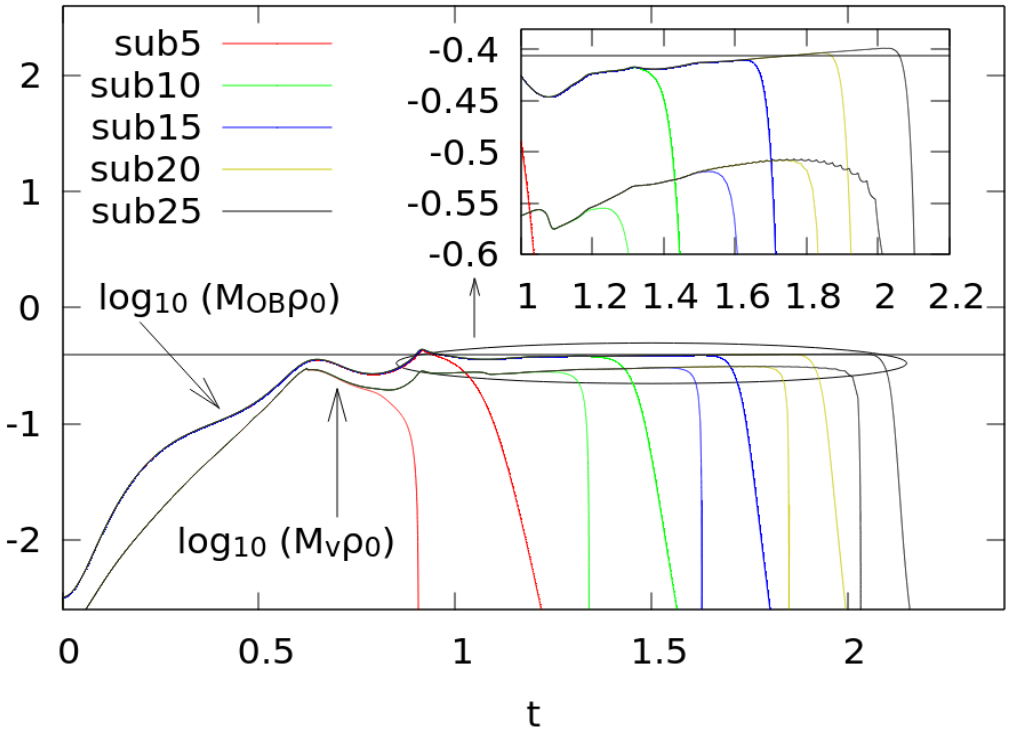

FIGURE 7.9: Log plot of $\rho_0(t)M_{\rm OB}(t)$, $\rho_0(t)M_v(t)$ for sub5 to sub25 data. The black horizontal line corresponds to $\log_{10}\left(\check{M}_\infty\check{\rho}_0\right)$ and shows that $M_{\rm OB}(t)$ is a good approximation for the total mass of the corresponding static solution.

In Fig. 7.10, we compare the fitted scale function $s(t)$ with the observed functions $R_v(t)$, $R_M(t)$ and $\rho_0(t)$, $M_{\rm OB}(t)$. We find that $x_\star s(t)$ approximately matches $R_v(t)$ in the critical regime, although the plot also suggests that $R_M \to x_\star s(t)$, very slowly. $s(t)$ also matches $R_M(t)$ and $\rho_0(t)M_{\rm OB}(t)$, up to constant factors.

We also see that $R_v \simeq s(t)\check{x}_c$, which suggests that $R_v \simeq R_{\rm AH}$ for supercritical data.

Finally, in Fig. 7.11, we provide some evidence for universality of the critical solution by plotting the numerical solution at a fixed time for different initial data. We plot the profiles of M, α, $R^2\rho$, and v for sub25 off-centered, centered and ingoing initial data with $\tilde{\mu} = 0.1$. Since $t_\#$ depends on the initial data, these three solutions were plotted at different times, namely $t \simeq 1.80$, 1.67, and 1.74, respectively, so that the profiles match up.

7.3.4.3 Derivation of scaling laws

In this section, we provide for a theoretical understanding of the observed law [Eq. (7.39)].

Motivated by our numerical results, we assume that the critical solution can, to leading order, be modeled as a quasistatic solution, $\check{Z}$; see Appendix G.

For this discussion, two properties of the family of static solution are of importance: First, the central density scales like $\check{\rho}_0 \sim \ell^{-2} \sim s^{-2}$; see Eq. (F.6). Second, the total mass of the system, assuming small $\mu \ll 1$, scales like $\check{M}_\infty \sim \mu \sim s^2$; see Eq. (F.18).

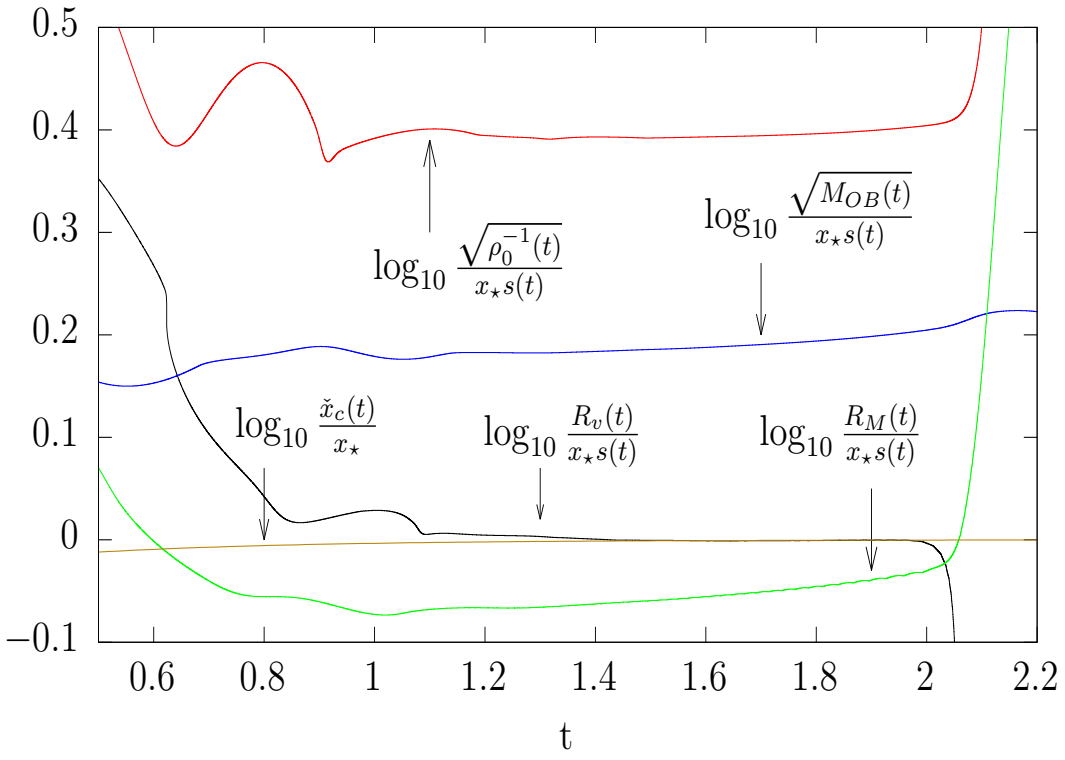

FIGURE 7.10: For sub25 data, we compare the values of $R_M(t)$, $R_v(t)$, $\rho_0(t)$, and $M_{\rm OB}(t)$ with $x_\star s(t)$ and $\check{x}_c(t)$, where $s(t)$ is the exponential function fitted to the numerical data in Fig. 7.7.

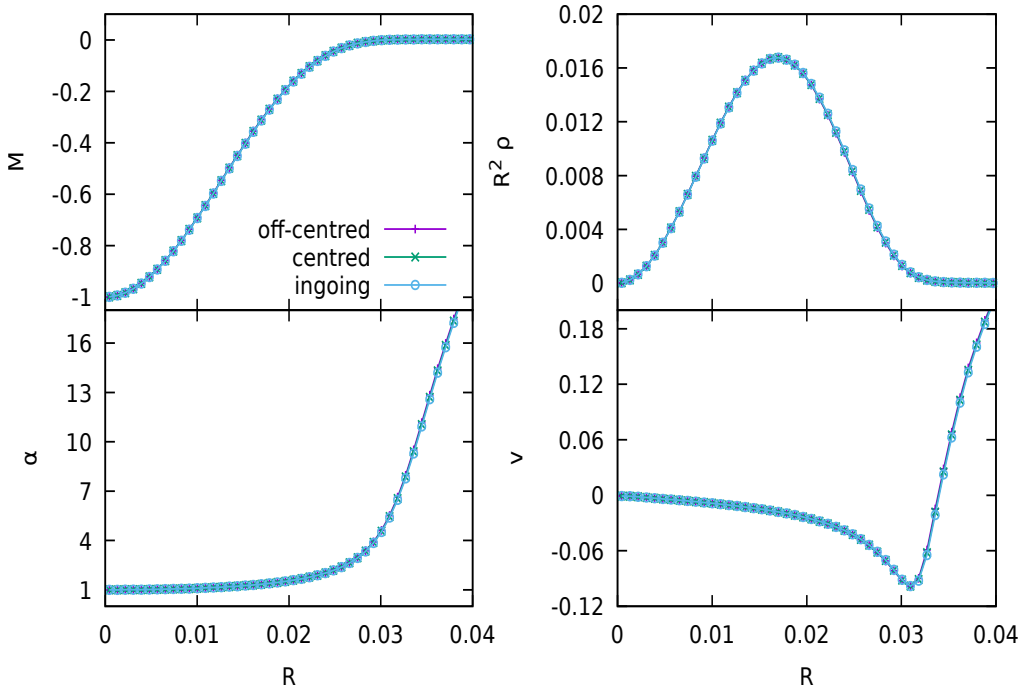

FIGURE 7.11: The profiles of M, $R^2\rho$, α, and v in the critical intermediate attractor solution for three different sub25 initial data, giving some evidence for universality. The data have been plotted at times $t \simeq 1.80$, 1.67, and 1.74, respectively, chosen to align them.

Since the maximum of the curvature is attained at the center, we can approximate

$$\rho_{\max} \simeq \rho_{0,\text{evolved}}(t_\#) \simeq \check{\rho}_0(-\Lambda s(t_\#)^2). \tag{7.47}$$

On the other hand, unlike for the density, one cannot simply make the approximation $M_{\text{AH}} \simeq M_\infty \simeq \check{M}_\infty$, since the total mass of the system is time independent and therefore cannot scale.

However, our numerical outer boundary does allow mass to escape. Moreover, we have seen that in the region from the surface of the shrinking star to the outer boundary, $M(t,r)$ is approximately constant in r and decreasing adiabatically in time, and that this observation does not depend on the location of the numerical outer boundary. We therefore conjecture that this atmosphere of constant mass flux is physical.

Somewhere further out, and beyond our numerical outer boundary, we would of course find enough mass to bring M_∞ to its time-independent value.

In the intermediate regime, between $R_v(t)$ (the point beyond which M is approximately constant in space) and the outer boundary M_{OB}, we can then approximate

$$M_{\text{intm.}}(t,R) \simeq \check{M}_\infty\left(-\Lambda s(t)^2\right) \sim s(t)^2. \tag{7.48}$$

As the black hole must form with $M>0$, and $M>0$ holds only in the intermediate regime, not inside the star, it follows that $R_{\text{AH}} > R_M(t)$. Furthermore, recall that from Fig. 7.10, in the critical regime $\check{x}_c(t) \simeq R_v(t)$, implying that $R_v(t_\#) \simeq R_{\text{AH}}$. It is then natural to assume that M_{AH} takes the above value, evaluated at $t_\#$. That is,

$$M_{\text{AH}} \simeq M_{\text{intm.}}(t_\#, R_{\text{AH}}) \sim s(t_\#)^{-2}. \tag{7.49}$$

Taking both approximations for $\rho_{\max}$ and M_{AH} in terms of $\check{\rho}_0$ and $\check{M}_\infty$ together into Eq. (F.21), we then infer the relation in Eq. (7.39).

This analysis also allows us to predict that $\mathcal{C} = (4\pi(1-\kappa))^{-1}$. For $\kappa = 0.5$, this gives $\mathcal{C} \simeq 0.16$, which is consistent with the numerical result; see Table 7.3.

7.3.5 Type I-II transition

For arbitrarily good fine-tuning, the type II apparent horizon mass becomes vanishingly small, while the type I mass is a family-dependent constant. In the region between $\kappa = 0.43$ and $\kappa = 0.5$, type II phenomena are still observed (see Fig. 7.12), but this is already a transition from type I to type II.

In Fig. 7.13, we compare the agreement between the quasistatic solution and the numerical results for $\check{v}_1$ for $\kappa = 0.47$ and 0.54, plotted at times $t = 1.3$, 1.45, 1.6, 1.75, 1.9 and $t = 0.9$, 1.0, 1.1, 1.2, 1.25, respectively.

For $\kappa = 0.54$, we find good agreement between the numerical time evolution and the quasistatic approximation inside the star. For $\kappa = 0.47$, we find much poorer agreement, even

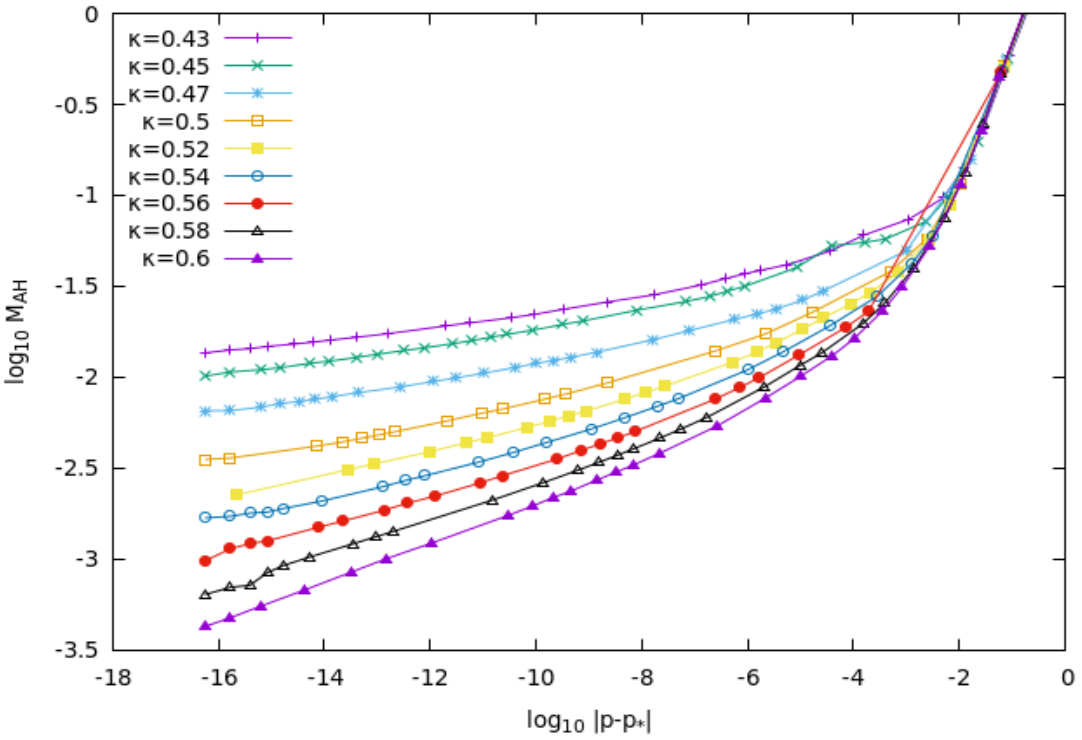

FIGURE 7.12: Apparent horizon mass scaling for different values of $\kappa \geq 0.43$. We find typical type II scaling. In all cases, the relation $\delta = 2\gamma$ is verified. Compare the equivalent (but flat) scaling laws for $\kappa \leq 0.42$ in Fig. 7.1.

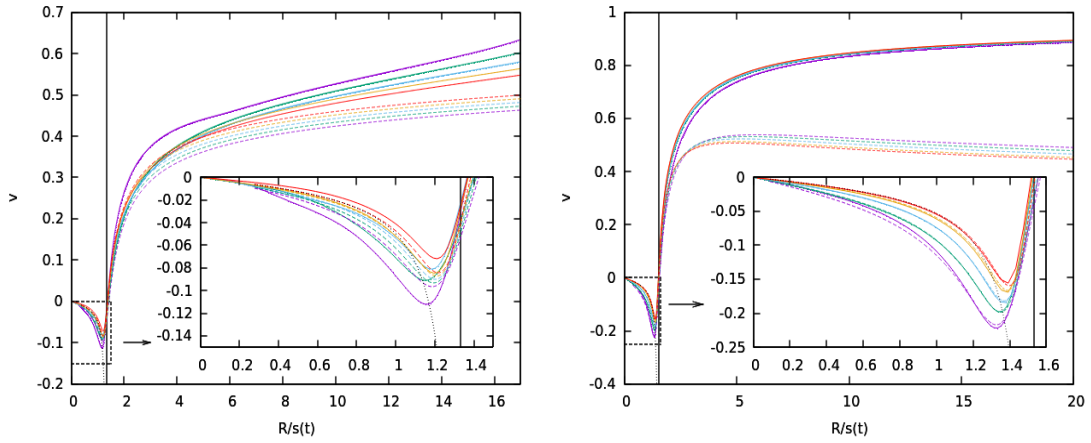

FIGURE 7.13: Comparison of the analytical and numerical expressions of $\check{v}_1$ for $\kappa = 0.47$ (left) and $\kappa = 0.54$ (right). The colored (dotted) lines follow a similar convention to Fig. 7.7.

near the center. As for the $\kappa = 0.5$ case, the test fluid solution is a much better model for the atmosphere of the critical solution for both $\kappa = 0.54$ and 0.47; see Fig. 7.14.

The exponential time dependence of the growing mode holds for both type I phenomena, where s is constant, and type II phenomena, where $s(t)$ is itself exponential. In the case of type II,

$$\text{growing mode} \sim e^{\frac{\sigma_0 t}{\ell}} \sim s(t)^{-\lambda_0} \sim \left(e^{-\frac{\nu t}{\ell}}\right)^{-\lambda_0}, \tag{7.50}$$

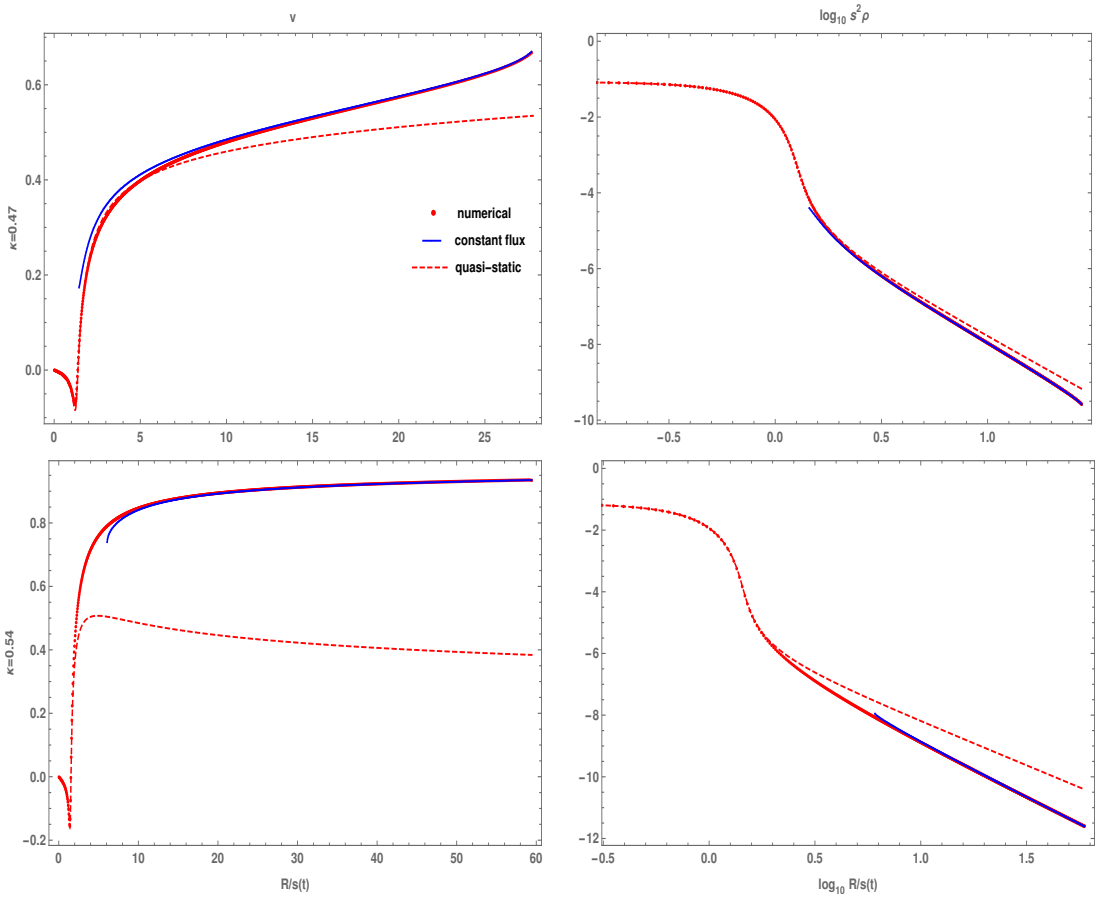

FIGURE 7.14: We compare the agreement between the numerical solution (red line), the quasistatic solution (dashed line), and the test fluid solution (blue line) for $\kappa = 0.47$ (top two plots) and $\kappa = 0.54$ (bottom two plots) for our best subcritical data at $t = 1.9$ and 1.25, respectively. Otherwise, as in Fig. 7.8.

and so we can express σ_0 in terms of λ_0 [Eq. (7.35)] (or γ) and ν [Eq. (7.46)] as

$$\sigma_0 = \nu\lambda_0, \tag{7.51}$$

and hence, with $\delta = 2/\lambda_0$,

$$\delta = \frac{2\nu}{\sigma_0}. \tag{7.52}$$

In Table 7.4, we give ν, δ, and σ_0 for different values of κ, and Eq. (7.52) is explicitly verified. The exponent σ_0 for the exponentially shrinking critical solution is computed in the same way as in the type I case.

Given that σ_0 is defined both in the type I and type II regimes of κ, one may ask if it is a smooth or at least continuous function of κ across both regimes. In Fig. 7.15, we plot σ_0 (top), ν (bottom left), and δ (bottom right) against κ. The data points are given in Tables 7.2 and 7.4. We find that ν and δ are monotonically increasing functions of κ. For $0.3 \leq \kappa \leq 0.42$ and $0.5 \leq \kappa \leq 0.6$, σ_0 depends linearly on κ. Due to shocks occurring for $\kappa \leq 0.42$ and causing a systematic error in the evaluation of σ_0 when we use a second-order limiter, the bisections and

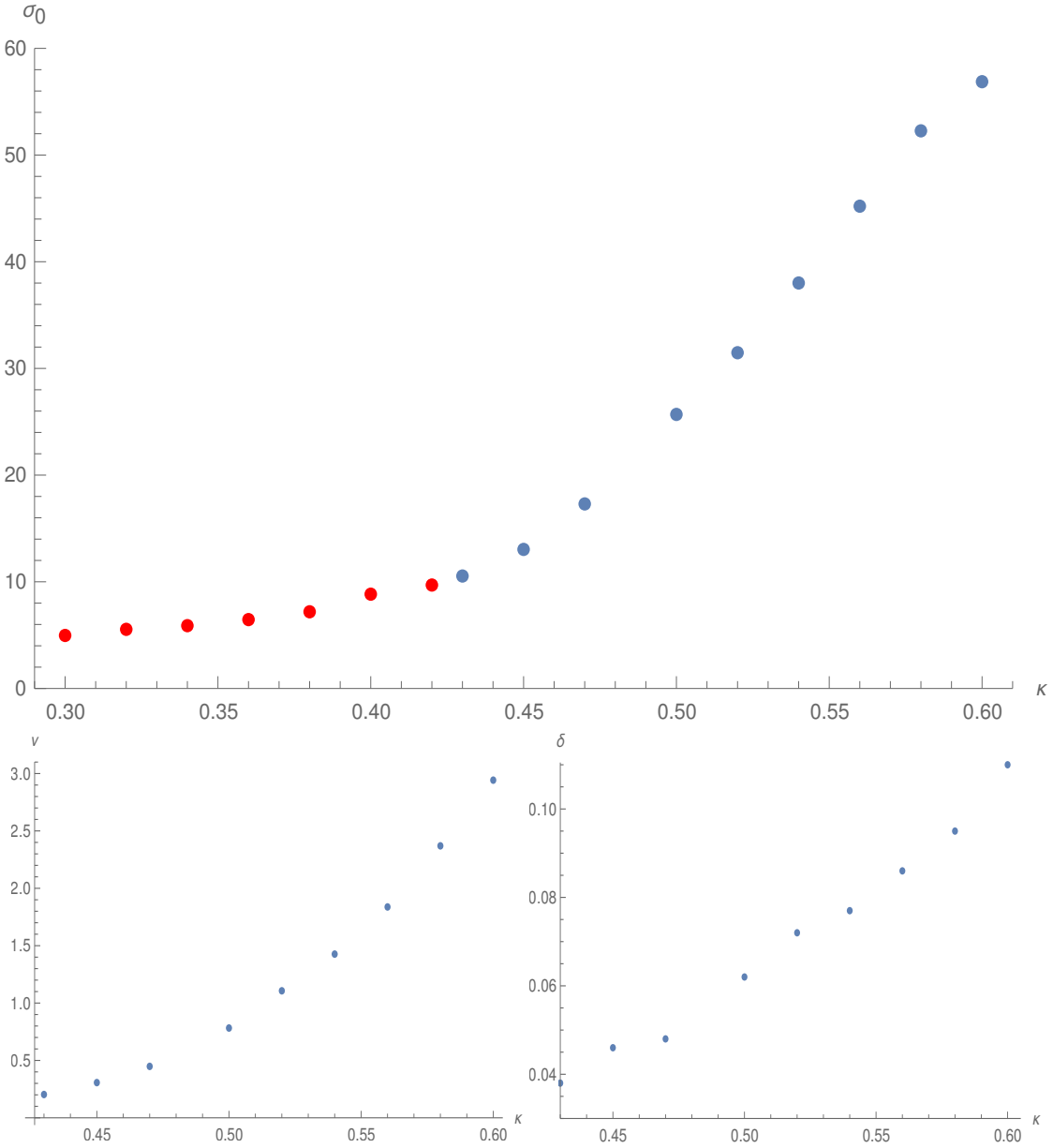

FIGURE 7.15: Plot of σ_0 (top), ν (bottom left) and δ (bottom right) against κ. We note that σ_0 appears to be continuous across the type I (red) to type II (blue) transition.

evolutions were performed using the Godunov limiter. We find that σ_0 is at least continuous in the transition from type I to type II phenomena.

Our plots are compatible with δ vanishing at $\kappa \simeq 0.42$ because ν vanishes there, while σ_0 remains finite. In other words, the unstable mode grows exponentially in time in the type I and type II critical solution, but this gives rise to type II mass and curvature power-law scaling only when the critical solution shrinks, also exponentially in time. At the transition from type II to type I in the equation-of-state parameter κ, the critical solution simply stops shrinking as $\nu(\kappa) \to 0$.

κ	ν	δ	σ_0	$\frac{\delta\sigma_0}{2\nu}$
0.43	0.203	0.038	10.54	0.99
0.45	0.307	0.046	13.03	0.98
0.47	0.448	0.048	17.30	0.93
0.50	0.782	0.062	25.69	1.02
0.52	1.107	0.072	31.47	1.02
0.54	1.427	0.077	38.01	1.03
0.56	1.838	0.086	45.21	1.06
0.58	2.370	0.095	52.27	1.05
0.60	2.943	0.110	56.88	1.06

TABLE 7.4: The values of ν, δ, and σ_0 as functions of κ. In type II, ν is obtained directly from the critical solution observed in our closest-to-critical time evolutions. As in type I, we have obtained σ_0 from the lifetime scaling [Eq. (7.30)] of the critical solution.

7.4 Conclusions

Critical collapse in 2+1 dimensions is an intriguing toy model for 3+1 dimensions, as in 2+1 dimensions axisymmetric solutions depend only on radius and time, making the simulation of rotating collapse as cheap as that of nonrotating collapse. By contrast, one expects complications from the fact that the existence and formation of black holes in 2+1 requires $\Lambda < 0$, which breaks the scale-invariance necessary for type II critical phenomena.

In our time evolutions of one-parameter families of initial data, for $\kappa \lesssim 0.42$ we find type I critical collapse: the maximum curvature and apparent horizon mass are constant beyond a certain level of fine-tuning. The critical solution is static, and the time for which it is observed scales as the logarithm of distance to the threshold of collapse.

For $\kappa \gtrsim 0.43$, we find type II critical collapse: At the threshold of (prompt) collapse, the maximum curvature diverges and the apparent horizon mass goes to zero. However, in contrast to 3+1 and higher dimensions, and even to scalar field collapse in 2+1, we find that the corresponding critical solution near the center is not self-similar, but quasistatic, moving through a family of regular static solutions of finite mass with scale parameter $s(t)$. Outside the central slowly shrinking star, the critical solution is better approximated as a test fluid in a background BTZ spacetime with $M \gtrsim 0$, moving mass away from the shrinking star at relativistic speeds.

The only other case of a critical solution at the boundary between blowup and dispersion that is quasistatic known to us is for a spherically symmetric ansatz for the Yang-Mills equations in 4+1 dimensions in flat spacetime (the critical dimension for that system, as 2+1 is for gravity). However, we have not been able to derive the observed exponential form of $s(t)$ from first principles along the lines of Refs. [175, 176].

However, there are also interesting parallels, not yet sufficiently understood, with the self-similar critical solution in 2+1 spherically symmetric scalar field collapse [78]. The critical solution in both 2+1-dimensional systems has a clear separation between a contracting inner region where M increases from -1 at the regular center to a very small positive value at the boundary of the shrinking central region, and an outer region, where M remains approximately constant and the matter is purely outgoing.

We have tentatively derived the type II mass scaling law $\delta = 2\gamma$ from the observation that the mass in the atmosphere of the quasistatic critical solution scales as $M(t) \sim -\Lambda s(t)^2$, and the natural assumption that the apparent horizon mass is given by this mass at the moment when the evolution leaves the critical solution.

In summary, general relativity finds a way of making arbitrarily large curvature and arbitrarily small black holes at the threshold of collapse, even in 2+1 spacetime dimensions. It has to do this in ingenious ways quite differently from 3+1 and higher dimensions. Moreover, it does so very differently for the perfect fluid with ultrarelativistic equation of state $P = \kappa\rho$ (for $\kappa \gtrsim 0.43$) and the massless scalar field [78].

Chapter 8

Critical collapse of an axisymmetric fluid in $2+1$ dimensions

This chapter is taken from a paper submitted to Phys. Rev. D; see Ref. [4]. The whole content of this chapter was done by me.

8.1 Introduction

Critical collapse is concerned with the threshold of black-hole formation in the space of initial data. Starting with Choptuik's study of the spherically symmetric, massless scalar field [52], and since then generalized to many other systems [56], one can enumerate several general features of critical phenomena. The more interesting kind is now called "type II" phenomena. As the black-hole threshold is approached through the fine-tuning of a one-parameter family of initial data, the black-hole mass and spacetime curvature scale as a power of distance to the black-hole threshold. Furthermore, for initial data close to the black-hole threshold, the solution will be, in an intermediary stage, well approximated by a *critical solution*. This critical solution has the general characteristics of being self-similar, universal (independent of the initial data) and possessing a single growing linear perturbation mode. By contrast, in "type I" phenomena, the mass and curvature do not scale, but instead approach a nontrivial constant. The critical solution is time-periodic or stationary. The above properties for type I and II phenomena hold for all matter systems studied thus far in $3+1$ and all higher dimensions; see Ref. [56] for a review.

The vast majority of research studies dedicated to critical collapse focuses on spherically symmetric initial data. Since black holes can carry angular momentum, the full picture of critical collapse requires us to go beyond spherical symmetry. However, the generalization from spherically symmetric to, say, axisymmetric initial data brings about many numerical and theoretical complications. In part, one has to deal with an additional independent variable. Moreover, gravitational waves exist beyond spherical symmetry, and they can exhibit (type II) critical phenomena by themselves [93]. In particular, this implies that, if one wishes to study the critical phenomena of some matter field in axisymmetry, one will have to disentangle the critical phenomena due to the matter field and those due to gravitational waves. This additional

difficulty is currently of great importance since the critical phenomena of pure gravitational waves are still poorly understood.

One way to work around those problems is to consider, as a toy model, the situation in $2+1$ dimensions, where gravitational waves do not exist. Furthermore, even in axisymmetry, all the variables are still only functions of "time" and "radius". Aside from those merits, gravity in $2+1$ dimensions is rather peculiar. Notably, black holes cannot form without a negative cosmological constant. The rotating black-hole solution, called the BTZ solution [58], is also quite unique. Its central singularity is not a usual curvature singularity, but a causal singularity. Furthermore, the black-hole spectrum is separated from the background (anti-de Sitter spacetime) configuration by a mass gap. A direct consequence of this is that small deviations from anti-de Sitter spacetime (from now, adS) cannot collapse into a black hole.

Pretorius and Choptuik investigated the black-hole threshold for the spherically symmetric, massless scalar field in $2+1$ dimensions [74]. They found type II phenomena (mass and curvature scaling). The critical solution is also found, near the center, to be approximately *continuously* self-similar (as opposed to discretely as is the case in $3+1$ dimensions). This system was investigated in more depth in Ref. [78]. The authors found good agreement between the numerical solution during the critical regime and an exact continuously self-similar $\Lambda = 0$ solution. However, one major unresolved issue is that this exact solution has *three* growing modes. Investigating the modes numerically, they surprisingly only find numerical evidence of the top (largest) growing mode. There is to date no satisfactory explanation for this, but it was conjectured that the nonlinear effect of the cosmological constant may be responsible for removing all but the top growing mode (adding the effect of the cosmological constant perturbatively does not alter the perturbation spectrum).

In Ref. [87], the same authors generalized the consideration to a complex rotating scalar field. It turns out that the effect of rotation is highly nontrivial: Neither the critical exponents, nor the critical solution are universal. The angular momentum does not show any scaling. The mass and curvature may or may not scale, depending on the one-parameter family of initial data. Finally, the threshold of mass and curvature scalings are different.

In Ch. 7, we investigated the spherically symmetric perfect fluid, with barotropic equation of state $P = \kappa\rho$. We found that the critical phenomena are of type I if $\kappa \lesssim 0.42$, while they are of type II if $\kappa \gtrsim 0.43$. The critical solution for type I is static (as expected), but for type II, it is *not* self-similar, but instead *quasistatic*. That is, the critical solution corresponds to an adiabatic sequence of static solutions whose size shrinks to zero (exponentially).

In this chapter, we now extend this previous work to *rotating* axisymmetric initial data. In Sec. 8.2, we give a quick overview of the Einstein-fluid matter system. In Sec. 8.3, we present and discuss our numerical findings.

8.2 Einstein and fluid equations in polar-radial coordinates

We refer the reader to Ch. 6 for a complete discussion. We use units where $c = G = 1$.

In axisymmetry in $2+1$ dimensions we introduce generalized polar-radial coordinates as

$$\mathrm{d}s^2 = -\alpha^2(t,r)\,\mathrm{d}t^2 + a^2(t,r)R'^2(r)\,\mathrm{d}r^2 + R^2(r)[\mathrm{d}\theta + \beta(t,r)\mathrm{d}t]^2. \tag{8.1}$$

We denote $\partial/\partial t$ by a dot and $\partial/\partial r$ by a prime. Note that our choice $g_{rr} = a^2R'^2$ makes a invariant under a redefinition of the radial coordinate, $r \to \tilde{r}(r)$. The "area" (circumference) radius R is defined geometrically as the length of the Killing vector $\partial/\partial\theta$.

We impose the gauge condition $\alpha(t,0) = 1$ (t is proper time at the center), and the regularity condition $a(t,0) = 1$ (no conical singularity at the center).

We define the auxiliary quantity

$$\gamma := \beta'. \tag{8.2}$$

anticipating that β will not appear undifferentiated in the Einstein or fluid equations, but only in the form of γ and its derivatives, since the form (8.1) of the metric is invariant under the change of angular variable $\theta \to \theta + f(t)$. It follows that the particular choice of gauge for β does not affect our evolution and for our numerical implementation, we choose $\beta(t,0) = 0$. The gauge is fully specified only after specifying the function $R(r)$. In our numerical simulations we use the compactified coordinate

$$R(r) = \ell\tan(r/\ell), \tag{8.3}$$

where

$$\ell := \frac{1}{\sqrt{-\Lambda}} \tag{8.4}$$

is the adS length scale, but for clarity we write R and R' rather than the explicit expressions.

In our coordinates, the Kodama mass M and angular momentum J are given by

$$J(t,r) := \frac{R^3\gamma}{R'a\alpha}, \tag{8.5}$$

$$M(t,r) := \frac{R^2}{\ell^2} - \frac{1}{a^2} + \frac{J^2}{4R^2}. \tag{8.6}$$

This local mass function generalizes the well-known Misner-Sharp mass from spherical symmetry (in any spacetime dimension) to axisymmetry (in $2+1$ only); see Ch. 6 and [170].

The stress-energy tensor for a perfect fluid is

$$T_{ab} = (\rho + P)u_a u_b + P g_{ab}, \tag{8.7}$$

where u^a is tangential to the fluid worldlines, with $u^a u_a = -1$, and P and ρ are the pressure and total energy density measured in the fluid frame. In the following, we assume the one-parameter family of ultrarelativistic fluid equations of state $P = \kappa\rho$, where $0 < \kappa < 1$.

The 3-velocity is decomposed as

$$u^\mu = \{u^t, u^r, u^\theta\} = \Gamma\left\{\frac{1}{\alpha}, \frac{v}{aR'}, \frac{w}{R} - \frac{\beta}{\alpha}\right\}, \tag{8.8}$$

where v and w are the physical radial and tangential velocities of the fluid relative to observers at constant R, satisfying $v^2 + w^2 < 1$, and

$$\Gamma := \left(1 - v^2 - w^2\right)^{-1/2} \tag{8.9}$$

is the corresponding Lorentz factor.

The stress-energy conservation law $\nabla_a T^{ab} = 0$, which together with the equation of state governs the fluid evolution, can be written in balance law form

$$\mathbf{q}_{,t} + \mathbf{f}_{,r} = \mathbf{S}, \tag{8.10}$$

where we have defined the conserved quantities

$$\mathbf{q} := \{\Omega, Y, Z\} \tag{8.11}$$

given by

$$\begin{aligned} Y &:= R' v \sigma, && (8.12)\\ Z &:= a R^2 R' w \sigma, && (8.13)\\ \Omega &:= R' R \tau + \frac{JZ}{2R^2}, && (8.14) \end{aligned}$$

the corresponding fluxes $\mathbf{f}$ given by

$$\begin{aligned} f_{(Y)} &:= \frac{\alpha}{a}(P + v^2\sigma), && (8.15)\\ f_{(Z)} &:= \alpha R^2 v w \sigma, && (8.16)\\ f_{(\Omega)} &:= \frac{\alpha}{a} R v \sigma + \frac{J f_{(Z)}}{2R^2}, && (8.17) \end{aligned}$$

the corresponding sources $\mathbf{S}$ given by

$$\begin{aligned} S_{(Y)} &= \frac{1}{a}\Big[(w^2 - v^2)\sigma\alpha\frac{R'}{R} - \tau\alpha_{,r} \\ &\quad -(P + v^2\sigma)\alpha(\ln a)_{,r} \\ &\quad +Rw\sigma\gamma - 2v\sigma R' a_{,t}\Big], && (8.18)\\ S_{(Z)} &= 0, && (8.19)\\ S_{(\Omega)} &= 0, && (8.20) \end{aligned}$$

and the shorthands

$$\begin{aligned} \sigma &:= \Gamma^2(1+\kappa)\rho, && (8.21)\\ P &:= \kappa\rho, && (8.22)\\ \tau &:= \sigma - P. && (8.23) \end{aligned}$$

At any given time, the balance laws (8.10) are used to compute time derivatives of the

conserved quantities $\mathbf{q}$, using standard high-resolution shock-capturing methods. The $\mathbf{q}$ are evolved to the next timestep via a fourth-order Runge-Kutta step. At each (sub-)timestep, the metric variables are then updated through the Einstein equations

$$M_{,r} = 16\pi\Omega, \tag{8.24}$$

$$J_{,r} = 16\pi Z, \tag{8.25}$$

$$(\ln \alpha a)_{,r} = 8\pi a^2 R R'(1+v^2)\sigma. \tag{8.26}$$

Our numerical scheme is totally constrained, in the sense that only the matter is updated through evolution equations. Our numerical scheme exploits the conservation laws for Ω and Z, and in consequence for M and J, to make their numerical counterparts exactly conserved in the discretized equations.

8.3 Numerical results

8.3.1 Initial data

The numerical grid is equally spaced in the compactified coordinate r, as defined in (8.3), with 800 grid points. We fix the cosmological constant to be $\Lambda = -\pi^2/4$, so that the adS boundary is located at $r = 1$. The numerical domain does not comprise the entire spacetime. Instead, we set an unphysical outer boundary with "copy boundary conditions" for the conserved variables $\mathbf{q}$. Unless otherwise stated, we fix the numerical outer boundary at $r = 0.7$, corresponding in area radius to $R_{\text{max}} \simeq 1.25 \simeq 1.96\ell$.

We choose to initialize the primitive fluid variables ρ and v as double Gaussians in R,

$$\rho(0,R) = \frac{p_\rho}{2}\left(e^{-\left(\frac{R-R_\rho}{\sigma_\rho}\right)^2} + e^{-\left(\frac{R+R_\rho}{\sigma_\rho}\right)^2}\right), \tag{8.27}$$

$$v(0,R) = \frac{p_v}{2}\left(e^{-\left(\frac{R-R_v}{\sigma_v}\right)^2} + e^{-\left(\frac{R+R_v}{\sigma_v}\right)^2}\right), \tag{8.28}$$

where p_ρ and p_v are the magnitudes, R_ρ and R_v the displacements from the center, and σ_ρ and σ_v the widths of the Gaussians. The initial data for w are defined through the combination $w\Gamma^2$, by

$$w(0,R)\Gamma^2 = p_w R. \tag{8.29}$$

Near the center, the fluid is "rigidly rotating" in the sense that $w \sim R$. The strength of the rotation is parametrized by p_w.

As for the spherically symmetric case, we consider three types of initial data:

1) time-symmetric off-centered: $p_v = 0$, $R_\rho = 0.4$,

2) time-symmetric centered: $p_v = 0$, $R_\rho = 0$, and

3) initially ingoing off-centered: $p_v = -0.15$, $R_v = 0.4$, $\sigma_v = 0.15$, $R_\rho = 0.4$.

In all cases, for $\kappa \leq 0.42$, we take $\sigma_\rho = 0.05$, while for $\kappa \geq 0.43$, we choose $\sigma_\rho = 0.2$. The reason for this choice is the fact that in spherical symmetry, where type I behavior occurs,

numerical instabilities form near the numerical outer boundary and travel inwards. These instabilities form strong shocks near the center for a second-order limiter. Making the initial data more compact partially mitigates this. Furthermore, for $\kappa \leq 0.42$, we use a first-order (Godunov) limiter, as we did in spherical symmetry. The dissipative properties of the Godunov limiter eliminate those shocks. As we will see, similar instabilities now also occur for $\kappa \gtrsim 0.43$, for "large" deviations from spherical symmetry. Unless otherwise stated, we therefore also use a Godunov limiter for $\kappa \geq 0.43$, although we will keep the width as $\sigma_\rho = 0.2$.

Finally, in all cases, p_w will be fixed to a particular value and $p_\rho =: p$ will be the parameter to be fine-tuned to the black-hole threshold.

Throughout this chapter, we will use the same conventions as in Ch. 7. In particular, we denote by $p = p_\star$ the critical parameter separating initial data that (promptly) collapse and disperse. We are interested in initial data where $p \simeq p_\star$ and we denote by sub$n$ subcritical data for which $\log_{10}(p_\star - p) \simeq -n$, and by super$n$ supercritical data with $\log_{10}(p - p_\star) \simeq -n$.

In the following, "apparent horizon" (AH) mass and angular momentum refer to the first appearance of a marginally outer-trapped surface in our time slicing, indicated by diverging metric component a.

8.3.2 $\kappa \lesssim 0.42$: Type I critical collapse

8.3.2.1 Lifetime scaling

In the spherically symmetric case, we showed in Ch. 7 that the critical phenomena depend on the value of κ. In particular, for $\kappa \lesssim 0.42$, we find typical type I behavior, where the mass and curvature do not scale and the critical solution near the center is static. How is this picture modified in the presence of angular momentum?

We start answering this question by showing, in Fig. 8.1, a log-log plot of the apparent horizon mass $M_{\rm AH}$ (green group of curves), the adimensionalised apparent horizon angular momentum $J_{\rm AH}/\ell$ (blue group of curves), and the maximum of curvature $-\Lambda\rho_{\rm max}^{-1}$ (orange group of curves), against $p - p_\star$, for different values of p_ω. $M_{\rm AH}$ and $J_{\rm AH}$ are computed via (8.5), evaluated at $R = R_{\rm AH}$. As in the spherically symmetric case $R_{\rm AH}$ is defined to be the point where a is maximal. For all these plots, we consider centered initial data with $\kappa = 0.4$. The range of p_ω is $p_\omega = 0.01$, 0.1, 0.2, 0.4, 0.6, 0.8 and 1.0. This corresponds to a range from "small" angular momentum (in the sense that $J_{\rm AH}/(M_{\rm AH}\ell) \ll 1$) to "large" angular momentum (for example, $p_\omega = 1.0$ corresponds to $J_{\rm AH}/(M_{\rm AH}\ell) \simeq 0.64$).

This behavior, as in spherical symmetry, persists up to some critical value of κ between $\kappa = 0.42$ and $\kappa = 0.43$. For comparison, we have also added an evolution with $\kappa = 0.43$ (dotted curves) and $p_\omega = 0.01$. The type I behavior also holds for the off-centered and ingoing initial data.

As in the spherically symmetric case, we consider the time-dependent quantity R_M, defined by

$$M(t, R_M(t)) := 0, \tag{8.30}$$

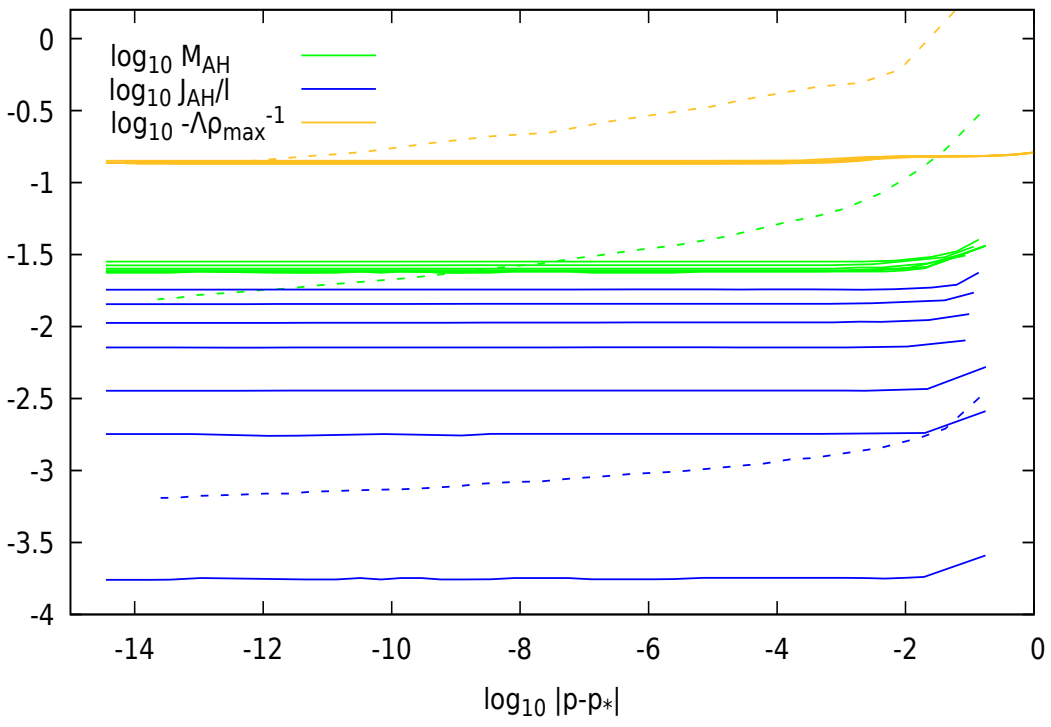

FIGURE 8.1: Log-log plot demonstrating the absence of scaling, for small κ, of $\rho_{\max}$ (upper group of curves, orange), $M_{\rm AH}$ (middle group of curves, green) and $J_{\rm AH}/\ell$ (bottom group of curves, blue) for different values of p_ω, corresponding to a range of "small" to "large" angular momenta. Solid lines correspond to $\kappa = 0.4$. We find typical type I behavior, irrespective of p_ω. This behavior still holds up to $\kappa = 0.42$. For comparison, the dotted curves show $\kappa = 0.43$ and "small" angular momentum, where type II behavior is instead observed within this range of fine-tuning; see Fig. 8.4 for more details.

as a measure of the length scale of the solution. Similarly, we define the central density ρ_0, mass $M_{\rm OB}$, and angular momentum $J_{\rm OB}$ at the numerical outer boundary,

$$\rho_0(t) := \rho(t,0), \tag{8.31}$$

$$M_{\rm OB}(t) := M(t,R_{\max}), \tag{8.32}$$

$$J_{\rm OB}(t) := J(t,R_{\max}). \tag{8.33}$$

In Fig. 8.2, we plot in a linear-log plot, $\sqrt{-\Lambda\rho_0^{-1}}$, $J_{\rm OB}/\ell$, $\sqrt{M_{\rm OB}}$, and R_M/ℓ against central proper time t, for sub6 to sub15 initial data. We consider here centered initial data with $p_\omega = 1.0$. Note that we have shifted $\log_{10} J_{\rm OB}/\ell$ by a constant $c = 1.2$ for clarity. As is typical for critical phenomena, the more fine-tuned the initial data to the black-hole threshold, the longer the critical regime, before the growing mode of the critical solution becomes dominant. In order to avoid cluttering, we truncate the plots after it is clear that the growing mode causes the curves to "peel off" from the critical regime.

For type I phenomena, it is not the mass and curvature that scale. Instead, it is the lifetime of the intermediate regime where the solution is approximated by the critical solution. Assuming that the critical solution is stationary, we can make the following ansatz for its linear

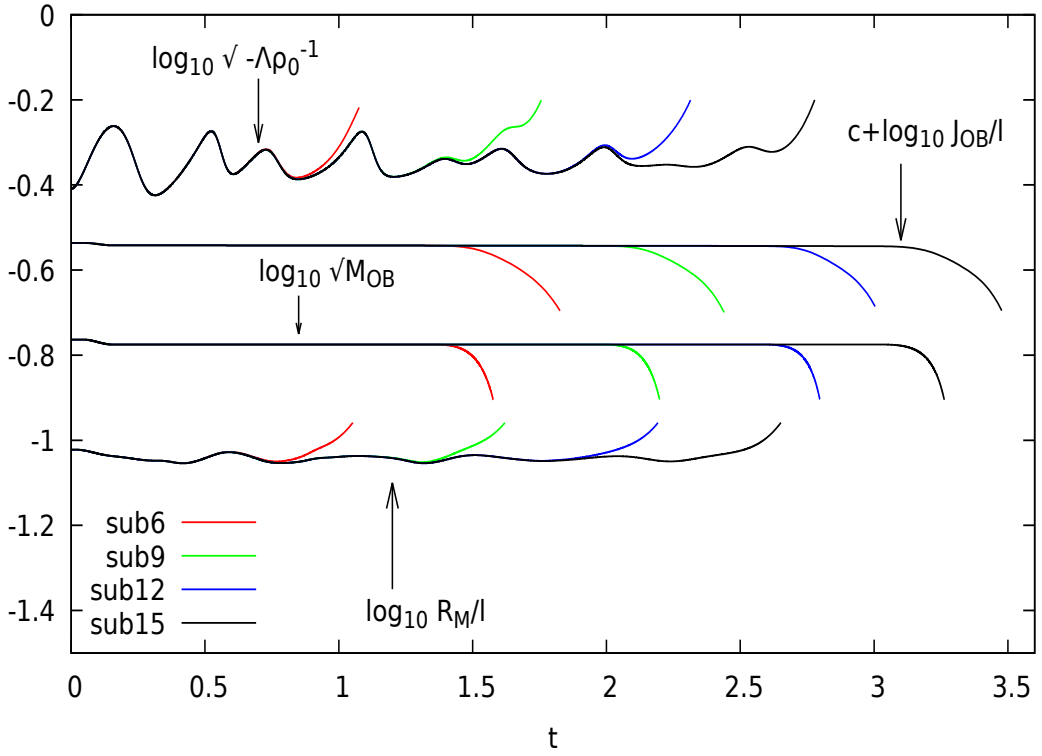

FIGURE 8.2: Lin-log plot of $R_M(t)/\ell$, $\sqrt{-\Lambda\rho_0^{-1}(t)}$, $\sqrt{M_{\rm OB}(t)}$, and $J_{\rm OB}(t)/\ell + c$ with $c = 1.2$, for sub6 to sub15 centered initial data with $p_w = 1.0$. We observe that, as we fine-tune to the black-hole threshold, the solution approaches an intermediate attractor solution in which all the variables are approximately constant. Less fine-tuned initial data peel off from the critical regime sooner than more fine-tuned data.

perturbations:

$$\delta Z(t,R) = \sum_{i=0}^{\infty} C_i(p)\, e^{\sigma_i \frac{t}{\ell}}\, Z_i(R), \tag{8.34}$$

where Z stands for any dimensionless metric or matter variable, such as $R^2\rho$, M, or α.

We assume the critical solution has a single growing mode, $\mathrm{Re}\,\sigma_0 > 0$. Since the solution is exactly critical at $p = p_\star$, this implies that $C_0(p) \sim p - p_\star$. We define the time $t = t_p$ to be the time where the growing perturbation becomes non-linear. This occurs when

$$(p - p_\star) e^{\sigma_0 \frac{t_p}{\ell}} \simeq 1, \tag{8.35}$$

and so

$$t_p = \frac{\ell}{\sigma_0} \ln|p - p_\star| + \text{constant}. \tag{8.36}$$

The exponent σ_0 can be read off from Fig. 8.2. We find $\sigma_0 \simeq 8.29$, close to its value in spherical symmetry (which was $\simeq 8.84$); see Ch. 7.

8.3.2.2 The critical solution

In Ch. 6, we showed the existence of a two-parameter family of rigidly rotating, stationary star solutions for any causal equation of state $P = P(\rho)$. These solutions are analytic everywhere including at the center, and have finite total mass M and angular momentum J. The two free parameters can be taken to be s, giving the overall length scale of the star, and $\tilde{\Omega}$, parametrizing the rotation of the star. The latter is defined so that $\tilde{\Omega} = 0$ corresponds to nonrotating stars. We can write these exact solutions as

$$Z(R) = \check{Z}\left(\frac{R}{s}; \mu, \tilde{\Omega}\right), \tag{8.37}$$

where $\check{Z}$ is the corresponding exact stationary solutions. The cosmological constant enters this picture through a specific combination, parametrized by the dimensionless quantity μ:

$$\mu := -\Lambda s^2 - \tilde{\Omega}^2. \tag{8.38}$$

In what follows, all quantities pertaining to the exact stationary solutions have a check symbol, as in (8.37).

The parameters μ and $\tilde{\Omega}$ correspond to μ and Ω in Ch. 6. (The tilde is used to distinguish $\tilde{\Omega}$ from the unrelated conserved variable Ω). Regular stationary solutions exist only for $0 \leq \mu \leq 1$, and μ can be interpreted as parametrizing the competition of the attractive acceleration induced by a negative cosmological constant and the centrifugal acceleration.

In Fig. 8.3, we compare our best subcritical numerical solution at $t = 2.1$, where the solution is approximately stationary, to the family of stationary solutions. Since the stationary solutions form a two-parameter family, we need to fit those two parameters. For this, we match the central density and total angular momentum, using the angular momentum at the numerical outer boundary as a proxy for the total angular momentum. The matching conditions are

$$J_{\rm OB}(1-\kappa) \equiv 4\kappa\ell(1-\mu)\tilde{\Omega}\sqrt{\mu+\tilde{\Omega}^2}, \tag{8.39}$$

$$1-\mu \equiv 8\pi\kappa\rho_0\ell^2(\mu+\tilde{\Omega}^2). \tag{8.40}$$

Note that there is a slight abuse of language here: the total angular momentum (and mass) of the system is a conserved quantity. The angular momentum (and mass) at the numerical outer boundary (at finite radius) differ from it, since a bit of spin (and mass) are radiated away through this boundary at the start of the evolution, when the solution has yet to enter the critical regime. At late times, the approximately time-independent value of the angular momentum (and mass) at the outer boundary during the critical regime is a fixed fraction of the constant total spin (and mass) of the system.

Our matching of the angular momentum therefore introduces a small systematic error. At first, we attempted to ask for the value of R_M between the numerical and exact solutions to agree. This is also possible, but R_M depends very weakly on rotation and such a matching condition is therefore very sensitive to numerical error.

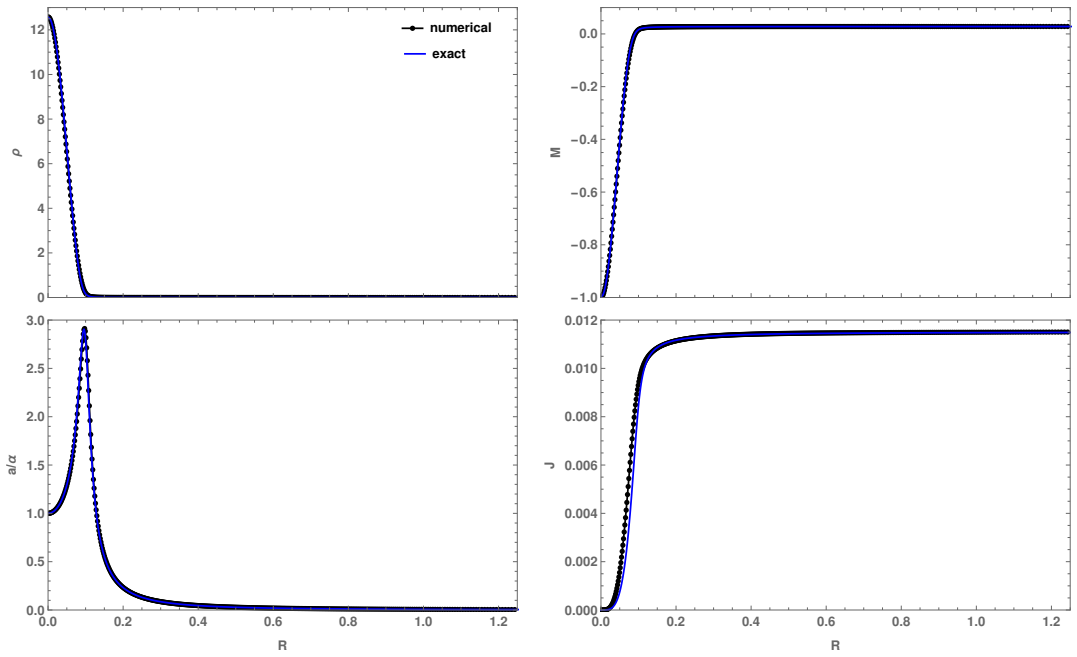

FIGURE 8.3: Comparison of the numerical solution for our best subcritical data during the critical regime (black dotted lines) with the exact stationary solutions (solid blue lines). For the numerical data, we chose here $\kappa = 0.4$ with $p_\omega = 1.0$.

In the example of Fig. 8.3, our matching procedure gives $s \simeq 0.0882$ and $\tilde{\Omega} \simeq 0.0498$. We then find very good agreement for ρ, M and a/α at all R. We find slightly less good agreement for the angular momentum. Since J is relatively small, it is likely that this is a numerical error, although its precise nature is unknown.

We remark here that, at first, we attempted to push the numerical outer boundary further out. We noticed however, for $R_{\rm max} \gtrsim 4$, there is a clear numerical error that builds up and causes mass and spin to slowly radiate away. For example, for $R_{\rm max} \simeq 1.25$, the total mass and angular momentum stay constant in the critical regime within $\ll 1\%$ (see Fig. 8.7). On the other hand, for $R_{\rm max} \simeq 4$, they decrease slowly and approximately linearly. As compared to the near constant value that they take for $R_{\rm max} \simeq 1.25$, they further decrease by about 29% and 16% for $R_{\rm max} \simeq 4$ respectively. This is measured up until the time when the "star" disperses. This decay rate is also different for larger $R_{\rm max}$. We do not have an explanation for this numerical error.

8.3.3 $\kappa \gtrsim 0.43$: Type II critical collapse

8.3.3.1 Curvature and mass scalings

In spherical symmetry, we have given strong evidence that the critical phenomena are type II for $\kappa \geq 0.43$ (the apparent-horizon mass and curvature scale as some power law and the critical solution shrinks quasistatically to arbitrarily small size); see Ch. 7. As we did for $\kappa \leq 0.42$, we now consider families of initial data with different initial angular momentum p_ω. In the following, we will focus our attention on the case $\kappa = 0.5$.

In Fig. 8.4, we plot $-\Lambda\rho_{\rm max}^{-1}$ (orange group of curves), M_{AH} (green group of curves) and J_{AH}/ℓ (blue group of curves) as a function of $p-p_\star$ for centered initial data and with different p_w, namely: $p_w = 0.02$, 0.04, 0.06, 0.08, 0.1, 0.16, 0.2, 0.3, 0.4 and 0.5 (solid lines). The dashed-dotted lines were obtained with $p_w = 0.2$, but using the MC limiter.

This plot illustrates multiple points: First, for "small" initial spin, we find typical type II phenomena where the density, mass and spin scale like power laws. Second, the angular momentum $J_{\rm AH}$ scales *more slowly* than $M_{\rm AH}$. In particular, the spin-to-mass ratio of the resulting black hole *increases* as we fine-tune to the black-hole threshold; see also Fig. 8.6. For larger initial spin such as $p_w \geq 0.2$ (or respectively more fine-tuning for smaller p_ω), the spin-to-mass ratio approaches extremality. It does not go beyond, however, because the critical solution becomes stationary and, as a result, the power-law scaling with respect to $p-p_*$ also smoothly levels off.

The phenomena highlighted above have also been checked to hold for the off-centered and initially ingoing data, although we chose not to include them in the plot to avoid cluttering.

Note that for the evolution using the MC limiter (dashed-dotted), the scaling stops abruptly and the spin-to-mass ratio seems to remain constant with further fine-tuning. For reasons that will be made clearer later, this is expected to be a numerical artifact: for relatively large spin-to-mass ratio, numerical instabilities are generated at the numerical outer boundary, similar to those we faced when simulating type I phenomena in the spherically symmetric case. These instabilities travel inward and produce shocks near the center, which are absent using a more dissipative limiter such as the first-order Godunov limiter.

In Fig. 8.5, we explore the relationship between $J_{\rm AH}$ and $M_{\rm AH}$ more explicitly, for the critical solution and the final black hole. On the left, we show a parametric plot of $M_{\rm AH}$ against $J_{\rm AH}/\ell$ for the same initial data as in Fig. 8.4 (and using the same convention for the lines). We have added the bisections from the off-centered and ingoing initial data with $p_w = 0.02$, 0.04 and 0.06 (dotted and dashed lines respectively). The red line corresponds to $J_{\rm AH} = M_{\rm AH}\ell$. The trajectories in the $(M_{\rm AH}, J_{\rm AH})$ plane are clearly family-dependent, although as we increase the fine-tuning and the black holes become smaller (the bottom left corner) all the curves become approximately parallel to each other. This provides some evidence that the critical phenomena are controlled by a unique one-parameter family of critical solutions (universality).

On the right, we show a parametric plot of the mass $M_{\rm OB}$ against the angular momentum $J_{\rm OB}/\ell$, for our best supercritical data. As expected, both plots are qualitatively very similar, since one expects the mass and spin at the apparent horizon to be in some fixed ratio to their values at the numerical outer boundary, at the time when the solution veers off from the critical solution. It turns out that, for close to critical data, $M_{\rm AH} \simeq M_{\rm OB}$ and $J_{\rm AH} \simeq J_{\rm OB}$ at this time, and so this fixed fraction is almost one.

In Fig. 8.6, we use again the same data as in Fig. 8.5. On the left plot, we show the spin-to-mass ratio $J_{\rm AH}/(M_{\rm AH}\ell)$ as a function of $p-p_\star$ for different levels of fine-tuning. The only addition is a second bisection using a MC limiter (a second dashed-dotted curve), but where the numerical outer boundary is at $R_{\rm max} \simeq 2.65 \simeq 4.17\ell$. The fact that both dashed-dotted lines do not level off at the same spin-to-mass ratio gives evidence that the unphysical numerical

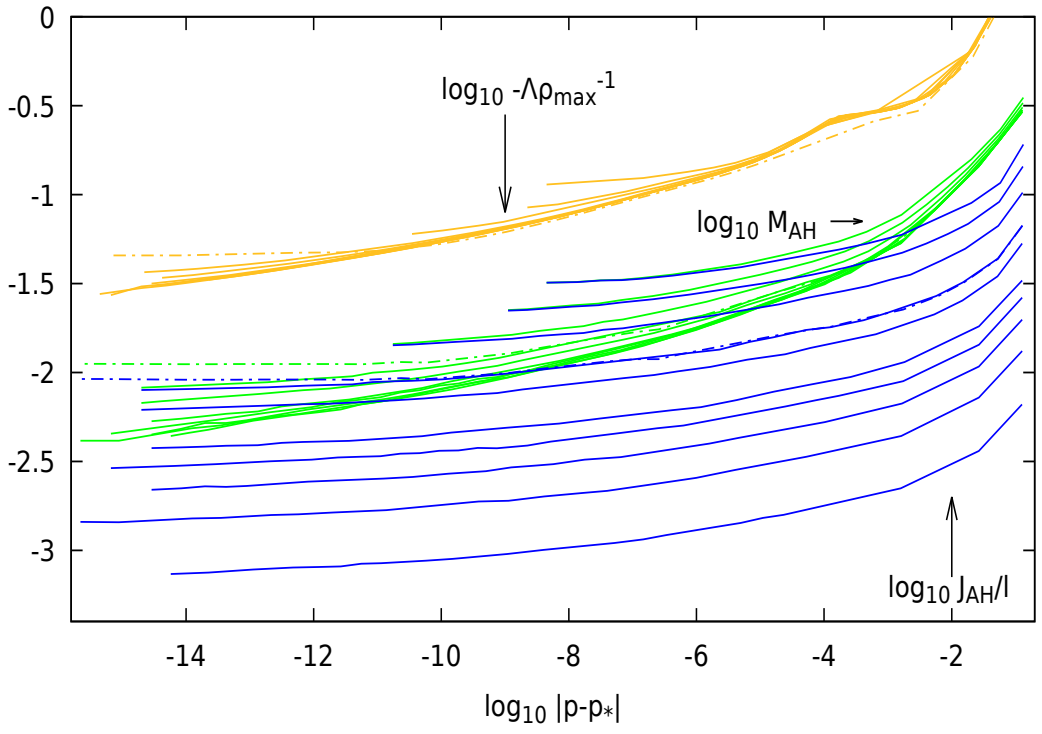

FIGURE 8.4: Log-log plot demonstrating the power-law scaling of $-\Lambda\rho_{\max}^{-1}$ (orange, upper group of curves), $M_{\rm AH}$ (green, middle group of curves) and $J_{\rm AH}/\ell$ (blue, lower group of curves) for different values of p_w. Solid lines correspond to centered initial data, using the Godunov limiter. $J_{\rm AH}$ decays more slowly than $M_{\rm AH}$. For small spin-to-mass ratio, we find typical type II behavior, while for larger spin-to-mass ratio, the scaling smoothly flattens as extremality is approached. Dashed-dotted lines show an evolution with large initial spin ($p_\omega = 0.2$), but using the MC limiter. There, the spin-to-mass ratio completely flattens beyond a certain level of fine-tuning, but this is a numerical artifact.

outer boundary spoils the numerical results in that highly-rotating regime. Instead, the results from the Godunov limiter, which removes the aforementioned instabilities, are more plausible: in the limit of fine-tuning, the black-hole is extremal.

Similarly, in the right plot, we show the spin-to-mass ratio evaluated at the numerical outer boundary, for our best supercritical data, against proper time t. Both left and right plots are qualitatively similar. This is expected since the more fine-tuned the initial data are to the black-hole threshold, the longer it takes for the growing mode to dominate the perturbation, and so the more the spin-to-mass ratio can grow, before the solution collapses.

If we define the time where the critical regime starts to be the time from which the central density shows critical scaling (at least for small rotation), then this occurs at $t \simeq 0.8$ for centered initial data (see for example Fig. 8.7), while it occurs at $t \simeq 1.0$ for ingoing and off-centered initial data. In the right plot of Fig. 8.6, the different trajectories do not cross during this critical regime. This again provides evidence that, in a suitable adiabatic limit, a given pair $(M_{\rm AH}, J_{\rm AH})$ in a quasistationary sequence uniquely determines its evolution.

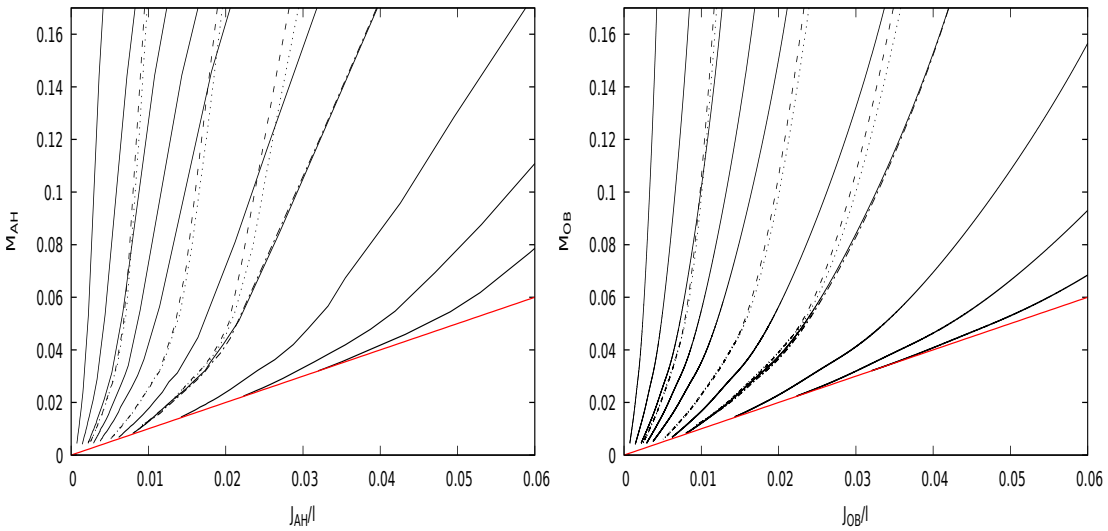

FIGURE 8.5: Left plot: Parametric plot of the trajectories of $M_{\rm AH}$ and $J_{\rm AH}$ in Fig. 8.4 (solid and dashed-dotted lines), in the $M_{\rm AH}$-$J_{\rm AH}$ plane. The parameter along each curve is $p - p_*$. We have also added the trajectories of off-centered (dotted lines) and ingoing (dashed lines) initial data for three different values of p_w. The red line corresponds to $J_{\rm AH} = M_{\rm AH}\ell$. Right plot: a similar plot, using the same convention, except that we now consider the mass and angular momentum evaluated at the numerical outer boundary, for our best supercritical data. The parameter along each curve is now time.

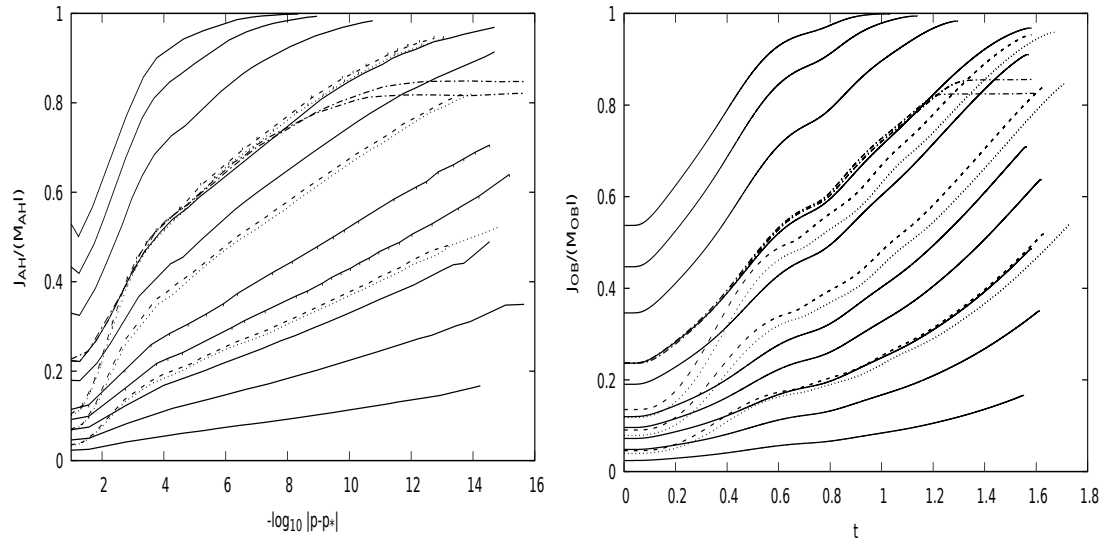

FIGURE 8.6: Left plot: Log-log plot of $\frac{J_{\rm AH}}{M_{\rm AH}\ell}$ against $p - p_\star$, for the same data as in Fig. 8.5, with the addition of a second dashed-dotted curve using the MC limiter but with a larger grid. The spin-to-mass ratio approaches extremality as we fine tune to the black-hole threshold, except for the two MC limiter cases. Right plot: Parametric plot of $\frac{J_{\rm OB}}{M_{\rm OB}\ell}$, as a function of time t, for our best supercritical evolutions. The critical regime begins at $t \simeq 0.8$ for centered initial data, and at $t \simeq 1.0$ for ingoing and off-centered initial data.

8.3.3.2 The critical solution

We have seen in Fig. 8.5 that for sufficient fine-tuning (on the left) or at sufficiently late times (on the right), the trajectories in the J-M plane do not cross, providing evidence that there is a universal one-parameter family of critical solutions that fibrate the J-M plane. Independently, the fact that we can make arbitrarily small black holes or arbitrarily large central densities by fine-tuning generic one-parameter families of initial data suggests that each member of this family of critical solutions has precisely one unstable perturbation mode.

As in the spherically symmetric case, the profile of the solution can be roughly split into two regions: one central region where most of the density lies and whose size shrinks in time, and an outer region ("atmosphere") where the mass and spin are approximately constant in space and decrease to zero (exponentially) in time.

At a stage where the effect of spin can still be regarded as perturbative, one would expect the critical solution to be approximated by the quasistatic solution in spherical symmetry, plus a (unique, growing) nonspherical perturbation proportional to p_w that carries the angular momentum. In particular, one would expect that the solution shrinks exponentially quickly in time.

To confirm this, we plot, on the left of Fig. 8.7, the logarithms of $R_M(t)/\ell$, $\sqrt{-\Lambda\rho_0^{-1}(t)}$, $\sqrt{M_{\rm OB}(t)}$ and $J_{\rm OB}/\ell$ for sub6, sub9, sub12 and sub15 centered data with $p_w = 0.01$. For those plots, we used the MC limiter, as even at sub15, the spin-to-mass ratio still remains relatively small and the aforementioned instabilities are not present.

We find, as anticipated from our study in spherical symmetry, that these quantities are exponential functions of t. $J_{\rm OB}$ scales slower then $M_{\rm OB}$ as it is the case for the apparent-horizon mass and spin, so that the spin-to-mass ratio $J_{\rm OB}/(M_{\rm OB}\ell)$ increases. Note that right after the critical regime, the trajectories for each variable at different level of fine-tuning align, up to a rescaling and a shift in time. This kind of behavior is expected in a spacetime where the cosmological constant is dynamically irrelevant and where the field equations become approximately scale-invariant.

Note that after the critical regime, $J_{\rm OB}$ enters what seems to be a second regime, still decreasing exponentially, but noticeably more slowly than during the critical regime.

On the right of Fig. 8.7, we plot the logarithm of $R_M(t)/\ell$ and $\sqrt{-\Lambda\rho_0^{-1}(t)}$ for our best subcritical evolution (sub15) with $p_w = 0.01, 0.05, 0.1, 0.16, 0.2$ using again centered initial data, but with the Godunov limiter. The solution first shrinks and displays typical type II phenomena for "small" p_w. During this phase, $R_M(t)/\ell$ and $\sqrt{-\Lambda\rho_0^{-1}(t)}$ are completely independent of p_ω, as we would expect while angular momentum is a perturbation.

As the spin-to-mass ratio has become sufficiently large, both R_M and ρ_0^{-1} decrease more slowly and start to level off. For the same fine-tuning, this corresponds to larger values of p_w, see the inset on the right of Fig. 8.7. We do not have a satisfactory dynamical explanation for this.

Together with Fig. 8.4, one expects that in the limit of perfect fine-tuning, the critical solution becomes stationary at late times, and, correspondingly, on the black-hole side of the threshold of collapse, the black hole becomes extremal.

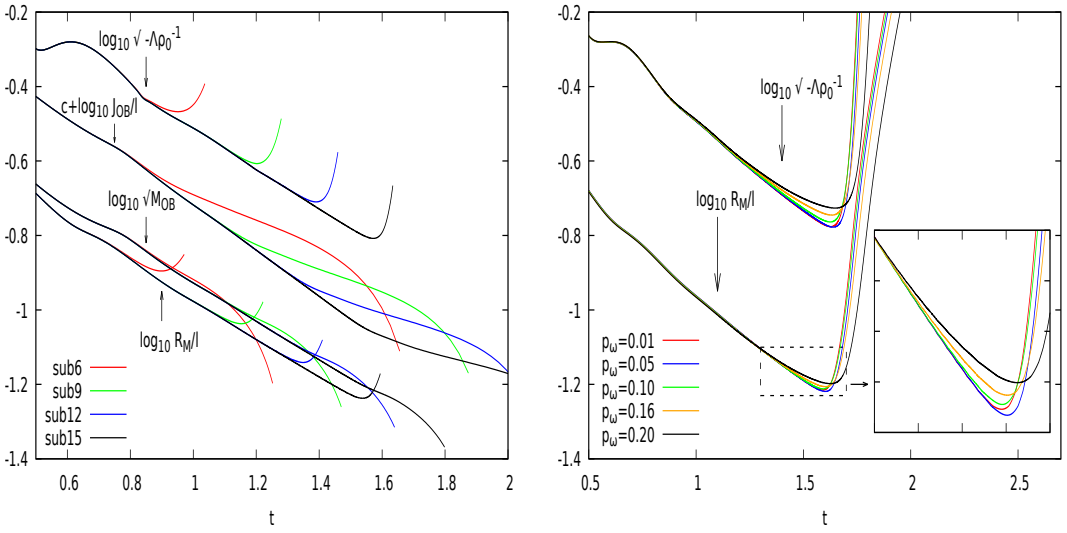

FIGURE 8.7: Left plot: Lin-log plot of $R_M(t)/\ell$, $\sqrt{-\Lambda\rho_0^{-1}(t)}$, $\sqrt{M_{\rm OB}(t)}$, and $J_{\rm OB}(t)/\ell$ for sub6 to sub15 centered initial data with $p_w = 0.01$, using the MC limiter. We observe that, as we fine-tune to the black-hole threshold, the solution approaches an intermediate attractor solution in which R_M, ρ_0^{-1}, $M_{\rm OB}$ and $J_{\rm OB}$ decrease exponentially. Less fine-tuned initial data peel off from this critical line sooner than more fine-tuned data, leading to critical scaling of the maximum density, etc. Note that $J_{\rm OB}$ decreases more slowly than $M_{\rm OB}$, as is the case for their value at the apparent horizon. There is a second regime for $J_{\rm OB}$, after the critical regime, where it takes on another, less pronounced, power-law scaling. Right plot: Lin-log plot of $\sqrt{-\Lambda\rho_0^{-1}(t)}$ and $\sqrt{R_M(t)/\ell}$ for our best subcritical (sub15) data with $p_w = 0.01$, 0.05, 0.1, 0.16, and 0.20 using the Godunov limiter. At late times, these quantities decrease more slowly for larger p_w and correspondingly larger spin-to-mass ratio.

In spherical symmetry, the critical solution is quasistatic, meaning that it adiabatically goes through the sequence of static solutions, with s now a function of t, and $|\dot{s}(t)| \ll 1$. Furthermore, $\mu \sim s^2$ and it follows that in the quasistatic ansatz, $\mu(t) \sim s(t)^2$. Since the solution shrinks exponentially, we have the following ansatz for $s(t)$:

$$s(t) \equiv s_0 e^{-\nu \frac{t}{\ell}}, \tag{8.41}$$

for constants s_0 and ν. To leading order in $\dot{s}$, the quasistatic ansatz then takes the form,

$$M(t,R) \simeq \check{M}\left(\frac{R}{s(t)}; \mu(t), \tilde{\Omega} = 0\right), \tag{8.42}$$

and similarly for other suitably rescaled variables.

As we hinted before, one can expect, at least in the regime where the effects of angular momentum are still perturbative, that the solution can be thought to shrink adiabatically to zero size, going through a sequence of *stationary* solutions. The picture in spherical symmetry can then be straightforwardly generalized to axisymmetric initial data. Specifically, we assume that, to leading order in $\dot{s}$, the critical solution can be well-approximated by

$$M(t,R) \simeq \check{M}\left(\frac{R}{s(t)}; \mu(t), \tilde{\Omega}(t)\right), \tag{8.43}$$

Initial data ($\kappa = 0.5$)	ν	ϕ
Off-centered	0.7844	0.0854
Centered	0.7925	0.1144
Ingoing	0.8049	0.0671

TABLE 8.1: The value of ν and ϕ for different families of initial data.

and so on. From the exponential form of $s(t)$, we further make a relatively agnostic ansatz for $\tilde{\Omega}$ of the form:

$$\tilde{\Omega}(t) =: \tilde{\Omega}_0 e^{-\phi \frac{t}{\ell}}, \tag{8.44}$$

where $\tilde{\Omega}_0$ and ϕ are constants. This exponential ansatz is justified from the fact that, for the family of stationary solutions, the angular momentum at infinity satisfies (8.39). In particular $J \sim \tilde{\Omega}$. From Fig. 8.7, $J_{\rm OB}$, seen as a proxy for the corresponding angular momentum at infinity, decays exponentially, thus suggesting the exponential form for $\tilde{\Omega}$. Together with the ansatz for $s(t)$ (8.41), we have now four parameters to fit: s_0 and ν (as in spherical symmetry), and $\tilde{\Omega}_0$ and ϕ.

For $p_w = 0.01$, where we only observe type II behavior to our level of fine-tuning, we choose to fix them by requiring the central density and spin at infinity to match those of the stationary solutions at times $t \simeq 1.0$ and 1.4, where we believe that the solution is in its critical regime; see Fig. 8.7. For the spin at infinity, we take the spin at the numerical outer boundary as a proxy. This is justified because in the atmosphere, where the density is small, the mass and spin are approximately constant in space. We find the following values:

$$\begin{aligned} s_0 &\simeq 0.1913, \qquad \nu \simeq 0.7925, \\ \tilde{\Omega}_0 &\simeq 0.002110, \quad \phi \simeq 0.1144. \end{aligned} \tag{8.45}$$

As expected, the above values of s_0 and ν are consistent with their values in the spherically symmetric case $p_w = 0$. We have repeated this procedure for the ingoing and off-centered initial data as well, and summarize the values of ν and ϕ in Table 8.1. Due to the smallness of ϕ, the relative variation of ϕ is important. In particular, it is difficult to confidently say if those variations are purely a numerical error. However, because Figs. 8.5 and 8.6 suggest some universality for the critical solution, we are inclined to believe it is so. That is, we believe that ϕ, just as ν, is family independent. We find good agreement between the numerical and exact solutions.

In Fig. 8.8 we compare the leading-order quasistationary solution for J, of the same form as in Eq. (8.43) (dotted lines), with the numerical data (solid lines) at constant time intervals $t \simeq 1$, 1.1, 1.2, 1.3 and 1.4.

Returning back to the left plot of Fig. 8.7, the quasistationarity of the critical solution can be used to explain the slope of $J_{\rm OB}$. Specifically, from (8.39), we have

$$J_{\rm OB} \sim \tilde{\Omega} s. \tag{8.46}$$

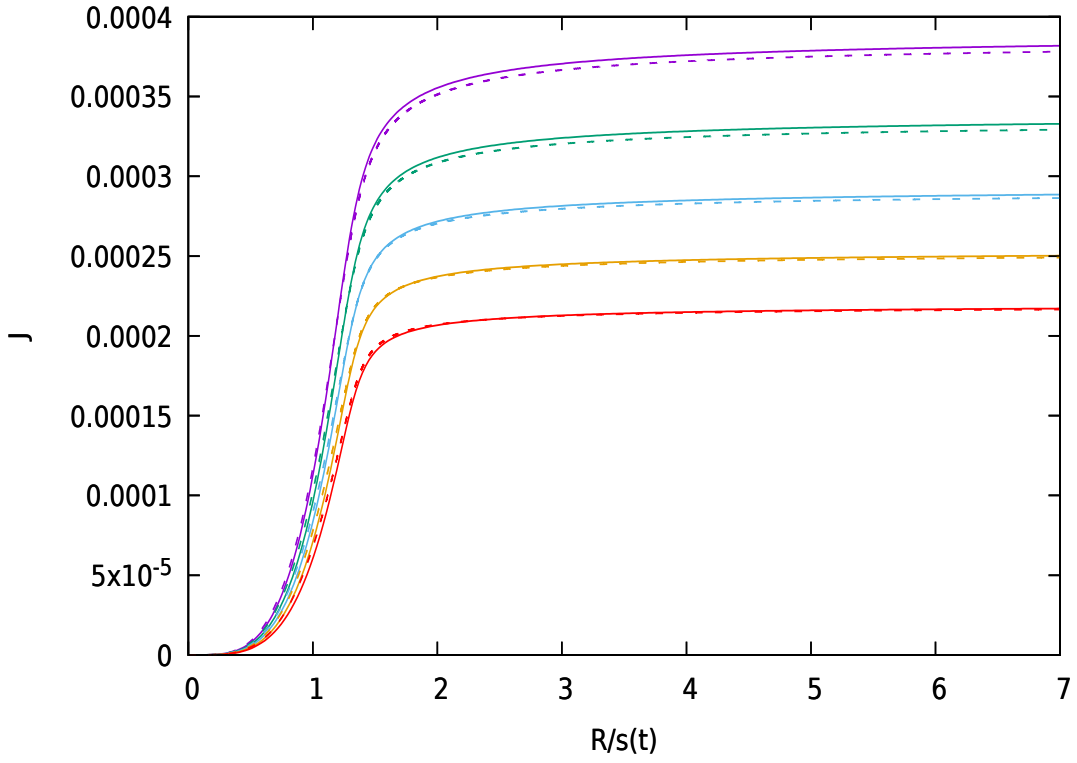

FIGURE 8.8: Numerical solution (solid lines) for J, plotted against $R/s(t)$, at different times during the critical regime, $t \simeq 1$, 1.1, 1.2, 1.3 and 1.4 for our best subcritical, centered initial data with $p_w = 0.01$. For comparison, we plot the leading-order term of the quasistationary solution for $J = \check{J}(R/s(t); \mu(t), \tilde{\Omega}(t))$ (dashed lines). We consider the ansatz $s(t) = s_0 e^{-\nu t/\ell}$ and $\tilde{\Omega}(t) = \tilde{\Omega}_0 e^{-\phi t/\ell}$, where the parameters s_0, ν, $\tilde{\Omega}_0$, and ϕ are given in Eq. (8.45).

In the spherically symmetric case, we showed that $M_{\rm OB} \sim s^2$. At the level where angular momentum is still viewed as a perturbation, this is still expected to hold, so that

$$J_{\rm OB}^2 \sim \tilde{\Omega}^2 M_{\rm OB}, \tag{8.47}$$

or

$$J_{\rm OB}^2 \sim M_{\rm OB}^{1+\Delta}, \tag{8.48}$$

where

$$\Delta = \phi/\nu \tag{8.49}$$

is small. For the centered initial data for example, (8.45) gives $\Delta \simeq 0.144$.

8.4 Conclusion

We have generalized our previous study [Ch. 7] of perfect fluid critical collapse in 2+1 spacetime dimension to rotating initial data. We have given evidence that, for $\kappa \lesssim 0.42$, the critical phenomena are type I, as in spherical symmetry. The critical solution is stationary and agrees well with the family of exact stationary solutions studied in Ch. 6.

The situation for $\kappa \gtrsim 0.43$ is more complicated. We give evidence for the existence of a universal one-parameter family of critical solutions, which fibrates the region $|J/\ell| < M$, $M > 0$ of the J-M plane. In the limit $|J|/(\ell M) \ll 1$, as well as $s/\ell \ll 1$, angular momentum can be approximated as a linear perturbation of the nonrotating critical solution. We then expect both s and J to be exponential functions of t, and so J to be a power of s.

However, for supercritical data, the angular momentum of the solution decreases more slowly than its mass as the black-hole threshold is approached. The spin-to-mass ratio therefore *increases* as we fine-tune to the black-hole threshold. We gave strong evidence that one can obtain in this way black holes arbitrarily close to extremality.

For small angular momentum, rotation can be treated as a linear perturbation of spherical symmetry. The universality of the one-parameter family of critical solutions, with increasing $|J|/(\ell M)$, then implies the existence of a single unstable rotating mode of the spherical critical solution. One may then wonder how super-extremality is avoided. We have seen that the answer is that the critical solution stops shrinking as $|J|/(\ell M) \to 1$, and so both J and M stop scaling.

Contrast this with the known situation in rotating fluid collapse in 3+1 [90, 92]: there, the existence of a single growing angular momentum mode is known for $\kappa < 1/9$ [88], but it turns out that nonlinear effects make J/M^2 decrease in the critical solution from the start, even for small J for $\kappa < 1/9$.

As $s/\ell \ll 1$, or $M \ll 1$, the physics become approximately scale-invariant, and the cosmological constant becomes essential only in a boundary layer at the surface of the contracting star. We expect that in this limit the one-parameter family of critical solutions degenerates to a single (somewhat singular) critical solution, up to an overall rescaling.

We have shown that type I critical collapse is controlled by rigidly rotating stationary solutions, and type II by an adiabatic shrinking sequence of such solutions. The matching between our numerical results and the exact stationary solutions of Ch. 6 is very good, even neglecting the adiabatic contraction. On the flip side, we have not been able to derive effective adiabatic equations of motion in the space of stationary solutions (even in the non-rotating case of Ch. 7), and so we are unable to derive either the universal time-dependence of the critical solutions, or their unique trajectories in the J-M plane.

It is fortunate that our critical solutions appear to be exactly rigidly rotating, as precisely all rigidly rotating stationary solutions are known in closed form (for arbitrary equation of state); see [168] and Ch. 5. It is plausible that the rigid rotation of the critical solutions is universal, but we have not tested this, as we have considered only one family of initial rotation profiles (in which the angular velocity is approximately constant).

Critical phenomena in $2+1$ dimensions primarily serves as toy model for the $3+1$ dimensional setting. Between the results from the scalar field case [78, 87] and the results for the perfect fluid here, one can see that the effects of angular momentum are generally far from trivial, and share little resemblance with their higher-dimensional counterparts.

Chapter 9

Conclusion

Critical collapse is a very active research area that has helped us shape our understanding of the weak and strong cosmic censorships. As we saw in the second chapter of this thesis, critical collapse has been studied for a plethora of matter fields. Nonetheless, most studies restrict themselves to spherically symmetric scenarios. Even generalizing to axisymmetric initial data brings tremendous complications, both on a practical and conceptual level. As we explained before, this is because beyond spherical symmetry, in $3+1$ and higher dimensions, metric and matter variables gain an additional independent variable. Furthermore, the existence of gravitational waves substantially complicates the analysis. This can be made particularly salient by realizing that the critical collapse of pure vacuum remains poorly understood, despite efforts starting already in the early 90s; see Sec. 2.6.4. However, the full picture of critical collapse necessitates going beyond spherical symmetry. This is currently the main hurdle that needs to be addressed in the area of critical collapse.

The main objective of this thesis was to investigate the effect of angular momentum in $2+1$ dimensions. The main advantage in working in $2+1$ dimensions is that we can bypass the difficulties mentioned above. This comes, however, at the cost of being required to work with a negative cosmological constant.

Chs 7 and 8 cover the main results of this thesis. In the first one, we focused on the critical collapse of a spherically symmetric fluid with equation of state $P = \kappa\rho$, before generalizing to axisymmetry with rotation in the second. Many of the results we found were quite surprising and completely novel in the domain of critical collapse. Notably, the critical phenomena are of type I or II, depending on κ. In the case of type I phenomena, the associated critical solution is static, as one could expect. However, unlike what was anticipated a priori, the type II critical solution is *not* self-similar, but quasistatic. In axisymmetry, we find the same separation between type I and II phenomena. The critical solution is then stationary or quasistationary respectively. More interestingly, for the type II case, we showed that the spin-to-mass ratio increases as we fine-tune to the black hole threshold, so that in the limit of perfect fine-tuning, the black hole is extremal. Most of these results are quite unfamiliar as compared to the critical collapse of the same system in higher dimensions.

It is perhaps also worth putting these results in contrast with the only other matter model studied in $2+1$ dimensions so far; the massless scalar field [78, 87]. There, the phenomena are

of type II, as they are in $3+1$, and the critical solution is approximately self-similar near the center. The picture in axisymmetry turns out to be highly nontrivial and poorly understood. Notably, the authors find weak evidence that the critical solution is self-similar and no evidence of universality. The spin of the black hole does not scale, while the mass and curvature may or may not scale, depending on the initial data. This is again quite different from the results in $3+1$ dimensions; see again Sec. 2.6.3. Unlike what is the case in higher dimensions, there seems to be little common ground between the critical phenomena of the scalar field and perfect fluid. This raises the question of what the critical phenomena look like for other matter fields.

It is enlightening to see how the cosmological constant paradox is resolved in both of these models. Recall that in type II collapse, the critical solution persists over arbitrarily small scales so that the cosmological constant becomes dynamically irrelevant. Yet, its existence is necessary for black holes to form and thus to talk about critical collapse. How can both of these facts be reconciled? Mathematically, in both the scalar and fluid models, a first hint is provided by analyzing the $\Lambda \to 0$ limit. Near the center, this limit is regular, signaling that Λ only plays a perturbative role there. On the other hand, for the scalar field, the $\Lambda \to 0$ limit is singular at the lightcone, while for the fluid, it is singular at the surface of the star. Specifically, for the critical solution of the scalar field with $\Lambda = 0$, every point beyond the lightcone is an apparent horizon. It turns out that the apparent horizons are removed when a negative cosmological constant is taken into account, even when only perturbatively. For the fluid, the situation is even more dramatic, since for $\Lambda = 0$, the family of static solutions has a singular surface. Furthermore, spacetime stops at that surface and is not even asymptotically flat.

There still remains a few open questions pertaining to the critical collapse of the perfect fluid matter model we investigated in this thesis.

First, the principal feature of the spherically symmetric critical solution is that it shrinks exponentially with proper time. We have not found a convincing reason as to why this is so. The answer to this question lies in solving the perturbation equations of the quasistatic solution. We showed that $s(t)$ is either polynomial or exponential. The exact nature of $s(t)$ can be fixed via some boundary condition. In particular, it *is* possible to find conditions which would make $s(t)$ an exponential, but these conditions are not particularly natural.

Second, we have constructed two models for the critical solution: one, through the quasistatic ansatz, valid near the center, and the other, through a stationary test fluid ansatz, valid in the atmosphere. Individually, both were shown to be in good agreement with the numerical results. However, it is unclear how they should be matched in some intermediate regime. In particular, it is not clear if this matching can be made smooth.

Lastly, the results for axisymmetric rotating initial data were obtained purely numerically. As we said above, during the critical regime, the solution contracts and the black-hole spin-to-mass ratio increases. At the level of perturbation theory, one would therefore expect a growing nonspherical mode that is responsible for this growth. This mode would then become suppressed as extremality is approached. It would certainly be enlightening if some, or all, of this can be seen in perturbation theory.

Appendices

Appendix A

3-fold degeneracy

We show how the 3-fold degeneracy of the critical solution for v at the sonic point naturally arises from the regularity constraints at the sonic point.

We may write the matter equations algebraically as

$$\begin{bmatrix} a & b \\ c & d \end{bmatrix} \begin{bmatrix} \omega' \\ v' \end{bmatrix} = \begin{bmatrix} e \\ f \end{bmatrix}. \tag{A.1}$$

Inverting the above gives

$$\omega' = \frac{N_\omega}{D}, \qquad v' = \frac{N_v}{D}. \tag{A.2}$$

This is of the same form as the matter equations (3.69), where we may identify,

$$D_\omega = D_v = D = ad - bc, \qquad N_\omega = de - ef, \qquad N_v = af - be. \tag{A.3}$$

At the sonic point $x = x_s$, we require that $D = N_\omega = N_v = 0$. By l'Hôpital's rule, we then have that,

$$\omega'(x_s) = \left.\frac{N'_\omega}{D'}\right|_{x_s}, \qquad v'(x_s) = \left.\frac{N'_v}{D'}\right|_{x_s}. \tag{A.4}$$

Using the chain rule yields,

$$\left(D_{,N}N' + D_{,A}A' + D_{,\omega}\omega' + D_{,v}v'\right)\omega' = \left(N_\omega\right)_{,N} N' + \left(N_\omega\right)_{,A} A' + \left(N_\omega\right)_{,\omega} \omega' + \left(N_\omega\right)_{,v} v', \tag{A.5}$$

$$\left(D_{,N}N' + D_{,A}A' + D_{,\omega}\omega' + D_{,v}v'\right)v' = \left(N_v\right)_{,N} N' + \left(N_v\right)_{,A} A' + \left(N_v\right)_{,\omega} \omega' + \left(N_v\right)_{,v} v', \tag{A.6}$$

where we suppressed the evaluation at the sonic point.

We can then make use of the equation of motion for N' and A', so that the above can be regarded as a system of two *second-order* algebraic equations for ω' and v',

$$\left(D_{,\omega}\omega' + D_{,v}v' + C_1\right)\omega' = \left(N_\omega\right)_{,\omega} \omega' + \left(N_\omega\right)_{,v} v' + C_2, \tag{A.7}$$

$$\left(D_{,\omega}\omega' + D_{,v}v' + C_3\right)v' = \left(N_v\right)_{,\omega} \omega' + \left(N_v\right)_{,v} v' + C_4, \tag{A.8}$$

where the C_i are functions of X and A, but not their derivatives.

D only depends on N and v, implying that $D_{,\omega} = 0$. Therefore, we see that (A.7) is, in terms of X, A and v', a *linear* equation for ω'. The solution is therefore of the form

$$\omega' = \frac{W_1(X, A, v')}{W_2(X, A, v')}, \tag{A.9}$$

where W_1, W_2 are *linear* functions of v'.

Inserting the above into (A.8) yields a *third-order* algebraic equation for v'. One should therefore expect three distinct solutions, in line with the results of Section 3.5.3.2.

Appendix B

Power-series solution of the CSS solution at the sonic point in $3+1$ dimensions

The leading expression X_0^s, in terms of $\check{v}$,

$$A_0^s = \frac{\kappa^2+6\kappa+\left(3\kappa^2-2\kappa-1\right)\check{v}^2+8\kappa^{3/2}\check{v}+1}{(1+\kappa)^2\left(1-\check{v}^2\right)}, \tag{B.1}$$

$$\omega_0^s = \frac{2\sqrt{\kappa}\left(\sqrt{\kappa}-\check{v}\right)\left(1+\sqrt{\kappa}\check{v}\right)}{(1+\kappa)^2\left(1-\check{v}^2\right)}, \tag{B.2}$$

$$N_0^s = \frac{1-\sqrt{\kappa}\check{v}}{\sqrt{\kappa}-\check{v}}. \tag{B.3}$$

Defining the shorthands,

$$b := \left(1-\kappa^2\right)\left(1-\check{v}^2\right), \tag{B.4}$$

$$c := -(1-\kappa)^2(1+\kappa)^3\left(1-v^2\right)^3\left(\sqrt{\kappa}-v\right), \tag{B.5}$$

$$\begin{aligned} d := &-(1+\kappa)^3\left(1-\check{v}^2\right)^3\Big(-2\kappa^{5/2}+\kappa^{3/2}+\sqrt{\kappa}-2\kappa^{5/2}\check{v}^4-5\kappa^{3/2}\check{v}^4-\kappa^3\check{v}^3+5\kappa^2\check{v}^3 \\ &+3\kappa^{7/2}\check{v}^2+\kappa^{5/2}\check{v}^2+\kappa^{3/2}\check{v}^2-\frac{1}{2}(\kappa+1)\left(\sqrt{\kappa}\check{v}-1\right)\Big(\kappa^{3/2}\left(\check{v}^2+3\right)+\kappa\left(\check{v}-5\check{v}^3\right) \\ &+\left(\check{v}^2-1\right)\left(\sqrt{\kappa(1-3\kappa)^2+2\sqrt{\kappa}\left(6\kappa^3-3\kappa^2+8\kappa+1\right)\check{v}+(5\kappa\check{v}+\check{v})^2}-\check{v}\right) \\ &-\sqrt{\kappa}\left(3\check{v}^2+1\right)+4\kappa^2\check{v}\Big)-\sqrt{\kappa}\check{v}^4+3\kappa\check{v}^3+3\sqrt{\kappa}\check{v}^2+\check{v}^3-\kappa^3\check{v}-\kappa^2\check{v}-5\kappa\check{v}-\check{v}\Big), \end{aligned} \tag{B.6}$$

the linear coefficients X_1^s are

$$N_1^s = \frac{(1-\sqrt{\kappa}\check{v})\left(\kappa+(3\kappa+1)\check{v}^2+2\sqrt{\kappa}(1+\kappa)\check{v}-1\right)}{(1+\kappa)\left(1-\check{v}^2\right)\left(\sqrt{\kappa}-\check{v}\right)}, \tag{B.7}$$

$$A_1^s = -\frac{4\sqrt{\kappa}\check{v}\left(1-\kappa\check{v}^2\right)\left(\kappa^2+6\kappa+\left(3\kappa^2-2\kappa-1\right)\check{v}^2+8\kappa^{3/2}\check{v}+1\right)}{(1+\kappa)^3\left(1-\check{v}^2\right)^3}, \tag{B.8}$$

$$bv_{1,1}^s = \left(\check{v}-\sqrt{\kappa}\right)\left(\sqrt{\kappa}\check{v}-1\right)\left(\kappa+(3\kappa+1)\check{v}^2+2\sqrt{\kappa}(\kappa+1)\check{v}-1\right), \tag{B.9}$$

$$\begin{aligned} c\omega_{1,1}^s = {} & 2\left(1-\sqrt{\kappa}\check{v}\right)\Big(\kappa^{3/2}\left(\kappa^3+3\kappa^2-\kappa-3\right)+\kappa\left(3\kappa^4+4\kappa^3-2\kappa^2+20\kappa+7\right)\check{v}^5 \\ & -\kappa^{3/2}\left(5\kappa^3-9\kappa^2+59\kappa+9\right)\check{v}^4-\left(\kappa^5+29\kappa^4-30\kappa^3+50\kappa^2+13\kappa+1\right)\check{v}^3 \\ & +\sqrt{\kappa}\left(4\kappa^4-21\kappa^3+45\kappa^2+5\kappa-1\right)\check{v}^2+\sqrt{\kappa}(\kappa+1)(3\kappa+1)^2\check{v}^6 \\ & +\left(2\kappa^5+9\kappa^4-4\kappa^3+14\kappa^2+10\kappa+1\right)\check{v}\Big), \end{aligned} \tag{B.10}$$

$$\begin{aligned} 2bv_{1,2}^s = {} & \left(1-\sqrt{\kappa}\check{v}\right)\Bigg[-(1-\check{v}^2)\left(\sqrt{\kappa(1-3\kappa)^2+2\sqrt{\kappa}\left(6\kappa^3-3\kappa^2+8\kappa+1\right)\check{v}+(5\kappa\check{v}+\check{v})^2}-\check{v}\right) \\ & \kappa^{3/2}\left(\check{v}^2+3\right)+\kappa\left(\check{v}-5\check{v}^3\right)-\sqrt{\kappa}\left(3\check{v}^2+1\right)+4\kappa^2\check{v}\Bigg], \end{aligned} \tag{B.11}$$

$$\begin{aligned} d\omega_{1,2}^s = {} & -2\sqrt{\kappa}\left(\sqrt{\kappa}-\check{v}\right)\left(\sqrt{\kappa}\check{v}-1\right)^2\left(\sqrt{\kappa}\check{v}+1\right)\Bigg[\check{v}\left(\kappa^4-20\kappa^2-12\kappa\right. \\ & +(3\kappa+1)\left(\kappa^3-\kappa^2-7\kappa-1\right)\check{v}^4+2\sqrt{\kappa}\left(\kappa^3+11\kappa^2-9\kappa-3\right)\check{v}^3 \\ & \left.+2\left(4\kappa^4-\kappa^3+23\kappa^2+5\kappa+1\right)\check{v}^2+2(\kappa-1)^2\sqrt{\kappa}\left(\kappa^2+7\kappa+2\right)\check{v}-1\right) \\ & \frac{(\kappa+1)}{2(1-\kappa)}\left(\sqrt{\kappa}+\check{v}\right)\left(\sqrt{\kappa}\check{v}-1\right)\left(\sqrt{\kappa}(\kappa+3)+3\kappa\check{v}+\check{v}\right)\Big(\kappa^{3/2}\left(\check{v}^2+3\right) \\ & -\left(\check{v}^2-1\right)\left(\sqrt{\kappa(1-3\kappa)^2+2\sqrt{\kappa}\left(6\kappa^3-3\kappa^2+8\kappa+1\right)\check{v}+(5\kappa\check{v}+\check{v})^2}+\check{v}\right) \\ & +\kappa\left(\check{v}-5\check{v}^3\right)-\sqrt{\kappa}\left(3\check{v}^2+1\right)+4\kappa^2\check{v}\Big)\Bigg], \end{aligned} \tag{B.12}$$

$$v_{1,3}^s = v_{1,2}^s+\frac{(1-\sqrt{\kappa}v)\sqrt{\kappa(1-3\kappa)^2+2\sqrt{\kappa}\left(6\kappa^3-3\kappa^2+8\kappa+1\right)v+(5\kappa v+v)^2}}{1-\kappa^2}, \tag{B.13}$$

$$\omega_{1,3}^s = \omega_{1,2}^s+\frac{2\left(v-\sqrt{\kappa}\right)\left(1-\kappa v^2\right)\sqrt{\kappa(1-3\kappa)^2+2\sqrt{\kappa}\left(6\kappa^3-3\kappa^2+8\kappa+1\right)v+(5\kappa v+v)^2}}{(1-\kappa)(1+\kappa)^2\left(1-v^2\right)^2} \tag{B.14}$$

Appendix C

Power-series solution of the linear perturbation at the sonic point in $3+1$ dimensions

The leading coefficients of the linear perturbations around the sonic point are explicitly given by

$$\begin{aligned} d\sqrt{\kappa}\bar{\omega}^{s}_{1,0} &= \check{\tilde{A}}_1 \Big[\kappa^6\check{v}\left(\check{v}^2-1\right)^2-\kappa^{11/2}\left(\check{v}^6-3\check{v}^4+\check{v}^2+1\right)+\kappa^5\left(\check{v}^2-1\right)\left(\check{v}\left(11\check{v}^2-3\right)\right. \\ &\quad \left.+2\left(\check{v}^2-1\right)v^{s0}_{1,3}\right)-2\kappa^{9/2}\check{v}^2\left(3\check{v}^4-16\check{v}^2+5\right)+2\kappa^4\left(v^{s0}_{1,3}+\check{v}\left(9\check{v}^4+2\check{v}^2\right.\right. \\ &\quad \left.\left.+\left(5\check{v}^2-6\right)v^{s0}_{1,3}\check{v}+5\right)\right)+2\kappa^{7/2}\left(-11\check{v}^6+13\check{v}^4-15\check{v}^2+8\left(\check{v}^2-1\right)v^{s0}_{1,3}\check{v}+5\right) \\ &\quad -2\kappa^3\left(\check{v}\left(13\check{v}^4+10\check{v}^2+9\right)+2\left(\check{v}^4-4\check{v}^2+3\right)v^{s0}_{1,3}\right)+2\kappa^{5/2}\left(\check{v}^6+7\check{v}^4-17\check{v}^2+1\right) \\ &\quad +\kappa^2\left(\check{v}\left(\check{v}\left(16v^{s0}_{1,3}-3\check{v}\left(\check{v}^2+4v^{s0}_{1,3}\check{v}-10\right)\right)+5\right)-4v^{s0}_{1,3}\right)+\kappa^{3/2}\left(3\check{v}^6-\check{v}^4+3\check{v}^2\right. \\ &\quad \left.-16\left(\check{v}^2-1\right)v^{s0}_{1,3}\check{v}+11\right)-\kappa\check{v}\left(\check{v}^2-1\right)^2+2\kappa\left(\check{v}^4-6\check{v}^2+5\right)v^{s0}_{1,3}-2\sqrt{\kappa}\left(\check{v}^4-1\right) \\ &\quad +2\left(\check{v}^2-1\right)^2v^{s0}_{1,3}\Big], \end{aligned} \tag{C.1}$$

$$\begin{aligned} dv^{s}_{1,0} &= \check{\tilde{A}}_1\left(1-\check{v}^2\right)^2\left(1-\sqrt{\kappa}\check{v}\right)\left[\kappa\left(-\kappa^3+\kappa^2+\kappa-11\right)+\left(\kappa^4+\kappa^3-25\kappa^2+\kappa+2\right)\check{v}^2\right. \\ &\quad \left.-\sqrt{\kappa}(\kappa(\kappa(\kappa+9)-3)-3)\check{v}^3+(\kappa-3)\sqrt{\kappa}(\kappa(3\kappa+10)+1)\check{v}-2\right], \end{aligned} \tag{C.2}$$

where

$$\begin{aligned} d &= 8\sqrt{\kappa}\left(\sqrt{\kappa}\check{v}+1\right)^2\left((\kappa-1)\kappa^{3/2}-\kappa^{3/2}(\kappa+3)\check{v}^4+2\sqrt{\kappa}\left(\kappa^2+1\right)\check{v}^2\right. \\ &\quad \left.+\left(\kappa^2-1\right)\left(\check{v}^2-1\right)v^{s0}_{1,3}+\kappa(\kappa+1)^2\check{v}^3-\kappa(\kappa+1)^2\check{v}\right). \end{aligned} \tag{C.3}$$

In the above, $v^{s0}_{1,3}$ stands for the linear coefficient of the background solution, and its expression is given in Appendix B.13.

Appendix D

Linear perturbation of the $\mu = \Omega = 0$ stationary solutions with $P = \kappa\rho$

D.1 Linearized equations

In Ch. 7, we show that the critical solution of the perfect fluid in spherical symmetry is *quasistatic*:. In particular, the critical solution is, to leading order in $\dot{s}$, static. It is therefore interesting to understand the perturbation spectrum of the static solution.

Since we consider the case $\mu = \Omega = 0$, we will work with respect to the variable x, instead of y. Let us then consider the following perturbations of the static $\mu = 0$ solution,

$$\chi(T,x) = \chi_0(x) + \epsilon\chi_0(x)\bar{\chi}_1(T,x), \tag{D.1}$$

$$M(T,x) = M_0(x) + \epsilon M_0(x)\bar{M}_1(T,x), \tag{D.2}$$

$$\varrho(T,x) = \varrho_0(x) + \epsilon\varrho_0(x)\bar{\varrho}_1(T,x), \tag{D.3}$$

$$\mathcal{V}(T,x) = \epsilon\bar{\mathcal{V}}_1(T,x), \tag{D.4}$$

where the coordinate $T := t/s$ is dimensionless and, for convenience, we defined

$$\mathcal{V} := v/x, \qquad \chi := \alpha/a, \qquad \varrho := 4\pi R^2\rho. \tag{D.5}$$

The background static solutions χ_0, M_0, ϱ_0 were factored out of the perturbation because the linearized equations are more compact in this form and the subsequent analysis is simplified. For convenience, we will make a small abuse of language and refer to $\bar{\chi}_1, \bar{M}_1, \bar{\varrho}_1, \bar{\mathcal{V}}_1$ as the perturbed variables.

The linearized equations read

$$\frac{\partial \bar{\chi}_1}{\partial x} = \frac{1-\kappa}{2}\frac{\partial \bar{M}_1}{\partial x}, \tag{D.6}$$

$$\frac{\partial \bar{M}_1}{\partial x} = \frac{4\varrho_0(\bar{\varrho}_1 - \bar{M}_1)}{xM_0}, \tag{D.7}$$

$$\frac{\partial \bar{M}_1}{\partial T} = -\frac{4(1+\kappa)\chi_0\varrho_0\bar{\mathcal{V}}_1}{M_0}, \tag{D.8}$$

$$\frac{\partial \bar{\varrho}_1}{\partial T} = -\frac{\chi_0(1+\kappa)\left\{(4\varrho_0+2M_0)\bar{\mathcal{V}}_1 + xM_0\frac{\partial \bar{\mathcal{V}}_1}{\partial x}\right\}}{M_0}, \tag{D.9}$$

$$\frac{\partial \bar{\mathcal{V}}_1}{\partial T} = \frac{\kappa\chi_0\left\{2(1+\kappa)\varrho_0(\bar{\varrho}_1 - \bar{M}_1) - xM_0\frac{\partial \bar{\varrho}_1}{\partial x}\right\}}{x^2(1+\kappa)M_0}, \tag{D.10}$$

The compatibility condition $\partial_x\partial_T M = \partial_T\partial_x M$ can be checked to be verified.

Note that the linearized equations do not depend explicitly on $\bar{\chi}_1$. As we will see shortly, this is linked to a gauge freedom to rescale the time coordinate. Furthermore, since (D.6) is easily integrable, we will ignore it in what follows.

D.2 Boundary asymptotics

From (D.6-D.10), we find near the center that

$$\left.\frac{\partial \bar{M}_1}{\partial x}\right|_{\text{center}} \sim x(\bar{\varrho}_1 + \bar{M}_1), \tag{D.11}$$

$$\left.\frac{\partial \bar{M}_1}{\partial T}\right|_{\text{center}} \sim x^2\bar{\mathcal{V}}_1, \tag{D.12}$$

$$\left.\frac{\partial \bar{\varrho}_1}{\partial T}\right|_{\text{center}} \sim \bar{\mathcal{V}}_1, \tag{D.13}$$

$$\left.\frac{\partial \bar{\mathcal{V}}_1}{\partial T}\right|_{\text{center}} \sim \bar{\varrho}_1 + \bar{M}_1 + \frac{1}{x}\frac{\partial \bar{\varrho}_1}{\partial x}, \tag{D.14}$$

In the above, constant factors in front of each term have been suppressed.

Note that the $\bar{\varrho}_1$, $\bar{M}_1$ and $\bar{\mathcal{V}}_1$ are all required to have an even expansions near the center, as expected (see again Sec. 3.5.2). Eq. (D.12) implies, assuming that the variables are bounded at the origin, that $\bar{M}_1(T, x=0)$ is constant. We impose that the perturbations do not produce conical singularities, which enforces that $\bar{M}_1(T,0) = 0$.

For $\mu = 0$, there is a surface $x = x_\star$ at which the metric variables α and a diverge. Usually, dealing with perturbations of a singular background is complicated, and requires special care. On the other hand, the variables that we use are all finite at the surface and, for now, we will not worry about it.

Near this surface, we have

$$\left.\frac{\partial \bar{M}_1}{\partial x}\right|_{\text{surface}} \sim \frac{\bar{M}_1 + \bar{\varrho}_1}{x_\star - x}, \tag{D.15}$$

$$\left.\frac{\partial \bar{M}_1}{\partial T}\right|_{\text{surface}} \sim \bar{\mathcal{V}}_1, \tag{D.16}$$

$$\left.\frac{\partial \bar{\varrho}_1}{\partial T}\right|_{\text{surface}} \sim \bar{\mathcal{V}}_1 + (x_\star - x)\frac{\mathrm{d}\bar{\mathcal{V}}_1}{\mathrm{d}x}, \tag{D.17}$$

$$\left.\frac{\partial \bar{\mathcal{V}}_1}{\partial T}\right|_{\text{surface}} \sim \bar{\varrho}_1 + \bar{M}_1 + \frac{\mathrm{d}\bar{\varrho}_1}{\mathrm{d}x}, \tag{D.18}$$

where, again, constant factors in front of each term are suppressed. The above asymptotics suggest that the leading order term in $x_\star - x$ in each variables is $\propto (x_\star - x)^p$ for the same constant $p \in \mathbb{R}$.

D.3 Stability analysis

To study the linear stability, we consider the perturbations of the form

$$\bar{M}_1(T, x) =: e^{\eta T} M_1(x), \tag{D.19}$$

and similarly for the other variables. This ansatz transforms the PDE system (D.7-D.10) into a system of three ODEs and one algebraic equation. The latter gives a relation between $\mathcal{V}_1$ and M_1,

$$\mathcal{V}_1 = -\frac{\eta}{4(1+\kappa)}\frac{M_0}{\chi_0 \varrho_0} M_1 = \frac{\eta\kappa}{2(1+\kappa)}\frac{M_1}{x^2}. \tag{D.20}$$

The regularity condition $M_1(0) = 0$ ensures that $\mathcal{V}_1$ is regular at the center, $x = 0$. Now, substituting this expression into the ODEs yields an ODE system for the remaining variables M_1, ϱ_1,

$$\frac{\mathrm{d}M_1}{\mathrm{d}x} = -\frac{4\varrho_0(M_1 - \varrho_1)}{xM_0}, \tag{D.21}$$

$$\frac{\mathrm{d}\varrho_1}{\mathrm{d}x} = \frac{\eta^2 x M_0 M_1}{4\kappa\chi_0^2\varrho_0} - \frac{2(1+\kappa)\varrho_0(M_1 - \varrho_1)}{xM_0}. \tag{D.22}$$

Note that the eigenmode frequency η appears in the above system squared. As a linear system, the above can be recast into the form

$$\frac{\mathrm{d}}{\mathrm{d}x}\begin{pmatrix} M_1 \\ \varrho_1 \end{pmatrix} = A \begin{pmatrix} M_1 \\ \varrho_1 \end{pmatrix}, \tag{D.23}$$

where the 2×2 matrix A only depends on the background solution.

D.4 Power-series solution near $x = x_\star$

As hinted in the boundary asymptotics, we analyze the singular surface more closely by making a Frobenius expansion of the form

$$M_1 = \sum_{n=0}^{\infty} M_1^s(n)(x_\star - x)^{p+n}, \tag{D.24}$$

and so on, where $p \in \mathbb{R}$ is some constant to be determined. One easily checks that the system admits a nontrivial solution only if the frequency η and exponent p are related by

$$\eta^2 = 2(1-\kappa)p(1+p). \tag{D.25}$$

From the above expression, if we parametrize the solution of the linearized equations by the parameter p, then we obtain two distinct solutions since the above is preserved under the symmetry $p \to -(1+p)$. This symmetry will play an important role later. Note that the perturbation is either oscillatory (in the sense that η is purely imaginary) if $-1 < p < 0$, and otherwise η is real. Thus, the modes can only be either purely oscillatory or growing/decaying. In both cases, these come in pairs since η appears squared.

D.5 Gauge freedom and scaling mode

Recall that the spherically symmetric metric enjoys a gauge freedom consisting of an arbitrary redefinition of the time coordinate $t \to t(t')$. Consider the metric

$$\mathrm{d}s^2 = -\alpha^2 \mathrm{d}t^2 + a^2 \mathrm{d}R^2 + R^2 \mathrm{d}\theta^2, \tag{D.26}$$

where the coefficients are the $\mu = 0$ static solution plus the linear perturbations: $\alpha(t, R) = \alpha_0(R) + \epsilon e^{\eta T}\alpha_0(R)\alpha_1(R)$, and so on. Now, let us consider an infinitesimal coordinate transformation $t \to t + \epsilon h(t)$. The lapse changes as

$$\delta\alpha = \epsilon\alpha_0 h'(t) + \mathcal{O}(\epsilon^2). \tag{D.27}$$

In order for this transformation to still represent an eigenmode solution, we then require that

$$h(t) = He^{\eta T}, \tag{D.28}$$

where H is a proportionality constant. This new lapse function is then still a solution to the linearized equations. This is because this coordinate transformation causes $\bar{\chi}_1$ to be shifted by a constant, leaving the linearized equation (D.6) unaltered. This freedom is fixed by fixing the value of $\alpha_1(x)$ at some point $x = x_0$. We will fix this freedom later.

Beside this gauge freedom, the eigenmode solution also enjoys a second kind of freedom, called a scaling or zero-mode. Note that the linear perturbation becomes time independent if $\eta = 0$. This particular perturbation is actually to be interpreted as a change in the overall

scale s of the star. More precisely, recall that the spherically symmetric static solutions is a one-parameter family of solution, parametrized by an overall scale s. Let $f_0(x)$ denotes the family of static solution. If we consider a perturbation of the scale $s' = s(1-\epsilon)$, then it is easy to check that

$$f_0(x') = f_0(x) - \epsilon \frac{\mathrm{d}}{\mathrm{d}\epsilon} f\left(\frac{R}{s'}\right)\Big|_{\epsilon=0} + \mathcal{O}(\epsilon^2), \tag{D.29}$$

$$= f_0(x) + \epsilon x f_0'(x) + \mathcal{O}(\epsilon^2). \tag{D.30}$$

Near the surface, $f_0 \sim (x_\star - x)^{p_0}$ for some constant p_0. Then,

$$x f_0'(x)|_{\text{surface}} \sim (x_\star - x)^{p_0 - 1}. \tag{D.31}$$

On the other hand, the linear perturbation, near the surface, is of the form

$$f_0 f_1|_{\text{surface}} \sim (x_\star - x)^{p_0 + p}. \tag{D.32}$$

The perturbation due to the rescaling of s (D.31) matches the linear perturbation (D.32) for $p = -1$. This result is also consistent with (D.25). We remark that the other possibility, namely $p = 0$, can also be obtained by exploiting the invariance of the ODE system by the symmetry $p \to -1 - p$.

D.6 Analytical solution

The ODE system (D.21-D.22) can be rewritten as a single second-order (linear) ODE for, say, M_1:

$$M_1''(x) - \left[\frac{1}{x} - \frac{4(1-\kappa)\varrho_0}{x M_0}\right] M'(x) - \frac{\eta^2}{\kappa \chi_0^2} M(x) = 0. \tag{D.33}$$

In terms of the variable

$$\chi := \chi_0 = 1 - (1-\kappa)\frac{x^2}{2\kappa} \tag{D.34}$$

and making use of (D.25), the above can be rewritten as a singular Sturm-Liouville equation, on the interval $\chi \in [0, 1]$,

$$(1-\chi)\left(\chi^2 M_1'\right)' = p(1+p) M_1, \tag{D.35}$$

where, from now on, a prime signifies a derivative with respect to χ. This ODE has three regular singular points, at $\chi = 0$, 1 and ∞. It can therefore be rewritten as an hypergeometric differential equation.

Recall that the standard form of the hypergeometric differential equation is

$$z(1-z)f'' + (c - (1+a+b)z)f' - abf = 0, \tag{D.36}$$

where a, b, c are constants. Note that the above ODE has regular singular points at $z = 0, 1, \infty$, which coincide with the singular points for (D.35). This means that we should take for the

independent variable $z \equiv \chi$. For the dependent variable, introduce

$$M_{HG}(\chi) := \chi^{-p} M_1(\chi). \tag{D.37}$$

M_{HG} then satisfies

$$\chi(1-\chi)M''_{HG} + 2(1+p)(1-\chi)M'_{HG} - p(1+p)M_{HG} = 0. \tag{D.38}$$

This is of the form (D.36), with $f \equiv M_{HG}$, $a = p$, $b = 1+p$, $c = 1+a+b$.

The general power-series solution of (D.36), around each of the regular singular points, is typically written in terms of the hypergeometric function ${}_2F_1\,(a,b;c;z) \equiv F(a,b;c;z)$.

Recall that the general hypergeometric function $F(a,b;c;z)$ may be defined via its power-series expansion as

$$F(a,b;c;z) := \sum_{n=0}^{\infty} \frac{a_n b_n}{c_n} \frac{z^n}{n!}, \tag{D.39}$$

where, for arbitrary $q \in \mathbb{C}$, q_n stands for the Pochhammer symbol,

$$q_n := \begin{cases} 1, & n = 0, \\ q(q+1)...(q+n-1), & n > 0. \end{cases} \tag{D.40}$$

The explicit form of the solution of the general hypergeometric equation (D.36) depends on the specific values of a, b, c. In our case (D.38), we mainly need to distinguish two cases, namely if p is a half integer or not.

Due to the symmetry of the system $p \to -1-p$, we can without loss of generality restrict to $p \geq -1/2$.

D.6.1 $p \notin \mathbb{N} - \frac{1}{2}$

The general solution of the hypergeometric equation (D.38) is

$$M_{HG} = C_1 F(p, 1+p, 2+2p, \chi) + C_2 \chi^{-1-2p} F(-1-p, -p, -2p, \chi), \tag{D.41}$$

where C_1 and C_2 are integration constants. We remark that if $p \in \mathbb{Z}$ and from (D.39), the power series is formally ill-defined since for some n, we have that $a_n = c_n = 0$. The power series is to be interpreted by considering $p - \delta$, instead of p, and taking the limit $\delta \to 0$. It is then easy to see that $\lim_{\delta \to 0} a_n/c_n$ is finite and the corresponding power-series is well-defined. Note that the solution displays the symmetry $p \to -1-p$ as expected. From the algebraic constraint (D.20), $\mathcal{V}_1$ is then

$$\mathcal{V}_1 \propto \frac{p\chi^p M_{HG}}{1-\chi}. \tag{D.42}$$

Let us now try to find constraints on the integration constants and p in order for the linear perturbation to be regular. Seeking for a nontrivial $\mathcal{V}_1$ which is also finite at the surface $\chi = 0$,

we need to take $p > 0$. M_{HG} then simplifies to

$$M_{HG} = C_1 F(p, 1+p, 2+2p, \chi). \tag{D.43}$$

The constant C_1 is simply a scale that emerges from the fact that we are dealing with linear equations. Note that the hypergeometric function in (D.43) converges up to and including the endpoint $\chi = 1$. One can check that this choice also makes the perturbations M_1 and ϱ_1 regular at the surface.

Turning now our attention at the center, $\chi = 1$, we have that,

$$M_{HG} \sim \frac{\Gamma(\frac{3}{2}+p)}{\Gamma(2+p)}, \tag{D.44}$$

where $\Gamma(\cdot)$ is the usual gamma function. $\mathcal{V}_1$ is regular at the center provided that M_1, and therefore M_{HG}, vanishes at the center. This would require $p = -2, -3, \cdots$, which is not permissible, since we require $p \geq 0$.

Thus, in this case, there is no solution that is regular everywhere, including at the center and surface.

D.6.2 $p \in \mathbb{N} - \frac{1}{2}$

In this particular case, the general solution is more subtle. Looking back at (D.41), the first term stays well-defined and in fact still remains a solution to the ODE. On the other hand, the second term is singular, since we have that for some n, $c_n = 0$, and, unlike with the case where $p \in \mathbb{Z}$ considered previously, $a_n, b_n \neq 0$. Therefore, this second solution is not valid anymore and needs to be replaced with a different power series. The second fundamental solution is more complicated and may be written schematically as,

$$F(p, 1+p, 2+2p, \chi) \ln \chi + \sum_{k=1}^{1+2p} A_k \chi^{-k} + \sum_{l=0}^{\infty} B_l \chi^l, \tag{D.45}$$

where the A_k and B_l are constants.

The second term vanishes in the case where $p = -\frac{1}{2}$. In any cases, this solution is neither analytic nor regular at the surface $\chi = 0$. This solution should be rejected. However, doing so again leads to the same conclusion drawn in the previous section, since the solution is just (D.43) again.

We therefore see that for all $p \neq -1, 0$, it is impossible to have a solution of the linear equations, which is regular at both the center and surface.

This shows that we should instead consider a singular expansion, where there really are two different regimes: one regime, close to the center, where the velocity and its gradient are small and thus the linear ansatz works, and a second region, close to the surface, where velocity grows quickly and has large gradient.

On hindsight, the failure to find a solution that is regular everywhere is not surprising. This is because, as we noted before, the background solution is singular at the surface in the first place! It is therefore a priori unclear what the proper boundary conditions are at the surface.

One workaround is to consider the perturbation of the static solution with $\mu \neq 0$, in the coordinate y, and study the limit $\mu \to 0$. Near the center, this limit is regular and we expect the above hypergeometric solution, along with the regularity condition at the center, to be consistent with it. On the other hand, near the surface, the effect of μ cannot be perturbative. In practice, it would suffice to find a suitable boundary condition at $y = \infty$ and take the limit $\mu \to 0$ of this boundary condition. From the above discussion, we expect the appropriate boundary condition to have a singular limit as $\mu \to 0$. See also Appendix G below.

Appendix E

No CSS solution for the perfect fluid in $2+1$ dimensions

We show here that in $2+1$ there are no nontrivial self-similar, spherically symmetric perfect fluid solutions with a barotropic equation of state, $P=\kappa\rho$, that is regular at the light cone.

We employ a similar notation as in Ref. [132] namely, the independent variables are defined by

$$x := -\frac{r}{t}, \quad \tau := -\ln(-t) \tag{E.1}$$

and

$$N := \frac{\alpha}{ax},\ A := a^2,\ \omega := 4\pi r^2 a^2 \rho. \tag{E.2}$$

The equations of motion read

$$\frac{A'}{A} = \frac{4\omega(1+v^2\kappa)}{x(1-v^2)}, \tag{E.3}$$

$$\frac{\omega'}{\omega} = \frac{\left(1+v^2\kappa\right)\left((1-\kappa)\left(v^2(2\omega+1)+2\omega\right)+2\right)}{x\left(1-v^2\right)\left(1-v^2\kappa\right)}, \tag{E.4}$$

$$\frac{v'}{v} = \frac{(1+v^2\kappa)(1+2\omega(1-\kappa))}{x(1-v^2\kappa)}, \tag{E.5}$$

$$N = -\frac{1+\kappa v^2}{v(1+\kappa)}. \tag{E.6}$$

It is important to notice that the velocity is restricted to negative values $-1 < v < 0$ and $A' \geq 0$, $\omega' \geq 0$, and $v' \leq 0$. By definition, the light cone, $x = x_{\rm lc}$, occurs at $v^2(x_{\rm lc}) = 1$.

First, we show that $x_{\rm lc}$ is finite. From Eq. (E.5), we can find an upper bound for $|v|'$,

$$\frac{|v|'}{|v|} \geq \frac{1+v^2\kappa}{x(1-v^2\kappa)}. \tag{E.7}$$

The above inequality is separable and upon integration we find

$$x \leq \frac{C|v|}{1+\kappa v^2}, \tag{E.8}$$

where $C > 0$ is an integration constant. In particular, we find an upper bound for $x_{\rm lc}$,

$$x_{\rm lc} \leq \frac{C}{1+\kappa} < \infty. \tag{E.9}$$

Since $x_{\rm lc}$ is finite, the ODE system needs to be regularized at that point. Specifically, we must impose the numerators in Eqs. (E.3) and (E.4) to vanish at the light cone. This gives the constraint

$$\omega(x_{\rm lc}) = 0. \tag{E.10}$$

This constraint, together with the property that $\omega' \geq 0$, implies

$$\omega(x) = 0, \qquad x \in [0, x_{\rm lc}], \tag{E.11}$$

which proves our claim.

Appendix F

Spherically symmetric static fluid in $2+1$ dimensions

We review and expand some relevant properties of the static perfect fluid solutions discussed in Ch. 5.

For a given equation of state, these can be parameterized by a length scale s, so that formally we can write

$$Z = \hat{Z}(R, s), \qquad Z := \{R^2\rho, a, \alpha, M\}, \tag{F.1}$$

where the hat denotes the static solution, when expressed in terms of the radial coordinate R and scale parameter s. (We come back to the interpretation of s below).

The functions $\hat{Z}(R, s)$ cannot be given in closed form, but the quantities Z and the area radius R can be given explicitly in terms of an auxiliary radial coordinate y that is defined by $\alpha =: y$.

We introduce the intermediate dimensionless quantities

$$x := \frac{R}{s} \tag{F.2}$$

and

$$\mu := -\Lambda s^2. \tag{F.3}$$

We can then write

$$\hat{Z} = \check{Z}(x, \mu), \qquad \check{R} = \sqrt{\mu}\ell x. \tag{F.4}$$

We then have the following explicit expressions for the static solution, but expressed in terms of the radial coordinate y and parameter μ:

$$\bar{\alpha} =: y, \tag{F.5}$$

$$\bar{\rho} = \frac{1-\mu}{8\pi\kappa\mu\ell^2} y^{-\frac{1+\kappa}{\kappa}}, \tag{F.6}$$

$$\bar{a}^{-1} = \mu y + (1-\mu) y^{-\frac{1}{\kappa}}, \tag{F.7}$$

$$\bar{M} = \bar{x}^2\mu - \bar{a}^{-2}, \tag{F.8}$$

$$\bar{x}^2 = \mu(y^2-1) + \frac{2\kappa(1-\mu)}{1-\kappa}\left(1 - y^{-\frac{1-\kappa}{\kappa}}\right). \tag{F.9}$$

$$\bar{R} = \sqrt{\mu}\ell\bar{x}. \tag{F.10}$$

The functions $\hat{Z}(R,s)$ are now given implicitly in terms of $\bar{R}(y,\mu)$ and $\bar{Z}(y,\mu)$.

Note that only values $0 \le \mu \le 1$ are physical, that $R=0$ is at $y=1$, and that (for $\mu > 0$ only) $R \to \infty$ as $y \to \infty$.

We also need to evaluate $\hat{Z}_{,R}$ and $\hat{Z}_{,s}$. For these, we can derive the following expressions that are explicit in y and μ:

$$\hat{Z}_{,s} = \frac{2}{\ell\sqrt{\mu}}\left(\mu\bar{Z}_{,\mu} - \frac{\mu(\bar{x}^2)_{,\mu} + \bar{x}^2}{(\bar{x}^2)_{,y}}\bar{Z}_{,y}\right), \tag{F.11}$$

$$\hat{Z}_{,R} = \frac{2\bar{x}}{\ell\sqrt{\mu}(\bar{x}^2)_{,y}}\bar{Z}_{,y}. \tag{F.12}$$

For $\mu \ll 1$, we can distinguish a stellar interior and an atmosphere, divided by a sharp turning point in $\hat{\rho}(R,s)$. While the surface of the star is not defined precisely in the presence of an atmosphere, we can take it to be at

$$y = y_c := \left(\frac{1-\mu}{\kappa\mu}\right)^{\frac{\kappa}{1+\kappa}}. \tag{F.13}$$

This marks both the maximum of $\bar{a}$ and the turning point of $\bar{x}^2$, with respect to y. Note that for $\mu \ll 1$,

$$\bar{x}(y_c,\mu) =: \check{x}_c \simeq x_\star \tag{F.14}$$

In the interior of the star we can neglect the first term in $\bar{x}^2$, obtaining the approximate closed-form expression for $\check{y}$,

$$\check{y} \simeq \left(1 - \frac{1}{1-\mu}\frac{x^2}{x_\star^2}\right)^{-\frac{\kappa}{1-\kappa}}, \tag{F.15}$$

where we have defined

$$x_\star^2 := \frac{2\kappa}{1-\kappa}. \tag{F.16}$$

Explicit approximate expressions for $\check{Z}$ then follow.

In the exterior of the star, we can approximate the second term in $\bar{x}^2$ by its asymptotic value, obtaining

$$\check{y} \simeq \mu^{-1}\left(-\check{M}_\infty + \mu x^2\right)^{\frac{1}{2}} = \mu^{-1}\left(-\check{M}_\infty + \frac{\check{R}^2}{\ell^2}\right)^{\frac{1}{2}}, \tag{F.17}$$

where

$$\check{M}_\infty := \frac{-(1+\kappa)\mu^2 + 2\kappa\mu}{1-\kappa}, \tag{F.18}$$

is the total mass of the system. This again gives explicit approximate expressions for $\check{Z}$, in particular

$$\mu^2\check{\alpha}^2 \simeq \check{a}^{-2} \simeq -\check{M}_\infty + \frac{\check{R}^2}{\ell^2}. \tag{F.19}$$

We see that in the atmosphere, the metric is approximated by the BTZ metric with fixed mass $\check{M}_\infty$ (and t rescaled relative to the convention for BTZ solutions), and so the fluid is approximated as a test fluid, neglecting its self-gravity.

Substituting Eq. (F.17) into Eq. (F.6), we find

$$\check{\rho} \simeq \frac{1-\mu}{8\pi\kappa\mu\ell^2}\left(-\frac{\check{M}_\infty}{\mu} + x^2\right)^{-\frac{1+\kappa}{2\kappa}}. \tag{F.20}$$

The central density $\check{\rho}_0 := \check{\rho}(0,\mu)$ is related to the total mass by

$$\lim_{\mu\to 0}\frac{\check{M}_\infty\check{\rho}_0}{-\Lambda} = \frac{1}{4\pi(1-\kappa)}. \tag{F.21}$$

We now come back to the interpretation of s as a length scale. For $0 < \mu \ll 1$, the surface $y = y_c$ is at $x \simeq x_\star$, and hence at $R \simeq x_\star s$. In this sense, $x_\star s$ is the size of the star. In the limiting case $\mu = 0$, the star has a sharp surface at $x = x_\star$, with $\check{M}_\infty = 0$ in the vacuum exterior. The exterior spatial geometry is then that of a cylinder of constant radius. The limit $\mu \to 0$ is singular in the sense that for vanishing μ, the approximation $\check{Z}(x,\mu) \simeq \check{Z}(x,0)$ is only valid for $x < x_\star$.

This means that in the limit where the size of the star is small compared to the cosmological length scale ℓ, $\mu = s^2/\ell^2 \ll 1$, the family of static solutions becomes invariant under rescaling R and ρ according to their dimensions, but only in the interior of the star. In the atmosphere, $Z = \check{Z}(x,0)$ is not a good approximation for small but finite μ, and we need the full form $Z = \check{Z}(x,\mu)$.

Appendix G

The quasistatic solution

We model the critical solution as quasistatic, meaning that it adiabatically goes through the sequence of static solutions, with s now a function of t, and $|\dot{s}(t)| \ll 1$. We can then formally expand the quantities Z in even powers of $\dot{s}$, and v in odd powers.

In fact, from the exponential form (7.46) of $s(t)$ it follows that $\dot{s} = -\nu s/\ell = -\nu\sqrt{\mu}$, and hence $\dot{s}^2 = s\ddot{s} = \nu^2\mu$, and so the quasistatic approximation is equivalent to the small ν approximation. For now, however, we do not assume the exponential form.

A crucial aspect of the analysis is that the spherically symmetric static solutions with $\Lambda \neq 0$ form a one-parameter family of solutions, parametrized by a scale parameter s; see Appendix F. This situation is reminiscent of a study of Bizon, Ovchinnikov and Sigal [175, 176], who considered the collapse of a spherically symmetric Yang-Mills field in $4+1$ dimensions Minkowski spacetime.

In general $d+1$ dimensions, the Yang-Mills equations are invariant under an appropriate rescaling of the coordinates and Yang-Mills potential $A_\alpha(R) \to \lambda^{-1}A_\alpha(R/\lambda)$. Thus, any solution of the Yang-Mills equations in fact gives rise to a one-parameter family of solutions, parametrized by λ. The energy associated with the Yang-Mills field scales as λ^{d-4}, which gives a heuristic explanation of the global regularity of the Yang-Mills equations for $d < 4$. In $d > 4$, the Yang-Mills equations are known to admit self-similar (and thus singular) solutions. For the "critical" dimension $d = 4$, the equations do not admit self-similar solutions, but they admit a one-parameter family of static (instanton) solutions, denoted by $\chi(R/\lambda)$. It was shown that near the time of collapse, a certain two-parameter family of initial data evolves into the universal profile of the static solution, with a size that shrinks adiabatically to zero, $\chi(R/\lambda(t))$.

In our case, it is the $\Lambda < 0$ static solution that plays the role of the instanton. A notable difference is that the underlying Einstein equations are not scale-invariant. On the other hand, since the solution shrinks, one would expect near the center that the critical solution can be expanded in powers of (length scale of the solution)/(cosmological length scale) so that near $t \simeq t_\#$, the critical solution is, to leading order, of the form

$$Z_\star(t,R) = Z_0\left(\frac{R}{s(t)},0\right) + \mathcal{O}(\Lambda,\dot{s}), \tag{G.1}$$

We emphasize that the above expansion is only expected to be valid near the center. This is because the cosmological constant is a necessary ingredient for black holes to form in $2+1$ and its effect cannot be perturbative over the whole of the critical solution. This can in particular be seen by noting that $Z_0(R/s(t), 0)$ is singular (see Appendix F) at a finite radius, corresponding to the location of the surface of the $\Lambda = 0$ static solution. This singular surface is removed if the cosmological constant is taken into account.

The leading and next order for Z in the quasistatic ansatz are

$$Z_\star(R,t) = Z_0(R,t) + \dot{s}^2(t) Z_2(R,t) + O(\dot{s}^4), v_\star(R,t) = \dot{s} v_1(R,t) \tag{G.2}$$

where

$$Z_0(R,t) := \hat{Z}(R, s(t)) = \bar{Z}(y,\mu) \tag{G.3}$$

and similarly for v_1. As noted above, we do not have $\hat{Z}(R,s)$ in explicit form, only $\bar{Z}(y,\mu)$.

Note that this ansatz respects the symmetry of the fluid equations to be invariant under the simultaneous transformation $t \to -t, v \to -v$.

Recall that the energy conservation law takes the form

$$R\frac{\partial \tau}{\partial t} + \frac{\partial (e^{\chi} R v \sigma)}{\partial R} = 0, \tag{G.4}$$

where $\chi := \ln \alpha/a$. Substituting the quasistatic ansatz in the conservation law, the order $\sim \mathcal{O}(1)$ vanishes identically and the leading perturbation equation reads

$$\frac{\partial \varrho_0}{\partial t} + R\dot{s}(1+\kappa)\frac{\partial \left(e^{\chi_0}\frac{v_1}{R}\varrho_0\right)}{\partial R} = 0. \tag{G.5}$$

Since the background variables are known explicitly in terms of (y,μ), we will first rewrite the above PDE in terms of these two coordinates. By the chain rule, the basis vectors $\left(\frac{\partial}{\partial t}, \frac{\partial}{\partial R}\right)$ are related to the new basis vectors $\left(\frac{\partial}{\partial \mu}, \frac{\partial}{\partial y}\right)$ by

$$\frac{1}{2}\frac{\partial \bar{x}^2}{\partial y}\frac{\partial}{\partial t} = \frac{\dot{s}}{s}\left(\mu \frac{\partial \bar{x}^2}{\partial y}\frac{\partial}{\partial \mu} - \left(\mu \frac{\partial \bar{x}^2}{\partial \mu} + \bar{x}^2\right)\frac{\partial}{\partial y}\right), \tag{G.6}$$

$$\frac{\partial \bar{x}^2}{\partial y}\frac{R}{2}\frac{\partial}{\partial R} = \bar{x}^2 \frac{\partial}{\partial y}. \tag{G.7}$$

Multiplying (G.5) by $\frac{1}{2}\frac{\partial \bar{x}^2}{\partial y}$ and setting the term $\sim \mathcal{O}(\dot{s})$ to zero, we obtain a linear PDE for v_1

$$\mu\left(\frac{\partial \bar{x}^2}{\partial y}\frac{\partial \bar{\varrho}}{\partial \mu} - \frac{\partial \bar{x}^2}{\partial \mu}\frac{\partial \bar{\varrho}}{\partial y}\right) = x^2 \frac{\partial \bar{F}}{\partial y}, \tag{G.8}$$

$$F := \bar{\varrho} - (1+\kappa)e^{\bar{\chi}}\bar{\varrho}\frac{\bar{v}_1}{x}. \tag{G.9}$$

The solution $\bar{v}_1(y,\mu)$ can be formally written as

$$\bar{v}_1 = \frac{x e^{-\bar{\chi}}}{1+\kappa}\left(1 - \mu\frac{\mathcal{I}}{\bar{\varrho}}\right), \tag{G.10}$$

where

$$\mathcal{I} := \int_1^y \frac{1}{x^2}\left(\frac{\partial x^2}{\partial y}\frac{\partial \bar{\varrho}}{\partial \mu} - \frac{\partial x^2}{\partial \mu}\frac{\partial \bar{\varrho}}{\partial y}\right) dy. \tag{G.11}$$

The integration constant is fixed so that at the center $y = 1$, we have $\bar{v}_1(1, \mu) = 0$. $\mathcal{I}$ can be evaluated explicitly and equals

$$\mathcal{I} = \frac{1}{2\kappa(1-\kappa)}\left[2\kappa^2(1-\mu)\left(1 - y^{-2/\kappa}\right) + (1+\kappa)(1-\mu)\left(y^{-1-1/\kappa} - y^{1-1/\kappa}\right) - 2\kappa\mu\left(1 - y^{1-1/\kappa}\right)\right], \tag{G.12}$$

from which an explicit expression for $v_1(y, \mu)$ follows.

The perturbation $\bar{v}_1(y, \mu)$ is regular for every $y \in [1, \infty)$. Its asymptotic value satisfies

$$\lim_{y\to\infty} y^{2-1/\kappa}\bar{v}_1 = \frac{2\kappa(\mu - \kappa(1-\mu))}{(1-\kappa^2)(1-\mu)\sqrt{\mu}}. \tag{G.13}$$

As $R \to \infty$, $\bar{v}_1$ goes to zero for $\kappa > 1/2$, approaches a constant value for $\kappa = 1/2$, and diverges for $\kappa < 1/2$. Hence the expansion in $\dot{s}$ breaks down in the atmosphere for $\kappa < 1/2$ at sufficiently large radius R and contraction speed $|\dot{s}|$. However, for the values of $\dot{s}$ for which we show plots, this is not a problem for values of R on our numerical grid.

As for $\hat{Z}$, we can compute $\bar{v}_1(y, \mu)$ explicitly, and as expected we find that $\check{v}_1(x, \mu) \simeq \check{v}_1(x, 0)$ for $x < x_\star$. However, $\check{v}_1(x, 0)$ blows up at the surface $x = x_\star$, while $\check{v}_1(x, \mu)$ is regular for all x.

For the velocity, we can define

$$u := \Gamma^2 v = \frac{v}{1 - v^2}. \tag{G.14}$$

The ansatz is

$$u_\star(R, t) = \dot{s}(t)u_1(R, t) + O(\dot{s}^3). \tag{G.15}$$

Clearly, for small $\dot{s}$ we have

$$v_\star(R, t) = \dot{s}(t)u_1 + O(\dot{s}^3), \tag{G.16}$$

but expanding u rather than v in a series in $\dot{s}$ makes sure that $|v| < 1$.

To order $\dot{s}$, the Einstein equation (7.21) becomes

$$M_{0,t} = \dot{s}\hat{M}_{,s} \simeq -16\pi f_\Omega. \tag{G.17}$$

This gives

$$\hat{u}_1 := -\frac{\hat{a}\hat{M}_{,s}}{16\pi(1+\kappa)R\hat{\rho}\hat{\alpha}}, \tag{G.18}$$

which can be checked to be equivalent to the above expression of v_1.

The momentum balance law is obeyed to leading order in $\dot{s}^2$ by construction. Going to the next order, we see that the $Y_{,t}$ term, with $Y \propto u_1\dot{s}$, produces a term proportional to $\ddot{s}$.We consider $s\ddot{s}$ as the same order as $\dot{s}^2$, which is true when $s(t)$ is either exponential or a power.

The second-order balance law can be written compactly as

$$\frac{s\ddot{s}}{\dot{s}^2} = K(y,\mu). \tag{G.19}$$

Since we are considering second order perturbation, each term in $K(y,\mu)$ is either proportional to Z_2 or v_1^2 and its derivatives. The LHS is a function of μ only and is evaluated at $t(\mu) = s^{-1}\left(\ell\sqrt{\mu}\right)$. Thus there exists some function $G(\mu)$ such that

$$\frac{s\ddot{s}}{\dot{s}^2} = G(\mu) = K(y,\mu). \tag{G.20}$$

The first equality, for given $G(\mu)$, can be viewed as an ODE for $s(t)$. Since the only appearance of derivatives of Z_2 terms in $K(y,\mu)$ is $\varrho_{2,y}$, the second equality is a linear inhomogeneous (because of terms involving v_1) PDE for ϱ_2. $G(\mu)$ is determined by the boundary conditions for this PDE.

Interestingly, the term $\sim \chi_2$ in the expression for $K(y,\mu)$ drops out so that to close the system, the PDE (G.20) needs to be supplemented with a second PDE for M_2, which can be computed from the expression for $M_{,r}$ given in (7.20). Altogether, the PDE system for M_2 and ϱ_2 is

$$\bar{M}_{2,y} = \frac{2\bar{x}_{,y}^2}{\bar{x}^2}\left(\bar{\varrho}_2 + (1+\kappa)\bar{\varrho}\bar{v}_1^2\right), \tag{G.21}$$

$$\bar{\varrho}_{2,y} = m\bar{M}_2 + n\bar{\varrho}_2 + I, \tag{G.22}$$

where for convenience we have defined

$$m := -\frac{\partial\bar{x}^2}{\partial y}\frac{(1+\kappa)\bar{\varrho}\left(2\kappa\bar{\varrho}+\mu\bar{x}^2\right)}{2\kappa\bar{x}^2\left(\bar{M}-\mu\bar{x}^2\right)^2}, \tag{G.23}$$

$$n := -\frac{\partial\bar{x}^2}{\partial y}\frac{\left(4\kappa(1+\kappa)\bar{\varrho}+2\kappa\bar{M}+\bar{x}^2(\mu-\kappa\mu)\right)}{\kappa\bar{x}\left(\mu\bar{x}^2-\bar{M}\right)}. \tag{G.24}$$

The inhomogeneous term I which consists only of terms proportional to either $\bar{v}_1, \bar{v}_{1,\mu}$ (from $Y_{,t}$), as well as terms proportional to $\bar{v}_1^2, \bar{v}_{1,y}^2$ (from the flux and source terms) and $G(\mu)$ is more complicated and will not be written here. For completeness, we also give the PDE for $\bar{\chi}_2$,

$$\bar{\chi}_{2,y} = \frac{4}{\bar{x}^2\bar{x}_{,y}^2}\left(\frac{\mu\bar{x}^2-(1-\kappa)\bar{\varrho}}{\mu\bar{x}^2-\bar{M}}\bar{M}_2 - (1-\kappa)\bar{\varrho}\right). \tag{G.25}$$

The system (G.21)-(G.22) can be rewritten as a single second-order PDE for M_2,

$$ay^2\bar{M}_{2,yy} + by\bar{M}_{2,y} + c\bar{M}_2 + d = 0, \tag{G.26}$$

$$a := \left(1 - \left(1 - y^{1+\frac{1}{\kappa}}\right)\mu\right), \tag{G.27}$$

$$b := \frac{3 + 2\kappa(1-\mu) - \left(3 - y^{1+\frac{1}{\kappa}}\right)\mu}{\kappa}, \tag{G.28}$$

$$c := \frac{2(1+\kappa)(1-\mu)}{\kappa^2}. \tag{G.29}$$

The complementary function of this ODE is

$$\bar{M}_{2,\text{homog}} = C_1\delta\bar{M} + C_2\bar{M}_c, \tag{G.30}$$

$$\begin{aligned}\delta\bar{M} :=\ & \kappa\mu(\mu - \kappa(1-\mu)) - y^{-2/\kappa}\kappa(1-\mu)(1-\mu-\kappa\mu) + \\ & y^{-1-\frac{1}{\kappa}}(1-y^2)\left(\mu^2(1+\kappa) - \mu\right) + y^{-1-\frac{1}{\kappa}}\kappa(1-2\mu),\end{aligned} \tag{G.31}$$

$$M_c := -\mu y^{1-\frac{1}{\kappa}} + \kappa(1-\mu)y^{-2/\kappa}. \tag{G.32}$$

$\delta\bar{M}$ corresponds to a perturbation of the background static solution of the form $a \to s + \delta s$, keeping R fixed (zero-mode). Note that in order to avoid a conical singularity at the origin, we need to impose $C_2 = 0$. Similarly, note that at $y \to \infty$, $\bar{M}_{2,\text{homog}}$ is an arbitrary constant.

It is interesting to note that the inhomogeneous term $d \sim y^{-2+2/\kappa}$ for large G and assuming $\nu \neq 0$. Assuming that M_2 and its derivatives remain finite at infinity, we can then only retain the first and last term in (G.26), which solution is schematically given by

$$\bar{M}_{2,\text{asympt}} = Cy^{-3+1/\kappa} + C_1 + yC_2. \tag{G.33}$$

C_1 and C_2 are integration constants, while C is given explicitly only in terms of κ and μ, but not G. Just as for the homogeneous equation, we have the regularity condition $C_2 = 0$, which mirrors the regularity condition one would need to impose at the center to avoid conical singularities. Finally, for $\kappa \geq 1/3$, $\bar{M}_{2,\text{asympt}}$ is again any arbitrary constant, while for $\kappa < 1/3$, it is singular. This singular region can already be spotted from (G.21), since for large y, $\bar{x}^2_{,y} \sim y$, $\bar{\varrho} \sim y^{1-1/\kappa}$ and $v_1 \sim y^{-2+1/\kappa}$.

In order to gain more analytic handle on this PDE, let us turn our attention to the singular case $\mu = 0$ which corresponds to $\Lambda = 0$ identically. We recall (see Appendix F) that in this case, $y \to \infty$ is mapped to a finite radius coordinate $x = x_\star$ where the background variables are singular. It is therefore not simple to decide on the appropriate boundary conditions to impose at the surface, although one would expect the solution for $\mu \ll 1$ to be well approximated by the solution for $\mu = 0$ at least near the center. The coordinates are then y and t instead of y and μ. The scale $s = s(t)$ is then a function of t only while (G.20) simplifies to

$$\frac{s\ddot{s}}{\dot{s}^2} = G(0) = K(y, 0). \tag{G.34}$$

$s(t)$ is then a power law if $G_0 := G(0) \neq 1$ and an exponential if $G_0 = 1$. The PDE system then reduces to an ODE system where the inhomogeneous term greatly simplifies to

$$d := 2y^{-1-\frac{1}{\kappa}} \frac{\left(1 - 6y^{-1+\frac{1}{\kappa}}\right)\kappa + G_0(1+\kappa)}{\kappa^2(1+\kappa)}. \tag{G.35}$$

The ODE is an inhomogeneous Cauchy-Euler equation. Using standard techniques, its general solution is

$$M_2 = C_1\delta\bar{M} + C_2\bar{M}_c + \frac{6\kappa\left(y^{-2} - y^{-\frac{2}{\kappa}}\right)}{(1-\kappa)^2(1+\kappa)} - \frac{2(G_0(1+\kappa)+\kappa)y^{-1-\frac{1}{\kappa}}\ln y}{\kappa\left(1-\kappa^2\right)} \tag{G.36}$$

where C_1 and C_2 are integration constants.

Imposing the regularity condition $M_2(1) = 0$ fixes $C_2 = 0$. As remarked before, it is not obvious what the appropriate boundary conditions are at infinity.

We had hoped to find a natural boundary condition for M_2 at infinity that would select the value $G(\mu) = 1$ of the separation constant, in order to predict the observed exponential form of $s(t)$. This would have been similar in spirit to the approach of Ref. [175] for a quasistatic critical solution (in Yang-Mills on flat spacetime in $4+1$ dimensions).

However, we have not found such a boundary condition. In particular, M_2 is finite at $R = \infty$ (and can then be set to zero there by adding a multiple of $\hat{M}_{,s}$) for all $\kappa \geq 1/2$, but for all $\kappa < 1/3$ it blows up at $R = \infty$, with $G(\mu)$ only affecting lower-order terms. For $1/3 < \kappa < 1/2$, M_2 is finite, but since u_1 is not, the quasistatic ansatz is also not valid in this case, as $\dot{s}u_1$ can then not be considered as small.

One can try to circumvent the problem by imposing a second boundary condition at the center. The advantage of restricting our attention to the center as opposed to the surface is that one expects the effects of μ to only play a perturbative role. However, there are many boundary conditions for which $G_0 = 1$, but we currently do not have a natural prescription justifying it a priori.

Appendix H

Stationary test fluid solutions

To understand better what happens for $\kappa \leq 1/2$, where u_1 diverges at infinity, we note that the fluid in the atmosphere can be approximated as a test fluid on a fixed BTZ spacetime with mass $\check{M}_\infty$.

The solutions describing a stationary test fluid with constant mass flux on a BTZ spacetime with mass M can be given in implicit form as

$$\begin{aligned} v(1-v^2)^{\frac{1-\kappa}{2\kappa}} &= \frac{f_\Omega}{C\rho_0(1+\kappa)} \frac{(-M-\Lambda R^2)^{\frac{1-\kappa}{2\kappa}}}{R} \qquad \text{(H.1)} \\ \rho &= \rho_0(-M-\Lambda R^2)^{-\frac{1+\kappa}{2\kappa}}(1-v^2)^{\frac{1+\kappa}{2\kappa}}. \qquad \text{(H.2)} \end{aligned}$$

Here, the free parameter f_Ω is the constant mass flux, $C := a\alpha$ is a constant in vacuum that depends on the normalization of the time coordinate t, and the free parameter ρ_0 is an overall factor in ρ chosen so that it is the density at the center in the static solution on adS spacetime.

We note that generically, Eq. (H.1) has either two solutions v or none. From

$$v(1-v^2)^{\frac{1-\kappa}{2\kappa}} \sim R^{\frac{1-2\kappa}{\kappa}}, \qquad \text{(H.3)}$$

we see that for $\kappa > 1/2$, either $v \to 0$ or $v \to \pm 1$ as $R \to \infty$. The $v \to 1$ solution is the one relevant for our critical solution. We then have

$$\rho \sim R^{-\frac{1+\kappa}{1-\kappa}}. \qquad \text{(H.4)}$$

However, for $\kappa < 1/2$, the right-hand side of Eq. (H.1) increases with R, and so v is defined only up to some maximum value of R, beyond which the constant flux solution does not exist (for given f_Ω and ρ_0).

In the top two plots of Fig. 7.14, we show that this ansatz for $\kappa = 0.47$ is in good agreement with our numerical solution up to the numerical outer boundary. The radius after which v is not defined as explained above lies outside our numerical grid.

Bibliography

[1] C. Gundlach and P. Bourg. "Rigidly rotating perfect fluid stars in $2+1$ dimensions". Phys. Rev. D **102**, 084023 (2020).

[2] C. Gundlach, P. Bourg, and A. Davey. "A fully constrained, high-resolution shock-capturing, formulation of the Einstein-fluid equations in $2+1$ dimensions". Phys. Rev. D **104**, 024061 (2021).

[3] P. Bourg and C. Gundlach. "Critical collapse of a spherically symmetric ultrarelativistic fluid in $2+1$ dimensions". Phys. Rev. D **103**, 124055 (2021).

[4] P. Bourg and C. Gundlach. "Critical collapse of an axisymmetric ultrarelativistic fluid in $2+1$ dimensions". Phys. Rev. D **104**, 104017 (2021).

[5] P. O. Mazur. "Proof of uniqueness of the Kerr-Newman black hole solution". J. Phys. A**15**, 3173 (1982).

[6] R. M. Wald. "General Relativity". University of Chicago Press (1984).

[7] C. A. R. Herdeiro and E. Radu. "Kerr black holes with scalar hair". Phys. Rev. Lett. **112**, 221101 (2014).

[8] R. Bartnik and J. McKinnon. "Particlelike Solutions of the Einstein-Yang-Mills Equations". Phys. Rev. Lett. **61**, 141 (1988).

[9] P. Bizoń. "Colored Black Holes". Phys. Rev. Lett. **64**, 2844 (1990).

[10] B. P. et al. Abbott. "Observation of Gravitational Waves from a Binary Black Hole Merger". Phys. Rev. Lett. **116**, 061102 (2016).

[11] B. P. Abbott et al. "GW170817: Observation of Gravitational Waves from a Binary Neutron Star Inspiral". Phys. Rev. Lett. **119**, 161101 (2017).

[12] The Event Horizon Telescope Collaboration et al. "First M87 Event Horizon Telescope Results. I. The Shadow of the Supermassive Black Hole". The Astrophysical Journal Letters, **875**, 1 (2019).

[13] R. et al Abbott. "Observation of Gravitational Waves from Two Neutron Star–Black Hole Coalescences". Astrophys. J. Lett. **915**, L5 (2021).

[14] J. R. Oppenheimer and H. Snyder. "On Continued Gravitational Contraction". Phys. Rev. **56**, 455 (1939).

[15] P. S. Joshi and D. Malafarina. "Recent developments in gravitational collapse and spacetime singularities". Int. J. Mod. Phys. D, 20 14 pp 2641-2729 (2011).

[16] J. M. M. Senovilla and D. Garfinkle. "The 1965 Penrose singularity theorem". Classical and Quantum Gravity (2015).

[17] M. V. Penston. "Dynamics of self-gravitating gaseous spheres- III. Analytical results in the free-fall of isothermal cases". Mon. Not. R. astr. Soc., **144**, 425 (1969).

[18] R. B. Larson. "Numerical calculations of the dynamics of collapsing proto-star". Mon. Not. R. astr. Soc., **145**, 271. (1969).

[19] R. Penrose. "Gravitational collapse and space-time singularities". Phys. Rev. Lett. **14**, 57 (1965).

[20] R. Penrose. "Gravitational collapse: the role of general relativity". Nuovo Cimento **1** 252-76 (1969).

[21] R. Geroch. "Domain of dependence". J. Math. Phys. **11**, 437 (1970).

[22] S.W. Hawking and G.F.R. Ellis. "The Large Scale Structure of Space-Time". Cambridge University Press (1973).

[23] R. Schoen and S. T. Yau. "The existence of a black hole due to condensation of matter". Commun. Math. Phys. **90**, 575-579 (1983).

[24] D. Christodoulou. "The Formation of Black Holes in General Relativity". arXiv:0805.3880 [gr-qc] (2009).

[25] M. Wald and V. Iyer. "Trapped surfaces in the Schwarzschild geometry and cosmic censorship". Phys. Rev. D **44**, R3719(R) (1991).

[26] R. Penrose. "Singularities in cosmology". *Confrontation of Cosmological Theories with Observational Data*. Vol. 63. 1974, pp. 263–271.

[27] D. Christodoulou. "On the global initial value problem and the issue of singularities". Class. Quant. Grav **16**, 12A (1998).

[28] G. T. Horowitz. "Finding a statement of cosmic censorship". Gen. Rel. Gravit. **10**, 1057–1061 (1979).

[29] H. S. Reall. "Part III Black Holes" (2017).

[30] Y. C. Ong. "Spacetime Singularities and Cosmic Censorship Conjecture: A Review with Some Thoughts". Int. J. Mod. Phys. A, 35 14, 2030007 (2020).

[31] P. Szekeres and A. Lun. "WHAT IS A SHELL-CROSSING SINGULARITY?" J. Austral. Math. Soc. Ser. B 41, 167-179 (1999).

[32] R. Penrose. "Singularities and time-asymmetry". Part of General Relativity : An Einstein Centenary Survey, 581-638 (1979).

[33] D. Christodoulou. "Violation of cosmic censorship in the gravitational collapse of a dust cloud". Comm. Math. Phys. **93**, 171-195 (1984).

[34] M. Dafermos and J. Luk. "The interior of dynamical vacuum black holes I: The C_0-stability of the Kerr Cauchy horizon". arXiv:1710.01722 [gr-qc] (2017).

[35] J. Sbierski. "C^0-inextendibility of the Schwarzschild spacetime and the spacelike diameter in Lorentzian geometry". J. Diff. Geom. **108**(2), 319-378 (2015).

[36] V. Cardoso et al. "Quasinormal Modes and Strong Cosmic Censorship". Phys. Rev. Lett. **120** 031103 (2018).

[37] V. Cardoso et al. "Strong Cosmic Censorship in Charged Black-Hole Spacetimes: Still Subtle". Phys. Rev. D **98**, 104007 (2018).

[38] O.J. Dias, H.S. Reall, and J.E. Santos. "Strong cosmic censorship for charged de Sitter black holes with a charged scalar field". Class. Quantum Grav. **36**, 045005 (2019).

[39] O.J. Dias et al. "Strong cosmic censorship in de Sitter space". Phys. Rev. D **97**, 104060 (2018).

[40] O.J. Dias, H.S. Reall, and J.E. Santos. "The BTZ black hole violates strong cosmic censorship". J. High Energ. Phys. **2019**, 97 (2019).

[41] R. Luna et al. "Strong cosmic censorship: The nonlinear story". Phys. Rev. D **99**, 064014 (2019).

[42] D. Christodoulou. "The Instability of Naked Singularities in the Gravitational Collapse of a Scalar Field". Ann. Math. (2), **149**, 183–217 (1999).

[43] M. Dafermos et al. "The non-linear stability of the Schwarzschild family of black holes". arXiv:2104.08222 [gr-qc] (2021).

[44] J. Sorce and R. M. Wald. "Gedanken experiments to destroy a black hole. II. Kerr-Newman black holes cannot be overcharged or overspun". Phys. Rev. D **96**, 104014 (2017).

[45] S.W. Hawking. "Black Holes in General Relativity". Commun. Math. Phys. **25**, 152 (1972).

[46] R. Emparan and H. S. Reall. "Black Holes in Higher Dimensions". Living Rev. Relativ. **11**, 6 (2007).

[47] R. Gregory and R. Laflamme. "Black strings and p-branes are unstable". Phys. Rev. Lett. **70**, 2837 (1993).

[48] L. Lehner and F. Pretorius. "Black Strings, Low Viscosity Fluids, and Violation of Cosmic Censorship". Phys. Rev. Lett. **105**, 101102 (2010).

[49] P. Figueras, M. Kunesch, and S. Tunyasuvunakool. "The Endpoint of Black Ring Instabilities and the Weak Cosmic Censorship Conjecture". Phys. Rev. Lett. **116**, 071102 (2016).

[50] P Figueras, L. Lehner, and S. Tunyasuvunakool. "The Endpoint of Ultraspinning Instability and Violation of Cosmic Censorship". Phys. Rev. Lett. **118**, 151103 (2017).

[51] T. Andrade, P. Figueras, and U. Sperhake. "Violations of Weak Cosmic Censorship in Black Hole collisions". arXiv:2011.03049 [hep-th] (2020).

[52] M. W. Choptuik. "Universality and scaling in gravitational collapse of a massless scalar field". Phys. Rev. Lett. **70**, 9 (1993).

[53] A. A. García and C. Gundlach. "Global structure of Choptuik's critical solution in scalar field collapse". Phys. Rev. D **68**, 024011 (2003).

[54] A. Ori and T. Piran. "Naked singularities and other features of self-similar general-relativistic gravitational collapse". Phys. Rev. D **42**, 4 (1990).

[55] B. J. Carr and C. Gundlach. "Spacetime structure of self-similar spherically symmetric perfect fluid solutions". Phys. Rev. D **67**, 024035 (2003).

[56] C. Gundlach and J. M. Martín-García. "Critical phenomena in gravitational collapse". Living Rev. Relativ. **10**, 5 (2007).

[57] T. W. Baumgarte, C. Gundlach, and D. Hilditch. "Critical phenomena in the gravitational collapse of electromagnetic waves". Phys. Rev. Lett. **123**, 17 (2019).

[58] M. Bañados, C. Teitelboim, and J. Zanelli. "Black Hole in Three-Dimensional Spacetime". Phys. Rev. Lett. **69**, 13 (1992).

[59] D. Ida. "No Black-Hole Theorem in Three-Dimensional Gravity". Phys. Rev. Lett. **85**, 18 (2000).

[60] É. Gourgoulhon. "Formalism and Bases of Numerical Relativity". arXiv:0703035 [gr-qc] (2007).

[61] V. Faraoni et al. "Foliation dependence of black hole apparent horizons in spherical symmetry". Phys. Rev. D **95**, 2 (2017).

[62] C. Gundlach. "Understanding critical collapse of a scalar field". Phys. Rev. D **55**, 2 (1996).

[63] S. Hod and T. Piran. "Critical behavior and universality in gravitational collapse of a charged scalar field". Phys. Rev. D **55**, 3485 (1997).

[64] P. R. Brady, C. M. Chambers, and S. M. C. V. Gonc̀alves. "Phases of massive scalar field collapse". Phys. Rev. D **56**, R6057 (1997).

[65] C. R. Evans and J. S. Coleman. "Critical Phenomena and Self-Similarity in the Gravitational Collapse of Radiation Fluid". Phys. Rev. Lett. **72**, 1782–1785 (1994).

[66] D. Maison. "Non-Universality of Critical Behaviour in Spherically Symmetric Gravitational Collapse". Phys. Lett. B **366**, 1 pp82-84 (1995).

[67] D. W. Neilsen and M. W. Choptuik. "Critical phenomena in perfect fluids". Class. Quant. Grav. **17**, 761 (2000).

[68] D. W. Neilsen and M. W. Choptuik. "Ultrarelativistic fluid dynamics". Class. Quant. Grav. **17**, 733 (2000).

[69] M. W. Choptuik, T. Chmaj, and P. Bizoń. "Critical Behaviour in Gravitational Collapse of a Yang-Mills Field". Phys. Rev. Lett. **77**, 3 (1996).

[70] C. Gundlach. "Echoing and scaling in Einstein-Yang-Mills critical collapse". Phys. Rev. D **55**, 6002 (1997).

[71] M. W. Choptuik, E. W. Hirschmann, and R. L. Marsa. "New critical behavior in Einstein-Yang-Mills collapse". Phys. Rev. D **60**, 12 (1999).

[72] M. Maliborski and O. Rinne. "Critical phenomena in the general spherically symmetric Einstein-Yang-Mills system". Phys. Rev. D **97**, 4 (2018).

[73] Y. Peleg and A. R. Steif. "Phase transition for gravitationally collapsing dust shells in $2+1$ dimensions". Phys. Rev. D **51**, 8 (1995).

[74] F. Pretorius and M. W. Choptuik. "Gravitational collapse in $2+1$ dimensional AdS spacetime". Phys. Rev. D **62**, 12 (2000).

[75] H. Kim, S. Moonb, and J. H. Yee. "Dimensional dependence of black hole formation in self-similar collapse of scalar field". JHEP 2002, 02 (2002).

[76] L. Álvarez-Gaumé, C. Gómez, and M. A. Vázquez-Mozo. "Scaling Phenomena in Gravity from QCD". Phys. Lett. B649, pp 478-482 (2007).

[77] J. Bland and G. Kunstatter. "The 5-D Choptuik critical exponent and holography". Phys. Rev. D **75**, 10 (2007).

[78] J. Jałmużna, C. Gundlach, and T. Chmaj. "Scalar field critical collapse in $2+1$ dimensions". Phys. Rev. D **92**, 12 (2015).

[79] V. Husain. "Critical Behaviour in Quantum Gravitational Collapse". Adv. Sci. Lett., **2**, 214–220 (2009).

[80] J. Ziprick and G. Kunstatter. "Dynamical singularity resolution in spherically symmetric black hole formation". Phys. Rev. D, **80**, 024032 (2009).

[81] S. Golod and T. Piran. "Choptuik's critical phenomenon in Einstein-Gauss-Bonnet gravity". Phys. Rev. D **85**, 104015 (2012).

[82] J. V. Rocha and M. Tomašević. "Self-similarity in Einstein-Maxwell-dilaton theories and critical collapse". Phys. Rev. D **98**, 10 (2018).

[83] D. Garfinkle, C. Gundlach, and J. M. Martín-García. "Angular momentum near the black hole threshold in scalar field collapse". Phys. Rev. D **59**, 104012 (1999).

[84] M. W. Choptuik et al. "Critical Collapse of the Massless Scalar Field in Axisymmetry". Phys. Rev. D **68**, 044007 (2003).

[85] M. W. Choptuik et al. "Critical Collapse of a Complex Scalar Field with Angular Momentum". Phys. Rev. Lett. **93**, 131101 (2004).

[86] J. Healy and P. Laguna. "Critical collapse of scalar fields beyond axisymmetry". Gen. Relativ. Gravit. **46**, 5 (2014).

[87] J. Jałmużna and C. Gundlach. "Critical collapse of a rotating scalar field in $2+1$ dimensions". Phys. Rev. D **95**, 084001 (2017).

[88] C. Gundlach. "Critical gravitational collapse of a perfect fluid: Nonspherical perturbations". Phys. Rev. D **65**, 8 (2002).

[89] T. W. Baumgarte and P. J. Montero. "Critical phenomena in the aspherical gravitational collapse of radiation fluids". Phys. Rev. D **92**, 12 (2015).

[90] T. W. Baumgarte and C. Gundlach. "Critical collapse of rotating radiation fluid". Phys. Rev. Lett. **116**, 22 (2016).

[91] C. Gundlach and T. W. Baumgarte. "Critical gravitational collapse with angular momentum". Phys. Rev. D **94**, 8 (2016).

[92] C. Gundlach and T. W. Baumgarte. "Critical gravitational collapse with angular momentum. II. Soft equations of state". Phys. Rev. D **97**, 06 (2018).

[93] A. M. Abrahams and C. R. Evans. "Critical Behavior and Scaling in Vacuum Axisymmetric Gravitational Collapse". Phys. Rev. Lett. **70**, 2980 (1993).

[94] A. M. Abrahams and C. R. Evans. "Universality in axisymmetric vacuum collapse". Phys. Rev. D **49**, 8 (1994).

[95] P. Bizoń, T. Chmaj, and B.G. Schmidt. "Critical Behavior in Vacuum Gravitational Collapse in $4 + 1$ Dimensions". Phys. Rev. Lett. **95**, 071102 (2005).

[96] T. Ledvinka and A. Khirnov. "Universality of curvature invariants in critical vacuum gravitational collapse". arXiv:2102.09579 [gr-qc] (2021).

[97] M. F. P. Mendoza and T. W. Baumgarte. "Critical phenomena in the gravitational collapse of electromagnetic dipole and quadrupole waves". Phys. Rev. D **103**, 124048 (2021).

[98] B. J. Carr and A. A. Coley. "Self-similarity in general relativity". Class. Quant. Grav. **16**, 7 (1998).

[99] T. Harada. "Self-Similar Solutions, Critical Behavior and Convergence to Attractor in Gravitational Collapse". **156** WU-AP (2003).

[100] B. J. Carr and A. A. Coley. "The Similarity Hypothesis in General Relativity". Gen. Rel. Grav. **37**, 2165-2188 (2005).

[101] T. Harada. "Singularities and self-similarity in gravitational collapse". Advanced Studies in Pure Mathematics **55**, pp 15-30 (2009).

[102] I. Musco and J. C. Miller. "Primordial black hole formation in the early universe: critical behaviour and self-similarity". Class. Quant. Grav. **30**, 14 (2013).

[103] F. Kühnel, C. Rampf, and M. Sandstad. "Effects of Critical Collapse on Primordial Black-Hole Mass Spectra". Euro. Phys. J. C **76**, 2 (2016).

[104] J. M. Maldacena. "The Large N limit of superconformal field theories and supergravity". Int. J. Theor. Phys. **38**, 1113–1133 (1999).

[105] B. Wu. "On holographic thermalization and gravitational collapse of massless scalar field". JHEP **1210**, 133 (2012).

[106] P. M. Chesler and B. Way. "Holographic Signatures of Critical Collapse". Phys. Lev. Lett. **122**, 23 (2019).

[107] H. Maeda and M. Nozawa. "Generalized Misner-Sharp quasi-local mass in Einstein-Gauss-Bonnet gravity". Phys. Rev. D **77**, 064031 (2008).

[108] L. B. Szabados. "Quasi-Local Energy-Momentum and Angular Momentum in GR: A Review Article". Living Rev. Relativ. **7**, 4 (2004).

[109] C. W. Misner and D. H. Sharp. "Relativistic Equations for Adiabatic, Spherically Symmetric Gravitational Collapse". Phys. Rev. **136**, B571 (1964).

[110] H. Kodama. "Conserved energy flux for the spherically symmetric system and the back-reaction problem in the black hole evaporation". Prog. Theor. Phys. **63**, 1217 (1980).

[111] István Rácz. "On the use of the Kodama vector field in spherically symmetric dynamical problems". Class. Quant. Grav. **23**, 115 (2005).

[112] S. A. Hayward. "Gravitational energy in spherical symmetry". Phys. Rev. D **53**, 1938-1949 (1996).

[113] L. I. Petrich, S. L. Shapiro, and S. A. Teukolsky. "Oppenheimer-Snyder collapse in polar time slicing". Phys. Rev. D **33**, 2100 (1986).

[114] S. L. Shapiro and S. A. Teukolsky. "Relativistic Stellar Dynamics on the Computer. IV. Collapse of a Star Cluster to a Black Hole". The Astrophysical Journal **307**, 575 (1986).

[115] J. Winicour. "Characteristic Evolution and Matching". Living Rev. Relativ. **12**, 3 (2009).

[116] S. Hod and T. Piran. "Fine structure of Choptuik's mass-scaling relation". Phys. Rev. D **55**, R440(R) (1997).

[117] D. Garfinkle and G. C. Duncan. "Scaling of curvature in sub-critical gravitational collapse". Phys. Rev. D **58**, 6 (1998).

[118] C. Gundlach and J. M. Martín-García. "Charge scaling and universality in critical collapse". Phys. Rev. D **54**, 7353 (1996).

[119] M. E. Cahill and A. H. Taub. "Spherically symmetric similarity solutions of the Einstein field equations for a perfect fluid". Commun. Math. Phys. **21**, 1-40 (1971).

[120] J. Wainwright and P.E.A. Yaremovicz. "Killing Vector Fields and the Einstein-Maxwell Field Equations with Perfect Fluid Source". arXiv:9607010 [gr-qc] (1997).

[121] C. Gundlach. "The Choptuik Spacetime as an Eigenvalue Problem". Phys. Rev. Lett. **75**, 3214–3217 (1995).

[122] C. Gundlach. "Angular momentum at the black hole threshold". Phys. Rev. D **57**, R7080 (1998).

[123] J. M. Martín-García and C. Gundlach. "All nonspherical perturbations of the Choptuik spacetime decay". Phys. Rev. D **59**, 064031 (1999).

[124] D. Hilditch, A. Weyhausen, and B. Brügmann. "Evolutions of centered Brill waves with a pseudospectral method". Phys. Rev. D **96**, 104051 (2017).

[125] S. A. Teukolsky. "Linearized quadrupole waves in general relativity and the motion of test particles". Phys. Rev. D **26**, 745 (1982).

[126] E. Sorkin. "On critical collapse of gravitational waves". Class. Quant. Grav. **28**, 025011 (2011).

[127] D. R. Brill. "On the positive definite mass of the Bondi Weber-Wheeler time-symmetric gravitational waves". Annals of Physics **7**, 466 (1959).

[128] P. Bizoń and A. Rostworowski. "Weakly turbulent instability of anti-de Sitter space". Phys. Rev. Lett. **107**, 031102 (2011).

[129] G. Martinon. "The instability of anti-de Sitter space-time". arXiv:1708.05600 [gr-qc] (2017).

[130] D. Garfinkle. "Exact solution for $(2+1)$-dimensional critical collapse". Phys. Rev. D **63**, 044007 (2001).

[131] D. Garfinkle and C. Gundlach. "Perturbations of an exact solution for 2+1 dimensional critical collapse". Phys. Rev. D **66**, 044015 (2002).

[132] T. Hara, T. Koike, and S. Adachi. "Renormalization group and critical behaviour in gravitational collapse". arXiv:9607010 [gr-qc] (1997).

[133] J. A. Font. "Numerical Hydrodynamics and Magnetohydrodynamics in General Relativity". Living Rev. Relativity **11**, 7 (2008).

[134] M. Alcubierre. "Introduction to $3+1$ numerical relativity". Oxford University Press, New York (2008).

[135] S. K. Godunov. "A difference method for numerical calculation of discontinuous solutions of the equations of hydrodynamics". Mat. Sb. **47**, pp.271-306 (1959).

[136] R. J. LeVeque. "Finite Volume Methods for Hyperbolic Problems". Cambridge University Press (2002).

[137] T. Koike, T. Hara, and S. Adachi. "Critical behaviour in gravitational collapse of radiation fluid — A renormalization group (linear perturbation) analysis —". Phys. Rev. Lett. **74**, 5170-5173 (1995).

[138] C. Hunter. "The collapse of unstable isothermal spheres". Astrophys. J., 218, 834. (1977).

[139] A. Ori and T. Piran. "Naked Singularities in Self-Similar Spherical Gravitational Collapse". Phys. Rev. Lett. **59**, 2137 (1987).

[140] T. Harada and H. Maeda. "Convergence to a self-similar solution in general relativistic gravitational collapse". Phys. Rev. D **63**, 084022 (2001).

[141] T. Harada. "Stability criterion for self-similar solutions with perfect fluids in general relativity". Class. Quantum Grav. **18**, 4549 (2001).

[142] H. Maeda and T. Harada. "Critical phenomena in Newtonian gravity". Phys. Rev. D **64**, 124024 (2001).

[143] T. Harada, H. Maeda, and B. Semelin. "Criticality and convergence in Newtonian collapse". Phys. Rev. D **67**, 084003 (2003).

[144] J. Celestino and T. W. Baumgarte. "Critical collapse of ultrarelativistic fluids: Damping or growth of aspherical deformations". Phys. Rev. D **98**, 024053 (2018).

[145] V. Husain et al. "Anti-de Sitter gravitational collapse". Class. Quantum Grav. **20**, L23 (2003).

[146] L. M. Sokołowski. "The bizarre anti-de Sitter spacetime". Int. J. Geom. Meth. Mod. Phys. **13**, 9 (2016).

[147] G. Compère and A. Fiorucci. "Advanced Lectures on General Relativity". arXiv:1801.07064 [hep-th] (2017).

[148] M. Bañados et al. "Geometry of the $2+1$ black hole". Phys. Rev. D **48**, 4 (1993).

[149] S. Carlip. "The $(2+1)$-Dimensional Black Hole". Class. Quant. Grav. **12**, 2853 (1995).

[150] L. Donnay. "Asymptotic dynamics of three-dimensional gravity". arXiv:1602.09021 [hep-th] (2016).

[151] S. S. Costa. "A Description of several coordinate systems for hyperbolic spaces". arXiv:math-ph/0112039 [gr-qc] (2001).

[152] A. Ishibashi and R. W. Wald. "Dynamics in Non-Globally-Hyperbolic Static Spacetimes". Class. Quant. Grav. **21**, pp 2981-3014 (2004).

[153] C. Dappiaggi and H. R. C. Ferreira. "Hadamard states for a scalar field in anti-de Sitter spacetime with arbitrary boundary conditions". Phys. Rev. D **94**, 125016 (2016).

[154] H. S. Reall. "Part III General Relativity" (2017).

[155] Ó. J. C. Oscar, G. T. Horowitz, and J. E. Santos. "Gravitational turbulent instability of anti-de Sitter space". Class. Quantum Grav. **29**, 194002 (2012).

[156] G. T. Horowitz and J. E. Santos. "Geons and the Instability of Anti-de Sitter Spacetime". arXiv:1408.5906 [gr-qc] (2014).

[157] G. Moschidis. "A proof of the instability of AdS for the Einstein–massless Vlasov system". arXiv:1812.04268 [math.AP] (2018).

[158] G. Moschidis. "A proof of the instability of AdS for the Einstein-null dust system with an inner mirror". Analysis & PDE 13.6 (2020), pp. 1671–1754.

[159] L. M. Sokołowski and Z. A. Golda. "Every timelike geodesic in anti–de Sitter spacetime is a circle of the same radius". Intern. J. Mod. Phys. **D25**, 1650007 (2016).

[160] S. Deser, R. W. Jackiw, and G.t Hooft. "Three-dimensional Einstein gravity: Dynamics of flat space". Annals of Physics **152**, 220 (1984).

[161] F. P. Schuller. "Lectures on the Geometric Anatomy of Theoretical Physics" (2013).

[162] N. Cruz and J. Zanelli. "Stellar Equilibrium in $2+1$ Dimensions". Class. Quantum Grav. **12**, 975 (1995).

[163] N. J. Cornish and N. E. Frankel. "Gravitation in $2+1$ dimensions". Phys. Rev. D **43**, 2555 (1991).

[164] P. M. Sá. "Polytropic Stars in Three-Dimensional Spacetime". Polytropic Stars in Three-Dimensional Spacetime (1999).

[165] A. A. García and C. Campuzano. "All static circularly symmetric perfect fluid solutions of gravity". Phys. Rev. D **67**, 064014 (2003).

[166] N. J. Cornish and N. E. Frankel. "Gravitation vs. Rotation in $2+1$ Dimensions". Class. Quantum Grav. **11**, 723 (1994).

[167] M. Lubo, M. Rooman, and Ph. Spindel. "$(2+1)$-dimensional stars". Phys. Rev. D **59**, 044012 (1999).

[168] M. Cataldo. "Rotating perfect fluids in $(2+1)$-dimensional Einstein gravity". Phys. Rev. D **69**, 064015 (2004).

[169] S. Holst and H. J. Matschull. "The anti-de Sitter Gott universe: a rotating BTZ wormhole". Class. Quant. Grav. **16**, 3095 (1999).

[170] S. Kinoshita. "Extension of Kodama vector and quasilocal quantities in three-dimensional axisymmetric spacetimes". Phys. Rev. D **103**, 124042 (2021).

[171] P. J. Montero, T. W. Baumgarte, and E. Müller. "General relativistic hydrodynamics in curvilinear coordinates". Phys. Rev. D **89**, 084043 (2014).

[172] B. van Leer. "Towards the ultimate conservative difference scheme I. The quest of monotonicity". Springer Lecture Notes Phys., 18, pp. 163–168 (1973).

[173] B. Einfeldt. "On Godunov-Type Methods for Gas Dynamics". SIAM Journal on Numerical Analysis, **25**, 2, pp. 294-318 (1988).

[174] D. Radice. "Advanced Numerical Approaches in the Dynamics of Relativistic Flows". Radice's PhD thesis (2013).

[175] P. Bizoń, Y. N. Ovchinnikov, and I. M. Sigal. "Collapse of an instanton". Nonlinearity **17**, 4 (2004).

[176] I. Rodnianski and J. Sterbenz. "On the formation of singularities in the critical $O(3)$ σ-model". Annals of Mathematics **172**, pp. 187-242 (2010).

[177] S. W. Hawking. "Gravitational radiation in an expanding universe". J. Math. Phys. **9**, 598-604 (1968).

[178] R. Ruffini and J. A. Wheeler. "Introducing the black hole". Physics Today 24, 1, p. 30 (1971).

[179] J. W. Jr. York. "Gravitational degrees of freedom and the initial-value problem". Phys. Rev. Lett. **26**, 1656-1658 (1971).

[180] J. W. Jr. York. "Role of Conformal Three-Geometry in the Dynamics of Gravitation". Phys. Rev. Lett. **28**, 1082 (1972).

[181] R. W. Wald. "Gedanken Experiments to Destroy a Black Hole". Ann. Phys. **82** 548. (1974).

[182] J. W. Jr. York. "Boundary terms in the action principles of general relativity". Found Phys **16**, 249–257 (1986).

[183] M. S. Volkov and D. Galtsov. "NonAbelian Einstein Yang-Mills black holes". JETP Lett. 50, 346 (1989).

[184] S. L. Shapiro and S. A. Teukolsky. "Formation of naked singularities: The violation of cosmic censorship". Phys. Rev. Lett. **66**, 994 (1991).

[185] R. J. LeVeque. "Numerical Methods for Conservation Laws". 2nd ed. Birkauser (1992).

[186] J. D. Brown and J. W. York. "Quasilocal Energy and Conserved Charges Derived from the Gravitational Action". Phys. Rev. D **47**, 1407-1419 (1992).

[187] D. Christodoulou and S. Klainerman. *The Global Nonlinear Stability of the Minkowski Space (PMS-41)*. Princeton University Press, 1993.

[188] R. B. Mann. "Lower Dimensional Black Holes: Inside and Out". arXiv:9501038 [gr-qc] (1995).

[189] P. Szekeres and A. Lun. "What is a shell-crossing singularity?" J. Austral. Math. Soc. Ser. B **41**, 167-179 (1995).

[190] B. Berger, P. T. Chrusciel, and V. Moncrief. "On "asymptotically flat" space–times with G_2–invariant Cauchy surfaces". Ann. Phys. **237**, 322 (1995).

[191] R. M. Wald. "Gravitational Collapse and Cosmic Censorship". arXiv:9710068 [gr-qc] (1997).

[192] R. B. Mann. "Topological Black Holes – Outside Looking In". arXiv:9709039 [gr-qc] (1997).

[193] M. Alcubierre et al. "Gravitational collapse of gravitational waves in 3D numerical relativity". Phys. Rev. D **61**, 041501(R) (2000).

[194] V. Husain and M. Olivier. "Scalar field collapse in three-dimensional AdS spacetime". Class. Quantum Grav. **18**, L1 (2001).

[195] S. Hod. "Weak Cosmic Censorship: As Strong as Ever". Phys. Rev. Lett. **100**, 121101 (2008).

[196] A. R. Parry. "A survey of spherically symmetric spacetimes". Anal. Math. Phys. **4**, 33-375 (2014).

[197] V. Cardoso et al. "Exploring New Physics Frontiers Through Numerical Relativity". arXiv:1409.0014 [gr-qc] (2014).

[198] A. Allahyari, J. T. Firouzjaee, and R. Mansouri. "Gravitational collapse in the AdS background and the black hole formation". Int. J. Mod. Phys. D **25**, 1 (2015).

[199] B. E. Niehoff, J. E. Santos, and B. Way. "Towards a violation of cosmic censorship". arXiv:1510.00709 [hep-th] (2015).

[200] T. Crisford and J. E. Santos. "Violating weak cosmic censorship in AdS_4". Phys. Rev. Lett. **118**, 181101 (2017).

[201] T. Crisford, G. T. Horowitz, and J. E. Santos. "Testing the Weak Gravity - Cosmic Censorship Connection". Phys. Rev. D **97**, 6 (2019).

[202] G. T. Horowitz and J. E. Santos. "Further evidence for the weak gravity - cosmic censorship connection". JHEP **122** (2019).

[203] T. W. Baumgarte, C. Gundlach, and D. Hilditch. “Critical phenomena in gravitational collapse with two competing massless matter field”. Phys. Rev. D **100**, 10 (2019).

[204] F. C. Eperon, B. Ganchev, and J. E. Santos. “Plausible scenario for a generic violation of the weak cosmic censorship conjecture in asymptotically flat four dimensions”. Phys. Rev. D **101**, 041502 (2019).

[205] O. Rinne. “Type II critical collapse on a single fixed grid: a gauge-driven ingoing boundary method”. Gen. Relativ. Gravit. **52**, 117 (2020).

[206] H. Bantilan, P. Figueras, and L. Rossi. “Cauchy Evolution of Asymptotically Global AdS Spacetimes with No Symmetries”. Phys. Rev. D 103, 086006 (2020).

[207] D. Garfinkle and F. Pretorius. “Spike behavior in the approach to spacetime singularities”. Phys. Rev. D **102**, 124067 (2020).

[208] C. Kelson-Packer and J. Belz. “Investigation into Length Scale Dominance in Critical Black Hole Formation”. Phys. Rev. D **102**, 084050 (2020).

[209] C. Palenzuela. “Introduction to Numerical Relativity”. Front. Astron. Space Sci. **7**, 58 (2020).